Topology optimization of incompressible structures for fluid-structure interaction problems

Universitat Politècnica de Catalunya - Barcelona Tech

Doctoral Program in Civil Engineering
Department of Civil & Environmental Engineering
School of Civil Engineering

Inocencio Castañar Pérez
Advisors: Joan Baiges Aznar – Ramon Codina Rovira

June 16, 2023

To my family

Contents

List of Figures

List of Tables

Acknowledgments

First and foremost, my deepest gratitude to my advisors Prof. Joan Baiges and Prof. Ramon Codina for the opportunity to pursue a PhD under their guidance. Their constant support, scientific rigor and valuable suggestions throughout these years are greatly appreciated.

I would like to thank all the members of the FEMUSS team with whom I have worked during these years, for the fantastic team we have built together. Secondly, I would like to thank all my office mates throughout these years: Alexis, Ricardo, Camilo, Domingo, Irene, Ernesto, Laura, Gabriel, Samuel, Alejandro, Arnau, Zulkeefal and Ignacio to create such an enjoyable environment inside and outside the office. I would like to make special mention to Samuel and Laura, my "Council of Wise persons". We have shared together several interesting projects (which also implies to spend plenty of time discussing about it in our dear gmeet room). I really appreciate the joint support and strength that pulled us together this experience. And, of course, I would like to extend my gratitude to my fellow researchers in CIMNE for the great work environment we have shared together and specially to Carlos and Henning. Special mention also for the "Big 5" group, David, Jordi, Alejandro and Samuel, I really enjoyed the coffee breaks.

Last but not least, I would like to thank the invaluable support of my family and friends, for the moral support and helping me keeping a balanced life. To my parents, role models who provided me with the education, motivation loving guidance and unconditional support that lead me successfully through this journey. To my brother and sister for everything we have shared over past years and for their unfailing support.

The work contained in this dissertation has been financially supported by CIMNE, together with the support received through the TOP-FSI: RTI2018-098276-B-I00 project of the Spanish Government. In addition, the financial support received from the Agència de Gestió d'Ajuts Universitaris i de Recerca through the predoctoral FI grant 2019-FI-B-00649 is gratefully acknowledged.

Abstract

Topology optimization of incompressible structures, in which the loads on the structure come from the stresses exerted by a surrounding fluid, is a highly complex problem. This work presents a compilation of the research conducted to reproduce such complex phenomena.

Firstly, two stabilized mixed finite element methods for finite strain solid dynamics are developed. These stabilized methods are stable for any interpolation spaces of the unknowns. On the one hand, a two-field mixed displacement/-pressure formulation capable of dealing with nearly and fully incompressible hyperelastic material behavior is presented. On the other hand, so as to be able to tackle the incompressible limit and at the same time, to obtain a higher accuracy in the computation of stresses, a three-field mixed displacement/pressure/deviatoric stress formulation is proposed. Stability, mesh convergence analysis and nonlinear iteration convergence analysis are performed together with several numerical examples for both formulations. It is shown that both formulations appropriately deal with the incompressibility constraint, but the three-field formulation exhibits higher accuracy in the stress field, even for very coarse meshes.

Secondly, we develop algorithms for topology optimization problems based on the topological derivative concept. To deal with incompressible materials, mixed formulations must be considered, but also a new decomposition of the well-known Polarization tensor is required for linear elastic materials. In the finite strain hyperelasticity assumption, an approximation of the topological derivative in combination with the mixed formulations previously presented is considered to deal with incompressibility. Several numerical examples are presented and discussed to assess the robustness of the proposed algorithms and their applicability to topology optimization problems for incompressible elastic solids.

Then, we analyze the numerical simulation of the interaction between viscoelastic fluid flows and hyperelastic solids. The fluid-structure interaction problem is solved sequentially. Flow equations are approximated using two stabilized three-field finite element formulations. To address flows with dominant

elasticity, a log-conformation reformulation of the constitutive equation is employed. Several numerical examples are presented and discussed to assess the robustness of the proposed scheme and its applicability to problems with viscoelastic fluids, in which elasticity dominates the interaction with hyperelastic solids.

Finally, all numerical tools are combined to reproduce the topology optimization problem of incompressible structures subjected to the interaction with a surrounding Newtonian fluid.

Acronyms

In this section a list of several acronyms which are used along the thesis is stated.

ALE	arbitrary Langrangian-Eulerian
ASGS	algebraic subgrid scales
BDF	backward differentiation formula
CFD	computational fluid dynamics
CVT	centroidal Voronoi Tessellation
DDF-ROM	data-driven filtered reduced order model
FE	finite element
FEM	finite element method
FEMUSS	finite element method using subgrid scales
FOM	full order model
FSI	fluid-structure interaction
HWNP	high Weissenberg number problem
LCR	log-conformation reformulation
LBB	Ladyzhenskaya-Babuška-Brezzi
MD	minimization direction
MIST	moving iso-surface threshold
OSGS	orthogonal subgrid scales
PK2	second Piola-Kirchhoff
ROM	reduced order model
SBFEM	scaled boundary finite element method
SGS	subgrid scale
SIMP	solid isotropic microstructure with penalization
S-OSGS	orthogonal subgrid scales
SUPG	streamline upwind Petrov-Galerkin
TD	topological derivative
TLF	total Lagrangian formulation
TO	topology optimization
ULF	updated Lagrangian formulation
VFSI	viscoelastic fluid-structure interaction
VMS	variational multiscale

Notation

The notation employed in this study is fairly standard in the literature on computational mechanics. As a general rule and with few exceptions stated in the text, tensors of rank greater than or equal to one are denoted by boldface characters and scalars by lightface italic characters. Moreover, we shall use standard Cartesian notation to refer to a particular coordinate system, hence denoting by $\mathbf{x}$ the position vector and (x, y, z) the Cartesian coordinates for the three-dimensional case.

Let us introduce some notation for deriving the weak formulation of the problems in this thesis. As usual, the space of square integrable functions in a domain ω is denoted by $L^2(\omega)$, whereas the space of functions whose first derivative is square integrable is denoted by $H^1(\omega)$. The space $H_0^1(\omega)$ consists of functions in $H^1(\omega)$ vanishing on boundaries. We shall use the symbol $\langle \cdot, \cdot \rangle_\omega$ to refer to the integral over a region ω of the product of two functions, assuming it is well-defined, whereas $(\cdot, \cdot)_\omega$ stands for the $L^2(\omega)$ inner product. These notations are simplified in the following case: $\langle \cdot, \cdot \rangle_\Omega := \langle \cdot, \cdot \rangle$ and $(\cdot, \cdot)_\Omega := (\cdot, \cdot)$, where Ω is the computational domain of the problem.

In Chapters 2 and 3 we employ index notation to identify a vector or tensor with its Cartesian coordinates, either in the reference or deformed configuration. As usual, repeated indices imply summation for all space dimensions (see, e.g., [1]). To denote scalar, vector and tensor quantities, we use uppercase letters when they are evaluated in the reference configuration and lowercase letters if they are reckoned in the deformed configuration. We employ the index zero for the quantities acting in the reference configuration.

[1]: Holzapfel (2000), *Nonlinear Solid Mechanics: A Continuum Approach for Engineering*

The remainder of the notation is explained in the text.

Introduction 1

1.1 Prologue

Structural optimization is a classical engineering discipline. The general objective is to obtain the optimal configuration of a structure subjected to a certain set of loads and boundary conditions, the optimality being determined by a given cost function. The arguments in the cost function, that is, the variables that need to be determined, may be the shape of the structure or material properties. Referring to the former, one may distinguish between two very different situations, namely, the one in which all possible shapes are topologically equivalent and the case in which there are topological changes. In the first situation, there is a continuous mapping from one configuration to the other; therefore, the boundary of the structure may be parameterized, and these parameters are considered as the arguments of the cost function. Topology optimization (TO) refers to a situation in which topological changes in the shape of the structure are possible. The key ingredient in moving from one configuration to another that is not topologically equivalent is the appearance of holes. Including this possibility in the optimization process can be performed in different ways, one of which is through the use of the topological derivative of the cost functional. See [2–4] for background on this topic.

[2]: A.A.Novotny et al. (2013), *Topological Derivatives in Shape Optimization*
[3]: A.A.Novotny et al. (2003), "Topological sensitivity analysis"
[4]: A.A.Novotny et al. (2007), "Topological sensitivity analysis for three-dimensional linear elasticity problem"

The irruption of additive manufacturing technologies and 3D printing in various branches of engineering has allowed engineers to design structures with complex geometries and topologies, which could not be addressed with classical manufacturing methods. This, in turn, has made TO of structures using computational methods a very attractive methodology. Although algorithms for TO in relatively simple cases, such as compressible structures subjected to small deformations and static loads, have already been developed, the topological design of incompressible structures with complex behavior and dynamic loads is still a field in which very little research has been conducted.

Energy efficiency and sustainability are major challenges for society. In structural design, minimizing weight and optimizing performance can lead to significant improvements in the

environmental impact of society. In this sense, TO of structures allows the design of high-performance structural elements in a range of engineering fields, such as aeronautics, civil engineering, and mechanical engineering. Combined with the rise of additive manufacturing, TO becomes a very powerful tool for the design of the structures of the future.

1.2 Motivation

The aim of this thesis is to develop a computational environment, ranging from the numerical formulation and the computer implementation to the simulation and analysis of cases of engineering interest, for TO problems, focusing on cases in which the loads on the structure come from the stresses exerted by a surrounding fluid. Thus, we wish to optimize the topology of the structure under a fluid-structure interaction (FSI). As a numerical formulation, we propose using the finite element method (FEM), and in particular, the Variational MultiScale (VMS) framework [5, 6], which allow us to overcome the numerical difficulties encountered with the standard Galerkin finite element (FE) formulation.

[5]: Hughes (1995), "Multiscale phenomena : Green's functions, the Dirichlet-to-Neumann formulation, subgrid scale models, bubbles and the origins of stabilized methods"
[6]: Hughes et al. (1998), "The variational multiscale method - A paradigm for computational mechanics"

FSI problems are prototypical examples of coupled problems. On the one hand, the solid responds to the loads exerted by the fluid; on the other hand, its dynamics are determined by the position and shape of the solid. A possible way to tackle the problem is to proceed iteratively by solving the solid with the loads given by the fluid, updating its position, and solving the fluid again with the new domain configuration. However, these natural transmission conditions may be sophisticated to improve the performance of the iterative procedure, and this is precisely one of the important issues to address in the numerical approximation of FSI problems [7].

[7]: Richter (2017), *Fluid-structure interactions: models, analysis and finite elements.*

The TO of structures subjected to FSI loads can be treated at different levels of complexity. Even in the simplest setting, which would be to consider the structure as a linear elastic material with small strains and a laminar fluid, is considered a highly complex multiphysics problem in the literature. Therefore, coupling TO and FSI in this "simplest" setting would be a novelty when dealing with incompressible structures. From the physical viewpoint, it makes no sense to study FSI problems in which the structure is considered to present small strains. Therefore, we wish to consider a more

complex setting, namely the possibility of considering finite strains in the solid as well as the possibility of dealing with viscoelastic incompressible flows.

Referring to the problem for the solid, we aim to consider finite strains, although with standard hyperelastic constitutive behavior. These finite strains render the problem nonlinear, with all difficulties inherent to this situation at the numerical level [8]. In our case, we also need to consider coupling the mechanics of the solid with those of the surrounding fluid. This poses restrictions and has consequences even in formulating the problem and, obviously, in its numerical approximation.

[8]: Belytschko et al. (2001), *Nonlinear Finite Elements for Continua and Structures*

Furthermore, we wish to include the possibility of addressing incompressible solids. For linear elastic materials, the way to cope with this problem is clear; namely, through the introduction of the mean stress as a new variable, the situation in finite strain theory is by far more complex. Some models propose the use of a linear model for the spherical component of stress in terms of volumetric strain. Although this may lead to the correct incompressible limit, the material behavior is altered in quasi-incompressible situations [9]. The proposed method for addressing this problem is described in this work.

[9]: Bonet et al. (1997), *Nonlinear Continuum mechanics for finite element analysis*

The use of a three-field formulation for the solid mechanics problem opens up the possibility of reaching the incompressible limit and obtaining a higher accuracy for the stresses when the problem is numerically approximated with FEs. In the linear elastic case, the natural choice is to consider the deviatoric Cauchy stress, displacement, and pressure (mean stress) as unknowns. This allows one to consider incompressible materials (because of the introduction of pressure) and to obtain higher accuracy for the stresses (if they are properly interpolated). The situation is more complex in the finite strain case. Apart from the variable needed to reach the incompressible limit, one may choose a stress measure (the second Piola-Kirchhoff stress, for example) or a deformation measure (the deformation gradient is often used) as unknowns [10, 11]. Our proposal is also detailed in this work. In any case, the main difficulty in dealing with a three-field formulation is the compatibility requirements between the unknowns. One may choose to deal with interpolations that are stable and satisfy appropriate inf-sup conditions. An alternative is to use a formulation that accommodates any in-

[10]: Cervera et al. (2010), "Mixed Stabilized Finite Element Methods in Nonlinear Solid Mechanics. Part I: Formulation"
[11]: Cervera et al. (2010), "Mixed Stabilized Finite Element Methods in Nonlinear Solid Mechanics. Part II: Strain Localization"

terpolation. We propose the use of a particular version of the VMS formulation that we have been using in our group for many years [12]. We wish to develop a completely novel application to finite strain solid dynamics that accounts for the incompressible limit.

[12]: R.Codina et al. (2017), *Variational Multiscale Methods in Computational Fluid Dynamics*

Apart from the solid, the second main component in the computational environment we wish to develop is the flow solver. Our group has longstanding experience in this field. In this particular case, we plan to consider an incompressible fluid flowing in a moving domain, where the domain motion is determined by the deformation of the solid. The numerical approximation of this problem suffers from several numerical difficulties, such as the stability of the interpolation of pressures and velocities, or the convective nature of the problem when the viscosity is small. These difficulties are well-documented, and we simply plan to employ the techniques we have developed in other contexts [13]. A particular issue to consider now, which we have also considered in other works, is domain motion; we plan to tackle it with an Arbitrary Lagrangian-Eulerian (ALE) formulation. The most relevant feature of the flows we wish to model is that they may be viscoelastic rather than Newtonian. Viscoelastic fluid flows are a topic on which our group has conducted extensive research [14–16].

[13]: Codina (2002), "Stabilized finite element approximation of transient incompressible flows using orthogonal subscales"

[14]: Castillo et al. (2014), "Variational multi-scale stabilized formulations for the stationary three-field incompressible viscoelastic flow problem"
[15]: Moreno et al. (2019), "Logarithmic conformation reformulation in viscoelastic flow problems approximated by a VMS-type stabilized finite element formulation"
[16]: Moreno et al. (2020), "Solution of transient viscoelastic flow problems approximated by a term-by-term VMS stabilized finite element formulation using time-dependent subgrid-scales"

In summary, the problem we wish to attempt is to find the optimal shape of a structure, including topology changes, behaving as a possibly incompressible finite strain hyperelastic material, subjected to the action of an incompressible fluid with a possible viscoelastic behavior. Both novel formulation ingredients at the continuous level and approximation strategies, the latter based on the VMS FE approach, are developed.

The computational model we have developed, including the novelties in the formulation of the continuous problem, and new numerical methods, has a wide spectrum of applications in engineering. In civil engineering, this tool would allow the design of frames subjected to aerodynamic loads, such as buildings or bridges, or shells under the action of wind, or submerged structures with loads coming from hydrodynamic currents, or the blades of wind turbines. Other fields of engineering also benefit from the developed tool: the car industry clearly can benefit from the use of the proposed tool for the design of car frames that are subjected to aerodynamic loads,

and in the aeronautical industry, the application is clear for the design of optimal airfoil wing structures and turbomachinery.

1.3 Goals

Accurate and high-performance computer optimization tools are required to design efficient structural elements. However, computer simulations that use numerical methods for the TO process are still at an early stage and are capable of dealing with static loads and small deformation cases in general. Several new developments are required that allow one to find topologically optimal geometries in the case of structures subjected to dynamic loads in a finite strain setting. In particular, this thesis focuses on the development of a strategy for structures subjected to FSI loads.

New methodologies are necessary to successfully develop a numerical method capable of dealing with this highly complex problem. First, a methodology for simulating dynamical three-dimensional solids in finite strain theory needs to be developed, also including the limit of incompressible materials. The methodology must be coupled with numerical simulation tools for FSI and, in turn, with a topological optimization algorithm.

Due to the fact that the numerical simulation of the TO of structures subjected to the effect of FSI is very expensive from a computational point of view, new developments need to be addressed with the objective of reducing the computational cost to an admissible level.

In summary, the main objective of this thesis is to design a numerical package, from formulation to implementation, capable of computing the TO process of structures subjected to FSI loads, with application to:

- Improving the design and performance of structures in the area of civil engineering, including wind generators, bridges, and other structures.

- Improving the design and performance of structures in the mechanical and aeronautical engineering areas, including airfoil optimization and car frame design.

We also aim to develop new numerical formulations for the various components of the model, particularly for:

- Solid mechanics formulations for finite strains, for materials reaching the incompressible limit. The proposed formulation is based in the VMS Method.
- Developing a TO algorithm capable of dealing with incompressible solids, for both linear elasticity and finite strain hyperelasticity theories.
- Developing a global strategy capable of finding optimal topologies for incompressible structures subjected to the effect of FSI.

1.4 Expected impact

The benefits of this thesis can be divided into three main contributions: the scientific contribution, the industrial contribution and the societal contribution.

From the scientific point of view, the developments presented in this work allow to further develop the current state of the art in the numerical TO through the development of robust numerical schemes which allow a better understanding of the complex process of TO of structures subjected to FSI. Also from the scientific point of view, important advances in the development and analysis of three field FE formulations applied to the problem of solid mechanics in the incompressible limit are expected. Of special interest are the results associated to the new algorithms for the derivation of the topological derivative, as well as the coupling with high performance computing strategies. In all of these problems the VMS formulation is used for the design of new numerical approaches.

From the industrial or technical point of view, the present work provide the industry with model that can be applied in industrial design. The use of the developed computational environment is useful in the optimization of the design structural elements subjected to aerodynamic and hydrodynamic loads. This includes applications in the aeronautical (airfoil engineering), industrial (car industry) and civil engineering fields (design of optimal structures subjected to aerodynamic or hydrodynamic loads, bridge elements and wind turbines).

As a consequence, the methods to be developed are of great interest for several branches of the industrial community. The development and implementation of numerical methods which allow one to find the optimal topology of a structure permit to exploit the insertion of this type of structures in industrial processes, in which industrial partners are able to (numerically) find the optimal working topologies. In this manner economical costs and the time required for the construction and verification of experimental prototypes is reduced.

Finally, from the society point of view, the present work allow to develop more efficient processes, which result in an important reduction in the energy consumption and ecological footprint of our society.

1.5 Outline

The specific content of this work is divided into 7 chapters, which are studied and developed progressively, and that are presented in the document as follows:

- **Chapter** 2 This chapter is devoted to formally state the state of the art and to give the basic equations which serve as a starting point for the developments in the following chapters. First of all, the solid dynamics problem is presented. The linear theory of elasticity is introduced and two well-known mixed formulations which are able to deal with nearly and fully incompressible materials are highlighted. Secondly, the nonlinear theory of finite strain hyperelasticity is introduced for hyperelastic constitutive models for the displacement-based formulation. Next, the Navier-Stokes equations of incompressible Newtonian fluid flows is presented and two different mixed formulations are stated.

- **Chapter** 3 In this chapter, two stabilized mixed formulations for finite strain solid dynamics are developed. Firstly, a new methodology for both the nearly and fully incompressible transient finite strain solid mechanics problem is presented in which displacement and pressure are taken as primary variables. To this end, the momentum equation is complemented with a constitutive law for the pressure which emerges from the

deviatoric/volumetric decomposition of the strain energy function for any hyperelastic material model. The incompressible limit is attained automatically depending on the material bulk modulus. The system is stabilized by means of the VMS-Orthogonal Subgrid Scale method based on the decomposition of the unknowns into resolvable and subgrid scales in order to prevent pressure fluctuations. Several numerical examples are presented to assess the robustness and applicability of the proposed formulation.

Next, a new methodology for finite strain solid dynamics problems for stress accurate analysis including the incompressible limit is presented. Previously, we presented the stabilized mixed displacement/pressure formulation to deal with the incompressibility constraint in finite strain solid dynamics. This formulation exploits the concept of mixed methods to formulate stable displacement/pressure/deviatoric stress FEs. The final goal is to design a FE technology able to tackle simultaneously problems which may involve incompressible behavior together with a high degree of accuracy of the stress field. The VMS stabilization technique and, in particular, the Orthogonal Subgrid Scale method allows the use of equal-order interpolations. These stabilization procedures lead to discrete problems which are fully stable, free of volumetric locking, stress oscillations and pressure fluctuations. Numerical benchmarks show that the results obtained compare very favorably with those obtained with the corresponding stabilized mixed displacement/pressure formulation.

- **Chapter 4** In this fourth chapter, an algorithm for TO, based on the topological derivative concept, is proposed for both nearly and fully incompressible materials. In order to deal with such materials, a new decomposition of the Polarization tensor is proposed in terms of its deviatoric and volumetric components for linear elasticity. In the finite strain hyperelasticity case, the decomposition of an approximation of the topological derivative is defined. Mixed formulations do not only allow to deal with incompressible material behavior but also to obtain a higher accuracy in the computation of stresses. The system is stabilized by means of the VMS method based on the decomposition of the unknowns into re-

solvable and subgrid scales in order to prevent fluctuations. Several numerical examples are presented and discussed to assess the robustness of the proposed formulation and its applicability to TO problems for incompressible elastic solids.

- **Chapter 5** In the fifth chapter of the thesis, the numerical simulation of the interaction between Oldroyd-B viscoelastic fluid flows and hyperelastic solids is approached. The algorithm employed is a classical block-iterative scheme, in which the solid and the fluid mechanics problems are solved sequentially. A Galerkin FE approach has been applied for the numerical approximation of the solid, while the flow equations are approximated using a stabilized FEM based on the Variational Multi-Scale approach to overcome the instabilities of the Galerkin method. To be able to deal with flows with dominant elasticity, a log-conformation reformulation of the constitutive equation can be considered; here this approach is extended to FSI problems. Several numerical examples are presented and discussed to assess the robustness of the scheme and its applicability to problems with viscoelastic fluids in which elasticity is dominant interacting with hyperelastic solids.

- **Chapter 6** In this chapter, the different numerical tools introduced in previous chapters are put together to develop an algorithm for TO problems of incompressible structures, in both small and finite strain assumptions, in which the loads come from the interaction with a surrounding fluid. This methodology is applied to fluid-structure interaction problems for Newtonian fluid flows.

- **Chapter 7** In this final chapter, the achievements of this study are summed up, final concluding remarks are drawn and future work lines are outlined.

Let us finally mention that chapters are quite self contained even if this implies the need of repeating some information. The self-contained nature of each chapter lends itself to including specific literature reviews in each chapter. Likewise, conclusions related to the specific contents of each chapter are pointed out at the end of them.

1.6 Research dissemination

This manuscript gathers most of the published original research done during this PhD thesis. The following lists organize the original contributions of this manuscript depending on the relation with the thesis.

1.6.1 Conference proceedings

During the development of the present PhD thesis, the partial advances and results have been presented in several international and specialized conferences or workshops. The list of attended conferences is included down below:

- **Inocencio Castañar**, Joan Baiges and Ramon Codina. *A stabilized mixed formulation in total Lagrangian approach for hyperelasticity for compressible, nearly and fully incompressible Neo-Hookean materials.* Congress on Numerical Methods in Engineering (CMN 2019). July 1–3, 2019, Guimarães, Portugal.

- **Inocencio Castañar**, Joan Baiges and Ramon Codina. *Topological derivative-based topology optimization of incompressible structures using mixed formulations.* IX International Conference on Computational Methods for Coupled Problems in Science and Engineering (Coupled Problems 2021). June 13–16, 2021, Sardinia , Italy.

- **Inocencio Castañar**, Joan Baiges, Ramon Codina and Henning Venghaus. *Topological derivative-based topology optimization of incompressible structures using mixed formulations.* 8th European Congress on Computational Methods in Applied Sciences and Engineering (ECCOMAS 2022). June 5–9, 2022, Oslo, Norway.

- **Inocencio Castañar**, Joan Baiges and Ramon Codina. *A stabilized mixed three-field formulation for stress accurate analysis including the incompressible limit in finite strain solid dynamics.* Congress on Numerical Methods in Engineering (CMN 2022). September 12–14, 2022, Las Palmas de Gran Canaria, Spain.

1.6.2 Scientific journal articles published

In addition to the above mentioned conferences, the results and findings of this thesis have been published in peer reviewed academic journals. The list of articles is provided down below:

- Joan Baiges, Ramon Codina, **Inocencio Castañar** and Ernesto Castillo. *A finite element reduced-order model based on adaptive mesh refinement and artificial neural networks.* In *International Journal for Numerical Methods in Engineering* (2020), vol. 121, p. 588–601.
  DOI = 10.1002/nme.6235.

- **Inocencio Castañar**, Joan Baiges and Ramon Codina. *A stabilized mixed finite element approximation for incompressible finite strain solid dynamics using a total Lagrangian formulation.* In *Computer Methods in Applied Mechanics and Engineering* (2020), vol. 368, artnum. 113164.
  DOI = 10.1016/j.cma.2020.113164.

- **Inocencio Castañar**, Joan Baiges, Ramon Codina and Henning Venghaus. *Topological derivative-based topology optimization of incompressible structures using mixed formulations.* In *Computer Methods in Applied Mechanics and Engineering* (2022), vol. 390, artnum. 114438.
  DOI = 10.1016/j.cma.2021.114438.

- **Inocencio Castañar**, Joan Baiges and Ramon Codina. *A stabilized mixed three-field formulation for stress accurate analysis including the incompressible limit in finite strain solid dynamics.* In *International Journal for Numerical Methods in Engineering* (2023), vol. 124 (10), p. 2341-2366.
  DOI = 10.1002/nme.7213.

- Laura Moreno, **Inocencio Castañar**, Ramon Codina, Joan Baiges and Domingo Cattoni. *Numerical simulation of Fluid-Structure Interaction problems with viscoelastic fluids using a log-conformation reformulation.* In *Computer Methods in Applied Mechanics and Engineering* (2023), vol. 410, artnum. 115986.
  DOI = 10.1016/j.cma.2023.115986.

- **Inocencio Castañar**, Joan Baiges and Ramon Codina. *Topology optimization of incompressible structures subject to Fluid-Structure Interaction.* Submitted.

1.7 FEMUSS

All the algorithms developed in this thesis are implemented in FEMUSS[1]. This is an object-oriented and Fortran-based finite element code which follows a modular approach for multiphysics interaction and performs parallel computations under MPI directives, thus setting an HPC environment. The included modules range from fluid dynamics (classical incompressible and compressible equations, wave equations, low Mach models, *etc.*), solid mechanics (plates, shells, incompressible materials, *etc.*), fluid-structure interaction or coupled thermal problems among others.

1: FEMUSS stands for Finite Element Method Using Subgrid Scales.

FEMUSS makes use of PETSc[2] [17], a suite of data routines and algorithms for the scalable (parallel) solution of different applications modeled by PDEs. It includes a large set of parallel linear and solvers that can be coupled to different application codes. Nowadays, FEMUSS relies on PETSc not only as a solver library, but also as a partitioner and communicator among subdomains, thanks to the PETSc broad set of capabilities. The interaction of FEMUSS with PETSc is achieved through an abstract and independent interface, what would allow to easily replace PETSc by another library if required (for example Trilinos).

2: PETSc stands for Portable, Extensible Toolkit for Scientific Computation.

[17]: Balay et al. (2015), *PETSc Web page*

For the preprocessing stage we use GiD, a processing system for computer analysis in science and engineering developed here at CIMNE, whereas most of the postprocessing has been done with Paraview [18] through the VTK library [19].

[18]: Ayachit (2015), *The ParaView Guide: A Parallel Visualization Application*

[19]: Schroeder et al. (2006), *The Visualization Toolkit (4th ed.).*

One of the main strengths of FEMUSS is the straightforward organization and accessibility of the code, which facilitates the introduction of new models and algorithms. Nevertheless, since it is mostly research-oriented and in constant development, the implementation of new formulations requires additional changes and improvements to reach the goals of the work.

Background and state of the art 2

2.1 The solid dynamics problem

From this point, the solid mechanics problem is formally stated. This section is devoted to the presentation of the basic equations which allow to study both the dynamic and mechanic behavior of a solid and which also serve as a starting point for the developments in Chapter 3.

The material here presented is basic and the different parts of this section can be found in classical textbooks of solid mechanics or continuum mechanics such as [1, 8, 9, 20, 21].

[1]: Holzapfel (2000), *Nonlinear Solid Mechanics: A Continuum Approach for Engineering*
[8]: Belytschko et al. (2001), *Nonlinear Finite Elements for Continua and Structures*
[9]: Bonet et al. (1997), *Nonlinear Continuum mechanics for finite element analysis*
[20]: X.Oliver et al. (2017), *Continuum Mechanics for Engineers. Theory and Problems, 2nd edition*
[21]: Saracibar (2022), *Nonlinear Continuum Mechanics. An Engineering Approach, 1st edition*

2.1.1 The linear theory of elasticity

The linear theory of elasticity can be considered a simplification of the general theory of elasticity which, for most engineering applications, is a close enough approximation. It considers the infinitesimal strain theory (also denominated small deformation theory) which is based on two simplifying hypotheses of the general theory. First of all, displacements are very small. Therefore, the material configuration is indistinguishable from the spatial one and, consequently both coordinates cannot be distinguished from each other,

As a consequence, there is no difference between the spatial and material descriptions of any property. The second hypothesis is related with displacement gradients which are supposed to be small enough to neglect second order terms. As a consequence, the material strain tensor and the spatial strain tensor collapses into the infinitesimal strain tensor $\boldsymbol{\varepsilon}$.

The continuum problem statement

In this subsection, the equations of motion are presented under the infinitesimal strain assumption. Let Ω be an open, bounded and polyhedral domain of $\mathbb{R}^d$, where d is the number of spacial dimensions. Any point of the body is labeled with the vector $\mathbf{x}$. The boundary of the domain is denoted as $\Gamma := \partial\Omega$ and is split into a Dirichlet boundary Γ_D, where the prescribed displacements are specified, and a Neumann

boundary Γ_N, where prescribed tractions are applied. The types of boundaries do not intersect, $\Gamma_D \cap \Gamma_N = \emptyset$ and together cover the whole boundary, $\Gamma_D \cup \Gamma_N = \Gamma$.

The continuum mechanical problem of linear elasticity is defined by the following system of equations

Linear elasticity. Solid mechanics problem

$$-\nabla \cdot \boldsymbol{\sigma} = \rho \mathbf{b} \quad \text{in } \Omega, \tag{2.1}$$

$$\boldsymbol{\sigma} = \mathbb{C} : \boldsymbol{\varepsilon} \quad \text{in } \Omega, \tag{2.2}$$

$$\boldsymbol{\varepsilon} = \nabla^s \mathbf{u} \quad \text{in } \Omega, \tag{2.3}$$

where $\mathbf{u}$ is the displacement field, $\boldsymbol{\sigma}$ the Cauchy stress field and $\boldsymbol{\varepsilon}$ the infinitesimal strain field. Eq. (2.1) is the balance of momentum equation, where $\rho\mathbf{b}$ represents the external load per unit of volume and $\nabla \cdot (\cdot)$ is the divergence operator. Eq. (2.2) is the constitutive equation for linear elasticity, where $\mathbb{C}$ is the 4th order constitutive tensor for isotropic materials defined as

$$\mathbb{C} = 2\mu\mathbb{I} + \lambda \mathbf{I} \otimes \mathbf{I}. \tag{2.4}$$

Here, $\mathbb{I}$ and $\mathbf{I}$ are the 4th rank and the 2nd rank identity tensors , respectively, and λ and μ are Lamé parameters. In the plane stress assumption they are expressed as

$$\lambda = \frac{\nu E}{1-\nu^2} \quad \text{and} \quad \mu = \frac{E}{2(1+\nu)}, \tag{2.5}$$

while in both 3D and plane strain they are defined as

$$\lambda = \frac{\nu E}{(1+\nu)(1-2\nu)} \quad \text{and} \quad \mu = \frac{E}{2(1+\nu)}. \tag{2.6}$$

Here E is the Young modulus and ν the Poisson ratio. Finally, Eq. (2.3) is the kinematic equation which relates the strain field with displacements, where $\nabla^s(\cdot) = \frac{1}{2}\{\nabla(\cdot) + \nabla^T(\cdot)\}$ denotes the symmetric gradient operator and $\nabla(\cdot)$ is the gradient operator.

The classical irreducible displacement-based formulation is obtained by substituting Eqs. (2.2-2.3) into Eq. (2.1). The result is known as Navier's equation

Linear elasticity. Navier's equation

$$-\nabla \cdot \{\mathbb{C} : \nabla^s \mathbf{u}\} = \rho \mathbf{b} \quad \text{in } \Omega, \tag{2.7}$$

which is written in terms of the displacement field only.

The volumetric/deviatoric split

The objective of this subsection is the split of both the constitutive and the kinematic equations into their volumetric and deviatoric parts. The volumetric/deviatoric split is the starting point to develop formulations able to tackle the incompressible limit.

Volumetric and deviatoric operators First of all, let us define the volumetric and deviatoric 4th order tensors $\mathbb{V}$ and $\mathbb{D}$ as

$$\mathbb{V} = \frac{1}{3}\mathbf{I} \otimes \mathbf{I}, \tag{2.8}$$

$$\mathbb{D} = \mathbb{I} - \frac{1}{3}\mathbf{I} \otimes \mathbf{I}, \tag{2.9}$$

$$\mathbb{I} = \mathbb{D} + \mathbb{V}. \tag{2.10}$$

Using the operators $\mathbb{V}$ and $\mathbb{D}$, it is possible to extract the spherical and the deviatoric parts of generic 2nd and 4th order tensors.

Split of stress and strain tensors Particularly, when applied to the stress tensor $\boldsymbol{\sigma}$ the result is

$$\mathbb{V} : \boldsymbol{\sigma} = \left\{\frac{1}{3}\mathbf{I} \otimes \mathbf{I}\right\} : \boldsymbol{\sigma} = \frac{1}{3}\mathrm{tr}(\boldsymbol{\sigma})\mathbf{I} \coloneqq -p\mathbf{I}, \tag{2.11}$$

where p is the pressure, taken as positive in compression regime and

$$\mathbb{D} : \boldsymbol{\sigma} = \left\{\mathbb{I} - \frac{1}{3}\mathbf{I} \otimes \mathbf{I}\right\} : \boldsymbol{\sigma} = \boldsymbol{\sigma} + p\mathbf{I} \coloneqq \mathbf{s}, \tag{2.12}$$

where $\mathbf{s}$ are the deviatoric stresses. Adding the volumetric and the deviatoric components, the Cauchy stress tensor is rebuilt as

$$\boldsymbol{\sigma} = \mathbf{s} - p\mathbf{I}. \tag{2.13}$$

In a similar way, it is possible to split the strain tensor $\boldsymbol{\varepsilon}$, as

$$\mathbb{V} : \boldsymbol{\varepsilon} = \left\{\frac{1}{3}\mathbf{I}\otimes\mathbf{I}\right\} : \boldsymbol{\varepsilon} = \frac{1}{3}\mathrm{tr}(\boldsymbol{\varepsilon})\mathbf{I} \coloneqq \frac{1}{3}e^{\mathrm{vol}}\mathbf{I}, \tag{2.14}$$

where e^{vol} is the volumetric deformation and

$$\mathbb{D} : \boldsymbol{\varepsilon} = \left\{\mathbb{I} - \frac{1}{3}\mathbf{I}\otimes\mathbf{I}\right\} : \boldsymbol{\varepsilon} = \boldsymbol{\varepsilon} - \frac{1}{3}e^{\mathrm{vol}}\mathbf{I} \coloneqq \mathbf{e}, \tag{2.15}$$

where $\mathbf{e}$ are the deviatoric strains which account for the distortions.

Split of the kinematic equation Applying the volumetric/deviatoric operators, Eq. (2.3) is split as

$$e^{\mathrm{vol}} = \nabla\cdot\mathbf{u}, \tag{2.16}$$

$$\mathbf{e} = \mathbb{D} : \nabla^{\mathrm{s}}\mathbf{u}. \tag{2.17}$$

Adding the volumetric and the deviatoric components, the kinematic equation is rebuilt as

$$\boldsymbol{\varepsilon} = \frac{1}{3}e^{\mathrm{vol}}\mathbf{I} + \mathbf{e} = \frac{1}{3}(\nabla\cdot\mathbf{u})\mathbf{I} + \mathbb{D} : \nabla^{\mathrm{s}}\mathbf{u}. \tag{2.18}$$

Split of the constitutive equation Let us assume that the constitutive relationship between stresses and strains can be expressed utilizing the constitutive equation (2.2). Hence, the volumetric and the deviatoric parts of the constitutive tensor $\mathbb{C}^{\mathrm{vol}}$ and $\mathbb{C}^{\mathrm{dev}}$ are obtained as

$$\mathbb{C}^{\mathrm{vol}} = \mathbb{V} : \mathbb{C} = (\lambda + \frac{2\mu}{3})\mathbf{I}\otimes\mathbf{I} \coloneqq \kappa\mathbf{I}\otimes\mathbf{I}, \tag{2.19}$$

$$\mathbb{C}^{\mathrm{dev}} = \mathbb{D} : \mathbb{C} = 2\mu\left\{\mathbb{I} - \frac{1}{3}\mathbf{I}\otimes\mathbf{I}\right\} = 2\mu\mathbb{D}, \tag{2.20}$$

$$\mathbb{C} = \mathbb{C}^{\mathrm{vol}} + \mathbb{C}^{\mathrm{dev}}, \tag{2.21}$$

where κ is the bulk modulus of the material. Introducing the split of stresses and strains, the constitutive relationship in Eq. (2.2) can be written as

$$\{\mathbf{s} - p\mathbf{I}\} = \left\{\mathbb{C}^{\mathrm{vol}} + \mathbb{C}^{\mathrm{dev}}\right\} : \left\{\frac{1}{3}(\nabla\cdot\mathbf{u})\mathbf{I} + \mathbf{e}\right\} \tag{2.22}$$

By taking into account that the contraction between volumetric and deviatoric tensors is identically null, Eq. (2.22) is split

into two equations

$$p = -\kappa \nabla \cdot \mathbf{u}, \tag{2.23}$$

$$\mathbf{s} = \mathbb{C}^{\text{dev}} : \boldsymbol{\varepsilon} = \mathbb{C}^{\text{dev}} : \mathbf{e}, \tag{2.24}$$

which are the volumetric and the deviatoric counterparts of the original constitutive equation.

The two-field $\mathbf{u}p$ formulation

In this subsection, the well-known mixed $\mathbf{u}p$ formulation is introduced in order to deal with nearly and fully incompressible scenarios. In the presented formulation the displacement and pressure fields $\mathbf{u}$ and p are used as independent variables.

Governing equations The governing equations of the problem are

Linear elasticity. $\mathbf{u}p$ formulation. Governing equations

$$-\nabla \cdot \mathbf{s} + \nabla p = \rho \mathbf{b} \qquad \text{in } \Omega, \tag{2.25}$$

$$\mathbf{s} - \mathbb{C}^{\text{dev}} : \nabla^{\text{s}} \mathbf{u} = \mathbf{0} \qquad \text{in } \Omega, \tag{2.26}$$

$$\nabla \cdot \mathbf{u} + \frac{p}{\kappa} = 0 \qquad \text{in } \Omega. \tag{2.27}$$

Eq. (2.25) allows us to formulate the linear momentum equation in terms of both displacements $\mathbf{u}$ and pressure p, where the stress tensor decomposition (2.13) has been introduced into the momentum equation. Furthermore, the constitutive law which relates deviatoric stresses with displacements (2.26) allows us to introduce the displacement field in the balance equation (2.25). Finally, Eq. (2.27) is in charge of both providing the constitutive equation for the pressure and imposing the incompressibility constraint.

Remark 2.1.1 Let us recall that in the incompressible limit $\kappa \to \infty$, and Eq. (2.27) will reduce automatically to

$$\nabla \cdot \mathbf{u} = 0, \tag{2.28}$$

which is the incompressibility condition for infinitesimal strain theory.

Strong form To complete this subsection, we introduce the mixed $\mathbf{u}p$ problem, which consists in finding both a displacement $\mathbf{u}$ and a pressure p such that

Linear elasticity. $\mathbf{u}p$ formulation. Strong form

$$-\nabla \cdot \left\{ \mathbb{C}^{\text{dev}} \,:\, \nabla^{\text{s}} \mathbf{u} \right\} + \nabla p = \rho \mathbf{b} \qquad \text{in } \Omega, \tag{2.29}$$

$$\nabla \cdot \mathbf{u} + \frac{p}{\kappa} = 0 \qquad \text{in } \Omega. \tag{2.30}$$

The governing equations must be supplied with a set of boundary conditions

$$\mathbf{u} = \mathbf{u}_D \qquad \text{on } \Gamma_D, \tag{2.31}$$

$$\boldsymbol{\sigma} \cdot \mathbf{n} \overset{(2.13)}{=} \left\{ \mathbb{C}^{\text{dev}} \,:\, \nabla^{\text{s}} \mathbf{u} \right\} \cdot \mathbf{n} - p\mathbf{n} = \mathbf{t}_N \qquad \text{on } \Gamma_N, \tag{2.32}$$

where $\mathbf{n}$ is the geometric unit outward normal vector on the boundary Γ. To simplify the exposition, we will consider $\mathbf{u}_D = 0$ in the following.

Variational form Let $\mathbb{U} = \left[H^1(\Omega)\right]^d$ and $\mathbb{P} = L^2(\Omega)$ be, respectively, the proper functional spaces where displacement and pressure solutions are well-defined. We denote by $\mathbb{U}_0$ functions in $\mathbb{U}$ which vanish in the Dirichlet boundary Γ_D. We shall be interested also in the spaces $\mathbb{W} := \mathbb{U} \times \mathbb{P}$, $\mathbb{W}_0 := \mathbb{U}_0 \times \mathbb{P}$. The variational statement of the problem is derived by testing the system presented in Eqs. (2.29-2.30) againts arbitrary test functions $\delta\mathbf{U} := [\delta\mathbf{u}, \delta p]^T$, $\delta\mathbf{u} \in \mathbb{U}_0$ and $\delta p \in \mathbb{P}$. The weak form of the problem reads: find $\mathbf{U} := [\mathbf{u}, p]^T \in \mathbb{W}_0$ such that

Linear elasticity. $\mathbf{u}p$ formulation. Variational form

$$\mathscr{A}(\mathbf{U}, \delta\mathbf{U}) = \mathscr{F}(\delta\mathbf{U}) \quad \forall\, \delta\mathbf{U} \in \mathbb{W}_0, \tag{2.33}$$

where $\mathscr{A}(\mathbf{U}, \delta\mathbf{U})$ is a bilinear form defined on $\mathbb{W}_0 \times \mathbb{W}_0$ as

$$\mathscr{A}(\mathbf{U}, \delta\mathbf{U}) := \left(\nabla^{\text{s}} \delta\mathbf{u}, \mathbb{C}^{\text{dev}} \,:\, \nabla^{\text{s}} \mathbf{u} \right) - (\nabla \cdot \delta\mathbf{u}, p)$$

$$+ (\delta p, \nabla \cdot \mathbf{u}) + \left(\delta p, \frac{1}{\kappa} p\right). \tag{2.34}$$

$\mathscr{F}(\delta \mathbf{U})$ is a linear form defined on $\mathbb{W}_0$ as

$$\mathscr{F}(\delta \mathbf{U}) := \langle \delta \mathbf{u}, \rho \mathbf{b} \rangle + \langle \delta \mathbf{u}, \mathbf{t}_N \rangle_{\Gamma_N}. \tag{2.35}$$

As usual, integration by parts has been used in order to decrease the continuity requirements of unknowns $\mathbf{u}$ and p and the traction vector $\mathbf{t}_N$ has been identified.

Galerkin spatial discretization The standard Galerkin approximation of this abstract variational problem is straightforward. Let $\mathscr{P}_h$ denote a FE partition of the domain Ω. The diameter of an element domain $K \in \mathscr{P}_h$ is denoted by h_K and the diameter on the FE partition by $h = \max\{h_K | K \in \mathscr{P}_h\}$. We can now construct conforming FE spaces $\mathbb{U}_h \subset \mathbb{U}$, $\mathbb{P}_h \subset \mathbb{P}$ and $\mathbb{W}_h = \mathbb{U}_h \times \mathbb{P}_h$ in the usual manner, as well as the corresponding subspaces $\mathbb{U}_{h,0} \subset \mathbb{U}_0$ and $\mathbb{W}_{h,0} = \mathbb{U}_{h,0} \times \mathbb{P}_h$, $\mathbb{U}_{h,0}$ being made with functions that vanish on the Dirichlet boundary.

The Galerkin discrete version of problem (2.33) is: Find $\mathbf{U}_h := [\mathbf{u}_h, p_h]^T \in \mathbb{W}_{h,0}$ such that

Linear elasticity. $\mathbf{u}p$ formulation. Galerkin discrete problem

$$\mathscr{A}(\mathbf{U}_h, \delta \mathbf{U}_h) = \mathscr{F}(\delta \mathbf{U}_h) \quad \forall\, \delta \mathbf{U}_h \in \mathbb{W}_{h,0}. \tag{2.36}$$

The well posedness of this problem relies on an inf-sup condition [22]. This condition is necessary and sufficient for the existence and uniqueness of the solution to the discrete saddle-point problem. Convenient displacement-pressure interpolations, such as equal interpolation, turn out to violate the inf-sup condition. This is why the so-called stabilized formulations have been proposed to approximate this kind of problems. The main idea is to replace (2.33) by another discrete variational problem in which the bilinear form $\mathscr{A}$ is enhanced so that it has improved stability properties. In order to overcome the instabilities previously discussed, we propose to use the stabilization technique described in next subsection.

[22]: Babuška (1971), "Error-Bounds for Finite Element Method"

Remark 2.1.2 In principle, we have posed no restrictions on the choice of the FE spaces. However, let us analyze the numerical stability of problem (2.36). If we take $\delta \mathbf{U}_h = \mathbf{U}_h$, it is found that

$$\begin{aligned} \mathscr{A}(\mathbf{U}_h, \mathbf{U}_h) &= \left(\nabla^s \mathbf{u}_h, \mathbb{C}^{\text{dev}} : \nabla^s \mathbf{u}_h\right) + \left(p_h, \frac{1}{\kappa} p_h\right) \\ &\geq 2\mu \|\mathbb{D} : \nabla^s \mathbf{u}_h\|^2 + \frac{1}{\kappa}\|p_h\|^2. \end{aligned} \tag{2.37}$$

where $\|\cdot\|$ is the $L^2(\Omega)$ norm . It is seen from Eq. (2.37) that $\mathscr{A}$ is not coercive in $\mathbb{W}_{h,0}$ when $\kappa \to \infty$, the pressure being out of control. Hence, in the nearly and fully incompressible cases the inf-sup condition is not satisfied.

[6]: Hughes et al. (1998), "The variational multiscale method - A paradigm for computational mechanics"
[12]: R.Codina et al. (2017), *Variational Multiscale Methods in Computational Fluid Dynamics*

Stabilization The stabilized FEM we propose to use in the following is based on the VMS concept [6, 12]. Let $\mathbb{W} = \mathbb{W}_h \oplus \tilde{\mathbb{W}}$, where $\tilde{\mathbb{W}}$ is any space to complete $\mathbb{W}_h$ in $\mathbb{W}$. $\tilde{\mathbb{W}}$ will be approximated by a finite-dimensional space despite the fact that it is infinite-dimensional. The elements of this space are denoted by $\tilde{\mathbf{U}} := [\tilde{\mathbf{u}}, \tilde{p}]^T$ and they are called subgrid scales (SGS). Likewise, let $\mathbb{W}_0 = \mathbb{W}_{h,0} \oplus \tilde{\mathbb{W}}_0$.

Taking into account that $\mathscr{A}$ is a bilinear form, the continuous problem (2.33) is equivalent to find $\mathbf{U} \in \mathbb{W}_{h,0}$ and $\tilde{\mathbf{U}} \in \tilde{\mathbb{W}}_0$ such that

$$\mathscr{A}(\mathbf{U}_h, \delta\mathbf{U}_h) + \mathscr{A}\left(\tilde{\mathbf{U}}, \delta\mathbf{U}_h\right) = \mathscr{F}(\delta\mathbf{U}_h) \quad \forall\, \delta\mathbf{U}_h \in \mathbb{W}_{h,0}, \tag{2.38}$$

$$\mathscr{A}\left(\mathbf{U}_h, \delta\tilde{\mathbf{U}}\right) + \mathscr{A}\left(\tilde{\mathbf{U}}, \delta\tilde{\mathbf{U}}\right) = \mathscr{F}\left(\delta\tilde{\mathbf{U}}\right) \quad \forall\, \delta\tilde{\mathbf{U}} \in \tilde{\mathbb{W}}_0, \tag{2.39}$$

where Eq. (2.38) is called the FE scale equation and Eq. (2.39) is called the SGS equation.

The main idea behind any stabilized FEM derived from the VMS framework is to obtain an expression for the SGS from the SGS equation (2.39). This is done to complement our FE scale equation (2.38) and to ensure consistency of the stabilized mixed formulation so that the discrete solution converges to the continuous solution on mesh refinement. We assume the subscales to behave as bubble functions, which means that they vanish across inter-element boundaries. Therefore, the SGS is expressed in terms of the residual of the projected (Galerkin) counterpart of Eqs. (2.29–2.30) to obtain

$$\tilde{\mathbf{u}} \approx \tau_{\mathbf{u}} \tilde{\Pi}\left(\nabla \cdot \left\{\mathbb{C}^{\text{dev}} : \nabla^s \mathbf{u}_h\right\} - \nabla p_h - \rho \mathbf{b}\right), \tag{2.40}$$

$$\tilde{p} \approx \tau_p \tilde{\Pi}\left(-\nabla\cdot\mathbf{u}_h - \frac{1}{\kappa}p_h\right), \tag{2.41}$$

where $\tilde{\Pi}$ is the $L^2(\Omega)$ projection onto the space of SGS and $\tau_{\mathbf{u}}$ and τ_p are coefficients coming from a Fourier analysis of the problem for the subscales. In this work, we use the stabilization parameters proposed in [10] for linear elastic cases

[10]: Cervera et al. (2010), "Mixed Stabilized Finite Element Methods in Nonlinear Solid Mechanics. Part I: Formulation"

$$\tau_{\mathbf{u}} = c_1\frac{h_K^2}{2\mu} \quad \text{and} \quad \tau_p = 2c_2\left(\frac{1}{\mu}+\frac{2}{3\kappa}\right)^{-1}, \tag{2.42}$$

where c_1 and c_2 are algorithmic parameters which must be determined.

Introducing the approximate fields (2.40-2.41) into the FE scale problem (2.38), the VMS stabilized formulation of the problem is obtained as (see [23] for further details on this procedure)

[23]: Baiges et al. (2017), "Variational Multiscale error estimators for solid mechanics adaptive simulations: an Orthogonal Subgrid Scale approach"

Linear elasticity. up formulation. Stabilized weak form

$$\mathscr{A}(\mathbf{U}_h,\delta\mathbf{U}_h) + \sum_K \left\langle -\nabla\cdot\delta\mathbf{u}_h + \frac{1}{\kappa}\delta p_h, \tilde{p}\right\rangle_K + \sum_K \langle -\nabla\delta p_h, \tilde{\mathbf{u}}\rangle_K = \mathscr{F}(\delta\mathbf{U}_h) \quad \forall\, \delta\mathbf{U}_h \in \mathbb{W}_{h,0}. \tag{2.43}$$

There exist several stabilization methods coming from the VMS technique depending on the selection of the projection onto the SGS space. In this work, two different options are considered:

1. We take the projection onto the SGS space as the identity when applied to the residual. This approach is called Algebraic SubGrid Scales (ASGS), see [24] for further details.
2. In [25] it is argued that the natural approximation for the unknown SGS space is to take it orthogonal to the FE space. This approach is called Orthogonal SubGrid Scales (OSGS).

[24]: Codina (2001), "A stabilized finite element method for generalized stationary incompressible flows"

[25]: Codina (2000), "Stabilization of incompressibility and convection through orthogonal subscales in finite element methods"

Remark 2.1.3 A key property of the OSGS stabilization is that thanks to the orthogonal projection onto the FE space, we keep the consistency of the formulation in a weak sense

despite including just the minimum number of terms to stabilize the solution if $\tilde{\Pi}$ does not include Dirichlet-type boundary conditions (see [12]). For this specific formulation, we can reduce the stabilization terms to solely $\sum_K \tau_{\mathbf{u}} \langle \nabla \delta p_h, \tilde{\Pi}(\nabla p_h) \rangle$.

[12]: R.Codina et al. (2017), *Variational Multiscale Methods in Computational Fluid Dynamics*

The three-field upe formulation

In this subsection we present the mixed three-field formulation used to deal with the solid mechanics problem. The methodology was originally developed in [26] to deal with the Stokes problem in fluid mechanics, and extended to solid mechanics in [27] by considering the deviatoric stresses as an additional unknown of the problem. More recently, in [28], the formulation was adapted so that the main unknowns are displacements, pressure and deviatoric strains, instead of deviatoric stresses, which is the approach we follow in this work. The displacement field $\mathbf{u}$, together with the deviatoric component of the strains $\mathbf{e}$, as well as the pressure field p are taken as primary unknowns of the problem. The objective is the definition of a general framework, which includes the well-known mixed $\mathbf{u}p$ formulation. Therefore we are capable of correctly describing nearly and fully incompressible material behavior. Adding the deviatoric strains as unknowns allows us to obtain a high degree of accuracy for the strain field but also for the stress field.

[26]: R.Codina (2009), "Finite element approximation of the three field formulation of the Stokes problem using arbitrary interpolations"

[27]: Chiumenti et al. (2015), "A mixed three-field FE formulation for stress accurate analysis including the incompressible limit"

[28]: Chiumenti et al. (2021), "Stress, strain and dissipation accurate 3-field formulation for inelastic isochoric deformation"

Governing equations The governing equations of the problem are

Linear elasticity. upe formulation. Governing equations

$$-\nabla \cdot \mathbf{s} + \nabla p = \rho \mathbf{b} \quad \text{in } \Omega, \tag{2.44}$$

$$\mathbf{s} - \mathbb{C}^{\text{dev}} : \mathbf{e} = \mathbf{0} \quad \text{in } \Omega, \tag{2.45}$$

$$\nabla \cdot \mathbf{u} + \frac{p}{\kappa} = 0 \quad \text{in } \Omega, \tag{2.46}$$

$$\mathbf{e} - \mathbb{D} : \nabla^{\text{s}} \mathbf{u} = \mathbf{0} \quad \text{in } \Omega. \tag{2.47}$$

We have introduced the deviatoric strains $\mathbf{e}$ in system (2.25-2.27) by incorporating the deviatoric constitutive equation (2.45). Furthermore, the kinematic equation for deviatoric

components (2.47) has been added to the system to relate the displacement field $\mathbf{u}$ with the deviatoric strains $\mathbf{e}$.

Remark 2.1.4 Note that Eq. (2.45) allows us to obtain the deviatoric stresses as a function of the deviatoric strains rather than the symmetric gradient of the displacements. Therefore, we are hopefully incrementing the accuracy of the stress field $\boldsymbol{\sigma}$, which now is going to be computed as a function of both the pressure p and the deviatoric strains $\mathbf{e}$.

Strong form To complete this subsection, we introduce the mixed $\mathbf{u}p\mathbf{e}$ problem, which consists in finding a displacement field $\mathbf{u}$, a pressure p and a deviatoric strain field $\mathbf{e}$ such that

Linear elasticity. $\mathbf{u}p\mathbf{e}$ formulation. Strong form

$$-\nabla\cdot\left\{\mathbb{C}^{\text{dev}} : \mathbf{e}\right\} + \nabla p = \rho\mathbf{b} \qquad \text{in } \Omega, \tag{2.48}$$

$$\nabla\cdot\mathbf{u} + \frac{p}{\kappa} = 0 \qquad \text{in } \Omega, \tag{2.49}$$

$$2\mu\mathbf{e} - \mathbb{C}^{\text{dev}} : \nabla^{\text{s}}\mathbf{u} = 0 \qquad \text{in } \Omega, \tag{2.50}$$

where the kinematic equation (2.47) has been multiplied by 2μ to symmetrize the system. The governing equations must be supplied with a set of boundary conditions

$$\mathbf{u} = \mathbf{u}_D \qquad \text{on } \Gamma_D, \tag{2.51}$$

$$\boldsymbol{\sigma}\cdot\mathbf{n} \overset{(2.13)}{=} \left\{\mathbb{C}^{\text{dev}} : \mathbf{e}\right\}\cdot\mathbf{n} - p\mathbf{n} = \mathbf{t}_N \qquad \text{on } \Gamma_N, \tag{2.52}$$

To simplify the exposition, we will consider $\mathbf{u}_D = 0$ in the following.

Variational form Let us consider the same spaces and tests functions we have defined previously for the mixed $\mathbf{u}p$ formulation. Let $\mathbb{E} = \left[L^2(\Omega)\right]^{d\times d}_{\text{sym}}$ be the proper functional space where deviatoric strain components are well-defined. We shall be interested also in the spaces $\mathbb{W} := \mathbb{U}\times\mathbb{P}\times\mathbb{E}$, $\mathbb{W}_0 := \mathbb{U}_0\times\mathbb{P}\times\mathbb{E}$. The variational statement of the problem is derived by testing system (2.48-2.50) against arbitrary test functions $\delta\mathbf{U} := [\delta\mathbf{u}, \delta p, \delta\mathbf{e}]^T$, $\delta\mathbf{u}\in\mathbb{U}_0$, $\delta p\in\mathbb{P}$ and $\delta\mathbf{e}\in\mathbb{E}$. The weak

form of the problem reads: find $\mathbf{U} := [\mathbf{u}, p, \mathbf{e}]^T \in \mathbb{W}_0$ such that

Linear elasticity. upe formulation. Variational form

$$\mathscr{A}(\mathbf{U}, \delta\mathbf{U}) = \mathscr{F}(\delta\mathbf{U}) \quad \forall\, \delta\mathbf{U} \in \mathbb{W}_0, \tag{2.53}$$

where $\mathscr{A}(\mathbf{U}, \delta\mathbf{U})$ is a bilinear form defined on $\mathbb{W}_0 \times \mathbb{W}_0$ as

$$\begin{aligned}\mathscr{A}(\mathbf{U}, \delta\mathbf{U}) := &\left(\nabla^s \delta\mathbf{u}, \mathbb{C}^{\text{dev}} : \mathbf{e}\right) - (\nabla \cdot \delta\mathbf{u}, p) + (\delta p, \nabla \cdot \mathbf{u}) \\ &+ \left(\delta p, \frac{1}{\kappa} p\right) - \left(\mathbb{C}^{\text{dev}} : \delta\mathbf{e}, \nabla^s \mathbf{u}\right) + (\delta\mathbf{e}, 2\mu\mathbf{e}).\end{aligned} \tag{2.54}$$

$\mathscr{F}(\delta\mathbf{U})$ is a linear form defined on $\mathbb{W}_0$ as

$$\mathscr{F}(\delta\mathbf{U}) := \langle \delta\mathbf{u}, \rho\mathbf{b} \rangle + \langle \delta\mathbf{u}, \mathbf{t}_N \rangle_{\Gamma_N}. \tag{2.55}$$

As usual, integration by parts has been used in order to decrease the continuity requirements of the unknowns and the traction vector $\mathbf{t}_N$ has been identified.

Galerkin spatial discretization We can now construct a conforming FE space $\mathbb{E}_h \subset \mathbb{E}$ and redefine $\mathbb{W}_h = \mathbb{U}_h \times \mathbb{P}_h \times \mathbb{E}_h$ as well as the corresponding subspace $\mathbb{W}_{h,0} = \mathbb{U}_{h,0} \times \mathbb{P}_h \times \mathbb{E}_h$ in the usual manner.

The Galerkin discrete version of problem (2.53) is: Find $\mathbf{U}_h := [\mathbf{u}_h, p_h, \mathbf{e}_h]^T \in \mathbb{W}_{h,0}$ such that

Linear elasticity. upe formulation. Galerkin discrete problem

$$\mathscr{A}(\mathbf{U}_h, \delta\mathbf{U}_h) = \mathscr{F}(\delta\mathbf{U}_h) \quad \forall\, \delta\mathbf{U}_h \in \mathbb{W}_{h,0}. \tag{2.56}$$

This problem also requires two inf-sup condition to be satisfied between the interpolation spaces. Otherwise, instabilities may appear. In order to overcome such instabilities, we use again the stabilization technique described in next subsection.

Remark 2.1.5 In principle, we have posed no restrictions on the choice of the FE spaces. However, let us analyze the numerical stability of problem (2.56). If we take $\delta\mathbf{U}_h = \mathbf{U}_h$,

it is found that

$$\mathscr{A}(\mathbf{U}_h, \mathbf{U}_h) = \left(p_h, \frac{1}{\kappa} p_h\right) + (\mathbf{e}_h, 2\mu \mathbf{e}_h) \geq 2\mu \|\mathbf{e}_h\|^2 + \frac{1}{\kappa}\|p_h\|^2. \tag{2.57}$$

It is seen from Eq. (2.57) that $\mathscr{A}$ is not coercive in $\mathbb{W}_{h,0}$, the displacement being out of control. Furthermore, in the nearly and fully incompressible cases, when $\kappa \to \infty$, also the pressure is out of control. Hence, the coercivity condition is not satisfied indepently of the incompressibility of the material.

Stabilization The elements of the SGS space are now denoted by $\tilde{\mathbf{U}} := [\tilde{\mathbf{u}}, \tilde{p}, \tilde{\mathbf{e}}]^T$. Taking into account that $\mathscr{A}$ is a bilinear form, the continuous problem (2.53) is equivalent to find $\mathbf{U} \in \mathbb{W}_{h,0}$ and $\tilde{\mathbf{U}} \in \tilde{\mathbb{W}}_0$ such that

$$\mathscr{A}(\mathbf{U}_h, \delta\mathbf{U}_h) + \mathscr{A}\left(\tilde{\mathbf{U}}, \delta\mathbf{U}_h\right) = \mathscr{F}(\delta\mathbf{U}_h) \quad \forall\, \delta\mathbf{U}_h \in \mathbb{W}_{h,0}, \tag{2.58}$$

$$\mathscr{A}\left(\mathbf{U}_h, \delta\tilde{\mathbf{U}}\right) + \mathscr{A}\left(\tilde{\mathbf{U}}, \delta\tilde{\mathbf{U}}\right) = \mathscr{F}\left(\delta\tilde{\mathbf{U}}\right) \quad \forall\, \delta\tilde{\mathbf{U}} \in \tilde{\mathbb{W}}_0. \tag{2.59}$$

The SGS is expressed in terms of the residual of the projected (Galerkin) counterpart of Eqs. (2.48–2.50) to obtain

$$\tilde{\mathbf{u}} \approx \tau_{\mathbf{u}} \tilde{\Pi}\left(\nabla \cdot \left\{\mathbb{C}^{\text{dev}} : \mathbf{e}_h\right\} - \nabla p_h - \rho \mathbf{b}\right), \tag{2.60}$$

$$\tilde{p} \approx \tau_p \tilde{\Pi}\left(-\nabla \cdot \mathbf{u}_h - \frac{1}{\kappa} p_h\right), \tag{2.61}$$

$$\tilde{\mathbf{e}} \approx \tau_{\mathbf{e}} \tilde{\Pi}\left(\mathbb{D} : \nabla^{\text{s}} \mathbf{u}_h - \mathbf{e}_h\right), \tag{2.62}$$

where $\tau_{\mathbf{u}}$, τ_p and $\tau_{\mathbf{e}}$ are coefficients coming from a Fourier analysis of the problem for the SGS. In this work, we use the stabilization parameters proposed in [10] for linear elastic cases

$$\tau_{\mathbf{u}} = c_1 \frac{h_K^2}{2\mu}, \quad \tau_p = 2c_2 \left(\frac{1}{\mu} + \frac{2}{3\kappa}\right)^{-1} \quad \text{and} \quad \tau_{\mathbf{e}} = c_3, \tag{2.63}$$

where c_1, c_2 and c_3 are algorithmic parameters which must be determined.

[10]: Cervera et al. (2010), "Mixed Stabilized Finite Element Methods in Nonlinear Solid Mechanics. Part I: Formulation"

Introducing the approximate fields (2.60-2.62) into the FE scale problem (2.58), the VMS stabilized formulation of the problem is obtained as (see [28] for further details on this procedure)

[28]: Chiumenti et al. (2021), "Stress, strain and dissipation accurate 3-field formulation for inelastic isochoric deformation"

Linear elasticity. u*p*e formulation. Stabilized weak form

$$\begin{aligned}\mathscr{A}(\mathbf{U}_h, \delta\mathbf{U}_h) &+ \sum_K \left\langle \mathbb{C}^{\text{dev}} : \nabla\delta\mathbf{e}_h - \nabla\delta p_h, \tilde{\mathbf{u}} \right\rangle_K \\ &+ \sum_K \left\langle -\nabla\cdot\delta\mathbf{u}_h + \frac{1}{\kappa} q_h, \tilde{p} \right\rangle_K \\ &+ \sum_K \left\langle \mathbb{C}^{\text{dev}} : \nabla^s\delta\mathbf{u}_h + 2\mu\delta\mathbf{e}_h, \tilde{\mathbf{e}} \right\rangle_K \\ &= \mathscr{F}(\delta\mathbf{U}_h) \quad \forall\, \delta\mathbf{U}_h \in \mathbb{W}_{h,0}. \end{aligned} \tag{2.64}$$

For this formulation, both the ASGS and the OSGS methods are also considered.

Remark 2.1.6 Let us recall that the OSGS stabilization allows us to include just the minimum number of terms to stabilize the solution while keeping it consistent in a weak sense. Therefore, we can reduce the stabilization terms to $\sum_K \tau_{\mathbf{u}} \left\langle \nabla\delta p_h, \tilde{\Pi}(\nabla p_h) \right\rangle$ to stabilize the p component and to $\sum_K \tau_{\mathbf{e}} \left\langle \mathbb{C}^{\text{dev}} : \nabla^s\delta\mathbf{u}_h, \tilde{\Pi}(\mathbb{D} : \nabla^s\mathbf{u}_h) \right\rangle$ to introduce stabilization terms in the $\mathbf{u}$ part.

2.1.2 The nonlinear theory of finite strain hyperelasticity

Despite the obvious success of the assumption of linearity in engineering analysis it is equally obvious that many situations demand consideration of nonlinear behavior. In the linear elasticity case an assumption is made that the deformation is sufficiently small to enable the effect of changes in the geometrical configuration of the solid to be ignored, whereas in the nonlinear case the magnitude of the deformation is unrestricted.

Lagrangian descriptions of the motion

Finite element discretizations with Lagrangian meshes are classified as updated Lagrangian formulations (ULF) and total Lagrangian formulations (TLF). Both formulations use Lagrangian descriptions, that is, the dependent variables are functions of the material (Lagrangian) coordinates and time.

In the ULF, the derivatives are taken with respect to the spatial (Eulerian) coordinates; the weak form involves integrals over the deformed (or current) configuration. In the TLF, the weak form involves integrals over the initial configuration (considered henceforth to be the reference configuration) and derivatives are taken with respect to the material coordinates.

Conservation equations

Let $\Omega_0 \coloneqq \Omega(0)$ be an open, bounded and polyhedral domain of $\mathbb{R}^d$, where $d \in \{2, 3\}$ is the number of space dimensions. The initial configuration of the body is Ω_0, whereas the current configuration of the body at time t is denoted by $\Omega(t)$. The motion is described by a function $\boldsymbol{\psi}$ which links a material particle $\mathbf{X} \in \Omega_0$ to the spatial configuration $\mathbf{x} \in \Omega(t)$ according to

$$\boldsymbol{\psi} : \Omega_0 \longrightarrow \Omega(t), \quad \mathbf{x} = \boldsymbol{\psi}(\mathbf{X}, t), \quad \forall \mathbf{X} \in \Omega_0, \quad t \geq 0. \tag{2.65}$$

The boundary of the reference configuration is denoted as $\Gamma_0 \coloneqq \partial\Omega_0$ and $\Gamma(t) \coloneqq \partial\Omega(t)$ represents the boundary of the current configuration at time t. We always assume that the mapping between both boundaries is defined through the motion, i.e., $\boldsymbol{\psi}(\Gamma_0, t) = \Gamma(t)$. We denote as $]0, T[$ the time interval of analysis.

The conservation of linear momentum in finite strain theory in a TLF framework reads as

$$\rho_0 \frac{\partial^2 u_a}{\partial t^2} - \frac{\partial}{\partial X_A}\{F_{aB} S_{BA}\} = \rho_0 b_a \quad \text{in } \Omega_0 \times]0, T[, \tag{2.66}$$

where ρ_0 is the initial density, $\mathbf{F} = \frac{\partial \mathbf{x}}{\partial \mathbf{X}}$ is the deformation gradient, $\mathbf{S}$ is the second Piola-Kirchhoff (PK2) stress tensor and $\rho_0 \mathbf{b}$ are the body forces. Mass conservation implies that

$$\rho J = \rho_0, \tag{2.67}$$

where ρ is the density at time t and $J = \det \mathbf{F} > 0$ is the Jacobian of $\mathbf{F}$. With regards to the balance of angular momentum, it implies that the PK2 stress tensor must be symmetric.

Hyperelastic constitutive model

In this chapter we consider isotropic hyperelastic models (see [1, 8, 9]). These models postulate the existence of a Helmholtz free-energy function (or strain energy function) $\Psi(\mathbf{C})$ such that

$$\mathbf{S} = 2\frac{\partial \Psi(\mathbf{C})}{\partial \mathbf{C}}, \tag{2.68}$$

where $\mathbf{C} = \mathbf{F}^T\mathbf{F}$ is the right Cauchy-Green tensor. Once the PK2 stress tensor $\mathbf{S}$ is obtained, the Cauchy stress tensor $\boldsymbol{\sigma}$ can be computed from the following relation

$$\boldsymbol{\sigma} = \frac{1}{J}\mathbf{F}\mathbf{S}\mathbf{F}^{\mathrm{T}}. \tag{2.69}$$

Two different material models are considered in this thesis.

[1]: Holzapfel (2000), *Nonlinear Solid Mechanics: A Continuum Approach for Engineering*
[8]: Belytschko et al. (2001), *Nonlinear Finite Elements for Continua and Structures*
[9]: Bonet et al. (1997), *Nonlinear Continuum mechanics for finite element analysis*

Saint Venant-Kirchhoff material The simplest example of a hyperelastic material is the St. Venant–Kirchhoff model, which is defined by the strain energy function

$$\Psi(\mathbf{E}) = \frac{1}{2}\lambda \mathrm{tr}(\mathbf{E})^2 + \mu \mathbf{E} : \mathbf{E}, \tag{2.70}$$

where $\mathbf{E} = \frac{1}{2}\{\mathbf{C} - \mathbf{I}\}$ is the Green-Lagrange strain tensor, $\mathbf{I}$ is the second rank identity tensor and λ and μ are the Lamé parameters. Using Eq. (2.68), we can obtain the PK2 stress tensor as

$$\mathbf{S} = \lambda \mathrm{tr}(\mathbf{E})\mathbf{I} + 2\mu\mathbf{E}. \tag{2.71}$$

The St. Venant-Kirchhoff material law is one of the most frequently used hyperelastic material laws in numerical simulations for finite strain theory. However, inherent shortcomings in the material law definition lead to nonphysical softening behavior and are thus inappropriate to be used in such scenarios [29].

[29]: Sautter et al. (2022), "Limitations of the St. Venant–Kirchhoff material model in large strain regimes"

Neo-Hookean material This material model is an extension of Hooke's law, widely used in linear elasticity, to large deformations. The stored energy function for a compressible Neo-Hookean material is expressed as

$$\Psi(\mathbf{C}) = \frac{1}{2}\lambda(\ln J)^2 - \mu \ln J + \frac{1}{2}\mu(\mathrm{tr}(\mathbf{C}) - \mathrm{tr}(\mathbf{I})). \tag{2.72}$$

Using Eq. (2.68), the expression for the PK2 stress tensor can be obtained:

$$\mathbf{S} = \lambda \ln J\mathbf{C}^{-1} + \mu(\mathbf{I} - \mathbf{C}^{-1}). \tag{2.73}$$

Time discretization

In this work implicit time integrators are considered. Let us now consider a partition of the time interval $[0, T]$ into N time steps of size Δt, assumed to be constant.

Backward differentiation formula (BDF) Given a generic time dependent function at a time step $t^{n+1} = t^n + \Delta t$, for $n = 0, 1, 2, ...$ the approximation of the time derivative of order $k = 1, 2, ...$ is written using information from already computed time instants and $\mathbf{u}^{n+1}$ which is being computed at this time step. In our problem, we have to approximate the second time derivative of the displacement, $\frac{\partial^2 \mathbf{u}}{\partial t^2}^{n+1} := \mathbf{a}^{n+1}$. Depending on the accuracy of the method, we can select for BDF1 and BDF2, respectively the specific formulae

$$\left.\frac{\delta^2 \mathbf{u}}{\delta t^2}\right|_{t^{n+1}} := \frac{1}{\Delta t^2}\left[\mathbf{u}^{n+1} - 2\mathbf{u}^n + \mathbf{u}^{n-1}\right] = \mathbf{a}^{n+1} + \mathcal{O}(\Delta t), \tag{2.74}$$

$$\left.\frac{\delta_2^2 \mathbf{u}}{\delta t^2}\right|_{t^{n+1}} := \frac{1}{\Delta t^2}\left[2\mathbf{u}^{n+1} - 5\mathbf{u}^n + 4\mathbf{u}^{n-1} - \mathbf{u}^{n-2}\right] = \mathbf{a}^{n+1} + \mathcal{O}\left(\Delta t^2\right). \tag{2.75}$$

Newmark-β equations This is a popular class of time integrators [8]. In this time integration formula, the updated acceleration $\mathbf{a}^{n+1}$ and velocity $\mathbf{v}^{n+1}$ are given by

[8]: Belytschko et al. (2001), *Nonlinear Finite Elements for Continua and Structures*

$$\mathbf{a}^{n+1} \approx \frac{1}{\beta \Delta t^2}[\mathbf{u}^{n+1} - \mathbf{u}^n - \Delta t \mathbf{v}^n - \frac{\Delta t^2}{2}(1 - 2\beta)\mathbf{a}^n], \tag{2.76}$$

$$\mathbf{v}^{n+1} \approx \mathbf{v}^n + (1 - \gamma)\Delta t \mathbf{a}^n + \gamma \Delta t \mathbf{a}^{n+1}. \tag{2.77}$$

Here β and γ are parameters to be tuned. When $\beta = \frac{1}{4}$ and $\gamma = \frac{1}{2}$ the Newmark-β method is implicit, unconditionally stable and second-order accurate for linear problems.

Remark 2.1.7 Newmark-β method is not unconditionally stable for nonlinear problems. The algorithmic energy con-

servation was recognized as the key to achieve stability in long term simulations according to the generalized theorem presented in [30]. The stability in time is further studied in [31, 32]. In [33, 34] several energy-momentum consistent time-stepping schemes are proposed for some mixed formulations in nonlinear problems.

[30]: Belytschko et al. (1975), "On the Unconditional Stability of an Implicit Algorithm for Nonlinear Structural Dynamics"
[31]: Simo et al. (1992), "Exact energy-momentum conserving algorithms and symplectic schemes for nonlinear dynamics"
[32]: Gonzalez (2000), "Exact energy and momentum conserving algorithms for general models in nonlinear elasticity"
[33]: Betsch et al. (2016), "An energy–momentum consistent method for transient simulations with mixed finite elements developed in the framework of geometrically exact shells"
[34]: Magisano et al. (2022), "Unconditional stability in large deformation dynamic analysis of elastic structures with arbitrary nonlinear strain measure and multi-body coupling"

Governing equations

We introduce now the solid dynamics problem in detail. Let $\mathfrak{D} = \{(\mathbf{X}, t) \,|\, \mathbf{X} \in \Omega_0,\ 0 < t < T\}$ be the space-time domain where the problem is defined. The problem consists of finding a displacement field, $\mathbf{u} : \mathfrak{D} \longrightarrow \mathbb{R}^d$ such that

Finite strain hyperelasticity. u formulation. Governing equations in TLF

$$\rho_0 \frac{\partial^2 \mathbf{u}}{\partial t^2} - \nabla \cdot \{\mathbf{F}(\mathbf{u})\mathbf{S}(\mathbf{u})\} = \rho_0 \mathbf{b} \quad \text{in } \Omega_0 \times]0, T[\,, \tag{2.78}$$

$$\mathbf{u} = \mathbf{u}_D \quad \text{on } \Gamma_{0_D} \times]0, T[\,, \tag{2.79}$$

$$\mathbf{n}_0 \cdot (\mathbf{F}(\mathbf{u})\mathbf{S}(\mathbf{u})) = \mathbf{t}_N \quad \text{on } \Gamma_{0_N} \times]0, T[\,, \tag{2.80}$$

$$\mathbf{u} = \mathbf{u}^0 \quad \text{in } \Omega_0,\ t = 0, \tag{2.81}$$

$$\frac{\partial \mathbf{u}}{\partial t} := \mathbf{v} = \mathbf{v}^0 \quad \text{in } \Omega_0,\ t = 0. \tag{2.82}$$

A set of boundary conditions is considered which can be split into Dirichlet boundary conditions (2.79), where the displacement is prescribed, and Neumann boundary conditions (2.80), where the value of tractions $\mathbf{t}_N$ is prescribed. Vector $\mathbf{n}_0$ is the geometric unit outward normal vector on the boundary of the initial configuration Γ_0. The governing equations must be supplied with initial conditions for both the displacement field (2.81) and the velocity field (2.82) in Ω_0, with $\mathbf{u}^0$ and $\mathbf{v}^0$ given.

2.1.3 Variational form

Let $\mathbb{U} := \{\mathbf{u} \in H^1(\Omega_0)^d \mid \mathbf{u} = \mathbf{u}_D \text{ on } \Gamma_{0_D}\}$ be the functional space where the displacement solution is well-defined for each fixed time $t \in]0, T[$. We denote by $\mathbb{U}_0$ functions in $H^1(\Omega_0)^d$ which vanish on the Dirichlet boundary Γ_{0_D}.

The variational statement of the problem is derived by testing Eq. (2.78) against arbitrary test function, $\delta\mathbf{u} \in \mathbb{U}_0$. The weak form of the problem reads: find $\mathbf{u} :]0, T[\to \mathbb{U}$ such that initial and Dirichlet boundary conditions are satisfied and

Finite strain hyperelasticity. u formulation. Variational form in TLF

$$\left\langle \delta u_a, \rho_0 \frac{\partial^2 u_a}{\partial t^2} \right\rangle + \mathscr{A}(\mathbf{u}, \delta\mathbf{u}) = \mathscr{F}(\delta\mathbf{u}) \quad \forall\, \delta\mathbf{u} \in \mathbb{U}_0, \tag{2.83}$$

where $\mathscr{A}(\mathbf{u}, \delta\mathbf{u})$ is a semilinear form defined on $\mathbb{U} \times \mathbb{U}_0$ as

$$\mathscr{A}(\mathbf{u}, \delta\mathbf{u}) := \left\langle \frac{\partial \delta u_a}{\partial X_A}, F_{aB} S_{BA} \right\rangle. \tag{2.84}$$

In addition, $\mathscr{F}(\delta\mathbf{u})$ is a linear form defined on $\mathbb{U}_0$ as

$$\mathscr{F}(\delta\mathbf{u}) := \langle \delta u_a, \rho_0 b_a \rangle + \left\langle \delta u_a, t_{N_a} \right\rangle_{\Gamma_{0_N}}. \tag{2.85}$$

As usual, integration by parts has been used in order to decrease the continuity requirements of the unknown $\mathbf{u}$.

2.1.4 Linearization

In order to solve the problem, the system needs to be linearized so that a bilinear operator which allows to compute a correction $\Delta\mathbf{u}$ of a given guess for the solution at time t^{n+1} is obtained, that we denote by $\mathbf{u}^{n+1}$. Iteration counters will be omitted to simplify the notation. After using a Newton-Raphson scheme and a time integrator, we obtain the following linearized form of the problem. Given $\mathbf{u}^{n+1}$ as the solution at time t^{n+1} and the previous iteration, find a correction $\Delta\mathbf{u} \in \mathbb{U}_0$ such that initial and Dirichlet boundary conditions are satisfied and

Finite strain hyperelasticity. u formulation. Linearized variational form in TLF

$$\left\langle \delta\mathbf{u}, \rho_0 \frac{C}{\Delta t^2} \Delta\mathbf{u} \right\rangle + \mathscr{B}(\Delta\mathbf{u}, \delta\mathbf{u}) = \mathscr{F}(\delta\mathbf{u})$$

$$- \mathscr{A}\left(\mathbf{u}^{n+1}, \delta\mathbf{u}\right) - \left\langle \delta\mathbf{u}, \rho_0 \mathbf{a}^{n+1} \right\rangle \quad \forall\, \delta\mathbf{u} \in \mathbb{U}_0, \tag{2.86}$$

where $\mathscr{B}(\Delta\mathbf{u}, \delta\mathbf{u})$ is the bilinear form obtained through the Newton-Raphson linearization and it is defined on $\mathbb{U}_0 \times \mathbb{U}_0$ as

$$\mathscr{B}(\Delta\mathbf{u}, \delta\mathbf{u}) := \left\langle \frac{\partial \delta u_a}{\partial X_A}, \frac{\partial \Delta u_a}{\partial X_B} S_{BA} \right\rangle + \left\langle \frac{\partial \delta u_a}{\partial X_A}, F_{aB} \mathbb{C}_{ABCD} F_{bC} \frac{\partial \Delta u_b}{\partial X_D} \right\rangle, \tag{2.87}$$

where $\mathbb{C}_{ABCD} = 2\frac{\partial^2 \Psi}{\partial C_{AB} \partial C_{CD}}$ is the constitutive tangent matrix which relates variations of the PK2 stress tensor, $\Delta\mathbf{S}$, with variations of the Right Cauchy tensor, $\Delta\mathbf{C}$. Let us remark that all terms are evaluated at $\mathbf{u}^{n+1}$.

Note that for every implicit time integrator presented here, we can write

$$\left.\frac{\partial^2 \mathbf{u}}{\partial t^2}\right|_{t^{n+1}} \approx \frac{C}{\Delta t^2} \Delta\mathbf{u} + \mathbf{a}^{n+1}, \tag{2.88}$$

where C is a coefficient depending on the time integration scheme, $\Delta\mathbf{u}$ is the displacement increment and $\mathbf{a}^{n+1}$ is the acceleration computed at the previous iteration, which in the time discretized problem will be given by any of the expressions introduced in Subsection 2.1.2.

2.1.5 Galerkin spatial discretization

We denote by $\mathscr{P}_h$ a FE partition of the domain Ω of the problem. The diameter of an element domain $K \in \mathscr{P}_h$ is denoted by h_K and the diameter on the FE partition by $h = \max\{h_K | K \in \mathscr{P}_h\}$. Now we consider the case in which $\Omega = \Omega_s(t)$ is the solid domain. From the FE partition we can construct conforming FE spaces $\mathbb{U}_h \subset \mathbb{U}$, as well as the corresponding subspace $\mathbb{U}_{h,0} \subset \mathbb{U}_0$ being made of functions that vanish on the Dirichlet boundary.

The Galerkin discrete version of problem (2.86) is: for a given time t^{n+1} and a fixed iteration, find $\Delta\mathbf{u}_h \in \mathbb{U}_{h,0}$ such that initial and Dirichlet boundary conditions are satisfied and

Finite strain hyperelasticity. u formulation. Galerkin discrete problem in TLF

$$\left\langle \delta\mathbf{u}_h, \rho_0 \frac{C}{\Delta t^2}\Delta\mathbf{u}_h \right\rangle + \mathscr{B}\left(\Delta\mathbf{u}_h, \delta\mathbf{u}_h\right) = \mathscr{F}\left(\delta\mathbf{u}_h\right) - \mathscr{A}\left(\mathbf{u}_h^{n+1}, \delta\mathbf{u}_h\right) - \left\langle \delta\mathbf{u}_h, \rho_0 \mathbf{a}_h^{n+1} \right\rangle \quad \forall\, \delta\mathbf{u}_h \in \mathbb{U}_{h,0}. \tag{2.89}$$

2.2 The Navier-Stokes equations of incompressible flows

From this point, the fluid mechanics problem is stated. This section is devoted to the presentation of the basic equations which allow to study both the dynamic behavior of an incompressible fluid and which also serve as a starting point for the developments in Chapter 5.

The material here presented is basic and the different parts of this section can be found in classical textbooks of fluid mechanics such as[35–37].

[35]: Landau et al. (1987), *Fluid Mechanics*
[36]: Aris (1989), *Vectors, Tensors and the Basic Equations of Fluid Mechanics*
[37]: Batchelor (2000), *An Introduction to Fluid Dynamics*

2.2.1 The continuous problem statement

In this subsection, the equations of motion are presented under the Newtonian incompressible fluid flow assumption. Let Ω be an open, bounded and polyhedral domain of $\mathbb{R}^d$ ($d = 2$ or 3) occupied by the fluid in the time interval $]0, T[$ and let $\Gamma := \partial\Omega$ be its boundary. The continuous Navier-Stokes problem for incompressible Newtonian fluid flows is defined by the following system of equations

Newtonian fluid flows. Navier-Stokes problem

$$\rho\left(\frac{\partial \mathbf{v}}{\partial t} + \mathbf{v}\cdot\nabla\mathbf{v}\right) - \nabla\cdot\boldsymbol{\sigma} + \nabla p = \mathbf{f} \qquad \text{in } \Omega\times]0,T[\,, \tag{2.90}$$

$$\nabla\cdot\mathbf{v} = 0 \qquad \text{in } \Omega\times]0,T[\,, \tag{2.91}$$

$$\frac{1}{2\mu}\boldsymbol{\sigma} - \nabla^{\mathrm{s}}\mathbf{v} = \mathbf{0} \qquad \text{in } \Omega\times]0,T[\,. \tag{2.92}$$

where $\mathbf{v}$ is the velocity field, p the pressure, $\boldsymbol{\sigma}$ the deviatoric component of the stress field, $\mathbf{f}$ the vector of body forces, μ the dynamic viscosity, ρ the fluid density and $\nabla^s\mathbf{v}$ is the symmetrical part of $\nabla\mathbf{v}$. Eq. (2.90) is the balance of momentum equation. Eq. (2.91) is the incompressibility equation and Eq. (2.92) is the deviatoric constitutive equation which relates deviatoric stresses $\boldsymbol{\sigma}$ with the velocity field $\mathbf{v}$.

2.2.2 Time discretization

Let us now consider a partition of the time interval $[0, T]$ into N time steps of size Δt, assumed to be constant. Regarding the time discretization, in this thesis, the first and second order backward differencing schemes are implemented to approximate the first order time derivative of the velocity. Given a generic time dependent function at a time step $t^{n+1} = t^n + \Delta t$, for $n = 0, 1, 2, ...$ the approximation of the time derivative of order $k = 1, 2, ...$ is written using information from already computed time instants and $\mathbf{v}^{n+1}$ which is being computed at this time step. Depending on the accuracy of the method, we can select the specific formulae

$$\left.\frac{\delta \mathbf{v}}{\delta t}\right|_{t^{n+1}} := \frac{1}{\Delta t}\left[\mathbf{v}^{n+1} - \mathbf{v}^n\right] = \frac{\partial \mathbf{v}^{n+1}}{\partial t} + \mathcal{O}\left(\Delta t\right), \tag{2.93}$$

$$\left.\frac{\delta_2 \mathbf{v}}{\delta t}\right|_{t^{n+1}} := \frac{1}{2\Delta t}\left[3\mathbf{v}^{n+1} - 4\mathbf{v}^n + \mathbf{v}^{n-1}\right] = \frac{\partial \mathbf{v}^{n+1}}{\partial t} + \mathcal{O}\left(\Delta t^2\right). \tag{2.94}$$

2.2.3 The two-field vp formulation

In this subsection, the well-known mixed vp formulation is introduced in order to deal with incompressible Newtonian fluid flows. In the presented formulation the velocity and pressure fields $\mathbf{v}$ and p are used as independent variables.

Governing equations

The governing equations of the problem are rewritten as

Newtonian fluid flows. vp formulation. Governing equations

$$\rho\left(\frac{\partial \mathbf{v}}{\partial t} + \mathbf{v}\cdot\nabla\mathbf{v}\right) - \nabla\cdot\boldsymbol{\sigma} + \nabla p = \mathbf{f} \qquad \text{in } \Omega\times]0,T[\,, \quad (2.95)$$

$$\nabla\cdot\mathbf{v} = 0 \qquad \text{in } \Omega\times]0,T[\,, \quad (2.96)$$

$$\boldsymbol{\sigma} - 2\mu\nabla^{s}\mathbf{v} = \mathbf{0} \qquad \text{in } \Omega\times]0,T[\,. \quad (2.97)$$

Eq. (2.95) allows us to formulate the linear momentum equation in terms of both velocities $\mathbf{v}$ and pressure p, where the stress tensor decomposition (2.97) is introduced into the momentum equation.

Strong form

To complete this subsection, we introduce the mixed $\mathbf{v}p$ problem, which consists in finding a velocity field $\mathbf{v}$ and a pressure p such that

Newtonian fluid flows. $\mathbf{v}p$ formulation. Governing equations

$$\frac{\partial \mathbf{v}}{\partial t} + \mathbf{v}\cdot\nabla\mathbf{v} - \nu\nabla^2\mathbf{v} + \nabla p = \mathbf{f} \qquad \text{in } \Omega\times]0,T[\,, \quad (2.98)$$

$$\nabla\cdot\mathbf{v} = 0 \qquad \text{in } \Omega\times]0,T[\,, \quad (2.99)$$

where $\nu = \mu/\rho$ is the kinematic viscosity. The equations above need to be solved together with initial conditions of the form $\mathbf{v} = \mathbf{v}^0$ at $t = 0$ and appropriate boundary conditions. For the sake of simplicity in the exposition, we will consider homogeneous boundary conditions $\mathbf{v} = \mathbf{0}$ on Γ.

Variational form

Let $\mathbb{V} = \left[H^1(\Omega)\right]^d$ and $\mathbb{P} = L^2(\Omega)$ be, respectively, the proper functional spaces where velocity and pressure solutions are well-defined. We denote by $\mathbb{V}_0$ functions in $\mathbb{V}$ which vanish in the Dirichlet boundary Γ_D. We shall be interested also in the spaces $\mathbb{W} := \mathbb{V}\times\mathbb{P}$, $\mathbb{W}_0 := \mathbb{V}_0\times\mathbb{P}$. The variational statement of the problem is derived by testing the system presented in Eqs. (2.98-2.99) against arbitrary test functions $\delta\mathbf{V} := [\delta\mathbf{v}, \delta p]^T$, $\delta\mathbf{v} \in \mathbb{V}_0$ and $\delta p \in \mathbb{P}$. The weak form of the problem reads: find $\mathbf{V} := [\mathbf{v}, p]^T \in \mathbb{W}_0$ such that initial conditions are satisfied and

Newtonian fluid flows. vp formulation. Variational form

$$\left\langle \frac{\partial \mathbf{v}}{\partial t}, \delta \mathbf{v} \right\rangle + \mathscr{A}(\mathbf{v}; \mathbf{V}, \delta \mathbf{V}) = \mathscr{F}(\delta \mathbf{V}) \quad \forall\, \delta \mathbf{V} \in \mathbb{W}_0, \quad (2.100)$$

where $\mathscr{A}(\hat{\mathbf{v}}; \mathbf{V}, \delta \mathbf{V})$ is a bilinear form defined on $\mathbb{W}_0 \times \mathbb{W}_0$ as

$$\mathscr{A}(\hat{\mathbf{v}}; \mathbf{V}, \delta \mathbf{V}) := \langle \hat{\mathbf{v}} \cdot \nabla \mathbf{v}, \delta \mathbf{v} \rangle + \nu (\nabla \mathbf{v}, \nabla \delta \mathbf{v}) - (p, \nabla \cdot \delta \mathbf{v}) + (\nabla \cdot \mathbf{v}, \delta p). \quad (2.101)$$

$\mathscr{F}(\delta \mathbf{V})$ is a linear form defined on $\mathbb{W}_0$ as

$$\mathscr{F}(\delta \mathbf{V}) := \langle \mathbf{f}, \delta \mathbf{v} \rangle. \quad (2.102)$$

Note that the Navier-Stokes problem to be solved has one source of nonlinearity, namely, the convective term. For the sake of conciseness, we will consider only a fixed-point iterative scheme (another possibility would be to use a Newton-Raphson scheme). In particular, a given velocity $\hat{\mathbf{v}}$ is taken as initial guess to solve an iterative procedure. As usual, integration by parts has been used in order to decrease the continuity requirements of unknowns $\mathbf{v}$ and p.

Galerkin spatial discretization

The standard Galerkin approximation of this abstract variational problem is now straightforward. Let $\mathscr{P}_h$ denote a FE partition of the domain Ω. The diameter of an element domain $K \in \mathscr{P}_h$ is denoted by h_K and the diameter on the FE partition by $h = \max\{h_K | K \in \mathscr{P}_h\}$. We can now construct conforming FE spaces $\mathbb{V}_h \subset \mathbb{V}$, $\mathbb{P}_h \subset \mathbb{P}$ and $\mathbb{W}_h = \mathbb{V}_h \times \mathbb{P}_h$ in the usual manner, as well as the corresponding subspaces $\mathbb{V}_{h,0} \subset \mathbb{V}_0$ and $\mathbb{W}_{h,0} = \mathbb{V}_{h,0} \times \mathbb{P}_h$, $\mathbb{V}_{h,0}$ being made with functions that vanish on the Dirichlet boundary.

The Galerkin discrete version of problem (2.100) is: Find $\mathbf{V}_h := [\mathbf{v}_h, p_h]^T \in \mathbb{W}_{h,0}$ such that

Newtonian fluid flows. vp formulation. Galerkin discrete problem

$$\left\langle \frac{\partial \mathbf{v}_h}{\partial t}, \delta \mathbf{v}_h \right\rangle + \mathscr{A}\left(\mathbf{v}_h; \mathbf{V}_h, \delta \mathbf{V}_h\right) = \mathscr{F}\left(\delta \mathbf{V}_h\right) \quad \forall\, \delta \mathbf{V}_h \in \mathbb{W}_{h,0}. \tag{2.103}$$

This problem also requires and inf-sup condition to be satisfied between the interpolation spaces. Otherwise, instabilities may appear. In order to overcome such instabilities, we use again the stabilization technique described in next subsection.

Remark 2.2.1 So far, no restrictions have been imposed on the choice of the FE spaces. However, there are restrictions that must be satisfied explicitly in the discrete formulation. To see this, let us consider the stationary Navier-Stokes problem. Taking $\delta \mathbf{V}_h = \mathbf{V}_h$, it is easily seen that the Galerkin formulation only provides control over the velocity field

$$\begin{aligned} \mathscr{A}\left(\mathbf{v}_h; \mathbf{V}_h, \mathbf{V}_h\right) &= \langle \mathbf{v}_h \cdot \nabla \mathbf{v}_h, \mathbf{v}_h \rangle + \nu \left(\nabla \mathbf{v}_h, \nabla \mathbf{v}_h\right) \\ &= \nu \|\nabla \mathbf{v}_h\|^2. \end{aligned} \tag{2.104}$$

It is seen from Eq. (2.104) that $\mathscr{A}$ is not coercive in $\mathbb{W}_{h,0}$, the pressure being out of control. Furthermore, when $\nu \to 0$ the velocity is also out of control.

From the numerical point of view, the spaces that fulfill the inf-sup conditions associated to the bilinear form are limited. In fact, equal order interpolations for both velocities and pressure turn out to violate the inf-sup conditions. The alternative is to use a stabilized formulation allowing any interpolation for the variables.

Stabilization

Let $\mathbb{W} = \mathbb{W}_h \oplus \tilde{\mathbb{W}}$, where $\tilde{\mathbb{W}}$ is any space to complete $\mathbb{W}_h$ in $\mathbb{W}$. $\tilde{\mathbb{W}}$ will be approximated by a finite-dimensional space despite the fact that it is infinite-dimensional. The elements of this space are denoted by $\tilde{\mathbf{V}} := [\tilde{\mathbf{v}}, \tilde{p}]^T$ and they are called subscales. Likewise, let $\mathbb{W}_0 = \mathbb{W}_{h,0} \oplus \tilde{\mathbb{W}}_0$.

We assume the subscales to behave as bubble functions, which means that they vanish across inter-element boundaries.In this case, we consider them to be time-dependent or dynamic.

Then, the sub-grid scale is expressed in terms of the residual of the projected (Galerkin) counterpart of Eqs. (2.98–2.99) to obtain

$$\frac{\partial \tilde{\mathbf{v}}}{\partial t} + \tau_{\mathbf{v}}^{-1}\tilde{\mathbf{v}} \approx \tilde{\Pi}\left(\mathbf{f} - \hat{\mathbf{v}}_h \cdot \nabla \mathbf{v}_h + \nu \nabla^2 \mathbf{v}_h - \nabla p_h\right), \tag{2.105}$$

$$\tilde{p} \approx \tau_p \tilde{\Pi}\left(-\nabla \cdot \mathbf{v}_h\right), \tag{2.106}$$

where $\tilde{\Pi}$ is the $L^2(\Omega)$ projection onto the space of SGS and $\tau_{\mathbf{v}}$ and τ_p are coefficients coming from a Fourier analysis of the problem for the subscales. In this work, we use the stabilization parameters proposed in [38] as

[38]: Codina et al. (2018), "Variational Multiscale Methods in Computational Fluid Dynamics"

$$\tau_{\mathbf{v}}^{-1} = c_1 \frac{2\nu}{h_K^2} + c_2 \frac{|\hat{\mathbf{v}}_h|}{h_K} \quad \text{and} \quad \tau_p = 2c_3\nu, \tag{2.107}$$

where term $|\hat{\mathbf{v}}_h|$ is the Euclidean norm of the velocity guess and c_1, c_2 and c_3 are algorithmic parameters which must be determined. The values used in the numerical examples for linear elements are $c_1 = 4.0$, $c_2 = 2.0$ and $c_3 = 0.1$. Values c_1 and c_2 are the optimal values for the approximation of the one-dimensional convection-diffusion equations , whereas c_3 has been found to give good results in the tests.

Introducing the approximate fields (2.105-2.106) into the FE scale problem (2.103), the VMS stabilized formulation of the problem is obtained as

Newtonian fluid flows. vp formulation. Stabilized weak form

$$\begin{aligned}\left\langle \frac{\partial \mathbf{v}_h}{\partial t}, \delta \mathbf{v}_h \right\rangle &+ \mathscr{A}\left(\mathbf{v}_h; \mathbf{V}_h, \delta \mathbf{V}_h\right) \\ &+ \sum_K \left\langle -\mathbf{v}_h \cdot \nabla \delta \mathbf{v}_h + \nu \nabla^2 \delta \mathbf{v}_h - \nabla \delta p_h, \tilde{\mathbf{v}} \right\rangle_K \\ &+ \sum_K \left\langle -\nabla \cdot \delta \mathbf{v}_h, \tilde{p} \right\rangle_K = \mathscr{F}\left(\delta \mathbf{V}_h\right) \quad \forall\, \delta \mathbf{V}_h \in \mathbb{W}_{h,0}.\end{aligned} \tag{2.108}$$

2.2.4 The three-field v$p\sigma$ formulation

In this subsection we present the mixed three-field formulation used to deal with incompressible Newtonian fluid flows. The methodology was developed in [39] with the purpose

[39]: Castillo et al. (2014), "Stabilized stress-velocity-pressure finite element formulations of the Navier-Stokes problem for fluids with non-linear viscosity"

of extending the formulation presented in [26] to deal with the Stokes problem in fluid mechanics. The velocity field $\mathbf{v}$, together with the deviatoric component of the stresses $\boldsymbol{\sigma}$, as well as the pressure field p (taken as positive in compression) are taken as primary unknowns of the problem. The objective is the definition of a general framework, which includes the well-known mixed $\mathbf{v}p$ formulation. Therefore we are capable of correctly describing incompressible material behavior. Adding the deviatoric stresses as unknowns allows us to obtain a high degree of accuracy for the stress field. The most salient problem that requires the interpolation of the (deviatoric) stresses is the viscoelastic one which is presented in Chapter 5.

[26]: R.Codina (2009), "Finite element approximation of the three field formulation of the Stokes problem using arbitrary interpolations"

Governing equations

The governing equations of the problem are rewritten as

Newtonian fluid flows. $\mathbf{v}p\boldsymbol{\sigma}$ formulation. Governing equations

$$\rho\left(\frac{\partial \mathbf{v}}{\partial t} + \mathbf{v}\cdot\nabla\mathbf{v}\right) - \nabla\cdot\boldsymbol{\sigma} + \nabla p = \mathbf{f} \quad \text{in } \Omega\times\,]0,T[\,, \tag{2.109}$$

$$\nabla\cdot\mathbf{v} = 0 \quad \text{in } \Omega\times\,]0,T[\,, \tag{2.110}$$

$$\frac{1}{2\mu}\boldsymbol{\sigma} - \nabla^{\mathrm{s}}\mathbf{v} = \mathbf{0} \quad \text{in } \Omega\times\,]0,T[\,. \tag{2.111}$$

Strong form

To complete this subsection, we introduce the mixed $\mathbf{v}p\boldsymbol{\sigma}$ problem, which consists in finding a velocity field $\mathbf{v}$, a pressure p and a deviatoric stress field $\boldsymbol{\sigma}$ such that

Newtonian fluid flows. $\mathbf{v}p\boldsymbol{\sigma}$ formulation. Strong form

$$\rho\left(\frac{\partial \mathbf{v}}{\partial t} + \mathbf{v}\cdot\nabla\mathbf{v}\right) - \nabla\cdot\boldsymbol{\sigma} + \nabla p = \mathbf{f} \quad \text{in } \Omega\times\,]0,T[\,, \tag{2.112}$$

$$\nabla\cdot\mathbf{v} = 0 \quad \text{in } \Omega\times\,]0,T[\,, \tag{2.113}$$

$$\frac{1}{2\mu}\boldsymbol{\sigma} - \nabla^{\mathrm{s}}\mathbf{v} = \mathbf{0} \quad \text{in } \Omega\times\,]0,T[\,. \tag{2.114}$$

The equations above need to be solved together with initial conditions of the form $\mathbf{v} = \mathbf{v}^0$ at $t = 0$ and appropriate boundary conditions. For the sake of simplicity in the exposition, we will consider homogeneous boundary conditions $\mathbf{v} = \mathbf{0}$ on Γ.

Remark 2.2.2 Note that deviatoric stresses have been added to the system as a primary unknown of the problem. Therefore, we are hopefully incrementing the accuracy of the deviatoric stress field $\boldsymbol{\sigma}$.

Variational form

Let us consider the same spaces and test functions we have defined previously for the mixed $\mathbf{v}p$ formulation. Let $\mathbb{Y} = \left[L^2(\Omega)\right]^{d\times d}_{\text{sym}}$ (symmetric second order tensors with square integrable components) be the proper functional space where deviatoric stress is well-defined. We shall be interested also in the spaces $\mathbb{W} := \mathbb{V} \times \mathbb{P} \times \mathbb{Y}$, $\mathbb{W}_0 := \mathbb{V}_0 \times \mathbb{P} \times \mathbb{Y}$. The variational statement of the problem is derived by testing system (2.112-2.114) against arbitrary test functions $\delta\mathbf{V} := [\delta\mathbf{v}, \delta p, \delta\boldsymbol{\sigma}]^T$, $\delta\mathbf{v} \in \mathbb{V}_0$, $\delta p \in \mathbb{P}$ and $\delta\boldsymbol{\sigma} \in \mathbb{Y}$. The weak form of the problem reads: find $\mathbf{V} := [\mathbf{v}, p, \boldsymbol{\sigma}]^T \in \mathbb{W}_0$ such that initial conditions are satisfied and

Newtonian fluid flows. $\mathbf{v}p\boldsymbol{\sigma}$ formulation. Variational form

$$\left(\rho\frac{\partial\mathbf{v}}{\partial t}, \delta\mathbf{v}\right) + \mathscr{A}(\mathbf{v}; \mathbf{V}, \delta\mathbf{V}) = \mathscr{F}(\delta\mathbf{V}) \quad \forall\, \delta\mathbf{V} \in \mathbb{W}_0, \tag{2.115}$$

where $\mathscr{A}(\hat{\mathbf{v}}; \mathbf{V}, \delta\mathbf{V})$ is a bilinear form defined on $\mathbb{W}_0 \times \mathbb{W}_0$ as

$$\begin{aligned}\mathscr{A}(\hat{\mathbf{v}}; \mathbf{V}, \delta\mathbf{V}) := \langle\rho\hat{\mathbf{v}}\cdot\nabla\mathbf{v}, \delta\mathbf{v}\rangle + (\boldsymbol{\sigma}, \nabla^s\delta\mathbf{v}) - (p, \nabla\cdot\delta\mathbf{v}) \\ + (\nabla\cdot\mathbf{v}, \delta p) + \left(\frac{1}{2\mu}\boldsymbol{\sigma}, \delta\boldsymbol{\sigma}\right) - (\nabla^s\mathbf{v}, \delta\boldsymbol{\sigma}).\end{aligned} \tag{2.116}$$

$\mathscr{F}(\delta\mathbf{V})$ is a linear form defined on $\mathbb{W}_0$ as

$$\mathscr{F}(\delta\mathbf{V}) := \langle\mathbf{f}, \delta\mathbf{v}\rangle. \tag{2.117}$$

We will consider again a fixed-point iterative scheme to linearize the convective term. Therefore, a given guess of the

velocity $\hat{\mathbf{v}}$ is taken to solve the iterative procedure. As usual, integration by parts has been used in order to decrease the continuity requirements of the unknowns.

Galerkin spatial discretization

We can now construct a conforming FE space $\mathbb{Y}_h \subset \mathbb{Y}$ and redefine $\mathbb{W}_h = \mathbb{U}_h \times \mathbb{P}_h \times \mathbb{E}_h$ as well as the corresponding subspace $\mathbb{W}_{h,0} = \mathbb{U}_{h,0} \times \mathbb{P}_h \times \mathbb{E}_h$ in the usual manner.

The Galerkin discrete version of problem (2.115) is: Find $\mathbf{V}_h := [\mathbf{v}_h, p_h, \boldsymbol{\sigma}_h]^T \in \mathbb{W}_{h,0}$ such that

Newtonian fluid flows. v$p\boldsymbol{\sigma}$ formulation. Galerkin discrete problem

$$\left\langle \rho \frac{\partial \mathbf{v}_h}{\partial t}, \delta \mathbf{v}_h \right\rangle + \mathscr{A}(\mathbf{v}_h; \mathbf{V}_h, \delta \mathbf{V}_h) = \mathscr{F}(\delta \mathbf{V}_h) \quad \forall\, \delta \mathbf{V}_h \in \mathbb{W}_{h,0}. \tag{2.118}$$

This problem also requires an inf-sup condition to be satisfied between the interpolation spaces. Otherwise, instabilities may appear. In order to overcome such instabilities, we use again the stabilization technique described in next subsection.

Remark 2.2.3 So far, no restrictions have been imposed on the choice of the FE spaces. However, there are restrictions that must be satisfied explicitly in the discrete formulation. To see this, let us consider the stationary Navier-Stokes problem. Taking $\delta \mathbf{V}_h = \mathbf{V}_h$, it is easily seen that the Galerkin formulation only provides control over the stress field

$$\begin{aligned} \mathscr{A}(\hat{\mathbf{v}}_h; \mathbf{V}_h, \mathbf{V}_h) &:= \langle \rho \hat{\mathbf{v}}_h \cdot \nabla \mathbf{v}_h, \mathbf{v}_h \rangle + \left(\frac{1}{2\mu} \boldsymbol{\sigma}_h, \boldsymbol{\sigma}_h \right) \\ &= \frac{1}{2\mu} \|\boldsymbol{\sigma}_h\|^2. \end{aligned} \tag{2.119}$$

It is seen from Eq. (2.119) that $\mathscr{A}$ is not coercive in $\mathbb{W}_{h,0}$, both the velocity and the pressure being out of control.

Stabilization

The elements of the SGS space are now denoted by $\tilde{\mathbf{V}} := [\tilde{\mathbf{v}}, \tilde{p}, \tilde{\boldsymbol{\sigma}}]^T$. The dynamic SGS are expressed in terms of the residual of the projected (Galerkin) counterpart of Eqs. (2.112–2.114) to obtain

$$\rho \frac{\partial \tilde{\mathbf{v}}}{\partial t} + \tau_{\mathbf{v}}^{-1} \tilde{\mathbf{v}} \approx \tilde{\Pi} \left(-\rho \hat{\mathbf{v}}_h \cdot \nabla \mathbf{v}_h - \nabla \cdot \boldsymbol{\sigma}_h + \nabla p_h + \mathbf{f} \right), \tag{2.120}$$

$$\tilde{p} \approx \tau_p \tilde{\Pi} \left(-\nabla \cdot \mathbf{v}_h \right), \tag{2.121}$$

$$\tilde{\boldsymbol{\sigma}} \approx \tau_{\boldsymbol{\sigma}} \tilde{\Pi} \left(-\frac{1}{2\mu} \boldsymbol{\sigma}_h + \nabla^{\mathrm{s}} \mathbf{v}_h \right), \tag{2.122}$$

where $\tilde{\Pi}$ is the $L^2(\Omega)$ projection onto the space of SGS and $\tau_{\mathbf{v}}$, τ_p and $\tau_{\boldsymbol{\sigma}}$ are coefficients coming from a Fourier analysis of the problem for the subscales. In this work, we use the stabilization parameters proposed in [39] as

[39]: Castillo et al. (2014), "Stabilized stress-velocity-pressure finite element formulations of the Navier-Stokes problem for fluids with non-linear viscosity"

$$\tau_{\mathbf{v}}^{-1} = c_1 \frac{\mu}{h_K^2} + c_2 \frac{\rho |\hat{\mathbf{v}}_h|}{h_K}, \quad \tau_p = 2 c_3 \mu \quad \text{and} \quad \tau_{\boldsymbol{\sigma}} = 2 c_4 \mu \tag{2.123}$$

where c_1, c_2, c_3 and c_4 are algorithmic parameters which must be determined. The values used in the numerical examples are $c_1 = 4.0$, $c_2 = 2.0$, $c_3 = 0.1$ and $c_4 = 0.1$. Values c_1 and c_2 are the optimal values for the approximation of the one-dimensional convection-diffusion equations , whereas c_3 and c_4 have been found to give good results in the tests.

Introducing the approximate fields (2.120-2.122) into the FE scale problem (2.118), the VMS stabilized formulation of the problem is obtained as

Newtonian fluid flows. v$p\boldsymbol{\sigma}$ formulation. Stabilized weak form

$$\begin{aligned} &\left\langle \frac{\partial \mathbf{v}_h}{\partial t}, \delta \mathbf{v}_h \right\rangle + \mathscr{A}\left(\mathbf{v}_h; \mathbf{V}_h, \delta \mathbf{V}_h\right) \\ &\quad + \sum_K \left\langle -\rho \mathbf{v}_h \cdot \nabla \delta \mathbf{v}_h + \nabla \cdot \delta \boldsymbol{\sigma}_h - \nabla \delta p_h, \tilde{\mathbf{v}} \right\rangle_K \\ &\quad + \sum_K \left\langle \frac{1}{2\mu} \delta \boldsymbol{\sigma}_h + \nabla^{\mathrm{s}} \delta \mathbf{v}_h, \tilde{\boldsymbol{\sigma}} \right\rangle_K \\ &\quad + \sum_K \left\langle -\nabla \cdot \delta \mathbf{v}_h, \tilde{p} \right\rangle_K = \mathscr{F}\left(\delta \mathbf{V}_h\right) \quad \forall\, \delta \mathbf{V}_h \in \mathbb{W}_{h,0}. \end{aligned} \tag{2.124}$$

Mixed formulations in finite strain solid dynamics

3

3.1 Introduction

An incompressible material is understood as the one which keeps its volume constant throughout a motion. In many cases, this is a common idealization and accepted assumption often invoked in continuum and computational mechanics [1]. Numerous polymeric materials can sustain finite strains without noticeable volume changes. Furthermore, many biological materials and several types of soils can be modeled as nearly or fully incompressible [40].

[1]: Holzapfel (2000), *Nonlinear Solid Mechanics: A Continuum Approach for Engineering*

[40]: Holzapfel (2001), "Biomechanics of soft tissue"

Standard irreducible low order FE, in which only the displacement field is considered as the unknown variable of the problem and both stress and strain fields are obtained a posteriori, are typically preferred in complex engineering finite strain solid dynamics problems [8]. Nevertheless, this approach performs poorly in nearly and fully incompressible scenarios, producing solutions which are completely locked by the constraint. Volumetric and shear locking, pressure fluctuations and poor performance in bending dominated scenarios are some of the effects that can be observed in such situations [41].

[8]: Belytschko et al. (2001), *Nonlinear Finite Elements for Continua and Structures*

[41]: T.J.R.Hughes (1987), *The Finite Element Method: Linear Static and Dynamic Finite Element Analysis*

Over the last years, different strategies and methodologies have been proposed to reduce or avoid these shortcomings by circumventing the inf-sup conditions (also called Ladyzhenskaya-Babuška-Brezzi (LBB) conditions) [22]. Popular solutions to tackle the nearly incompressible limit in the solid mechanics community are reduced and selective integration techniques [42], the B-bar and the F-bar methods [43] or the well-known mean dilatation FEM, which avoid these numerical instabilities by reducing the evaluations of the incompressibility constraints at quadrature points. However, these strategies are only prepared to work with structured quadrilateral and structured hexahedral meshes and they are not able to tackle the fully incompressible regime. Many of these displacement-based methods have been shown to be equivalent to mixed methods in which the stresses are approximated by fields of order lower than the displacements over the elements [42].

[22]: Babuška (1971), "Error-Bounds for Finite Element Method"

[42]: Malkus et al. (1978), "Mixed finite element methods - Reduced and selective integration techniques: A unification of concepts"

[43]: Elguedj et al. (2008), "$\bar{B}$ and $\bar{F}$ projection methods for nearly incompressible linear and nonlinear elasticity and plasticity using higher-order NURBS elements"

When considering the static, infinitesimal strain, incompressible case of the solid mechanics problem, we obtain an elliptic problem which is identical to the equations of the Stokes problem in fluid mechanics [24, 44]. Mixed formulations are well established and regularly used to avoid these instabilities. For this reason, it makes sense to extend the mixed velocity/pressure pair used in the latter to the former for the mixed displacement/pressure approach [23, 45].

The use of different stabilization techniques, and particularly those based on the VMS framework [6], allows for the use of equal-order interpolations for all master fields. This idea facilitated the extension of different implementations in the field of fluid mechanics to the solid mechanics area. A particular formulation of this type, namely, the OSGS method [13], was used in [46] to design a stabilized FE formulation for the three-field linear Stokes problem, using displacements, pressure and deviatoric stresses as variables. The analysis and FE approximation of Darcy's problem presented in [47] motivated the introduction of both strains/displacements and stresses/displacements pairs as primary variables in [10] for infinitesimal strain elasticity; in this particular case, one can change the functional framework to increase the accuracy in the calculation of the stresses. To tackle the incompressible limit, the pressure needs to be introduced as a variable [23, 48, 49], although it is also possible to design a formulation using the volumetric strain as unknown [50]. Formulations including stresses as unknowns produce a considerable increase in the number of unknowns per node, but they also increase the accuracy for strains and stresses. Furthermore, in [27] the idea of using a three-field displacement/pressure/deviatoric stress formulation was tested and seen to be very effective when solving incompressible cases in which accurate results for stress and strain fields are required. These FE technologies have demonstrated enhanced stress accuracy as well as the ability to capture stress concentrations and strain localizations guaranteeing stress convergence upon mesh refinement for first order elements.

The majority of the previous works were developed for the static case. When considering the transient case, the elliptic problem becomes hyperbolic due to the second order derivative of the displacements which appears in the momentum equation. Mixed formulations are also applied under the transient finite strain assumption. On the one hand, a new first-order mixed form of the equations of finite strain solid dy-

[24]: Codina (2001), "A stabilized finite element method for generalized stationary incompressible flows"

[44]: Hughes et al. (1986), "A new finite element formulation for computational fluid dynamics: V. Circumventing the babuška-brezzi condition: a stable Petrov-Galerkin formulation of the stokes problem accommodating equal-order interpolations"

[23]: Baiges et al. (2017), "Variational Multiscale error estimators for solid mechanics adaptive simulations: an Orthogonal Subgrid Scale approach"

[45]: Franca et al. (1988), "A new family of stable elements for nearly incompressible elasticity based on a mixed Petrov-Galerkin finite element formulation"

[6]: Hughes et al. (1998), "The variational multiscale method - A paradigm for computational mechanics"

[13]: Codina (2002), "Stabilized finite element approximation of transient incompressible flows using orthogonal subscales"

[46]: Codina (2009), "Finite element approximation of the three field formulation of the Stokes problem using arbitrary interpolations"

[47]: Badia et al. (2009), "Unified stabilized finite element formulations for the Stokes and the Darcy problems"

[10]: Cervera et al. (2010), "Mixed Stabilized Finite Element Methods in Nonlinear Solid Mechanics. Part I: Formulation"

namics is presented in [51–54]. In these works, the authors propose to use as primary variables the linear momentum $\mathbf{p}$ and the deformation gradient $\mathbf{F}$. In order to effectively solve bending dominated scenarios in nearly incompressible cases they consider the introduction of the Jacobian J as an extra unknown [55–57]. In more recent works [58–60], they insert the cofactor tensor of the deformation gradient $\mathbf{H} = \text{cof}\,\mathbf{F}$ as an additional primary variable. The objective for this choice of variables is to ease dealing with some complex constitutive laws, and in particular with polyconvex hyperelastic potentials. The resulting system turns out to be unstable and for this reason, the authors stabilize the problem through a combination of the streamline upwind/Petrov Galerkin (SUPG) stabilization and different penalties on the deformation gradient. This methodology is very promising and it has been tested to be very effective to solve nearly incompressible cases. However, the number of unknowns per node increases drastically taking into account that both $\mathbf{F}$ and $\mathbf{H}$ are non-symmetric tensors. On the other hand, an effective alternative taking the velocity/pressure pair as unknowns of the problem and updating the displacement explicitly as a final step was proposed in [61, 62]. The authors suggest to complement the momentum equation with a rate equation for the evolution of the pressure field and solve it by means of a two-step block Gauss-Seidel strategy, stabilized by means of the VMS method. This formulation is also very powerful despite the necessity of introducing the velocity field as a primary variable of the problem in addition to the pressure field. In [63] the incompressibility of the material is treated with the displacement/pressure pair in an updated Lagrangian formulation framework. Another possibility is to consider Finite Volume schemes to present a conservative cell-centered Lagrangian Finite Volume scheme for solving the hyperelasticity equations on unstructured multidimensional grids [64].

The idea of this chapter is to develop mixed formulations for finite strain solid dynamics which are capable of dealing with hyperelastic materials including the incompressible limit case.

This chapter is organized as follows. Firstly, in Section 3.2 the conservation equations which govern the finite strain solid dynamic problem are presented. In the second place, the constitutive equations for isotropic hyperelastic material models are stated in Section 3.3. Next, in Section 3.4 several implicit

[23]: Baiges et al. (2017), "Variational Multiscale error estimators for solid mechanics adaptive simulations: an Orthogonal Subgrid Scale approach"
[48]: Chiumenti et al. (2002), "A stabilized formulation for incompressible elasticity using linear displacement and pressure interpolations"
[49]: Codina et al. (2022), "Modal analysis of elastic vibrations of incompressible materials using a pressure-stabilized finite element method"
[50]: Rossi et al. (2021), "A stabilized displacement-volumetric strain formulation for nearly incompressible and anisotropic materials"
[27]: Chiumenti et al. (2015), "A mixed three-field FE formulation for stress accurate analysis including the incompressible limit"
[51]: Bonet et al. (1998), "A simple average nodal pressure tetrahedral element for incompressible and nearly incompressible dynamic explicit applications"
[52]: Lee et al. (2013), "Development of a cell centred upwind finite volume algorithm for a new conservation law formulation in structural dynamics"
[53]: Aguirre et al. (2014), "A vertex centred finite volume Jameson-Schmidt-Turkel (JST) algorithm for a mixed conservation formulation in solid dynamics"
[54]: J. Haider et al. (2017), "A first-order hyperbolic framework for large strain computational solid dynamics. An upwind cell centred Total Lagrangian scheme"

[55]: Lee et al. (2014), "Development of a stabilised Petrov-Galerkin formulation for linear tetrahedral elements in compressible, nearly incompressible and truly incompressible fast dynamics"

[56]: Lee et al. (2014), "A stabilised Petrov-Galerkin formulation for linear tetrahedral elements in compressible, nearly incompressible and truly incompressiblefast dynamics"

[57]: Aguirre et al. (2015), "An upwind vertex centred finite volume solver for Lagrangian solid dynamics"

[58]: Bonet et al. (2015), "A first order hyperbolic framework for large strain computational solid dynamics. Part I : Total Lagrangian isothermal elasticity"

[59]: Gil et al. (2016), "A first order hyperbolic framework for large strain computational solid dynamics. Part II : Total Lagrangian compressible, nearly incompressible and truly incompressible elasticity"

[60]: Hassan et al. (2019), "An upwind vertex centred finite volume algorithm for nearly and truly incompressible explicit fast solid dynamic applications: Total and Updated Lagrangian formulations"

[61]: Scovazzi et al. (2016), "A simple, stable, and accurate linear tetrahedral finite element for transient, nearly, and fully incompressible solid dynamics: a dynamic variational multiscale approach"

[62]: Rossi et al. (2016), "Implicit finite incompressible elastodynamics with linear finite elements: A stabilized method in rate form"

[63]: Nemer et al. (2021), "Stabilized finite element method for incompressible solid dynamics using an updated Lagrangian formulation"

time integrators are shown to perform the time discretization of the problem. Two different mixed formulations are introduced afterwards. On the one hand, in Section 3.5 the mixed two-field $\mathbf{u}p$ formulation is presented to deal with nearly and fully incompressible materials. On the other hand, in Section 3.6 the mixed three-field $\mathbf{u}p\mathbf{S}'$ formulation is elaborated to be capable of giving a higher stress accuracy and performance, at the same time, in the incompressible limit. Finally, in Section 3.7 some conclusions of the proposed mixed formulations are drawn.

3.2 Conservation equations

Let $\Omega_0 \coloneqq \Omega(0)$ be an open, bounded and polyhedral domain of $\mathbb{R}^d$, where $d \in \{2,3\}$ is the number of space dimensions. The initial configuration of the body is Ω_0, whereas the current configuration of the body at time t is denoted by $\Omega(t)$. The motion is described by a function $\boldsymbol{\psi}$ which links a material particle $\mathbf{X} \in \Omega_0$ to the spatial configuration $\mathbf{x} \in \Omega(t)$ according to

$$\boldsymbol{\psi} : \Omega_0 \longrightarrow \Omega(t), \quad \mathbf{x} = \boldsymbol{\psi}(\mathbf{X}, t), \quad \forall \mathbf{X} \in \Omega_0, \quad t \geq 0. \tag{3.1}$$

The boundary of the reference configuration is denoted as $\Gamma_0 \coloneqq \partial\Omega_0$ and $\Gamma(t) \coloneqq \partial\Omega(t)$ represents the boundary of the current configuration at time t. We always assume that the mapping between both boundaries is defined through the motion, i.e., $\boldsymbol{\psi}(\Gamma_0, t) = \Gamma(t)$. We denote as $]0, T[$ the time interval of analysis.

The conservation of linear momentum in finite strain theory in a TLF framework reads as

$$\rho_0 \frac{\partial^2 u_a}{\partial t^2} - \frac{\partial}{\partial X_A}\{F_{aB} S_{BA}\} = \rho_0 b_a \quad \text{in } \Omega_0 \times]0, T[, \tag{3.2}$$

where ρ_0 is the initial density, $\mathbf{F} = \frac{\partial \mathbf{x}}{\partial \mathbf{X}}$ is the deformation gradient, $\mathbf{S}$ is the second Piola-Kirchhoff (PK2) stress tensor and $\rho_0 \mathbf{b}$ are the body forces. Mass conservation implies that

$$\rho J = \rho_0, \tag{3.3}$$

where ρ is the density at time t and $J = \det \mathbf{F} > 0$ is the Jacobian of $\mathbf{F}$. With regards to the balance of angular momentum,

it implies that the PK2 stress tensor must be symmetric.

The objective of this section is to obtain mixed formulations able to deal with the incompressible limit. The volumetric/deviatoric split *of the Cauchy stress tensor* $\boldsymbol{\sigma}$ (2.13) is the starting point to develop such formulations

$$\boldsymbol{\sigma} = \mathbf{s} - p\mathbf{I}, \tag{3.4}$$

where $\mathbf{s}$ is the deviatoric part of $\boldsymbol{\sigma}$, p is the pressure and $\mathbf{I}$ the second-order identity tensor. We can now use the relation between stresses to obtain a proper decomposition for the PK2 stress tensor [9]

$$S_{AB} = JF^{-1}_{Aa}F^{-1}_{Bb}\sigma_{ab} \overset{(3.4)}{=} JF^{-1}_{Aa}F^{-1}_{Bb}s_{ab} - pJC^{-1}_{AB} \coloneqq S'_{AB} - pJC^{-1}_{AB}, \tag{3.5}$$

where we have introduced the 'deviatoric' PK2 stresses $\mathbf{S}'$ (see Remark 3.2.1 below) and the right Cauchy-Green tensor $\mathbf{C} = \mathbf{F}^T\mathbf{F}$.

Thanks to the decomposition in Eq. (3.5), the conservation of linear momentum can be reformulated as

$$\rho_0 \frac{\partial^2 u_a}{\partial t^2} - \frac{\partial}{\partial X_A}\left\{F_{aB}S'_{BA}\right\} + \frac{\partial}{\partial X_A}\left\{pJF^{-1}_{Aa}\right\} = \rho_0 b_a \quad \text{in } \Omega_0 \times]0, T[\,. \tag{3.6}$$

Eq. (3.6) allows us to separate the linear momentum equation in terms of both volumetric and deviatoric parts. However, we will need to add extra equations to obtain a well-posed problem. These equations will be in charge of both providing a constitutive equation for the pressure and imposing the incompressibility constraint and to give the deviatoric constitutive behavior. These constitutive equations depends upon the type of material considered, and they are presented in the following section.

Remark 3.2.1 Tensor $\mathbf{S}'$ is often referred to as the 'true' deviatoric component of $\mathbf{S}$. The trace of $\mathbf{s}$ is zero by construction. However, it does not imply that the trace of $\mathbf{S}'$ also vanishes, and thus $\mathbf{S}'$ is not deviatoric in the algebraic sense. In fact, the 'true' deviatoric component of $\mathbf{S}$ satisfies the following equation (see for instance [9])

$$\mathbf{S}' : \mathbf{C} = 0, \tag{3.7}$$

[64]: Boscheri et al. (2022), "A 3D cell-centered ADER MOOD Finite Volume method for solving updated Lagrangian hyperelasticity on unstructured grids"

[9]: Bonet et al. (1997), *Nonlinear Continuum mechanics for finite element analysis*

which can be interpreted as the trace with respect to the metric tensor $\mathbf{C}$. The above equation enables the hydrostatic pressure p to be evaluated directly from $\mathbf{S}$ as

$$p = \frac{1}{3J}\mathbf{S} : \mathbf{C}. \tag{3.8}$$

3.3 Constitutive models

[1]: Holzapfel (2000), *Nonlinear Solid Mechanics: A Continuum Approach for Engineering*
[8]: Belytschko et al. (2001), *Nonlinear Finite Elements for Continua and Structures*
[9]: Bonet et al. (1997), *Nonlinear Continuum mechanics for finite element analysis*

In this thesis we consider isotropic hyperelastic models (See [1, 8, 9] for further details on such models). These models postulate the existence of a Helmholtz free-energy function (or strain energy function) Ψ such that

$$\mathbf{S} = 2\frac{\partial \Psi(\mathbf{C})}{\partial \mathbf{C}}. \tag{3.9}$$

We want to deal with compressible models that can reach the incompressible limit case. To characterise such models, it is convenient to adopt a decoupled representation of the strain energy function of the specific form [1, 9]

$$\Psi(\mathbf{C}) = W\left(\bar{\mathbf{C}}\right) + U(J), \tag{3.10}$$

where $\bar{\mathbf{C}} = J^{-2/3}\mathbf{C}$ is the volume-preserving part of $\mathbf{C}$. Let us remark that this decomposition allows one to split the elastic response of the material into the so-called deviatoric and volumetric parts, respectively, measured in the initial configuration. We can now derive the PK2 stress tensor by introducing equation (3.10) into equation (3.9)

$$\mathbf{S} = 2\frac{\partial \Psi}{\partial \mathbf{C}} = 2\frac{\partial W}{\partial \mathbf{C}} + 2\frac{\partial U}{\partial \mathbf{C}} = 2\frac{\partial W}{\partial \mathbf{C}} + \frac{dU}{dJ}J\mathbf{C}^{-1}. \tag{3.11}$$

By comparing this definition with Eq. (3.5) we obtain expressions for both the pressure and the deviatoric PK2 stress tensor

$$\mathbf{S}' = 2\frac{\partial W}{\partial \mathbf{C}} \quad \text{and} \quad p = -\frac{dU}{dJ}. \tag{3.12}$$

Once we are able to deal with the decoupled form of the strain energy function, we describe a number of constitutive models for both the deviatoric and the volumetric components.

3.3.1 Deviatoric models of the strain energy function

First of all, let us recall that as we are considering isotropic hyperelastic models, the strain energy density must be written in terms of the strain invariants which are defined for the volume-preserving $\bar{\mathbf{C}}$ by

$$\bar{I}_1 = \text{trace}\, \bar{\mathbf{C}}, \tag{3.13}$$

$$\bar{I}_2 = \frac{1}{2}\left[\left(\text{trace}\, \bar{\mathbf{C}}\right)^2 - \text{trace}\left(\bar{\mathbf{C}}^2\right)\right], \tag{3.14}$$

$$\bar{I}_3 = \det \bar{\mathbf{C}} = \det\left(J^{-2/3}\mathbf{C}\right) = 1. \tag{3.15}$$

From the strain invariants, it can be concluded that $W\left(\bar{\mathbf{C}}\right)$ must be written in terms of the first and second invariants. Let us present suitable functions for the deviatoric component of the strain energy function:

- Neo-Hookean model
  This model results from considering only the first principal invariant

  $$W\left(\bar{I}_1\right) = \frac{\mu}{2}\left(\bar{I}_1 - 3\right), \tag{3.16}$$

  where μ is the shear modulus. This function involves a single parameter and provides the simplest mathematical model for the nonlinear deformation behavior of rubber-like materials. However, experimental data of several isotropic elastic materials cannot be reproduced by this model and it is worthwhile considering the dependency on $\bar{I}_2$.
- Mooney-Rivlin model
  This model is derived considering the dependance on the second invariant as

  $$W\left(\bar{I}_1, \bar{I}_2\right) = \alpha_1\left(\bar{I}_1 - 3\right) + \alpha_2\left(\bar{I}_2 - 3\right), \tag{3.17}$$

  where α_1 and α_2 are material parameters that must satisfy $\mu = 2(\alpha_1 + \alpha_2) > 0$. This function is often employed in the description of the behavior of isotropic rubber-like materials. Note that when $\alpha_2 = 0$, we recover the Neo-Hookean model.
- Yeoh model
  This model makes the assumption that the variation of the strain energy function with respect to the second invariant is equal to zero and it proposes a three-term

function in terms of the first invariant

$$W\left(\bar{I}_1\right) = \alpha_1\left(\bar{I}_1 - 3\right) + \alpha_2\left(\bar{I}_1 - 3\right)^2 + \alpha_3\left(\bar{I}_1 - 3\right)^3, \quad (3.18)$$

where α_1, α_2 and α_3 are material parameters which must satisfy that $\mu = 2\alpha_1 + 4\alpha_2\left(\bar{I}_1 - 3\right) + 6\alpha_3\left(\bar{I}_1 - 3\right)^2 > 0$. This model was motivated to simulate the mechanical behavior of carbon-black filled rubber vulcanizates.

[8]: Belytschko et al. (2001), *Nonlinear Finite Elements for Continua and Structures*
[61]: Scovazzi et al. (2016), "A simple, stable, and accurate linear tetrahedral finite element for transient, nearly, and fully incompressible solid dynamics: a dynamic variational multiscale approach"

Readers are referred to [8, 61] for further details on this kind of models.

3.3.2 Volumetric models of the strain energy function

Several nonlinear materials such as rubbers, polymers or soft tissues among others are often slightly compressible and associated with minor dilatational deformations. Due to the decoupled form of the strain energy density, compressibility is accounted for by the volumetric strain energy function. Let us now show some variety of models which are widely used in nonlinear computations and which depend upon the bulk modulus κ.

[65]: Horgan et al. (2009), "On the volumetric part of strain-energy functions used in the constitutive modeling of slightly compressible solid rubbers"

- Quadratic [65]
  This model is given by the following relation

$$U(J) = \frac{\kappa}{2}(J-1)^2; \quad \frac{dU}{dJ} = \kappa(J-1). \quad (3.19)$$

  Despite of being widely used in practice, this model does not satisfy the fundamental condition of requiring an infinite amount of strain energy in order to compress the body to a single point with vanishing volume state.

[66]: Simo et al. (1985), "Variational and projection methods for the volume constraint in finite deformation elasto-plasticity"

- Simo et al [66]
  This model circumvents previous problems by adding the logarithm of J as a principal function

$$U(J) = \frac{\kappa}{4}(\log J)^2; \quad \frac{dU}{dJ} = \frac{\kappa}{2J}\log J. \quad (3.20)$$

- Simo-Taylor [66]
  This model satisfies all stability requirements

$$U(J) = \frac{\kappa}{4}\left(J^2 - 1 - 2\log J\right); \quad \frac{dU}{dJ} = \frac{\kappa}{2}\left(J - \frac{1}{J}\right). \quad (3.21)$$

- Miehe et al [67]
  In this model, $U(J)$ is given by

$$U(J) = \kappa\,(J - \log J - 1)\,;\ \frac{dU}{dJ} = \kappa\left(1 - \frac{1}{J}\right). \tag{3.22}$$

[67]: Miehe (1994), "Aspects of the formulation and finite element implementation of large strain isotropic elasticity"

- Liu et al [68]
  In this model, $U(J)$ is expressed as

$$U(J) = \kappa\,(J \log J - J + 1)\,;\ \frac{dU}{dJ} = \kappa \log J. \tag{3.23}$$

[68]: Liu et al. (1994), "3D finite element analysis of rubber-like materials at finite strains"

- Ogden [1]
  For rubber-like materials, Ogden proposed a volumetric response function in terms of the volume ratio J of the following form

$$U(J) = \kappa\frac{1}{\beta^2}\left(\beta \log J + J^{-\beta} - 1\right);\ \frac{dU}{dJ} = \frac{\kappa}{\beta J}\left(1 - \frac{1}{J^{\beta}}\right), \tag{3.24}$$

  where $\beta > 0$ is an empirical coefficient which must be fixed according to experimental data.

[1]: Holzapfel (2000), *Nonlinear Solid Mechanics: A Continuum Approach for Engineering*

Remark 3.3.1 It is important to note that all volumetric functions here presented can be written as $U(J) = \kappa G(J)$. Therefore, Eq. (3.12) can be used to obtain a proper way to impose the incompressibility of an hyperelastic material

$$p = -\frac{dU}{dJ} \quad \Leftrightarrow \quad p = -\kappa\frac{dG}{dJ} \quad \Leftrightarrow \quad \frac{p}{\kappa} + \frac{dG}{dJ} = 0. \tag{3.25}$$

This equation can be applied regardless of the compressibility of the material under study. It is interesting to observe that in the incompressible limit, when Poisson's ratio $\nu \to 0.5$ (for isotropic materials) then $\kappa \to \infty$ and Eq. (3.25) reduces automatically to

$$\frac{dG}{dJ} = 0. \tag{3.26}$$

For all the volumetric strain energy functions presented here, Eq. (3.26) imposes directly that $J = 1$ which is in fact the condition that a material must satisfy to be incompressible in finite strain theory.

Remark 3.3.2 It is interesting to show how to impose in-

compressibility if the real deviatoric/volumetric decomposition of the PK2 stress tensor is considered. The following relation holds

$$\mathbf{S} = \mathbf{S}^{\text{dev}} - p^*\mathbf{I} = \mathbf{S}' - pJ\mathbf{C}^{-1}, \tag{3.27}$$

where $p^* = \frac{1}{3}\,\text{trace}\,\mathbf{S}$. If we take the trace of the PK2 stress tensor, we can obtain an expression for the pseudo-pressure p^* as

$$p^* = -\frac{1}{3}\left(S'_{AA} + \kappa\frac{dG}{dJ}JC^{-1}_{AA}\right), \tag{3.28}$$

which allows us to write the volumetric component of the constitutive equation as

$$\frac{1}{\kappa}\frac{3p^* + S'_{AA}}{JC^{-1}_{AA}} + \frac{dG}{dJ} = 0. \tag{3.29}$$

Taking into account the widely used decomposition of the strain energy function given by Eq. (3.10), it seems more natural and effective to consider the classical decomposition, which gives us simpler equations in nearly incompressible scenarios.

3.4 Time discretization

In this work implicit time integrators are considered. When the material under study is either nearly or fully incompressible, the Courant-Friedrichs-Lewy condition, which involves the bulk modulus, becomes very restrictive. If explicit time integrators are considered, extremely small time steps are needed in order to satisfy it. Furthermore, in the fully incompressible case, as $\kappa \to \infty$, solving the problem with explicit time integration is not possible [62].

[62]: Rossi et al. (2016), "Implicit finite incompressible elastodynamics with linear finite elements: A stabilized method in rate form"

Although in principle any implicit time discretization method can be applied, it has to be taken into account that a hyperbolic system of equations of second order in time is being solved. It is important to control spurious high-frequency oscillations that might appear in the solution for both nearly and fully incompressible hyperelastic materials. As a consequence, numerical time integrators with high-frequency dissipation will be applied.

Let us now consider a partition of the time interval $[0, T]$ into N time steps of size Δt, assumed to be constant. We consider the implicit time integrators presented in Subsection 2.1.2 and its corresponding linearization.

3.5 The stabilized two-field $\mathbf{u}p$ formulation

3.5.1 Introduction

In this section we propose a novel way to solve the finite strain solid dynamics problem. Through the well-known deviatoric/volumetric decomposition of the strain energy [69] we complement the momentum equation in the context of the TLF framework with the constitutive equation of the pressure. This equation is written so as to allow imposing the incompressibility constraint on hyperelastic materials naturally, introducing any change or additional equation in the system. The complete system which results from this formulation is unstable and it presents the well-known saddle-point structure. The resulting formulation will be stabilized by means of the OSGS method, which is a stabilization technique well known for its low dissipative and highly accurate performance. The resulting method is very simple and only the addition of a scalar field as an extra primary variable is required.

[69]: Sansour (2008), "On the physical assumptions underlying the volumetric-isochoric split and the case of anisotropy"

3.5.2 Governing equations

To start this section, we introduce the two-field mixed $\mathbf{u}p$ formulation. Let $\mathfrak{D} = \{(\mathbf{X}, t) \,|\, \mathbf{X} \in \Omega_0,\ 0 < t < T\}$ be the space-time domain where the problem is defined. The problem consists of finding a displacement field, $\mathbf{u} : \mathfrak{D} \longrightarrow \mathbb{R}^d$, and a pressure field, $p : \mathfrak{D} \longrightarrow \mathbb{R}$ such that

Finite strain hyperelasticity. $\mathbf{u}p$ formulation. Governing equations in TLF

$$\rho_0 \frac{\partial^2 u_a}{\partial t^2} - \frac{\partial}{\partial X_A}\left\{F_{aB}(\mathbf{u}) S'_{BA}(\mathbf{u})\right\}$$

$$+\frac{\partial}{\partial X_A}\left\{pJ(\mathbf{u})F_{Aa}(\mathbf{u})^{-1}\right\} = \rho_0 b_a \quad \text{in } \Omega_0 \times]0,T[\,, \tag{3.30}$$

$$\frac{p}{\kappa} + \frac{dG}{dJ}(\mathbf{u}) = 0 \quad \text{in } \Omega_0 \times]0,T[\,. \tag{3.31}$$

The governing equations must be supplied with initial conditions of the form $\mathbf{u} = \mathbf{u}^0$, $\frac{\partial \mathbf{u}}{\partial t} = \mathbf{v}^0$ in Ω_0 at $t = 0$, with $\mathbf{u}^0$ and $\mathbf{v}^0$ given, and a set of boundary conditions which can be split into Dirichlet boundary conditions (3.32), where the displacement is prescribed, or Neumann boundary conditions (3.33), where the value of tractions $\mathbf{t}_N$ are prescribed:

$$\mathbf{u} = \mathbf{u}_D \quad \text{on } \Gamma_{0,D}, \tag{3.32}$$

$$\mathbf{n}_0 \cdot (\mathbf{FS}) \overset{(3.5)}{=} \mathbf{n}_0 \cdot (\mathbf{FS}') - pJ\mathbf{n}_0 \cdot \mathbf{F}^{-T} = \mathbf{t}_N \quad \text{on } \Gamma_{0,N}, \tag{3.33}$$

where $\mathbf{n}_0$ is the geometric unit outward normal vector on the boundary of the reference configuration Γ_0. To simplify the exposition, we will consider $\mathbf{u}_D = 0$ in the following.

Remark 3.5.1 Verifying that this formulation reduces to the mixed formulation in linear elasticity when infinitesimal strain theory is considered is crucial. Regarding to the momentum equation (3.30), the following simplifications are obtained

$$F_{aB}S'_{BA} \overset{(3.5)}{\approx} Js_{ab} \approx \left(1 + \frac{\partial u_c}{\partial x_c}\right) s_{ab} = s_{ab} + \cancelto{\approx 0}{(\nabla \cdot \mathbf{u})\, s_{ab}} \approx s_{ab}, \tag{3.34}$$

$$pJ\mathbf{F}^{-1} \approx p\,(1 + \nabla \cdot \mathbf{u})\,\mathbf{I} = p\mathbf{I} + \cancelto{\approx 0}{p(\nabla \cdot \mathbf{u})\mathbf{I}} \approx p\mathbf{I}, \tag{3.35}$$

and taking into account that both the reference and current configurations match, we obtain the simplified momentum equation (2.25) for linear elasticity

$$\rho \frac{\partial^2 u_a}{\partial t^2} - \frac{\partial s_{ab}}{\partial x_b} + \frac{\partial p}{\partial x_a} = \rho b_a. \tag{3.36}$$

With respect to the incompressibility equation (3.31), as it was previously mentioned, $\frac{dG}{dJ}$ is a function which imposes

$J = 1$. Therefore,

$$\frac{p}{\kappa}+\frac{dG}{dJ} \approx \frac{p}{\kappa}+J-1 \approx \frac{p}{\kappa}+(1+\nabla\cdot\mathbf{u})-1 = \frac{p}{\kappa}+\nabla\cdot\mathbf{u} = 0, \quad (3.37)$$

which is exactly the constitutive law (2.27) of the pressure when considering linear elasticity. Let us recall that in the incompressible limit $\kappa \to \infty$, and this equation will reduce automatically to

$$\nabla\cdot\mathbf{u} = 0, \quad (3.38)$$

which is the incompressibility condition for infinitesimal strain theory.

3.5.3 Variational form

Let $\mathbb{U}$ and $\mathbb{P}$ be, respectively, the proper functional spaces where displacement and pressure solutions are well-defined for each fixed time $t \in]0,T[$. We denote by $\mathbb{U}_0$ functions in $\mathbb{U}$ which vanish in the Dirichlet boundary $\Gamma_{0,D}$. We shall be interested also in the spaces $\mathbb{W} := \mathbb{U}\times\mathbb{P}$, $\mathbb{W}_0 := \mathbb{U}_0\times\mathbb{P}$.

The variational statement of the problem is derived by testing the system (3.30)-(3.31) againts arbitrary test functions, $\delta\mathbf{U} := [\delta\mathbf{u}, \delta p]^T$, $\delta\mathbf{u} \in \mathbb{U}_0$ and $\delta p \in \mathbb{P}$. The weak form of the problem reads: find $\mathbf{U} := [\mathbf{u}, p]^T :]0,T[\to \mathbb{W}_0$ such that initial conditions and the Dirichlet condition are satisfied and

Finite strain hyperelasticity. $\mathbf{u}p$ formulation. Variational form in TLF

$$\left\langle \delta u_a, \rho_0 \frac{\partial^2 u_a}{\partial t^2} \right\rangle + \mathscr{A}(\mathbf{U}, \delta\mathbf{U}) = \mathscr{F}(\delta\mathbf{U}) \quad \forall\, \delta\mathbf{U} \in \mathbb{W}_0, \quad (3.39)$$

where $\mathscr{A}(\mathbf{U}, \delta\mathbf{U})$ is a semilinear form defined on $\mathbb{W}_0 \times \mathbb{W}_0$ as

$$\mathscr{A}(\mathbf{U}, \delta\mathbf{U}) := \left\langle \frac{\partial \delta u_a}{\partial X_A}, F_{aB}S'_{BA} \right\rangle - \left\langle \frac{\partial \delta u_a}{\partial X_A}, pJF^{-1}_{Aa} \right\rangle + \left\langle \delta p, \frac{dG}{dJ} \right\rangle + \left\langle \delta p, \frac{p}{\kappa} \right\rangle. \quad (3.40)$$

In addition, $\mathscr{F}(\delta\mathbf{U})$ is a linear form defined on $\mathbb{W}_0$ as

$$\mathscr{F}(\delta\mathbf{U}) := \langle \delta u_a, \rho_0 b_a \rangle + \left\langle \delta u_a, t_{N_a} \right\rangle_{\Gamma_{0_N}}. \quad (3.41)$$

As usual, integration by parts has been used in order to decrease the continuity requirements of unknowns $\mathbf{u}$ and p.

3.5.4 Linearization

In order to solve the problem, the system needs to be linearized so that a bilinear operator which allows to compute a correction $\Delta\mathbf{U}$ of a given guess for the solution at time t^{n+1} is obtained, that we denote by $\mathbf{U}^{n+1}$. Iteration counters will be omitted to simplify the notation. After using a Newton-Raphson scheme, we obtain the following linearized form of the problem. Given $\mathbf{U}^{n+1}$ as the solution at time t^{n+1} and the previous iteration, find a correction $\Delta\mathbf{U} := [\Delta\mathbf{u}, \Delta p]^T \in \mathbb{W}_0$ such that

Finite strain hyperelasticity. $\mathbf{u}p$ formulation. Linearized variational form in TLF

$$\left\langle \delta\mathbf{u}, \rho_0 \frac{C}{\Delta t^2} \Delta\mathbf{u} \right\rangle + \mathscr{B}\left(\Delta\mathbf{U}, \delta\mathbf{U}\right) = \mathscr{F}\left(\delta\mathbf{U}\right) - \mathscr{A}\left(\mathbf{U}^{n+1}, \delta\mathbf{U}\right) - \left\langle \delta\mathbf{u}, \rho_0 \mathbf{a}^{n+1} \right\rangle \quad \forall\, \delta\mathbf{U} \in \mathbb{W}_0, \tag{3.42}$$

where $\mathscr{B}\left(\Delta\mathbf{U}, \delta\mathbf{U}\right)$ is the bilinear form obtained through the Newton-Raphson linearization and it is defined on $\mathbb{W}_0 \times \mathbb{W}_0$ as

$$\begin{aligned}
\mathscr{B}\left(\Delta\mathbf{U}, \delta\mathbf{U}\right) := & \left\langle \frac{\partial \delta u_a}{\partial X_A}, \frac{\partial \Delta u_a}{\partial X_B} S'_{BA} \right\rangle + \left\langle \frac{\partial \delta u_a}{\partial X_A}, F_{aB} \mathbb{C}'_{ABCD} F_{bC} \frac{\partial \Delta u_b}{\partial X_D} \right\rangle \\
& - \left\langle \frac{\partial \delta u_a}{\partial X_A}, J p F^{-1}_{Bb} \frac{\partial \Delta u_b}{\partial X_B} F^{-1}_{Aa} \right\rangle \\
& + \left\langle \frac{\partial \delta u_a}{\partial X_A}, J p F^{-1}_{Ab} \frac{\partial \Delta u_b}{\partial X_B} F^{-1}_{Ba} \right\rangle - \left\langle \frac{\partial \delta u_a}{\partial X_A}, J \Delta p F^{-1}_{Aa} \right\rangle \\
& + \left\langle \delta p, \mathrm{f}(J)\, F^{-1}_{Aa} \frac{\partial \Delta u_a}{\partial X_A} \right\rangle + \left\langle \delta p, \frac{\Delta p}{\kappa} \right\rangle,
\end{aligned} \tag{3.43}$$

where $\mathrm{f}(J)$ is a function coming from the linearization of $\frac{dG}{dJ}$ and depends upon the volumetric strain energy function into consideration and $\mathbb{C}'_{ABCD} = 2\frac{\partial^2 W}{\partial C_{AB} \partial C_{CD}}$ is the deviatoric constitutive tangent matrix which relates variations of the deviatoric PK2 stress tensor, $\Delta\mathbf{S}'$, with variations of the Right

Cauchy tensor, $\Delta\mathbf{C}$. Let us remark that all terms are evaluated at $\mathbf{U}^{n+1}$.

3.5.5 Symmetrization

In the way we have written the problem, it is not symmetric. To achieve symmetry[1], it is possible to modify Eq. (3.42) by

1: In the case of homogeneous boundary conditions.

Finite strain hyperelasticity. $\mathbf{u}p$ formulation. Symmetrized linearized variational form in TLF

$$\begin{aligned}\left\langle \delta\mathbf{u}, \rho_0 \frac{C}{\Delta t^2}\Delta\mathbf{u}\right\rangle + \mathscr{B}^{\text{mod}}(\Delta\mathbf{U},\delta\mathbf{U}) = \mathscr{F}(\delta\mathbf{U}) \\ - \mathscr{A}^{\text{mod}}\left(\mathbf{U}^{n+1},\delta\mathbf{U}\right) - \left\langle \delta\mathbf{u}, \rho_0\mathbf{a}^{n+1}\right\rangle \\ \forall\, \delta\mathbf{U}\in\mathbb{W}_0, \end{aligned} \tag{3.44}$$

where $\mathscr{B}^{\text{mod}}(\Delta\mathbf{U},\delta\mathbf{U})$ is the bilinear form defined on $\mathbb{W}_0\times\mathbb{W}_0$ as

$$\begin{aligned}\mathscr{B}^{\text{mod}}(\Delta\mathbf{U},\delta\mathbf{U}) := &\left\langle \frac{\partial\delta u_a}{\partial X_A}, \frac{\partial\Delta u_a}{\partial X_B}S'_{BA}\right\rangle \\ &+ \left\langle \frac{\partial\delta u_a}{\partial X_A}, F_{aB}\mathbb{C}'_{ABCD}F_{bC}\frac{\partial\Delta u_b}{\partial X_D}\right\rangle \\ &- \left\langle \frac{\partial\delta u_a}{\partial X_A}, Jp F^{-1}_{Bb}\frac{\partial\Delta u_b}{\partial X_B}F^{-1}_{Aa}\right\rangle \\ &+ \left\langle \frac{\partial\delta u_a}{\partial X_A}, Jp F^{-1}_{Ab}\frac{\partial\Delta u_b}{\partial X_B}F^{-1}_{Ba}\right\rangle - \left\langle \frac{\partial\delta u_a}{\partial X_A}, J\Delta p F^{-1}_{Aa}\right\rangle \\ &+ \left\langle \delta p, JF^{-1}_{Aa}\frac{\partial\Delta u_a}{\partial X_A}\right\rangle + \left\langle \delta p, \frac{J}{\mathrm{f}(J)}\frac{\Delta p}{\kappa}\right\rangle, \end{aligned} \tag{3.45}$$

and $\mathscr{A}^{\text{mod}}\left(\mathbf{U}^{n+1},\delta\mathbf{U}\right)$ is a semilinear form defined on $\mathbb{W}_0\times\mathbb{W}_0$ as

$$\begin{aligned}\mathscr{A}^{\text{mod}}\left(\mathbf{U}^{n+1},\delta\mathbf{U}\right) := &\left\langle \frac{\partial\delta u_a}{\partial X_A}, F_{aB}S'_{BA}\right\rangle - \left\langle \frac{\partial\delta u_a}{\partial X_A}, pJF^{-1}_{Aa}\right\rangle \\ &+ \left\langle \delta p, \frac{J}{\mathrm{f}(J)}\frac{dG}{dJ}\right\rangle + \left\langle \delta p, \frac{J}{\mathrm{f}(J)}\frac{p}{\kappa}\right\rangle, \end{aligned} \tag{3.46}$$

where we have multiplied the second equation by the linearized term $\frac{J}{\mathrm{f}(J)}$.

The symmetric form of the problem can be interesting from both the theoretical and the practical point of views. From

the theoretical point of view, the problem to be solved corresponds to the minimization of a certain mechanical energy, whereas from the practical point of view the symmetry can be exploited when solving the linear system.

For simplicity, we will employ the non-symmetric form of the problem in what follows, although the use of the symmetric version would be straightforward.

3.5.6 Galerkin spatial discretization

The standard Galerkin approximation of this abstract variational problem is now straightforward. Let $\mathscr{P}_h$ denote a FE partition of the domain Ω_0. The diameter of an element domain $K \in \mathscr{P}_h$ is denoted by h_K and the diameter on the FE partition by $h = \max\{h_K | K \in \mathscr{P}_h\}$. We can now construct conforming FE spaces $\mathbb{U}_h \subset \mathbb{U}$, $\mathbb{P}_h \subset \mathbb{P}$ and $\mathbb{W}_h = \mathbb{U}_h \times \mathbb{P}_h$ in the usual manner, as well as the corresponding subspaces $\mathbb{U}_{h,0} \subset \mathbb{U}_0$ and $\mathbb{W}_{h,0} = \mathbb{U}_{h,0} \times \mathbb{P}_h$, $\mathbb{U}_{h,0}$ being made of functions that vanish on the Dirichlet boundary. In principle, functions in $\mathbb{U}_h$ are continuous, whereas functions in $\mathbb{P}_h$ not necessarily.

The Galerkin discrete version of problem (3.42) is: for a given time t^{n+1} and a fixed iteration, find $\Delta \mathbf{U}_h := [\Delta \mathbf{u}_h, \Delta p_h]^T \in \mathbb{W}_{h,0}$ such that

Finite strain hyperelasticity. up formulation. Galerkin discrete problem in TLF

$$\begin{aligned}\left\langle \delta\mathbf{u}_h, \rho_0 \frac{C}{\Delta t^2} \Delta \mathbf{u}_h \right\rangle + \mathscr{B}(\Delta \mathbf{U}_h, \delta \mathbf{U}_h) = \mathscr{F}(\delta \mathbf{U}_h) \\ - \mathscr{A}\left(\mathbf{U}_h^{n+1}, \delta \mathbf{U}_h\right) - \left\langle \delta\mathbf{u}_h, \rho_0 \mathbf{a}_h^{n+1} \right\rangle \\ \forall\, \delta \mathbf{U}_h \in \mathbb{W}_{h,0}. \end{aligned} \tag{3.47}$$

The stability of the discrete formulation depends on compatibility restrictions on the interpolation functions chosen for the displacement, deviatoric PK2 stress and pressure fields, as stated by the appropriate inf–sup condition [22]. According to these restrictions, mixed elements with continuous equal order linear interpolation for all fields are not stable. However, the inf–sup condition can be circumvented by using a stabilization technique. This is why the so-called stabilized

[22]: Babuška (1971), "Error-Bounds for Finite Element Method"

formulations have been proposed to approximate this kind of problems. The main idea is to replace Eq. (3.42) by another discrete variational problem in which the bilinear form $\mathscr{B}$ is enhanced so that it has improved stability properties.

Remark 3.5.2 In principle, we have posed no restrictions on the choice of the FE spaces. However, the Galerkin formulation is only stable if an inf-sup condition is satisfied between the displacements and the pressure. Displacements can be controlled with the Galerkin formulation, and in the case of compressible materials also the pressure, but this control disappears as $\kappa \to \infty$. The alternative to using the Galerkin method with FE spaces satisfying the inf-sup conditions is to use a stabilized FEM, as the one we describe next.

3.5.7 Stabilization

In this subsection, the VMS method [6, 12] is introduced to stabilize the discrete formulation of the mixed problem allowing for the use of linear interpolations for all master fields. The basic idea of the VMS approach is to enlarge Galerkin's space of approximation, $\mathbb{W}_h$, adding a finer resolution space, $\tilde{\mathbb{W}}$, referred to as the SGS space. Let $\mathbb{W} = \mathbb{W}_h \oplus \tilde{\mathbb{W}}$. The elements of this space are denoted by $\tilde{\mathbf{U}} := [\tilde{\mathbf{u}}, \tilde{p}]^T$ and they are called SGSs. Likewise, let $\mathbb{W}_0 = \mathbb{W}_{h,0} \oplus \tilde{\mathbb{W}}_0$, where $\tilde{\mathbb{W}}_0$ is being made of displacement SGSs (defined at element level) that vanish at all the element boundaries.

[6]: Hughes et al. (1998), "The variational multiscale method - A paradigm for computational mechanics"
[12]: R.Codina et al. (2017), *Variational Multiscale Methods in Computational Fluid Dynamics*

Taking into account that $\mathscr{B}$ is a bilinear form, the continuous problem (3.47) is equivalent to find $\Delta\mathbf{u}_h \in \mathbb{W}_{h,0}$ and $\tilde{\mathbf{U}} \in \tilde{\mathbb{W}}_0$ such that

$$\begin{aligned}\left\langle \delta\mathbf{u}_h, \rho_0 \frac{C}{\Delta t^2}\Delta\mathbf{u}_h \right\rangle + \left\langle \delta\mathbf{u}_h, \rho_0 \tilde{\mathbf{a}}^{n+1} \right\rangle + \mathscr{B}\left(\Delta\mathbf{U}_h, \delta\mathbf{U}_h\right) \\ + \mathscr{B}\left(\tilde{\mathbf{U}}, \delta\mathbf{U}_h\right) = \mathscr{F}\left(\delta\mathbf{U}_h\right) - \mathscr{A}\left(\mathbf{U}_h^{n+1}, \delta\mathbf{U}_h\right) \\ - \left\langle \delta\mathbf{u}_h, \rho_0 \mathbf{a}_h^{n+1} \right\rangle \quad \forall\, \delta\mathbf{U}_h \in \mathbb{W}_{h,0}, \end{aligned} \tag{3.48}$$

$$\begin{aligned}\left\langle \delta\tilde{\mathbf{u}}, \rho_0 \frac{C}{\Delta t^2}\Delta\mathbf{u}_h \right\rangle + \left\langle \delta\tilde{\mathbf{u}}, \rho_0 \tilde{\mathbf{a}}^{n+1} \right\rangle + \mathscr{B}\left(\Delta\mathbf{U}_h, \delta\tilde{\mathbf{U}}\right) \\ + \mathscr{B}\left(\tilde{\mathbf{U}}, \delta\tilde{\mathbf{U}}\right) = \mathscr{F}\left(\delta\tilde{\mathbf{U}}\right) - \mathscr{A}\left(\mathbf{U}_h^{n+1}, \delta\tilde{\mathbf{U}}\right) \\ - \left\langle \delta\tilde{\mathbf{u}}, \rho_0 \mathbf{a}_h^{n+1} \right\rangle \quad \forall\, \delta\tilde{\mathbf{U}} \in \tilde{\mathbb{W}}_0, \end{aligned} \tag{3.49}$$

where Eq. (3.48) is called the FE scale equation and Eq. (3.49)

is called the SGS equation. The approximation to the acceleration obtained from the displacement SGS at time t^{n+1} has been denoted by $\tilde{\mathbf{a}}^{n+1}$.

The main idea behind any stabilized FEM derived from the VMS framework is to obtain an expression for the SGSs from the SGS equation in order to complement our FE scale equation. First of all let us make some assumptions about the SGS functions. In this thesis we consider the SGSs to be quasi-static, which means that we neglect their time derivative. We also assume the SGSs to behave as bubble functions, which means that their velocity component vanishes across inter-element boundaries. Taking this into account, we can integrate by parts within each element in Eq. (3.49) to obtain:

$$\begin{aligned}\sum_K \left\langle \delta\tilde{\mathbf{u}}, \rho_0 \frac{C}{\Delta t^2}\Delta\mathbf{u}_h \right\rangle_K + \sum_K \left\langle \delta\tilde{\mathbf{U}}, \mathrm{B}\left(\Delta\mathbf{U}_h\right)\right\rangle_K + \sum_K \left\langle \delta\tilde{\mathbf{U}}, \mathrm{B}\left(\tilde{\mathbf{U}}\right)\right\rangle_K \\ = \sum_K \left\langle \delta\tilde{\mathbf{U}}, \mathrm{F}\right\rangle_K - \sum_K \left\langle \delta\tilde{\mathbf{U}}, \mathrm{A}\left(\mathbf{U}_h^{n+1}\right)\right\rangle_K \\ - \sum_K \left\langle \delta\tilde{\mathbf{u}}, \rho_0 \mathbf{a}_h^{n+1}\right\rangle_K \;\; \forall\, \delta\tilde{\mathbf{U}} \in \tilde{\mathbb{W}}_0, \quad (3.50)\end{aligned}$$

where $\sum_K$ stands for the summation over all $K \in \mathscr{P}_h$ and $\mathrm{B} = \left[\mathrm{B}_{\mathbf{u}}, \mathrm{B}_p\right]^T$ is a linear operator coming from the integration by parts of $\mathscr{B}$ such that $\mathscr{B}\left(\Delta\mathbf{U}_h, \delta\tilde{\mathbf{U}}\right) = \sum_K \left\langle \delta\tilde{\mathbf{U}}, \mathrm{B}\left(\Delta\mathbf{U}_h\right)\right\rangle_K$ and it is defined as

$$\begin{aligned}\mathrm{B}_{\mathbf{u}}\left(\Delta\mathbf{U}_h\right)_a = &-\frac{\partial}{\partial X_A}\left\{\frac{\partial \Delta u_{h_a}}{\partial X_B} S'_{AB}\right\} - \frac{\partial}{\partial X_A}\left\{F_{aB}\mathbb{C}'_{ABCD}F_{bC}\frac{\partial \Delta u_{h_b}}{\partial X_D}\right\} \\ &+ \frac{\partial}{\partial X_A}\left\{J p F^{-1}_{Bb}\frac{\partial \Delta u_{h_b}}{\partial X_B}F^{-1}_{Aa}\right\} - \frac{\partial}{\partial X_A}\left\{J p F^{-1}_{Ab}\frac{\partial \Delta u_{h_b}}{\partial X_B}F^{-1}_{Ba}\right\} \\ &+ \frac{\partial}{\partial X_A}\left\{J \Delta p_h F^{-1}_{Aa}\right\}, \quad (3.51)\end{aligned}$$

$$\mathrm{B}_p\left(\Delta\mathbf{U}_h\right) = \mathrm{f}(J)\, F^{-1}_{Aa}\frac{\partial \Delta u_{h_a}}{\partial X_A} + \frac{\Delta p_h}{\kappa}. \quad (3.52)$$

Regarding the right-hand side, $\mathrm{F} = \left[\mathrm{F}_{\mathbf{u}}, \mathrm{F}_p\right]^T$ appears from the external forces form $\mathscr{F}$ and it is given by

$$\mathrm{F}_{u_a} = \rho_0 b_a \quad ; \quad \mathrm{F}_p = 0, \quad (3.53)$$

and finally $\mathrm{A}\left(\mathbf{U}_h^{n+1}\right) = \left[\mathrm{A}_{\mathbf{u}}\left(\mathbf{U}_h^{n+1}\right), \mathrm{A}_p\left(\mathbf{U}_h^{n+1}\right)\right]^T$ comes from

the integration by parts of $\mathscr{A}$ and it is defined as

$$\mathrm{A}_{\mathbf{u}}\left(\mathbf{U}_h^{n+1}\right)_a = -\frac{\partial}{\partial X_A}\{F_{aB}S'_{BA}\} + \frac{\partial}{\partial X_A}\{JpF^{-1}_{Aa}\}, \tag{3.54}$$

$$\mathrm{A}_p\left(\mathbf{U}_h^{n+1}\right) = \frac{dG}{dJ} + \frac{p}{\kappa}. \tag{3.55}$$

Eq. (3.50) must be satisfied for all elements $K \in \mathscr{P}_h$ and for any $\delta\tilde{\mathbf{U}} \in \tilde{\mathbb{W}}_0$, which strictly enforces that

$$\tilde{\Pi}\left(\mathrm{B}\left(\Delta\mathbf{U}_h\right) + \mathrm{B}\left(\tilde{\mathbf{U}}\right)\right) = \tilde{\Pi}\left(\mathrm{F} - \mathrm{A}\left(\mathbf{U}_h^{n+1}\right)\right), \tag{3.56}$$

where $\tilde{\Pi}$ is the $L^2(\Omega_0)$ projection onto the SGS space. This equation allows us to obtain an expression for the SGSs

$$\begin{aligned}\tilde{\Pi}\left(\mathrm{B}\left(\tilde{\mathbf{U}}\right)\right) &= \tilde{\Pi}\left(\mathrm{F} - \mathrm{A}\left(\mathbf{U}_h^{n+1}\right) - \mathrm{B}\left(\Delta\mathbf{U}_h\right)\right) \\ &\coloneqq \tilde{\Pi}\left(\mathrm{R}\left(\mathbf{U}_h^{n+1}\right) + \mathrm{R}_{\Delta\mathbf{U}}\left(\Delta\mathbf{U}_h\right)\right),\end{aligned} \tag{3.57}$$

where the residuals are defined as $\mathrm{R}_{\Delta\mathbf{u}}\left(\Delta\mathbf{u}_h\right) := -\mathrm{B}\left(\Delta\mathbf{u}_h\right)$ and $\mathrm{R}\left(\mathbf{U}_h^{n+1}\right) \coloneqq \mathrm{F} - \mathrm{A}\left(\mathbf{U}_h^{n+1}\right)$.

The idea now is to approximate operator B by a matrix $\boldsymbol{\tau}_K^{-1}$ within each element K. Since we may consider that $\boldsymbol{\tau}_K^{-1}\tilde{\mathbf{U}}$ already belongs to the SGS space, $\tilde{\Pi}\left(\boldsymbol{\tau}_K^{-1}\tilde{\mathbf{U}}\right) = \boldsymbol{\tau}_K^{-1}\tilde{\mathbf{U}}$, and from Eq. (3.57) we obtain

$$\tilde{\mathbf{U}} \approx \boldsymbol{\tau}_K\tilde{\Pi}\left(\mathrm{R}\left(\mathbf{U}_h^{n+1}\right) + \mathrm{R}_{\Delta\mathbf{u}}\left(\Delta\mathbf{u}_h\right)\right) \quad \text{in } K \in \mathscr{P}_h, \tag{3.58}$$

where $\boldsymbol{\tau}_K$ is a matrix of algorithmic parameters depending on K and the operator B. This approximation for $\tilde{\mathbf{U}}$ is intended to mimic the effect of $\mathrm{B}\left(\tilde{\mathbf{U}}\right)$ in the volume integral (3.48). Let us remark that $\boldsymbol{\tau}_K$ is taken as a diagonal matrix of stabilization parameters, $\boldsymbol{\tau}_K = \mathrm{diag}\left(\tau_{\mathbf{u}}\mathbf{I}_d, \tau_p\right)$, with $\mathbf{I}_d$ the identity on vectors of $\mathbb{R}^d$ and parameters $\tau_{\mathbf{u}}$ and τ_p are coefficients coming from the study of the behavior of the stabilization parameters based on a Fourier analysis of the problem for the SGSs. In this work, we propose to use the stabilization parameters presented in [27] for linear elastic cases:

[27]: Chiumenti et al. (2015), "A mixed three-field FE formulation for stress accurate analysis including the incompressible limit"

$$\tau_{\mathbf{u}} = c_1\frac{h_K^2}{2\mu} \quad \text{and} \quad \tau_p = 2c_2\mu, \tag{3.59}$$

where c_1 and c_2 are algorithmic parameters which must be determined.

Finally, Eq. (3.58) can be introduced into the FE scale equation to obtain the following stabilized weak form

Finite strain hyperelasticity. up formulation. Stabilized weak form In TLF

$$\begin{aligned}&\left\langle \delta\mathbf{u}_h, \rho_0 \frac{C}{\Delta t^2}\Delta\mathbf{u}_h \right\rangle + \mathscr{B}\left(\Delta\mathbf{U}_h, \delta\mathbf{U}_h\right)\\&+ \sum_K \boldsymbol{\tau}_K \left\langle \mathrm{L}\left(\delta\mathbf{U}_h\right), \tilde{\Pi}\left(\mathrm{R}\left(\mathbf{U}_h^{n+1}\right) + \mathrm{R}_{\Delta\mathbf{U}}\left(\Delta\mathbf{U}_h\right)\right)\right\rangle\\&= \mathscr{F}\left(\delta\mathbf{U}_h\right) - \mathscr{A}\left(\mathbf{U}_h^{n+1}, \delta\mathbf{U}_h\right) - \left\langle \delta\mathbf{u}_h, \rho_0 \mathbf{a}_h^{n+1}\right\rangle \;\forall\, \delta\mathbf{U}_h \in \mathbb{W}_{h,0},\end{aligned} \tag{3.60}$$

where $\mathrm{L}\left(\delta\mathbf{U}_h\right) \coloneqq \left[\mathrm{L}_{\mathbf{u}}\left(\delta\mathbf{U}_h\right), \mathrm{L}_p\left(\delta\mathbf{U}_h\right)\right]^T$ is a linear operator coming from the integration by parts of $\mathscr{B}$ such that $\mathscr{B}\left(\tilde{\mathbf{U}}, \delta\mathbf{U}_h\right) = \sum_K \left\langle \mathrm{L}\left(\delta\mathbf{U}_h\right), \tilde{\mathbf{U}}\right\rangle_K$ and it is defined as

$$\begin{aligned}\mathrm{L}_{\mathbf{u}}\left(\delta\mathbf{U}_h\right)_a = &-\frac{\partial}{\partial X_A}\left\{\frac{\partial \delta u_{h_a}}{\partial X_B} S'_{AB}\right\} + \frac{\partial}{\partial X_A}\left\{J p F^{-1}_{Aa}\frac{\partial \delta u_{h_b}}{\partial X_B}F^{-1}_{Bb}\right\}\\&- \frac{\partial}{\partial X_A}\left\{J p F^{-1}_{Ba}\frac{\partial \delta u_{h_b}}{\partial X_B}F^{-1}_{Ab}\right\} - \frac{\partial}{\partial X_A}\left\{\delta p f(J) F^{-1}_{Aa}\right\},\end{aligned} \tag{3.61}$$

$$\mathrm{L}_p\left(\delta\mathbf{U}_h\right) = \frac{\partial \delta u_{h_a}}{\partial X_A} J F^{-1}_{Aa} + \frac{\delta p}{\kappa}. \tag{3.62}$$

There exist several stabilization methods coming from the VMS technique depending on the selection of the projection onto the SGS space. In this work, three different options are considered.

Remark 3.5.3 Matrix $\boldsymbol{\tau}_K$ can be understood as an algebraic approximation to the inverse of the tangent operator introduced in the linearization of the originally nonlinear problem. Therefore, different linearization strategies could lead to different stabilized FE formulations. This idea is further elaborated in [70].

[70]: Codina et al. (2008), "Finite element approximation of the modified Boussinesq equations using a stabilized formulation"

Algebraic SubGrid Scales (ASGS)

This is the simplest choice. We take the projection onto the SGS space as the identity when applied to the residual (see [47] for further details), so that

[47]: Badia et al. (2009), "Unified stabilized finite element formulations for the Stokes and the Darcy problems"

$$\tilde{\Pi}\left(\mathrm{R}\left(\mathbf{U}_h^{n+1}\right) + \mathrm{R}_{\Delta\mathbf{U}}\left(\Delta\mathbf{U}_h\right)\right) = \mathrm{R}\left(\mathbf{U}_h^{n+1}\right) + \mathrm{R}_{\Delta\mathbf{U}}\left(\Delta\mathbf{U}_h\right), \tag{3.63}$$

and we obtain as a final stabilized formulation

$$\begin{aligned}\left\langle \delta\mathbf{u}_h, \rho_0 \frac{C}{\Delta t^2}\Delta\mathbf{u}_h \right\rangle &+ \mathscr{B}\left(\Delta\mathbf{u}_h, \delta\mathbf{U}_h\right) \\ &+ \sum_K \boldsymbol{\tau}_K \left\langle \mathrm{L}\left(\delta\mathbf{U}_h\right), \mathrm{R}_{\Delta\mathrm{U}}\left(\Delta\mathbf{U}_h\right)\right\rangle = \mathscr{F}\left(\delta\mathbf{U}_h\right) \\ &- \mathscr{A}\left(\mathbf{U}_h^{n+1}, \delta\mathbf{U}_h\right) - \left\langle \delta\mathbf{u}_h, \rho_0 \mathbf{a}_h^{n+1}\right\rangle \\ &- \sum_K \boldsymbol{\tau}_K \left\langle \mathrm{L}\left(\delta\mathbf{U}_h\right), \mathrm{R}\left(\mathbf{U}_h^{n+1}\right)\right\rangle \;\forall\, \delta\mathbf{U}_h \in \mathbb{W}_{h,0}.\end{aligned} \tag{3.64}$$

Orthogonal Subgrid Scales (OSGS)

In [25] it is argued that a natural approximation for the unknown SGS space it to take it orthogonal to the FE space:

[25]: Codina (2000), "Stabilization of incompressibility and convection through orthogonal subscales in finite element methods"

$$\begin{aligned}\tilde{\Pi}\left(\mathrm{R}\left(\mathbf{U}_h^{n+1}\right) + \mathrm{R}_{\Delta\mathrm{U}}\left(\Delta\mathbf{U}_h\right)\right) &= \mathrm{R}\left(\mathbf{U}_h^{n+1}\right) \\ &+ \mathrm{R}_{\Delta\mathrm{U}}\left(\Delta\mathbf{U}_h\right) - \Pi^h\left(\mathrm{R}\left(\mathbf{U}_h^{n+1}\right)\right),\end{aligned} \tag{3.65}$$

where Π^h is the $L^2\left(\Omega_0\right)$ projection onto the FE space. Due to the fact that this projection would increase the size of our system if we compute it in an implicit way, we have decided to approximate it with the residual of the previous iteration by neglecting the projection of the operator $\mathrm{R}_{\Delta\mathbf{u}}\left(\Delta\mathbf{u}_h\right)$. The final form of the stabilized problem with OSGS method emerges as

$$\begin{aligned}\left\langle \delta\mathbf{u}_h, \rho_0 \frac{C}{\Delta t^2}\Delta\mathbf{u}_h \right\rangle &+ \mathscr{B}\left(\Delta\mathbf{U}_h, \delta\mathbf{U}_h\right) \\ &+ \sum_K \boldsymbol{\tau}_K \left\langle \mathrm{L}\left(\delta\mathbf{U}_h\right), \mathrm{R}_{\Delta\mathrm{U}}\left(\Delta\mathbf{U}_h\right)\right\rangle = \mathscr{F}\left(\delta\mathbf{U}_h\right) \\ &- \mathscr{A}\left(\mathbf{U}_h^{n+1}, \delta\mathbf{U}_h\right) - \left\langle \delta\mathbf{u}_h, \rho_0 \mathbf{a}_h^{n+1}\right\rangle \\ &- \sum_K \boldsymbol{\tau}_K \left\langle \mathrm{L}\left(\delta\mathbf{U}_h\right), \mathrm{R}\left(\mathbf{U}_h^{n+1}\right) - \Pi^h\left(\mathrm{R}\left(\mathbf{U}_h^{n}\right)\right)\right\rangle \\ &\forall\, \delta\mathbf{U}_h \in \mathbb{W}_{h,0}.\end{aligned} \tag{3.66}$$

3.5.8 Numerical examples

In this subsection, several numerical examples are presented to assess the performance of the proposed two-field formulation. The first case we consider is a test with a manufactured solution in order to analyze the spatial discretization

errors with respect the mesh size. Later, we evaluate the performance of our FE formulation in the incompressible limit through the standard Cook's membrane test. The third case we consider is a bending problem for a beam-like structure in order to show the behavior of the method in incompressible bending dominated scenarios. Finally, a twisting column is set which presents extreme nonlinear deformations. All these examples are widely used in incompressible hyperelastic cases [58, 59, 61, 62].

For all the numerical examples included next, hyperelastic models are considered fully incompressible, and so the bulk modulus is $\kappa = \infty$. The algorithmic parameters are set to $c_1 = 1$ and $c_2 = 1$. As previously discussed, the nonlinearities in the problem are solved via a Newton-Raphson scheme. Depending on the nonlinearities, the initial guess of the iterative procedure needs to be close enough to the solution to guarantee convergence of the nonlinear iterations. In time-depending schemes, the time step is the parameter which controls the evolution of the nonlinear iterations, so we will have to tune it depending on the nonlinearities of each numerical example. A maximum of 10 iterations is set, and the numerical tolerance for the L^2 norm is 10^{-7}. In order to solve the monolithic system of linear equations, we use the Biconjugate Gradients solver, `BiCGstab` [71], which is already implemented in the `PETSc` parallel solver library [17].

Remark 3.5.4 Some works prefer to choose the time step size based on either the characteristic shear wave speed or the stabilization parameter size. We prefer not to use this approach since it mixes the definition of the stabilization parameter with the time discretization of the problem.

[58]: Bonet et al. (2015), "A first order hyperbolic framework for large strain computational solid dynamics. Part I : Total Lagrangian isothermal elasticity"
[59]: Gil et al. (2016), "A first order hyperbolic framework for large strain computational solid dynamics. Part II : Total Lagrangian compressible, nearly incompressible and truly incompressible elasticity"
[61]: Scovazzi et al. (2016), "A simple, stable, and accurate linear tetrahedral finite element for transient, nearly, and fully incompressible solid dynamics: a dynamic variational multiscale approach"
[62]: Rossi et al. (2016), "Implicit finite incompressible elastodynamics with linear finite elements: A stabilized method in rate form"
[71]: Vorst (1992), "Bi-CGSTAB: A fast and smoothly converging variant of Bi-CG for the solution of nonsymmetric linear systems"
[17]: Balay et al. (2015), *PETSc Web page*

A test with analytical solution

Let us first perform a simple test whose main objective is to numerically check the order of convergence of the proposed scheme with respect to the mesh size. For this purpose we use the so-called method of manufactured solutions.

In this procedure, an exact analytical solution is defined a priori and later substituted into the continuum equations in order to obtain associated forcing terms. These forcing terms are then introduced as perturbations in the FE computation.

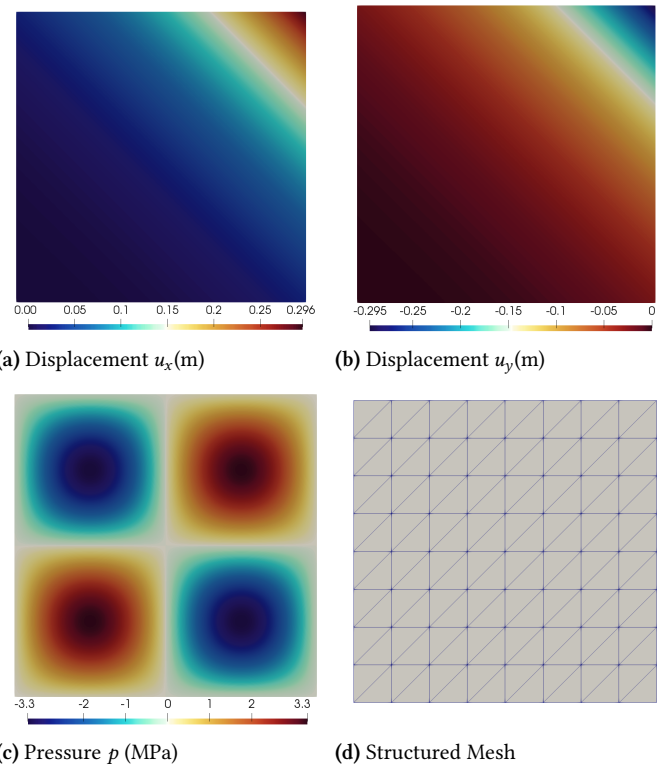

(a) Displacement u_x(m)

(b) Displacement u_y(m)

(c) Pressure p (MPa)

(d) Structured Mesh

Figure 3.1: Manufactured convergence test. Displacement and Pressure solutions (3.1a ,3.1b and 3.1c) and an example of a linear triangular structured mesh (3.1d).

The manufactured solutions are composed of smooth functions. Dirichlet boundary conditions are prescribed over the boundaries upon evaluation of the displacement analytical solution. So as to avoid mixing both spatial and time errors, we consider static solutions.

The region we consider is the unit square plate $\Omega_0 = [0,1] \times [0,1]\ \mathrm{m}^2$ under plain strain assumption and we impose the following manufactured displacement and pressure fields

$$\mathbf{u}(X,Y) = k\left[(X+Y)^2 \exp(X+Y), -(X+Y)^2 \exp(X+Y)\right], \tag{3.67}$$

$$p(X,Y) = \frac{E}{3} \sin(2\pi X) \sin(2\pi Y), \tag{3.68}$$

where $k = 0.01\ \mathrm{m}^{-1}$ and X and Y referring to the Cartesian axes in the reference configuration (cf Figs. 3.1a-3.1b-3.1c).

It is important to note that this displacement field gives an incompressible motion due to the fact that the Jacobian $J = 1$ for all X, Y. We set a Neo-Hookean material with quadratic

law for the deviatoric part of the stresses, with Young Modulus $E = 10$ MPa. We study the convergence behavior of the proposed method by running the case on seven meshes obtained by refinement of the grid shown in Fig. 3.1d. The sequence is of structured grids of $2\times n^2$ linear elements, being n the number of FEs along each side of the domain.

The normalized error has been computed in the $L^2(\Omega_0)$-norm for displacement and pressure with ASGS and OSGS stabilization techniques. Figs. 3.2a-3.2b show the convergence plot for the proposed formulation. The reader can note that the scheme proposed shows the desired rate of convergence regardless the stabilization technique.

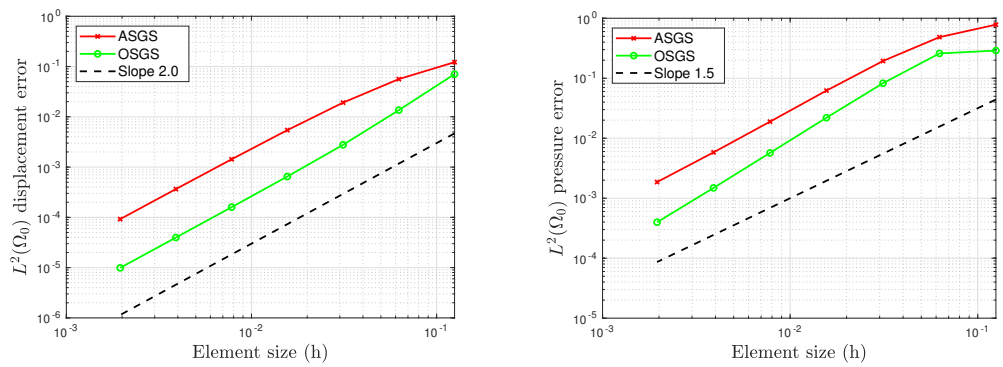

(a) Displacement error upon mesh refinement

(b) Pressure error upon mesh refinement

Figure 3.2: Manufactured convergence test. Convergence rate of the $\mathbf{u}p$ formulation upon mesh refinement.

Plane Strain Cook's Membrane

In this case, we study the dynamic Cook's membrane, a bending dominated example. This is the standard test used by many authors as a reference test to check their formulations. Although this test was firstly introduced for static cases [48, 61], an extension to transient problems can be found in [62]. We are going to keep the finite strain assumption in order to evaluate our nonlinear FE formulation, even if in this case the strains could be considered small.

The problem consists of a tapered panel, clamped on the left side and subjected to a shearing vertical load at the free right edge, $\mathbf{t}_0 = (0, 6.25)$ Pa. Stress free boundary conditions are applied on the remaining boundaries. We set a Neo-Hookean material with Young Modulus $E = 250$ Pa and density $\rho_0 =$

[48]: Chiumenti et al. (2002), "A stabilized formulation for incompressible elasticity using linear displacement and pressure interpolations"

[61]: Scovazzi et al. (2016), "A simple, stable, and accurate linear tetrahedral finite element for transient, nearly, and fully incompressible solid dynamics: a dynamic variational multiscale approach"

[62]: Rossi et al. (2016), "Implicit finite incompressible elastodynamics with linear finite elements: A stabilized method in rate form"

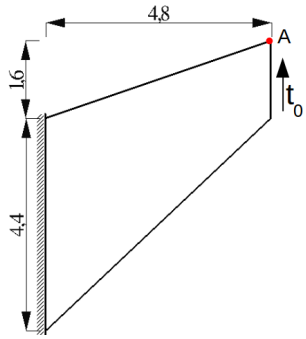

(a) Geometry (m)

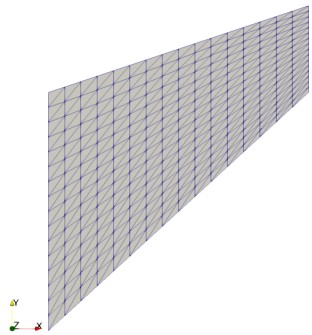

(b) Linear triangular mesh with N FEs along each side

Figure 3.3: Cook's membrane problem. Geometry (3.3a) and an example of a linear triangular mesh (3.3b).

$1\,\mathrm{kg/m^3}$. To define the deviatoric part of the material, we consider a quadratic law. The initial conditions are $\mathbf{u}^0 = \mathbf{0}$ and $\mathbf{v}^0 = \mathbf{0}$. The geometry of this problem is shown in Fig. 3.3a.

In order to test the evolution of the solution while refining our mesh, the problem has been discretized into linear triangular structured meshes with N FEs along each side (see Fig. 3.3b).

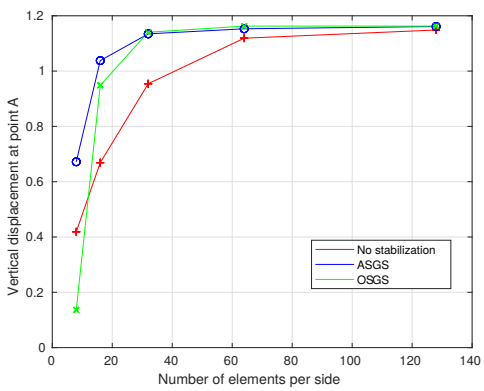

Figure 3.4: Cook's membrane problem. Convergence of the vertical displacement (m) at point A at $t = 7$ s.

In Fig. 3.4, we present a comparison of the vertical displacement at point A at $t = 7$ s using the mixed $\mathbf{u}p$ formulation without stabilization and stabilized with both the ASGS and the OSGS methods. For all cases, we fix the time step as $\Delta t = 0.05$ s and the BDF2 time integration scheme is applied.

Remark 3.5.5 In this case, we have selected BDF2 in order to ensure that the numerical dissipation introduced by the time integration scheme is enough to eliminate the non-physical high-frequency modes appearing in the numerical solution (see Fig. 3.6).

Fig. 3.4 illustrates the convergence of our mixed proposed formulation depending upon the chosen stabilization. Both OSGS and ASGS deal appropriately with the incompressibility constraint whereas when no stabilization is considered we observe a poor convergence rate. Despite the fact that the momentum equation does not need to be stabilized, the error introduced for the constitutive law of the pressure causes the poor accuracy of the displacement. As expected, the proposed stabilized mixed formulation does not exhibit volume locking for neither the ASGS nor the OSGS methods.

It is interesting to observe that the ASGS stabilization method behaves better than the OSGS one only when using really coarse meshes. This behavior is justified due to the fact that in the OSGS technique, we are approximating the projection onto the FE space evaluated in the previous time step. This approximation may be introducing an error that clearly depends on the mesh as well as the time step size.

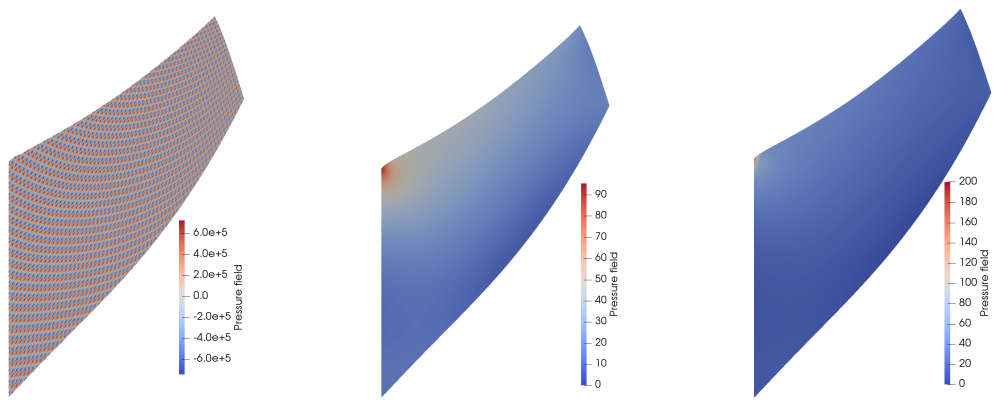

(a) No Stabilization **(b)** ASGS **(c)** OSGS

Figure 3.5: Cook's membrane problem. Pressure field (Pa) for a $64 \times 64 \times 2$ triangular linear mesh.

For the sake of completeness, Fig. 3.5 shows the pressure field for the three cases and the deformed solution at $t = 7$ s. As mentioned before, when no stabilization is applied, pressure gradients appear over the inner element boundaries due to the jumps of pressure values in the elements as it can be

observed in Fig. 3.5a. On the other hand, we can see that both the ASGS and the OSGS methods yield the pressure field properly, as it is shown in Figs. 3.5b-3.5c. Let us remark that the OSGS method is able to concentrate more accurately the maximum values of the pressure.

In order to study the relation between the different proposed formulations with the several time integration schemes we have introduced in this work, we show in Fig. 3.6 the evolution up to $T = 7$ s of both the vertical displacement and the pressure at the right top corner of the membrane for $\Delta t = 0.05$ s and for a fixed $128 \times 128 \times 2$ linear triangular mesh.

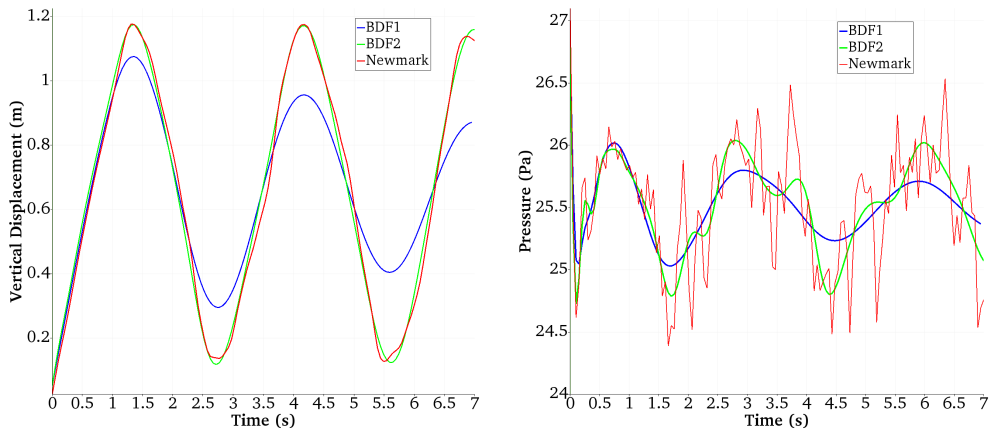

(a) Vertical Displacement (m)

(b) Pressure (Pa)

Figure 3.6: Cook's membrane problem. Comparison between several time integrators with $\Delta t = 0.05$ s and a linear triangular mesh with 128 elements per side.

The comparison of the BDF1, the BDF2 and the Newmark time integrators of Fig. 3.6 clearly demonstrates the following facts. On the one hand, BDF1 is only first-order accurate and it is highly dissipative, affecting the accuracy of the method by eliminating physical modes of the pressure. On the other hand, in spite of the fact that Newmark scheme is second-order for $\beta = \frac{1}{4}$ and $\gamma = \frac{1}{2}$, it does not introduce any numerical dissipation, which would help preventing high frequency oscillations of nonphysical modes. With regards to BDF2, it is seen that it is able to dissipate the nonphysical modes while keeping the accuracy of the method and it can be safely used.

Remark 3.5.6 In order to overcome the problem described with the Newmark scheme, several time integrators have been introduced over last decades. Among them, the well-known Generalized-α method [72], to control the numerical dissipation that needs to be added to the system.

[72]: Chung et al. (1993), "A Time Integration Algorithm for Structural Dynamics with improved numerical dissipation: The Generalized-α Method"

A 3D bending beam problem

As a third test in finite elasticity, we consider a three dimensional beam of square section clamped on its bottom face very similar to the one presented in [61]. The initial geometry is a parallelepiped of dimension $1 \times 1 \times 6$ m as shown in Fig. 3.7a. We consider stress free conditions and zero displacement initial conditions are applied. In order to initialize the bending of the column, we impose an initial velocity condition (see Fig. 3.7b) and an initial displacement field such that

$$\mathbf{v}^0(X,Y,Z) = \left(\frac{5}{3}Z, 0, 0\right)^T \text{ m/s}; \mathbf{u}^0(X,Y,Z) = \mathbf{0} \text{ m}. \quad (3.69)$$

[61]: Scovazzi et al. (2016), "A simple, stable, and accurate linear tetrahedral finite element for transient, nearly, and fully incompressible solid dynamics: a dynamic variational multiscale approach"

The material is considered Mooney-Rivlin with initial density $\rho_0 = 1.1 \times 10^3$ kg/m^3, $\alpha_1 = 2.69$ MPa and $\alpha_2 = 0.142$ MPa, identical to the one proposed in [62]. Due to the fact that the beam is clamped on its bottom face, we impose homogeneous boundary conditions for the displacement field. The rest of the boundary is prescribed with zero traction.

[62]: Rossi et al. (2016), "Implicit finite incompressible elastodynamics with linear finite elements: A stabilized method in rate form"

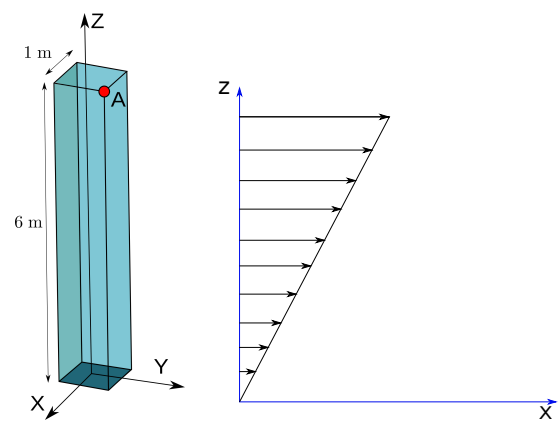

(a) Geometry **(b)** Initial velocity, $\mathbf{v}^0(X,Y,Z,t=0)$

Figure 3.7: Bending beam. Geometry (3.7a) and initial velocity field (3.7b).

The interest of this example is to show the performance of

Mesh	Number of elements
1	$6 \times 6 \times 36 \times 6$
2	$8 \times 8 \times 48 \times 6$
3	$12 \times 12 \times 72 \times 6$

Table 3.1: Bending beam. Different meshes and number of elements.

the proposed formulation in bending dominated scenarios. As explained before, this method is independent of the kind of hyperelastic material model. Therefore, we have selected a Mooney-Rivlin model to simulate this bending dominated problem. The main goal of this example is to show that our stabilized mixed formulation works properly in bending dominated scenarios and in 3D cases for truly incompressible materials. For this reason, we have selected 3 different linear tetrahedral meshes, which are built from original meshes made of hexahedra further subdivided into 6 tetrahedra, specified in Table 3.1.

In order to avoid nonphysical modes appearing from the time integration scheme, we have selected the high-dissipative BDF2 time integrator with time step $\Delta t = 0.01$ s.

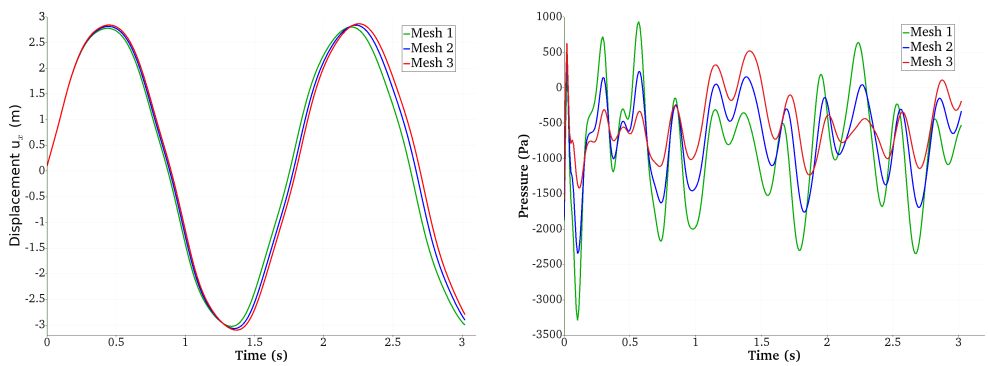

(a) Displacement u_x (m)

(b) Pressure (Pa)

Figure 3.8: Bending beam. Comparison between several meshes with $\Delta t = 0.01$ s and ASGS as stabilization technique.

Fig. 3.8 displays a comparison among several refinement levels up to $T = 3$ s at the red point of Fig. 3.7a. Fig. 3.8 clearly shows the effectiveness of the proposed scheme to produce locking-free behavior without spurious oscillations in the pressure field. It is interesting to see that even for very coarse meshes like Mesh 1, where the spatial error is propagated along time, the method is able to capture well-solved fields without nonphysical modes in the pressure field.

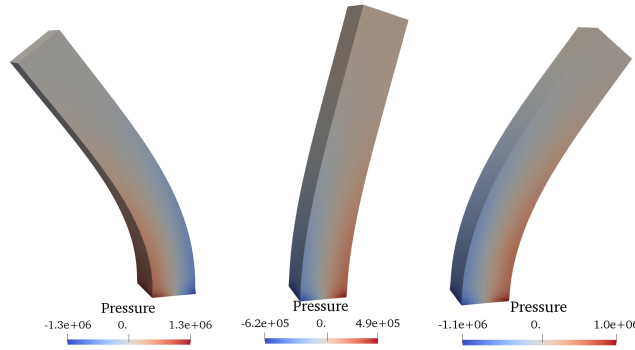

(a) 0.5 s **(b)** 1 s **(c)** 1.5 s

Figure 3.9: Bending beam. Deformation and pressure field (Pa) for $\Delta t = 0.01$ s with ASGS stabilization technique from $t = 0.5$ s to $t = 1.5$ s.

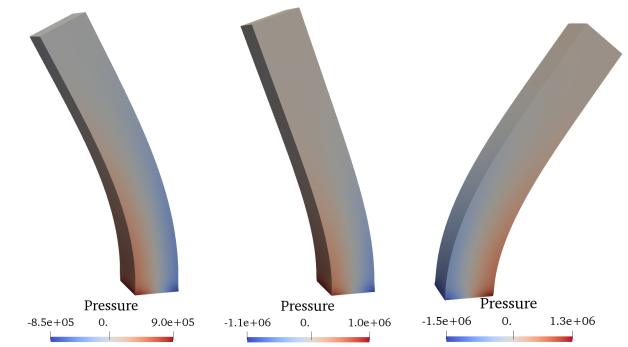

(a) 2 s **(b)** 2.5 s **(c)** 3 s

Figure 3.10: Bending beam. Deformation and pressure field for $\Delta t = 0.01$ s with ASGS stabilization technique from $t = 2$ s to $t = 3$ s.

To end up this problem, Figs. 3.9-3.10 show the evolution of the deformation and the pressure field along time up to $T = 3$ s for Mesh 3. It can be observed that the deformation is accurately reproduced even for complex hyperelastic material models like the Mooney-Rivlin model in fully incompressible scenarios. Regarding the pressure field, we can state that it is correctly captured by our mixed formulation, placing the maximum values of the pressure at the bottom of the beam, where the structure is clamped and where they are expected to appear.

Twisting column

As a final example, we present the twisting column test. This test is widely used to assess the robustness of any formulation in extreme nonlinear deformations [58, 59, 61, 62].

The geometry is identical to the bending beam described in the previous example. The beam is also clamped on its bot-

[58]: Bonet et al. (2015), "A first order hyperbolic framework for large strain computational solid dynamics. Part I : Total Lagrangian isothermal elasticity"
[59]: Gil et al. (2016), "A first order hyperbolic framework for large strain computational solid dynamics. Part II : Total Lagrangian compressible, nearly incompressible and truly incompressible elasticity"
[61]: Scovazzi et al. (2016), "A simple, stable, and accurate linear tetrahedral finite element for transient, nearly, and fully incompressible solid dynamics: a dynamic variational multiscale approach"
[62]: Rossi et al. (2016), "Implicit finite incompressible elastodynamics with linear finite elements: A stabilized method in rate form"

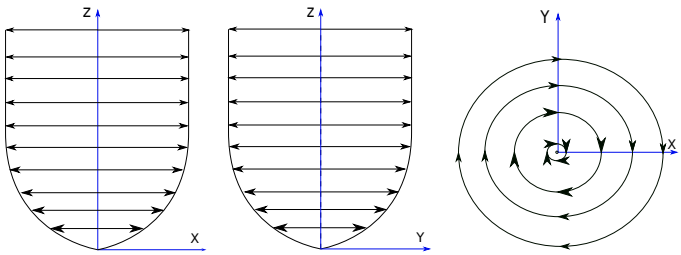

Figure 3.11: Twisting column. Initial velocity field.

tom face. In order to make the column twist, we apply an initial sinusoidal velocity field:

$$\mathbf{v}^0(X,Y,Z) = \omega \sin\left(\frac{\pi Z}{12}\right)(Y,-X,0)^T \quad \text{m/s}, \tag{3.70}$$

where $\omega = 100$ rad/s. The material is considered Neo-Hookean with initial density $\rho_0 = 1.1 \times 10^3$ kg/m^3, Young modulus $E = 1.7 \times 10^7$ Pa and Poisson ratio $\nu = 0.5$. To define the deviatoric part of the material, we consider a Simo-Taylor law. The geometry of the column is shown in Fig. 3.7a and the applied initial velocity in Fig. 3.11. Several levels of refinement have been considered to perform the computations. To construct the meshes, we start with hexahedral elements which are further subdivided into 6 tetrahedral ones each. So we consider 3 different meshes. Mesh 1, with $8 \times 8 \times 48 \times 6$ linear FEs, Mesh 2 with $12 \times 12 \times 72 \times 6$ FEs and we end up with Mesh 3 with $16 \times 16 \times 96 \times 6$ FEs. We consider the BDF2 time integrator.

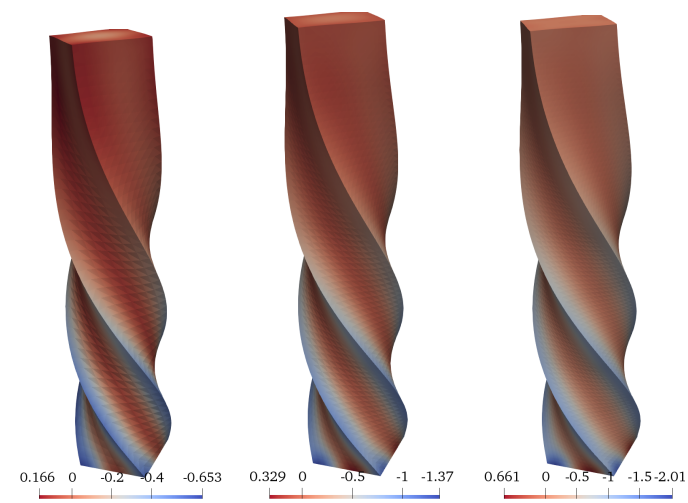

(a) Mesh 1 **(b)** Mesh 2 **(c)** Mesh 3

Figure 3.12: Twisting column. Deformation and pressure field (MPa) for $\Delta t = 0.01$ s at $t = 0.1$ s with the OSGS stabilization technique.

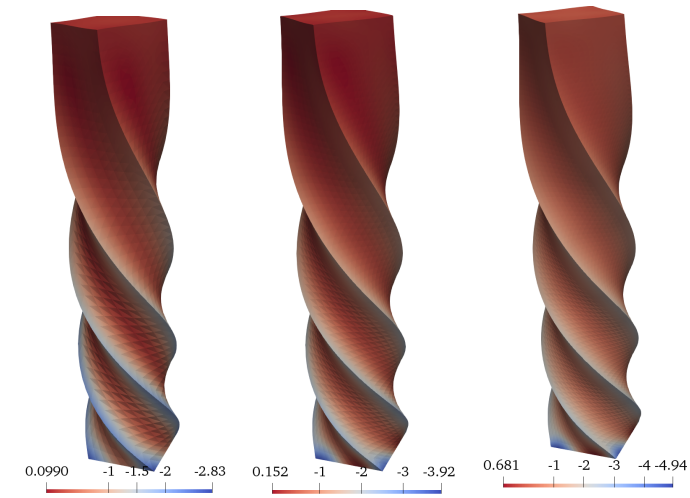

(a) Mesh 1 **(b)** Mesh 2 **(c)** Mesh 3

Figure 3.13: Twisting column. Deformation and pressure field (MPa) for $\Delta t = 0.001$ s at $t = 0.1$ s with the OSGS stabilization technique.

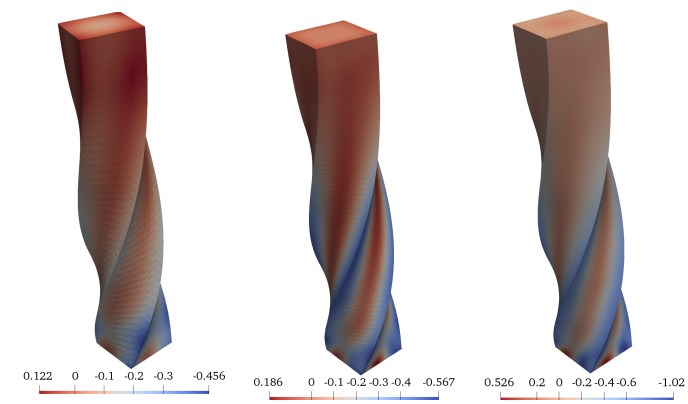

(a) Mesh 1 **(b)** Mesh 2 **(c)** Mesh 3

Figure 3.14: Twisting column. Deformation and pressure field (MPa) for $\Delta t = 0.01$ s at $t = 0.3$ s with the OSGS stabilization technique.

The deformation and the pressure field are shown for $t = 0.1$ s and $t = 0.3$ s in Figs. 3.12-3.13 and Figs. 3.14-3.15 respectively. We have included the results for $\Delta t = 0.01$ s and $\Delta t = 0.001$ s in order to observe the roll of the time step.

With regard to the time step, we can observe that Figs. 3.13-3.15 are able to locate the maximum and minimum values of the pressure in the more stressed areas, in this case, near to the clamped boundary. It is interesting to see that the mixed formulation proposed here produces a smooth and accurate pressure field for the fully incompressible case. Let us also remark that for coarse meshes, we observe a spatial error which is propagated along time causing the difference in the deformation that we can appreciate in Figs. 3.14-3.15.

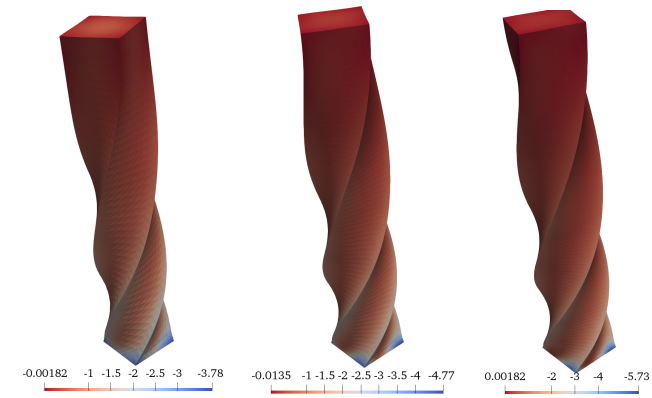

(a) Mesh 1 **(b)** Mesh 2 **(c)** Mesh 3

Figure 3.15: Twisting column. Deformation and pressure field (MPa) for $\Delta t = 0.001$ s at $t = 0.3$ s with the OSGS stabilization technique.

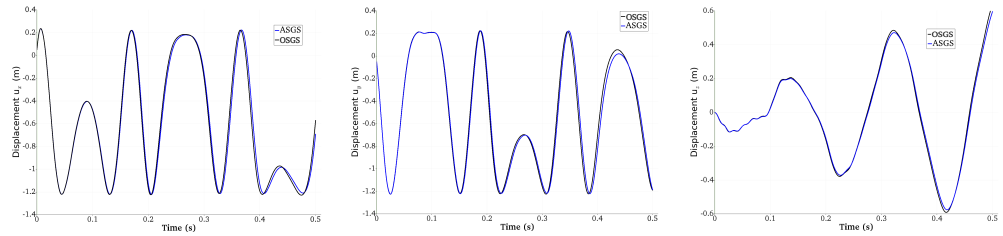

(a) Displacement u_x **(b)** Displacement u_y **(c)** Displacement u_z

Figure 3.16: Twisting column. Displacement field at point A.

Clearly, our stabilized two-field mixed implementation produces locking-free solutions and it does not exhibit nonphysical pressure fluctuations thanks to both the application of BDF2, a high-frequency dissipation time integrator, and the application of VMS stabilization technique, which include sufficient numerical stabilization to the problem.

In Fig. 3.16, we consider a comparison of the ASGS and OSGS stabilization techniques of the mixed formulation for Mesh 3 and $\Delta t = 0.001$ s. Both stabilizations seem to closely track each other, also considering the fact that the OSGS technique is more dependent of the time step size due to the approximation in the computation of the projection onto the FE space, which is computed in the previous time step to save computational effort. According to the solutions presented in [61], the displacement field is correctly captured with both stabilization methods.

Fig. 3.17 shows the evolution of the deformation of the twisting column along time up to $T = 0.5$ s for Mesh 3 and with $\Delta t = 0.001$ s and using the ASGS stabilization method. It is

[61]: Scovazzi et al. (2016), "A simple, stable, and accurate linear tetrahedral finite element for transient, nearly, and fully incompressible solid dynamics: a dynamic variational multiscale approach"

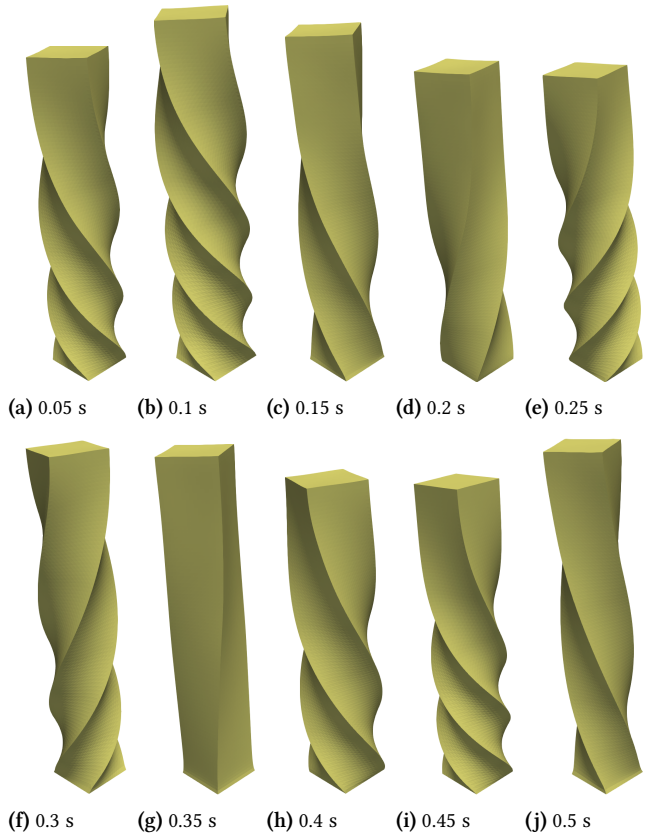

Figure 3.17: Twisting column. Deformation along time.

easy to observe the well-reproduced evolution of the deformation of the column. Taking into account that this example is considered very challenging due to the extreme nonlinear deformations and huge number of pressure modes that appear, we remark the robustness and applicability of our stabilized mixed formulation.

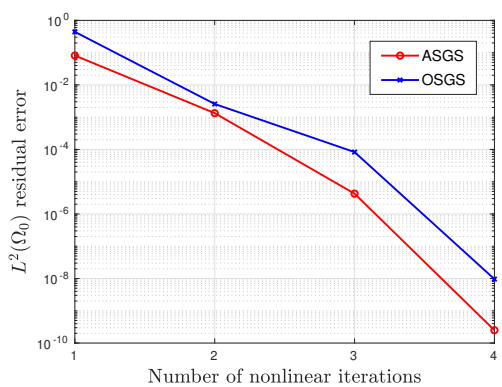

Figure 3.18: Twisting column. Nonlinear iteration convergence at $t = 0.5$ s.

To end up this problem, Fig. 3.18 displays the nonlinear iteration convergence at time $t = 0.5$ s for Mesh 3 and with $\Delta t = 0.001$ s. The method shows almost quadratic convergence no matter the stabilization technique we are applying. It is important to remark some stabilization terms have been linearized only up to first order, as the FE projections in the OSGS method.

3.6 The stabilized three-field $\mathbf{u}p\mathbf{S}^{'}$ formulation

3.6.1 Introduction

Several industrial manufacturing processes such as metal forming, forging, or friction stir welding among many others require, at the same time, stress accuracy and performance in the incompressible limit [73, 74]. It becomes crutial in these cases to use a FE technology capable of dealing with complex phenomena such as strain localization [11], the formation of shear bands, the prediction of crack propagation [75] or the isochoric behavior of the inelastic strains [28].

In biomechanics, several materials can be modeled as nearly or fully incompressible [40]. Stress accuracy enhancement becomes very useful in many fields, such as cardiac electromechanics [76, 77] in which stress tensor acts as the coupling field with the equations describing electrical propagation in stress-assisted diffusion models [78].

In Section 3.5, a stabilized mixed displacement/pressure is presented for both nearly and fully incompressible hyperelastic material models. In the present section, we make a step forward introducing a mixed three-field formulation based on displacement/pressure/deviatoric stress[2] elements interpolated with equal-order elements for all master fields. The only requirement is the introduction of the constitutive law for deviatoric stresses in the system of equations to be solved. This technology is expected to enhance stress accuracy as well as to increase the ability to capture stress concentrations with the guarantee of stress convergence upon mesh refinement.

[73]: Moreira et al. (2022), "Accurate thermal-induced structural failure analysis under incompressible conditions"

[74]: Dialami et al. (2020), "Defect Formation and Material Flow in Friction Stir Welding"

[11]: Cervera et al. (2010), "Mixed Stabilized Finite Element Methods in Nonlinear Solid Mechanics. Part II: Strain Localization"

[75]: Cervera et al. (2022), "A Comparative Review of XFEM, Mixed FEM and Phase-Field Models for Quasi-brittle Cracking"

[28]: Chiumenti et al. (2021), "Stress, strain and dissipation accurate 3-field formulation for inelastic isochoric deformation"

[40]: Holzapfel (2001), "Biomechanics of soft tissue"

[76]: Farrell et al. (2021), "Mixed Kirchhoff stress-displacement-pressure formulations for incompressible hyperelasticity"

[77]: Ruiz-Baier et al. (2020), "Thermo-electric effects in an anisotropic active-strain electromechanical model"

[78]: Propp et al. (2020), "An orthotropic electro-viscoelastic model for the heart with stress-assisted diffusion"

2: As it will be shown, the stress used as unknown is deviatoric in the deformed configuration only.

3.6.2 Governing equations

In this section, a novel three-field formulation is introduced. The objective is the definition of a general framework, which includes the mixed two-field formulation presented in Section 3.5 to be able to tackle the incompressible limit and introduces $\mathbf{S}'$ as primary unknown to obtain a higher accuracy in the computation of stresses in finite strain problems. To this end, let us introduce the three-field mixed $\mathbf{u}p\mathbf{S}'$ formulation. Let $\mathfrak{D} = \{(\mathbf{X}, t) \,|\, \mathbf{X} \in \Omega_0,\ 0 < t < T\}$ be the space-time domain where the problem is defined. The problem consists of finding a displacement field, $\mathbf{u} : \mathfrak{D} \longrightarrow \mathbb{R}^d$, together with a deviatoric component of the PK2 stress tensor, $\mathbf{S}' : \mathfrak{D} \longrightarrow \mathbb{R}^d \otimes \mathbb{R}^d$ and a pressure field, $p : \mathfrak{D} \longrightarrow \mathbb{R}$ such that

Finite strain hyperelasticity. $\mathbf{u}pS'$ formulation. Governing equations in TLF

$$\rho_0 \frac{\partial^2 u_a}{\partial t^2} - \frac{\partial}{\partial X_A}\left\{F_{aB}(\mathbf{u}) S'_{BA}\right\} + \frac{\partial}{\partial X_A}\left\{pJ(\mathbf{u}) F_{Aa}(\mathbf{u})^{-1}\right\} = \rho_0 b_a \quad \text{in } \Omega_0 \times]0,T[\,, \tag{3.71}$$

$$\frac{p}{\kappa} + \frac{dG}{dJ}(\mathbf{u}) = 0 \quad \text{in } \Omega_0 \times]0,T[\,, \tag{3.72}$$

$$S'_{AB} - 2\frac{\partial W}{\partial C_{AB}}(\mathbf{u}) = 0 \quad \text{in } \Omega_0 \times]0,T[\,. \tag{3.73}$$

The governing equations must be supplied with initial conditions of the form $\mathbf{u} = \mathbf{u}^0$, $\frac{\partial \mathbf{u}}{\partial t} = \mathbf{v}^0$ in Ω_0 at $t = 0$, with $\mathbf{u}^0$ and $\mathbf{v}^0$ given, and a set of boundary conditions which can be split into Dirichlet boundary conditions (3.74), where the displacement is prescribed, or Neumann boundary conditions (3.75), where the value of tractions $\mathbf{t}_N$ are prescribed, i.e.:

$$\mathbf{u} = \mathbf{u}_D \text{ on } \Gamma_{0,D}, \tag{3.74}$$

$$\mathbf{n}_0 \cdot (\mathbf{FS}) \overset{(3.5)}{=} \mathbf{n}_0 \cdot (\mathbf{FS}') - pJ\mathbf{n}_0\mathbf{F}^{-T} = \mathbf{t}_N \text{ on } \Gamma_{0,N}, \tag{3.75}$$

where $\mathbf{n}_0$ is the geometric unit outward normal vector on the boundary of the reference configuration Γ_0. To simplify the exposition, we will consider $\mathbf{u}_D = 0$ in the following.

Remark 3.6.1 Verifying that this formulation reduces to the mixed three-field formulation in linear elasticity when infinitesimal strains theory is considered is crucial. As it is shown in Remark 3.5.1 both the momentum equation (3.71) and the incompressibility equation (3.72) reduce to

$$\rho \frac{\partial^2 u_a}{\partial t^2} - \frac{\partial s_{ab}}{\partial x_b} + \frac{\partial p}{\partial x_a} = \rho b_a, \tag{3.76}$$

and

$$\frac{p}{\kappa} + \nabla \cdot \mathbf{u} = 0, \tag{3.77}$$

respectively. With respect to the deviatoric constitutive law (3.73) we can observe that

$$\begin{aligned} \mathbf{S}' = J\mathbf{F}^{-1}\mathbf{s}\mathbf{F}^{-T} &\approx (1 + \nabla \cdot \mathbf{u})\left(\mathbf{I} + \nabla \mathbf{u}\right)^{-1} \mathbf{s} \left(\mathbf{I} + \nabla \mathbf{u}\right)^{-T} \\ &= \mathbf{s} + \mathcal{O}\left(\|\nabla \mathbf{u}\|^2\right) \approx \mathbf{s} \end{aligned} \tag{3.78}$$

and all the deviatoric models of the strain energy (which are presented in Section 3.3) must satisfy that, in the infinitesimal strain assumption, they recover the deviatoric constitutive law of linear elasticity when second order terms are neglected. Therefore

$$\mathbf{s} = 2\frac{\partial W}{\partial \mathbf{C}} \approx \mathbb{C}^{\text{dev}} : \boldsymbol{\varepsilon}, \tag{3.79}$$

where $\boldsymbol{\varepsilon}$ is the infinitesimal strain field and $\mathbb{C}^{\text{dev}}$ is the 4th order deviatoric constitutive tensor for isotropic linear elastic materials and it is defined as

$$\mathbb{C}^{\text{dev}} = 2\mu\left\{\mathbb{I} - \frac{1}{3}\mathbf{I} \otimes \mathbf{I}\right\}. \tag{3.80}$$

With Eqs. (3.76-3.77-3.79) we recover automatically the three-field formulation for linear elasticity presented in [27].

[27]: Chiumenti et al. (2015), "A mixed three-field FE formulation for stress accurate analysis including the incompressible limit"

3.6.3 Variational form

Let $\mathbb{U}$, $\mathbb{P}$ and $\mathbb{S}$ be, respectively, the proper functional spaces where displacement, pressure and deviatoric PK2 stress solutions are well-defined for each fixed time $t \in]0, T[$. We denote by $\mathbb{U}_0$ functions in $\mathbb{U}$ which vanish in the Dirichlet boundary $\Gamma_{0,D}$. We shall be interested also in the spaces $\mathbb{W} :=$

$\mathbb{U} \times \mathbb{P} \times \mathbb{S}$ and $\mathbb{W}_0 := \mathbb{U}_0 \times \mathbb{P} \times \mathbb{S}$.

The variational statement of the problem is derived by testing system (3.71)-(3.73) against arbitrary test functions, $\delta\mathbf{U} := [\delta\mathbf{u}, \delta p, \delta\mathbf{S}']^T$, $\delta\mathbf{u} \in \mathbb{U}_0$, $\delta p \in \mathbb{Q}$ and $\delta\mathbf{S}' \in \mathbb{S}$. The weak form of the problem reads: find $\mathbf{U} := [\mathbf{u}, p, \mathbf{S}']^T :]0, T[\to \mathbb{W}_0$ such that initial conditions are satisfied and

Finite strain hyperelasticity. upS′ formulation. Variational form in TLF

$$\left\langle \delta u_a, \rho_0 \frac{\partial^2 u_a}{\partial t^2} \right\rangle + \mathscr{A}(\mathbf{U}, \delta\mathbf{U}) = \mathscr{F}(\delta\mathbf{U}) \quad \forall\, \delta\mathbf{U} \in \mathbb{W}_0, \tag{3.81}$$

where $\mathscr{A}(\mathbf{U}, \delta\mathbf{U})$ is a semilinear form defined on $\mathbb{W}_0 \times \mathbb{W}_0$ as

$$\begin{aligned}\mathscr{A}(\mathbf{U}, \delta\mathbf{U}) := &\left\langle \frac{\partial \delta u_a}{\partial X_A}, F_{aB} S'_{BA} \right\rangle - \left\langle \frac{\partial \delta u_a}{\partial X_A}, p J F^{-1}_{Aa} \right\rangle + \left\langle \delta p, \frac{dG}{dJ} \right\rangle \\ &+ \left\langle \delta p, \frac{p}{\kappa} \right\rangle + \langle \delta S'_{AB}, S'_{AB} \rangle - \left\langle \delta S'_{AB}, 2 \frac{\partial W}{\partial C_{AB}} \right\rangle. \end{aligned} \tag{3.82}$$

In addition, $\mathscr{F}(\delta\mathbf{U})$ is a linear form defined on $\mathbb{W}_0$ as

$$\mathscr{F}(\delta\mathbf{U}) := \langle \delta u_a, \rho_0 b_a \rangle + \left\langle \delta u_a, t_{N_a} \right\rangle_{\Gamma_{0,N}}. \tag{3.83}$$

Integration by parts has been used in order to decrease the continuity requirements of unknowns p and $\mathbf{S}'$.

3.6.4 Linearization

In order to solve the problem, the system needs to be linearized so that a bilinear operator which allows to compute a correction $\Delta\mathbf{U}$ of a given guess for the solution at time t^{n+1} is obtained, that we denote by $\mathbf{U}^{n+1}$. Iteration counters will be omitted to simplify the notation. After using a Newton-Raphson scheme, we obtain the following linearized form of the problem. Given $\mathbf{U}^{n+1}$ as the solution at time t^{n+1} and the previous iteration, find a correction $\Delta\mathbf{U} := [\Delta\mathbf{u}, \Delta p, \Delta\mathbf{S}']^T \in \mathbb{W}_0$ such that

Finite strain hyperelasticity. $\mathbf{u}p\mathbf{S}'$ formulation. Linearized variational form in TLF

$$\left\langle \delta\mathbf{u}, \rho_0 \frac{C}{\Delta t^2}\Delta\mathbf{u}\right\rangle + \mathscr{B}\left(\Delta\mathbf{U}, \delta\mathbf{U}\right) = \mathscr{F}\left(\delta\mathbf{U}\right) - \mathscr{A}\left(\mathbf{U}^{n+1}, \delta\mathbf{U}\right) - \left\langle \delta\mathbf{u}, \rho_0 \mathbf{a}^{n+1}\right\rangle \quad \forall\, \delta\mathbf{U} \in \mathbb{W}_0, \tag{3.84}$$

where $\mathscr{B}\left(\Delta\mathbf{U}, \delta\mathbf{U}\right)$ is the bilinear form obtained through the Newton-Raphson linearization and it is defined on $\mathbb{W}_0 \times \mathbb{W}_0$ as

$$\begin{aligned}\mathscr{B}\left(\Delta\mathbf{U}, \delta\mathbf{U}\right) = &\left\langle \frac{\partial \delta u_a}{\partial X_A}, \frac{\partial \Delta u_a}{\partial X_B} S'_{BA}\right\rangle + \left\langle \frac{\partial \delta u_a}{\partial X_A}, F_{aB}\Delta S'_{BA}\right\rangle \\ &- \left\langle \frac{\partial \delta u_a}{\partial X_A}, Jp F^{-1}_{Bb}\frac{\partial \Delta u_b}{\partial X_B} F^{-1}_{Aa}\right\rangle \\ &+ \left\langle \frac{\partial \delta u_a}{\partial X_A}, Jp F^{-1}_{Ab}\frac{\partial \Delta u_b}{\partial X_B} F^{-1}_{Ba}\right\rangle - \left\langle \frac{\partial \delta u_a}{\partial X_A}, J\Delta p F^{-1}_{Aa}\right\rangle \\ &- \left\langle \delta S'_{AB}, \mathbb{C}'_{ABCD} F_{aC}\frac{\partial \Delta u_a}{\partial X_D}\right\rangle + \left\langle \delta S'_{AB}, \Delta S'_{AB}\right\rangle \\ &+ \left\langle \delta p, \mathrm{f}(J)\, F^{-1}_{Aa}\frac{\partial \Delta u_a}{\partial X_A}\right\rangle + \left\langle \delta p, \frac{\Delta p}{\kappa}\right\rangle,\end{aligned} \tag{3.85}$$

where $\mathrm{f}(J)$ is a function coming from the linearization of $\frac{dG}{dJ}$ and depends upon the volumetric strain energy function into consideration and $\mathbb{C}'_{ABCD} = 2\frac{\partial^2 W}{\partial C_{AB}\partial C_{CD}}$ is the deviatoric constitutive tangent matrix which relates variations of the deviatoric PK2 stress tensor, $\Delta\mathbf{S}'$, with variations of the Right Cauchy tensor, $\Delta\mathbf{C}$. Let us remark that all terms are evaluated at $\mathbf{U}^{n+1}$.

3.6.5 Symmetrization

In the way we have written the problem, it is not symmetric. To achieve symmetry[3], it is possible to modify Eq. (3.84) by

3: In the case of homogeneous boundary conditions, obviously.

Finite strain hyperelasticity. $\mathbf{u}p\mathbf{S}'$ formulation. Symmetrized linearized variational form in TLF

$$\left\langle \delta\mathbf{u}, \rho_0 \frac{C}{\Delta t^2}\Delta\mathbf{u}\right\rangle + \mathscr{B}^{\text{mod}}(\Delta\mathbf{U}, \delta\mathbf{U}) = \mathscr{F}(\delta\mathbf{U}) - \mathscr{A}^{\text{mod}}\left(\mathbf{U}^{n+1}, \delta\mathbf{U}\right) - \left\langle \delta\mathbf{u}, \rho_0 \mathbf{a}^{n+1}\right\rangle \quad \forall\, \delta\mathbf{U} \in \mathbb{W}_0, \tag{3.86}$$

where $\mathscr{B}^{\text{mod}}(\Delta\mathbf{U}, \delta\mathbf{U})$ is the bilinear form defined on $\mathbb{W}_0 \times \mathbb{W}_0$ as

$$\begin{aligned}\mathscr{B}^{\text{mod}}(\Delta\mathbf{U}, \delta\mathbf{U}) = &\left\langle \frac{\partial \delta u_a}{\partial X_A}, \frac{\partial \Delta u_a}{\partial X_B} S'_{BA}\right\rangle + \left\langle \frac{\partial \delta u_a}{\partial X_A}, F_{aB}\Delta S'_{BA}\right\rangle \\ &- \left\langle \frac{\partial \delta u_a}{\partial X_A}, J p F^{-1}_{Bb} \frac{\partial \Delta u_b}{\partial X_B} F^{-1}_{Aa}\right\rangle \\ &+ \left\langle \frac{\partial \delta u_a}{\partial X_A}, J p F^{-1}_{Ab} \frac{\partial \Delta u_b}{\partial X_B} F^{-1}_{Ba}\right\rangle - \left\langle \frac{\partial \delta u_a}{\partial X_A}, J \Delta p F^{-1}_{Aa}\right\rangle \\ &- \left\langle \delta S'_{AB}, F_{aA} \frac{\partial \Delta u_a}{\partial X_B}\right\rangle + \left\langle \delta S'_{AB}, \mathbb{C}'^{-1}_{ABCD}\Delta S_{CD}\right\rangle \\ &+ \left\langle \delta p, J F^{-1}_{Aa} \frac{\partial \Delta u_a}{\partial X_A}\right\rangle + \left\langle \delta p, \frac{J}{\mathrm{f}(J)}\frac{\Delta p}{\kappa}\right\rangle,\end{aligned} \tag{3.87}$$

and $\mathscr{A}^{\text{mod}}\left(\mathbf{U}^{n+1}, \delta\mathbf{U}\right)$ is a semilinear form defined on $\mathbb{W}_0 \times \mathbb{W}_0$ as

$$\begin{aligned}\mathscr{A}^{\text{mod}}\left(\mathbf{U}^{n+1}, \delta\mathbf{U}\right) := &\left\langle \frac{\partial \delta u_a}{\partial X_A}, F_{aB} S'_{BA}\right\rangle - \left\langle \frac{\partial \delta u_a}{\partial X_A}, p J F^{-1}_{Aa}\right\rangle \\ &+ \left\langle \delta S'_{AB}, \mathbb{C}'^{-1}_{ABCD} S'_{CD}\right\rangle - \left\langle \delta S'_{AB}, \mathbb{C}'^{-1}_{ABCD} 2 \frac{\partial W}{\partial C_{CD}}\right\rangle \\ &+ \left\langle \delta p, \frac{J}{\mathrm{f}(J)}\frac{dG}{dJ}\right\rangle + \left\langle \delta p, \frac{J}{\mathrm{f}(J)}\frac{p}{\kappa}\right\rangle,\end{aligned} \tag{3.88}$$

where we have multiplied the second equation by the linearized term $\frac{J}{\mathrm{f}(J)}$ and we have introduced $\mathbb{C}'^{-1}$ as the inverse deviatoric constitutive tangent matrix. To define such 4^{th} order tensor, it is necessary to obtain the inverse strain energy function, which involves a nonlinear problem.

From the conceptual standpoint, the test functions for the constitutive equation in the non-symmetric case are in fact strains, whereas in the symmetric case they are stresses. Let us also remark that, while in the infinitesimal strain theory it is equivalent to use stresses or strains as unknowns, in finite strain elasticity the symmetrization of the problem using strains (e.g. the Green-Lagrange strain $\mathbf{E}$) is much more involved than using the PK2 stress that we have presented. In any case, we will not discuss here the introduction of strains

as unknowns of the problem.

For simplicity, we will employ the non-symmetric form of the problem in what follows, although the use of the symmetric version would be straightforward.

3.6.6 Galerkin spatial discretization

The standard Galerkin approximation of this abstract variational problem is now straightforward. Let $\mathscr{P}_h$ denote a FE partition of the domain Ω_0. The diameter of an element domain $K \in \mathscr{P}_h$ is denoted by h_K and the diameter on the FE partition by $h = \max\{h_K | K \in \mathscr{P}_h\}$. We can now construct conforming FE spaces $\mathbb{U}_h \subset \mathbb{U}$, $\mathbb{P}_h \subset \mathbb{P}$, $\mathbb{S}_h \subset \mathbb{S}$ and $\mathbb{W}_h = \mathbb{U}_h \times \mathbb{P}_h \times \mathbb{S}_h$ in the usual manner, as well as the corresponding subspaces $\mathbb{U}_{h,0} \subset \mathbb{U}_0$ and $\mathbb{W}_{h,0} = \mathbb{U}_{h,0} \times \mathbb{P}_h \times \mathbb{S}_h$, $\mathbb{U}_{h,0}$ being made of functions that vanish on the Dirichlet boundary. In principle, functions in $\mathbb{U}_h$ are continuous, whereas functions in both $\mathbb{P}_h$ and $\mathbb{S}_h$ not necessarily.

The Galerkin discrete version of problem (3.84) is: for a given time t^{n+1} and a fixed iteration, find $\Delta\mathbf{U}_h \equiv \left[\Delta\mathbf{u}_h, \Delta p_h, \Delta\mathbf{S}'_h\right]^T \in \mathbb{W}_{h,0}$ such that

Finite strain hyperelasticity. $\mathbf{u}p\mathbf{S}'$ formulation. Galerkin discrete problem in TLF

$$\begin{aligned}\left\langle \delta\mathbf{u}_h, \rho_0 \frac{C}{\Delta t^2}\Delta\mathbf{u}_h \right\rangle + \mathscr{B}\left(\Delta\mathbf{U}_h, \delta\mathbf{U}_h\right) &= \mathscr{F}\left(\delta\mathbf{U}_h\right) \\ &\quad - \mathscr{A}\left(\mathbf{U}_h^{n+1}, \delta\mathbf{U}_h\right) - \left\langle \delta\mathbf{u}_h, \rho_0 \mathbf{a}_h^{n+1} \right\rangle \\ &\quad \forall\, \delta\mathbf{U}_h \in \mathbb{W}_{h,0}. \end{aligned} \tag{3.89}$$

The stability of the discrete formulation depends on compatibility restrictions on the interpolation functions chosen for the displacement, deviatoric PK2 stress and pressure fields, as stated by the appropriate inf–sup condition [22]. According to these restrictions, mixed elements with continuous equal order linear interpolation for all fields are not stable. However, the inf–sup condition can be circumvented by using a stabilization technique. This is why the so-called stabilized formulations have been proposed to approximate this kind of problems. The main idea is to replace Eq. (3.84) by another discrete variational problem in which the bilinear form

[22]: Babuška (1971), "Error-Bounds for Finite Element Method"

$\mathscr{B}$ is enhanced so that it has improved stability properties. In order to overcome the instabilities previously discussed, we propose the stabilization technique described in next section.

Remark 3.6.2 In principle, we have posed no restrictions on the choice of the FE spaces. However, the Galerkin formulation is only stable if two inf-sup conditions are satisfied, one between the displacements and the stresses and another one between the displacements and the pressure. This conditions are explained in [46] for the linear Stokes problem, and are obviously inherited in the nonlinear problem considered now. Only stresses can be controlled with the Galerkin formulation, and in the case of compressible materials also the pressure, but this control disappears as $\kappa \to \infty$. Displacement gradients need to be controlled using an inf-sup condition and pressures (regardless of the compressibility) using another one. The alternative to using the Galerkin method with FE spaces satisfying the inf-sup conditions is to use a stabilized FEM, as the one we describe next.

[46]: Codina (2009), "Finite element approximation of the three field formulation of the Stokes problem using arbitrary interpolations"

3.6.7 Stabilization

In this section, the VMS method [6, 12] already introduced in Section 3.5.7 is applied to stabilize the discrete formulation of the mixed three-field problem allowing for the use of linear interpolations for all master fields. Galerkin's space of approximation, $\mathbb{W}_h$, is enlarged by adding the SGS space, $\tilde{\mathbb{W}}$. Let $\mathbb{W} = \mathbb{W}_h \oplus \tilde{\mathbb{W}}$. The SGS are denoted by $\tilde{\mathbf{U}} := [\tilde{\mathbf{u}}, \tilde{p}, \tilde{\mathbf{S}}']^T$. Likewise, let $\mathbb{W}_0 = \mathbb{W}_{h,0} \oplus \tilde{\mathbb{W}}_0$, where $\tilde{\mathbb{W}}_0$ is being made of displacement SGSs (defined at element level) that vanish at all the element boundaries.

[6]: Hughes et al. (1998), "The variational multiscale method - A paradigm for computational mechanics"
[12]: R.Codina et al. (2017), *Variational Multiscale Methods in Computational Fluid Dynamics*

Taking into account that $\mathscr{B}$ is a bilinear form, the continuous problem (3.89) is equivalent to find $\Delta\mathbf{u}_h \in \mathbb{W}_{h,0}$ and $\tilde{\mathbf{U}} \in \tilde{\mathbb{W}}$ such that

$$\begin{aligned}
&\left\langle \delta\mathbf{u}_h, \rho_0 \frac{C}{\Delta t^2} \Delta\mathbf{u}_h \right\rangle + \left\langle \delta\mathbf{u}_h, \rho_0 \tilde{\mathbf{a}}^{n+1} \right\rangle + \mathscr{B}\left(\Delta\mathbf{U}_h, \delta\mathbf{U}_h\right) \\
&\qquad + \mathscr{B}\left(\tilde{\mathbf{U}}, \delta\mathbf{U}_h\right) = \mathscr{F}\left(\delta\mathbf{U}_h\right) - \mathscr{A}\left(\mathbf{U}_h^{n+1}, \delta\mathbf{U}_h\right) \\
&\qquad - \left\langle \delta\mathbf{u}_h, \rho_0 \mathbf{a}_h^{n+1} \right\rangle \quad \forall\, \delta\mathbf{U}_h \in \mathbb{W}_{h,0}, \qquad (3.90) \\
&\left\langle \delta\tilde{\mathbf{u}}, \rho_0 \frac{C}{\Delta t^2} \Delta\mathbf{u}_h \right\rangle + \left\langle \delta\tilde{\mathbf{u}}, \rho_0 \tilde{\mathbf{a}}^{n+1} \right\rangle + \mathscr{B}\left(\Delta\mathbf{U}_h, \delta\tilde{\mathbf{U}}\right)
\end{aligned}$$

$$+\mathscr{B}\left(\tilde{\mathbf{U}},\delta\tilde{\mathbf{U}}\right)=\mathscr{F}\left(\delta\tilde{\mathbf{U}}\right)-\mathscr{A}\left(\mathbf{U}_h^{n+1},\delta\tilde{\mathbf{U}}\right)$$
$$-\left\langle\delta\tilde{\mathbf{u}},\rho_0\mathbf{a}_h^{n+1}\right\rangle\quad\forall\,\delta\tilde{\mathbf{U}}\in\tilde{\mathbb{W}}_0,\tag{3.91}$$

The approximation to the acceleration obtained from the displacement SGS at time t^{n+1} has been denoted by $\tilde{\mathbf{a}}^{n+1}$.

In this section we consider again the SGSs to be quasi-static. We also assume the SGSs to behave as bubble functions. Taking this into account, we can integrate by parts within each element in Eq. (3.91) to obtain:

$$\sum_K\left\langle\delta\tilde{\mathbf{u}},\rho_0\frac{C}{\Delta t^2}\Delta\mathbf{u}_h\right\rangle_K+\sum_K\left\langle\delta\tilde{\mathbf{U}},\mathrm{B}\left(\Delta\mathbf{U}_h\right)\right\rangle_K+\sum_K\left\langle\delta\tilde{\mathbf{U}},\mathrm{B}\left(\tilde{\mathbf{U}}\right)\right\rangle_K$$
$$=\sum_K\left\langle\delta\tilde{\mathbf{U}},\mathrm{F}\right\rangle_K-\sum_K\left\langle\delta\tilde{\mathbf{U}},\mathrm{A}\left(\mathbf{U}_h^{n+1}\right)\right\rangle_K$$
$$-\sum_K\left\langle\delta\tilde{\mathbf{u}},\rho_0\mathbf{a}_h^{n+1}\right\rangle_K\ \forall\,\delta\tilde{\mathbf{U}}\in\tilde{\mathbb{W}}_0,\tag{3.92}$$

where $\mathrm{B}=\left[\mathrm{B}_{\mathbf{u}},\mathrm{B}_p,\mathrm{B}_{\mathbf{S}'}\right]^T$ is a linear operator coming from the integration by parts of $\mathscr{B}$ such that $\mathscr{B}\left(\delta\mathbf{U}_h,\delta\tilde{\mathbf{U}}\right)=\sum_K\left\langle\delta\tilde{\mathbf{U}},\mathrm{B}\left(\Delta\mathbf{U}_h\right)\right\rangle_K$ and it is defined as

$$\mathrm{B}_{\mathbf{u}}\left(\Delta\mathbf{U}_h\right)_a=-\frac{\partial}{\partial X_A}\left\{\frac{\partial\Delta u_{h_a}}{\partial X_B}S'_{AB}\right\}-\frac{\partial}{\partial X_A}\left\{F_{aB}\Delta S'_{h_{AB}}\right\}$$
$$+\frac{\partial}{\partial X_A}\left\{Jp F^{-1}_{Bb}\frac{\partial\Delta u_{h_b}}{\partial X_B}F^{-1}_{Aa}\right\}+\frac{\partial}{\partial X_A}\left\{J\Delta p_h F^{-1}_{Aa}\right\}$$
$$-\frac{\partial}{\partial X_A}\left\{Jp F^{-1}_{Ab}\frac{\partial\Delta u_{h_b}}{\partial X_B}F^{-1}_{Ba}\right\},\tag{3.93}$$

$$\mathrm{B}_p\left(\Delta\mathbf{U}_h\right)=\mathrm{f}(J)\,F^{-1}_{Aa}\frac{\partial\Delta u_{h_a}}{\partial X_A}+\frac{\Delta p_h}{\kappa},\tag{3.94}$$

$$\mathrm{B}_{\mathbf{S}'}\left(\Delta\mathbf{U}_h\right)_{AB}=-\mathbb{C}'_{ABCD}F_{aC}\frac{\partial\Delta u_{h_a}}{\partial X_D}+\Delta S'_{h_{AB}}.\tag{3.95}$$

Regarding the right-hand side, $\mathrm{F}=\left[\mathrm{F}_{\mathbf{u}},\mathrm{F}_p,\mathrm{F}_{\mathbf{S}'}\right]^T$ appears from the external forces form $\mathscr{F}$ and it is given by

$$\mathrm{F}_{\mathbf{u}_a}=\rho_0 b_a\quad;\quad\mathrm{F}_p=0\quad;\quad\mathrm{F}_{\mathbf{S}'_{AB}}=0,\tag{3.96}$$

and finally $\mathrm{A}\left(\mathbf{U}_h^{n+1}\right)=\left[\mathrm{A}_{\mathbf{u}}\left(\mathbf{U}_h^{n+1}\right),\mathrm{A}_p\left(\mathbf{U}_h^{n+1}\right),\mathrm{A}_{\mathbf{S}'}\left(\mathbf{U}_h^{n+1}\right)\right]^T$ comes from the integration by parts of $\mathscr{A}$ and it is defined as

$$\mathrm{A}_{\mathbf{u}}\left(\mathbf{U}_h^{n+1}\right)_a=-\frac{\partial}{\partial X_A}\{F_{aB}S'_{BA}\}+\frac{\partial}{\partial X_A}\{Jp F^{-1}_{Aa}\},\tag{3.97}$$

$$\mathrm{A}_p\left(\mathbf{U}_h^{n+1}\right) = \frac{dG}{dJ} + \frac{p}{\kappa}, \tag{3.98}$$

$$\mathrm{A}_{\mathbf{S}'}\left(\mathbf{U}_h^{n+1}\right)_{AB} = S'_{AB} - 2\frac{\partial W}{\partial C_{AB}}. \tag{3.99}$$

Eq. (3.92) must be satisfied for all elements $K \in \mathscr{P}_h$ and for any $\delta\tilde{\mathbf{U}} \in \tilde{\mathbb{W}}$, which strictly enforces that

$$\tilde{\Pi}\left(\mathrm{B}\left(\Delta\mathbf{U}_h\right) + \mathrm{B}\left(\tilde{\mathbf{U}}\right)\right) = \tilde{\Pi}\left(\mathrm{F} - \mathrm{A}\left(\mathbf{U}_h^{n+1}\right)\right), \tag{3.100}$$

This equation allows us to obtain an expression for the SGSs:

$$\begin{aligned}\tilde{\Pi}\left(\mathrm{B}\left(\tilde{\mathbf{U}}\right)\right) &= \tilde{\Pi}\left(\mathrm{F} - \mathrm{A}\left(\mathbf{U}_h^{n+1}\right) - \mathrm{B}\left(\Delta\mathbf{U}_h\right)\right) \\ &:= \tilde{\Pi}\left(\mathrm{R}\left(\mathbf{U}_h^{n+1}\right) + \mathrm{R}_{\Delta\mathbf{U}}\left(\Delta\mathbf{U}_h\right)\right),\end{aligned} \tag{3.101}$$

where the residuals are defined as $\mathrm{R}_{\Delta\mathbf{U}}\left(\Delta\mathbf{U}_h\right) := -\mathrm{B}\left(\Delta\mathbf{U}_h\right)$ and $\mathrm{R}\left(\mathbf{U}_h^{n+1}\right) := \mathrm{F} - \mathrm{A}\left(\mathbf{U}_h^{n+1}\right)$.

The idea now is to approximate operator B by a matrix $\boldsymbol{\tau}_K^{-1}$ within each element K. Since we may consider that $\boldsymbol{\tau}_K^{-1}\tilde{\mathbf{U}}$ already belongs to the SGS space, $\tilde{\Pi}\left(\boldsymbol{\tau}_K^{-1}\tilde{\mathbf{U}}\right) = \boldsymbol{\tau}_K^{-1}\tilde{\mathbf{U}}$, and from Eq. (3.101) we obtain

$$\tilde{\mathbf{U}} \approx \boldsymbol{\tau}_K\tilde{\Pi}\left(\mathrm{R}\left(\mathbf{U}_h^{n+1}\right) + \mathrm{R}_{\Delta\mathbf{U}}\left(\Delta\mathbf{U}_h\right)\right) \quad \text{in } K \in \mathscr{P}_h, \tag{3.102}$$

where $\boldsymbol{\tau}_K$ is a matrix of algorithmic parameters depending on K and the operator B. This approximation for $\tilde{\mathbf{U}}$ is intended to mimic the effect of $\mathrm{B}\left(\tilde{\mathbf{U}}\right)$ in the volume integral (3.90). Let us remark that $\boldsymbol{\tau}_K$ is taken as a diagonal matrix of stabilization parameters, $\boldsymbol{\tau}_K = \mathrm{diag}\left(\tau_{\mathbf{u}}\mathbf{I}_d, \tau_p, \tau_{\mathbf{S}'}\mathbf{I}\right)$, with $\mathbf{I}_d$ the identity on vectors of $\mathbb{R}^d$ and parameters $\tau_{\mathbf{u}}$, τ_p and $\tau_{\mathbf{S}'}$ are coefficients coming from the study of the behavior of the stabilization parameters based on a Fourier analysis of the problem for the SGSs. In this work, we propose to use the stabilization parameters presented in [27] for linear elastic cases:

[27]: Chiumenti et al. (2015), "A mixed three-field FE formulation for stress accurate analysis including the incompressible limit"

$$\tau_{\mathbf{u}} = c_1\frac{h_K^2}{2\mu} \quad \text{and} \quad \tau_p = 2c_2\mu \quad \text{and} \quad \tau_{\mathbf{S}'} = c_3, \tag{3.103}$$

where c_1, c_2 and c_3 are algorithmic parameters which must be determined.

Finally, Eq. (3.102) can be introduced into the FE scale equation to obtain the following stabilized weak form

Finite strain hyperelasticity. $\mathbf{u}p\mathbf{S}'$ formulation. Stabilized weak form in TLF

$$\begin{aligned}&\left\langle \delta\mathbf{u}_h, \rho_0 \frac{C}{\Delta t^2}\Delta\mathbf{u}_h \right\rangle + \mathscr{B}\left(\Delta\mathbf{U}_h, \delta\mathbf{U}_h\right)\\ &+ \sum_K \boldsymbol{\tau}_K \left\langle \mathrm{L}\left(\delta\mathbf{U}_h\right), \tilde{\Pi}\left(\mathrm{R}\left(\mathbf{U}_h^{n+1}\right) + \mathrm{R}_{\Delta\mathbf{U}}\left(\Delta\mathbf{U}_h\right)\right)\right\rangle\\ &= \mathscr{F}\left(\delta\mathbf{U}_h\right) - \mathscr{A}\left(\mathbf{U}_h^{n+1}, \delta\mathbf{U}_h\right) - \left\langle \delta\mathbf{u}_h, \rho_0 \mathbf{a}_h^{n+1}\right\rangle \quad \forall\, \delta\mathbf{U}_h \in \mathbb{W}_{h,0},\end{aligned} \tag{3.104}$$

where $\mathrm{L}\left(\delta\mathbf{U}_h\right) = \left[\mathrm{L}_{\mathbf{u}}\left(\delta\mathbf{U}_h\right), \mathrm{L}_p\left(\delta\mathbf{U}_h\right), \mathrm{L}_{\mathbf{S}'}\left(\delta\mathbf{U}_h\right)\right]^T$ is a linear operator coming from the integration by parts of $\mathscr{B}$ such that $\mathscr{B}\left(\tilde{\mathbf{U}}, \delta\mathbf{U}_h\right) = \sum_K \left\langle \mathrm{L}\left(\delta\mathbf{U}_h\right), \tilde{\mathbf{U}}\right\rangle_K$ and it is defined as

$$\begin{aligned}\mathrm{L}_{\mathbf{u}}\left(\delta\mathbf{U}_h\right)_a = &-\frac{\partial}{\partial X_A}\left\{\frac{\partial \delta u_{h_a}}{\partial X_B} S'_{AB}\right\} + \frac{\partial}{\partial X_A}\left\{Jp F^{-1}_{Aa}\frac{\partial \delta u_{h_b}}{\partial X_B}F^{-1}_{Bb}\right\}\\ &-\frac{\partial}{\partial X_A}\left\{Jp F^{-1}_{Ba}\frac{\partial \delta u_{h_b}}{\partial X_B}F^{-1}_{Ab}\right\} - \frac{\partial}{\partial X_A}\left\{\delta p f(J) F^{-1}_{Aa}\right\}\\ &+\frac{\partial}{\partial X_D}\left\{\delta S'_{AB}\mathbb{C}'_{ABCD}F_{aC}\right\},\end{aligned} \tag{3.105}$$

$$\mathrm{L}_p\left(\delta\mathbf{U}_h\right) = \frac{\partial \delta u_{h_a}}{\partial X_A} J F^{-1}_{Aa} + \frac{\delta p}{\kappa}, \tag{3.106}$$

$$\mathrm{L}_{\mathbf{S}'}\left(\delta\mathbf{U}_h\right)_{AB} = \frac{\partial \delta u_{h_a}}{\partial X_A} F_{aB} + \delta S'_{AB}. \tag{3.107}$$

In this work, three different stabilization methods are considered.

Algebraic SubGrid Scales (ASGS)

We take the projection onto the SGS space as the identity when applied to the residual, so that

$$\tilde{\Pi}\left(\mathrm{R}\left(\mathbf{U}_h^{n+1}\right) + \mathrm{R}_{\Delta\mathbf{U}}\left(\Delta\mathbf{U}_h\right)\right) = \mathrm{R}\left(\mathbf{U}_h^{n+1}\right) + \mathrm{R}_{\Delta\mathbf{U}}\left(\Delta\mathbf{U}_h\right), \tag{3.108}$$

and we obtain as a final stabilized formulation

$$\begin{aligned}&\left\langle \delta\mathbf{u}_h, \rho_0 \frac{C}{\Delta t^2}\Delta\mathbf{u}_h \right\rangle + \mathscr{B}\left(\Delta\mathbf{U}_h, \delta\mathbf{U}_h\right)\\ &\qquad + \sum_K \boldsymbol{\tau}_K \left\langle \mathrm{L}\left(\delta\mathbf{U}_h\right), \mathrm{R}_{\Delta\mathbf{U}}\left(\Delta\mathbf{U}_h\right)\right\rangle = \mathscr{F}\left(\delta\mathbf{U}_h\right)\\ &\qquad - \mathscr{A}\left(\mathbf{U}_h^{n+1}, \delta\mathbf{U}_h\right) - \left\langle \delta\mathbf{u}_h, \rho_0 \mathbf{a}_h^{n+1}\right\rangle\end{aligned}$$

$$- \sum_K \boldsymbol{\tau}_K \left\langle \mathrm{L}\left(\delta \mathbf{U}_h\right), \mathrm{R}\left(\mathbf{U}_h^{n+1}\right)\right\rangle \quad \forall\, \delta \mathbf{U}_h \in \mathbb{W}_{h,0}. \tag{3.109}$$

Orthogonal SubGrid Scales (OSGS)

We take the SGS space orthogonal to the FE space:

$$\begin{aligned}\tilde{\Pi}\left(\mathrm{R}\left(\mathbf{U}_h^{n+1}\right) + \mathrm{R}_{\Delta \mathrm{U}}\left(\Delta \mathbf{U}_h\right)\right) = \mathrm{R}\left(\mathbf{U}_h^{n+1}\right) \\ + \mathrm{R}_{\Delta \mathrm{U}}\left(\Delta \mathbf{U}_h\right) - \Pi^h\left(\mathrm{R}\left(\mathbf{U}_h^{n+1}\right)\right),\end{aligned} \tag{3.110}$$

where Π^h is the $L^2\left(\Omega_0\right)$ projection onto the FE space. Due to the fact that this projection would increase the size of our system if we compute it in an implicit way, we have decided to approximate it with the residual of the previous iteration by neglecting the projection of the operator $\mathrm{R}_{\Delta \mathrm{U}}\left(\Delta \mathbf{U}_h\right)$. The final form of the stabilized problem with OSGS method emerges as

$$\begin{aligned}\left\langle \delta \mathbf{u}_h, \rho_0 \frac{C}{\Delta t^2} \Delta \mathbf{u}_h \right\rangle + \mathscr{B}\left(\Delta \mathbf{U}_h, \delta \mathbf{U}_h\right) \\ + \sum_K \boldsymbol{\tau}_K \left\langle \mathrm{L}\left(\delta \mathbf{U}_h\right), \mathrm{R}_{\Delta \mathrm{U}}\left(\Delta \mathbf{U}_h\right)\right\rangle = \mathscr{F}\left(\delta \mathbf{U}_h\right) \\ - \mathscr{A}\left(\mathbf{U}_h^{n+1}, \delta \mathbf{U}_h\right) - \left\langle \delta \mathbf{u}_h, \rho_0 \mathbf{a}_h^{n+1}\right\rangle \\ - \sum_K \boldsymbol{\tau}_K \left\langle \mathrm{L}\left(\delta \mathbf{U}_h\right), \mathrm{R}\left(\mathbf{U}_h^{n+1}\right) - \Pi^h\left(\mathrm{R}\left(\mathbf{U}_h^n\right)\right)\right\rangle \\ \forall\, \delta \mathbf{U}_h \in \mathbb{W}_{h,0}.\end{aligned} \tag{3.111}$$

Split Orthogonal SubGrid Scales (S-OSGS)

A key property of the OSGS stabilization is that, thanks to the projection onto the FE space, we keep the consistency of the formulation in a weak sense in spite of including just the minimum number of terms to stabilize the solution. This property allows us to propose the following split version of the OSGS method:

$$\begin{aligned}\left\langle \delta \mathbf{u}_h, \rho_0 \frac{C}{\Delta t^2} \Delta \mathbf{u}_h \right\rangle + \mathscr{B}\left(\Delta \mathbf{U}_h, \delta \mathbf{U}_h\right) \\ + \sum_K \boldsymbol{\tau}_K \left\langle \mathrm{L}^*\left(\delta \mathbf{U}_h\right), \mathrm{R}^*_{\Delta \mathrm{U}}\left(\Delta \mathbf{U}_h\right)\right\rangle = \mathscr{F}\left(\delta \mathbf{U}_h\right) \\ - \mathscr{A}\left(\mathbf{U}_h^{n+1}, \delta \mathbf{U}_h\right) - \left\langle \delta \mathbf{u}_h, \rho_0 \mathbf{a}_h^{n+1}\right\rangle\end{aligned}$$

$$- \sum_K \boldsymbol{\tau}_K \left\langle \mathrm{L}^* \left(\delta \mathbf{U}_h\right), \mathrm{R}^* \left(\mathbf{U}_h^{n+1}\right) - \Pi^h \left(\mathrm{R}^* \left(\mathbf{U}_h^n\right)\right)\right\rangle$$

$$\forall\, \delta \mathbf{U}_h \in \mathbb{W}_{h,0}, \tag{3.112}$$

where the split operators are defined as

$$\mathrm{B}^*_{\mathbf{u}} \left(\Delta \mathbf{U}_h\right)_a = \frac{\partial}{\partial X_A} \left\{J \Delta p_h F^{-1}_{Aa}\right\},\ \mathrm{B}^*_p \left(\Delta \mathbf{U}_h\right) = 0, \tag{3.113}$$

$$\mathrm{B}^*_{\mathrm{S}'} \left(\Delta \mathbf{U}_h\right)_{AB} = -\mathbb{C}'_{ABCD} F_{aC} \frac{\partial \Delta u_{h_a}}{\partial X_D}, \tag{3.114}$$

$$\mathrm{A}^*_{\mathbf{u}} \left(\mathbf{U}_h^{n+1}\right)_a = \frac{\partial}{\partial X_A} \{J p F^{-1}_{Aa}\},\ \mathrm{A}^*_p \left(\mathbf{U}_h^{n+1}\right) = 0, \tag{3.115}$$

$$\mathrm{A}^*_{\mathrm{S}'} \left(\mathbf{U}_h^{n+1}\right)_{AB} = -2 \frac{\partial W}{\partial C_{AB}}, \tag{3.116}$$

$$\mathrm{L}^*_{\mathbf{u}} \left(\delta \mathbf{U}_h\right)_a = -\frac{\partial}{\partial X_A} \left\{\delta p f(J) F^{-1}_{Aa}\right\},\ \mathrm{L}^*_p \left(\delta \mathbf{U}_h\right) = 0, \tag{3.117}$$

$$\mathrm{L}^*_{\mathrm{S}'} \left(\delta \mathbf{U}_h\right)_{AB} = \frac{\partial \delta u_{h_a}}{\partial X_A} F_{aB}. \tag{3.118}$$

The S-OSGS method is not just a simplification of the OSGS one. For smooth solutions, both have an optimal convergence rate in mesh size. However, in problems where the solution has strong gradients, we have found the S-OSGS more robust, similarly to what it is explained in [15].

[15]: Moreno et al. (2019), "Logarithmic conformation reformulation in viscoelastic flow problems approximated by a VMS-type stabilized finite element formulation"

3.6.8 Numerical examples

In this section, several numerical examples are presented to assess the performance of the proposed three-field formulation. As a first case, a test with a manufactured solution is considered to analyze the spatial discretization errors upon mesh refinement and the nonlinear iteration convergence error with a Newton-Raphson scheme for each unknown of the problem. Later, we consider a bending problem for a beam-like structure in order to show the behavior of the method in bending dominated scenarios. Finally, a twisting column is set which presents extreme nonlinear deformations. All these examples are widely used in incompressible hyperelastic cases [58, 59, 61, 62]. To highlight the main advantages of the presented three field mixed $\mathbf{u}p\mathbf{S}'$ formulation with respect to the two-field one presented in Section 3.5, some comparisons will be done against the stabilized mixed $\mathbf{u}p$ formulation proposed in the previous section.

[58]: Bonet et al. (2015), "A first order hyperbolic framework for large strain computational solid dynamics. Part I : Total Lagrangian isothermal elasticity"

[59]: Gil et al. (2016), "A first order hyperbolic framework for large strain computational solid dynamics. Part II : Total Lagrangian compressible, nearly incompressible and truly incompressible elasticity"

[61]: Scovazzi et al. (2016), "A simple, stable, and accurate linear tetrahedral finite element for transient, nearly, and fully incompressible solid dynamics: a dynamic variational multiscale approach"

[62]: Rossi et al. (2016), "Implicit finite incompressible elastodynamics with linear finite elements: A stabilized method in rate form"

For all the numerical examples included next, hyperelastic models are considered fully incompressible, and so the bulk modulus is $\kappa = \infty$, unless otherwise specified. With regards to the stabilization technique, we select the S-OSGS method except where otherwise stated. The algorithmic parameters are set to $c_1 = 1$, $c_2 = 1$ and $c_3 = 0.5$. As previously discussed, the nonlinearities in the problem are solved via a Newton-Raphson scheme. Depending on these nonlinearities, the initial guess of the iterative procedure needs to be close enough to the solution to guarantee convergence of the nonlinear iterations. In time-depending schemes, the time step is the parameter which controls the evolution of the nonlinear iterations, so we will have to tune it depending on the nonlinearities of each numerical example. A maximum of 10 iterations is set, and the numerical tolerance for the $L^2(\Omega_0)$ norm is 10^{-7}. In order to solve the monolithic system of linear equations, we use the Biconjugate Gradients solver, `BiCGstab` [71], which is already implemented in the `PETSc` parallel solver library [17].

[71]: Vorst (1992), "Bi-CGSTAB: A fast and smoothly converging variant of Bi-CG for the solution of nonsymmetric linear systems"

[17]: Balay et al. (2015), *PETSc Web page*

A test with analytical solution

Let us first perform a simple test whose main objective is to numerically check the order of convergence of the proposed scheme with respect to the mesh size. For this purpose we use the so-called method of manufactured solutions.

In this procedure, an exact analytical solution is defined a priori and later substituted into the continuum equations in order to obtain the associated forcing terms. These forcing terms are then introduced in the FE computation. The manufactured solutions are composed of smooth functions. Dirichlet boundary conditions are prescribed over the boundaries upon evaluation of the displacement analytical solution. So as to avoid mixing both spatial and time errors, we consider static solutions.

The region we consider is the unit square plate $\Omega_0 = [0,1] \times [0,1]$ under plain strain assumption and we impose the following manufactured displacement and pressure fields

$$\mathbf{u}(X,Y) = k\left[\exp(X+Y), -\exp(X+Y)\right], \tag{3.119}$$

$$p(X,Y) = \mu \sin(2\pi X)\sin(2\pi Y), \tag{3.120}$$

where $k = 0.01$ and X and Y referring to the Cartesian axes in the reference configuration. All quantities are assumed dimensionless in this example. It is important to note that this displacement field gives an incompressible motion due to the fact that the Jacobian is $J(\mathbf{u}(X,Y)) = 1$ for all X, Y. We set a Neo-Hookean material for the deviatoric part of the stresses, with shear modulus $\mu = 3.3\times10^6$ and Poisson ratio $\nu = 0.5$ and a quadratic law for the volumetric response. Therefore, the manufactured deviatoric PK2 stress field is computed with respect to the manufactured displacement field as

$$\mathbf{S}'(X,Y) = \mu\left\{\mathbf{I} - \frac{1}{3}\text{trace}\left[\mathbf{C}\left(\mathbf{u}(X,Y)\right)\right]\mathbf{C}^{-1}\left(\mathbf{u}(X,Y)\right)\right\}. \quad (3.121)$$

We study the convergence behavior of the proposed method by running the case on seven meshes obtained by refinement. The sequence is of structured grids of n^2 linear quadrilateral elements, being n the number of FEs along each side of the domain.

The normalized error has been computed in the $L^2(\Omega_0)$ norm for displacement, pressure and deviatoric PK2 stress fields with ASGS, OSGS and S-OSGS stabilization techniques. Fig. 3.19a shows the displacement convergence rate upon mesh size. As expected, all stabilization methods present the same slope of 2.0. With respect to both pressure and deviatoric PK2 stress fields, all methods converge with a slope of 1.5 upon mesh refinement, as it can be observed in Figs. 3.19c-3.19e. This, in fact, corresponds to a superconvergent behavior, as the theoretical order of convergence should be 1 using linear elements. In [46] it is shown for the linear problem that the convergence order for displacements is $k+1$ and for stresses and pressures it is k in the $L^2(\Omega_0)$ norm, k being the polynomial order of the FE interpolation. For the stress-displacement formulation presented in [10] one can consider dual formulations and increase the order of convergence for the stresses and the expense of decreasing it for the displacements, but this is not possible when pressures are introduced as unknowns.

[46]: Codina (2009), "Finite element approximation of the three field formulation of the Stokes problem using arbitrary interpolations"

[10]: Cervera et al. (2010), "Mixed Stabilized Finite Element Methods in Nonlinear Solid Mechanics. Part I: Formulation"

For the sake of completeness, Figs. 3.19b-3.19d-3.19f show the nonlinear iteration convergence error for each unknown of the formulation. As it can be seen, a quadratic convergence is attained thanks to the Newton-Raphson linearization of the problem.

More interesting results are obtained when comparing these

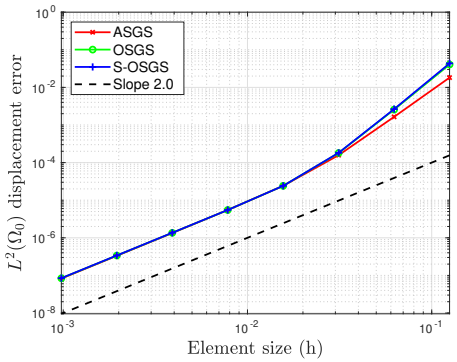

(a) Displacement error upon mesh refinement

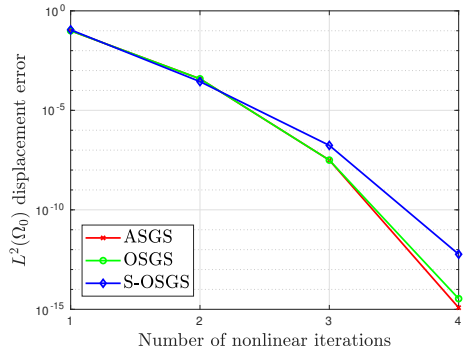

(b) Displacement nonlinear convergence error

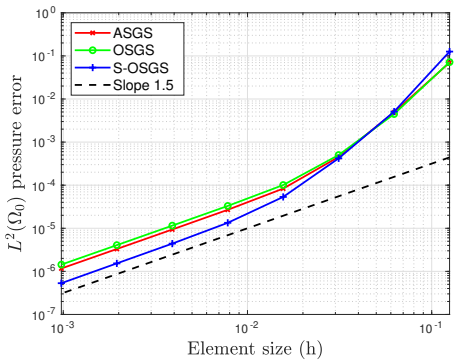

(c) Pressure error upon mesh refinement

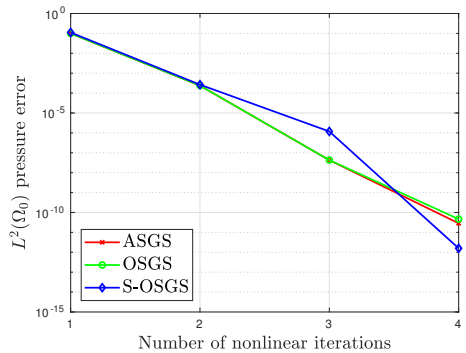

(d) Pressure nonlinear convergence error

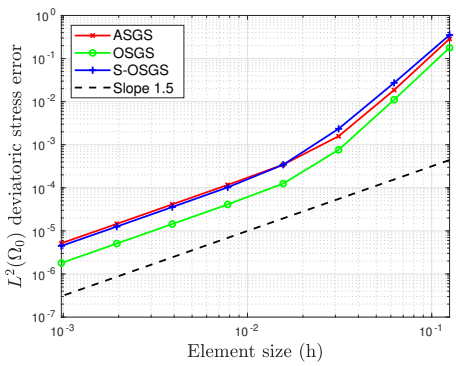

(e) Deviatoric stress error upon mesh refinement

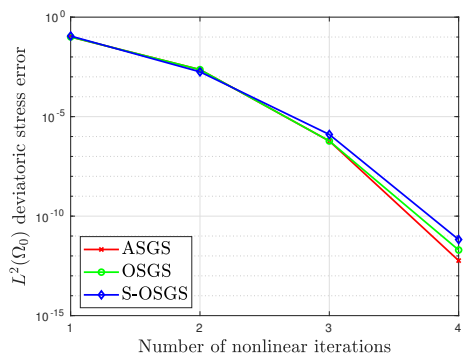

(f) Deviatoric stress nonlinear convergence error

Figure 3.19: Manufactured convergence test. Convergence rate of the $\mathbf{u}p\mathbf{S}'$ formulation upon mesh refinement and nonlinear iteration convergence error.

convergence rates with respect to the ones obtained with the mixed $\mathbf{u}p$ formulation. Figs 3.20a-3.20b show the displacement and pressure convergence rates upon mesh refine-

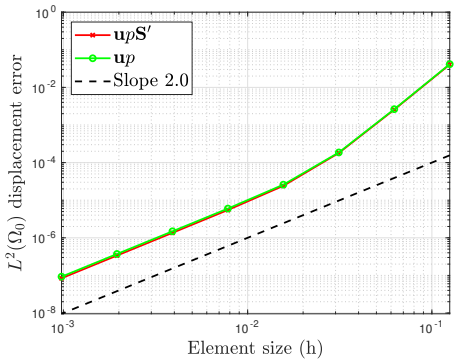

(a) Displacement error upon mesh refinement

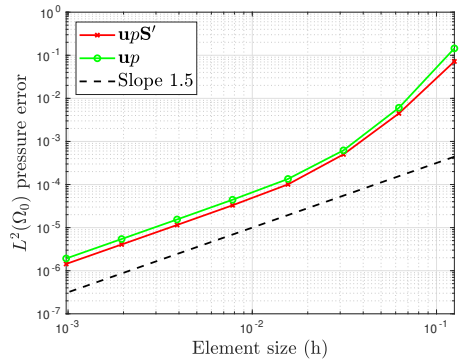

(b) Pressure error upon mesh refinement

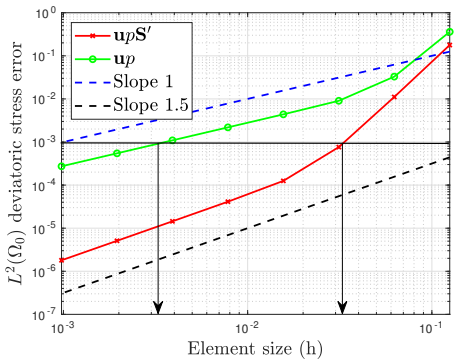

(c) Deviatoric stress error upon mesh refinement

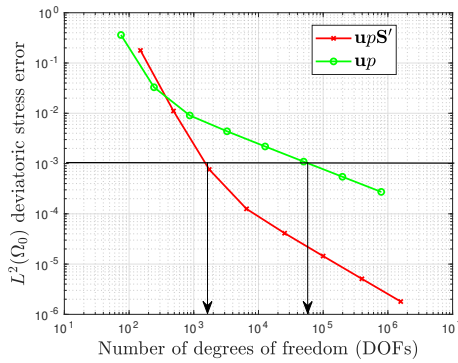

(d) Deviatoric stress error upon number of DOFs

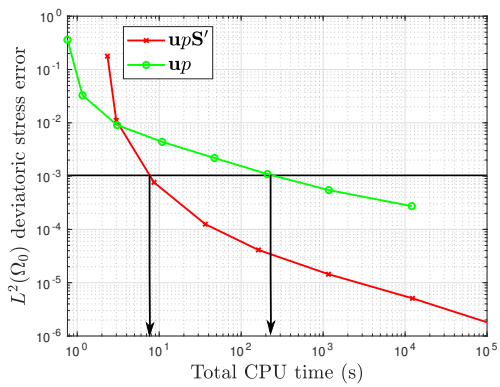

(e) Deviatoric stress error upon CPU time

Figure 3.20: Manufactured convergence test. Comparison of convergence between the $\mathbf{u}p\mathbf{S}'$ formulation and the $\mathbf{u}p$ formulation

ment, respectively. Both fields are considered as primary unknowns of both formulations and therefore a similar ac-

curacy for a given mesh size can be expected. Fig. 3.20c displays the deviatoric PK2 stress convergence rates upon mesh refinement for both formulations. As expected, higher accuracy is achieved for a given mesh size for the mixed $\mathbf{u}p\mathbf{S}'$ formulation. To achieve the same accuracy, e.g. 0.1% of global error, the $\mathbf{u}p$ formulation requires a mesh size, h, almost 10 times finer ($h \approx 0.003$) than the $\mathbf{u}p\mathbf{S}'$ formulation ($h \approx 0.03$).

Furthermore, to obtain a fairer comparison, the same study is conducted in terms of the number of degrees of freedom (DOFs) in Fig. 3.20d. To get an error lower than 0.1%, the $\mathbf{u}p$ formulation requires $6 \cdot 10^4$ DOFs approximately, while the $\mathbf{u}p\mathbf{S}'$ formulation needs less than $2 \cdot 10^3$ DOFs (25 times lesser than the $\mathbf{u}p$ formulation). Results clearly show that both the $\mathbf{u}p\mathbf{S}'$ and the $\mathbf{u}p$ formulations deal appropriately with the incompressibility constraint but the three-field formulation exhibits a higher accuracy in the stress field, even for very coarse meshes.

For the sake of exhaustiveness, Fig. 3.20e depicts the total CPU time needed by each FE technology to achieve a given global deviatoric stress accuracy. In particular, to reduce the simulation error below 0.1%, the $\mathbf{u}p\mathbf{S}'$ formulation is more or less 10 times faster compared to the $\mathbf{u}p$ one.

Remark 3.6.3 Note that the $\mathbf{u}p$ formulation computes the stresses (locally) at the numerical integration points, while the $\mathbf{u}p\mathbf{S}'$ formulation adopts a continuous stress field. To compare stress accuracy, a local smoothing technique has been applied to the original discontinuous stress fields of the mixed $\mathbf{u}p$ formulation. So, Figs. 3.20c-3.20d-3.20e show the continuous values obtained after the smoothing operation.

Bending beam

As a second test in finite strain elasticity, we consider a three dimensional beam of square section clamped on its bottom face very similar to the one presented in [61]. The initial geometry is a thick column of dimensions $1 \times 1 \times 6$ m as shown in Fig. 3.21a. We consider stress free conditions in all boundaries except the clamped one in which zero displacement is imposed. An initial linear in space velocity field

[61]: Scovazzi et al. (2016), "A simple, stable, and accurate linear tetrahedral finite element for transient, nearly, and fully incompressible solid dynamics: a dynamic variational multiscale approach"

$\mathbf{v}^0\,(X,Y,Z) = \left(\frac{5}{3}Z, 0, 0\right)^T$ m/s is imposed so as to start the column oscillations in time, leading to a large oscillatory bending deformation.

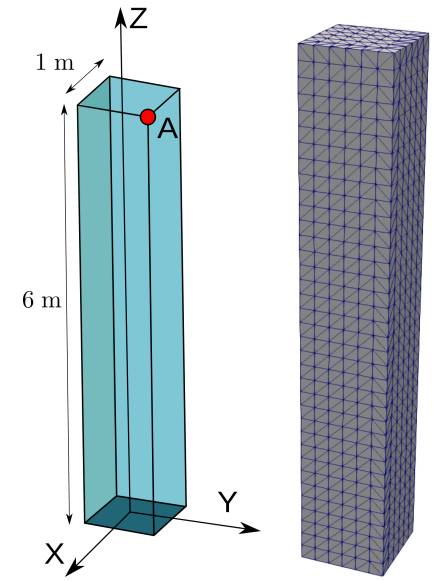

(a) Geometry **(b)** Mesh

Figure 3.21: Bending Beam. Geometry (3.21a) and tetrahedral structured mesh (3.21b).

A Mooney-Rivlin material with initial density $\rho_0 = 1.1 \times 10^3$ kg/m^3 and material parameters $\alpha_1 = 2.69$ MPa and $\alpha_2 = 0.142$ MPa is considered. In order to avoid unphysical modes appearing from the time integration scheme, we have selected the mildly-dissipative BDF2 time integrator with time step $\Delta t = 0.01$ s.

The main goal of this example is to show that our stabilized mixed formulation works properly in bending dominated scenarios and in 3D cases. For this reason, we have selected 3 different structured linear tetrahedral meshes (as the one shown in Fig. 3.21b), specified in Table 3.2.

Mesh	Number of elements
1	$6 \times 6 \times 36 \times 6$
2	$8 \times 8 \times 48 \times 6$
3	$12 \times 12 \times 72 \times 6$

Table 3.2: Bending Beam. Different mesh and number of elements.

Let us start showing some interesting properties about the three-field mixed $\mathbf{u}p\mathbf{S}'$ formulation presented here with respect to the classical displacement-based formulation [9] (from

[9]: Bonet et al. (1997), *Nonlinear Continuum mechanics for finite element analysis*

now on named as **u** formulation). To do so, let us consider the bending beam problem for several compressible regimes. We consider 3 different scenarios: $\nu = 0.2$, which reproduces a compressible material, $\nu = 0.49$, which mimics a nearly incompressible material and finally, we take $\nu = 0.5$ to reach the incompressible limit. All these cases are performed with Mesh 2. Fig. 3.22a displays the evolution in time up to $T = 3$ for the first component of the displacement field at point A. As expected, in the compressible regime ($\nu = 0.2$), both formulations exhibit very similar results.

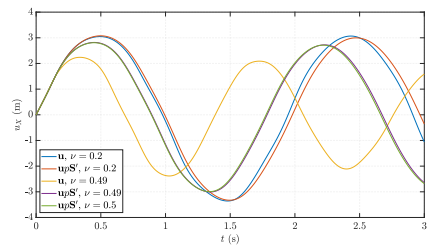

(a) $\mathbf{u}_X$ (m)

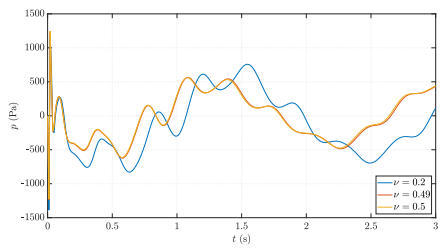

(b) p (Pa)

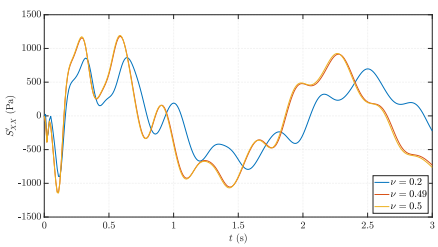

(c) $\mathbf{S}'_{XX}$ (Pa)

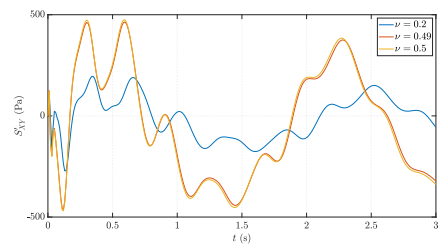

(d) $\mathbf{S}'_{XY}$ (Pa)

Figure 3.22: Bending beam. Comparison between **u** and **u***p***S′** formulations while increasing the incompressibility of the material at point A.

More interesting conclusions can be drawn when moving to the nearly incompressible regime ($\nu = 0.49$). In such case, the displacement-based formulation presents volumetric locking, which tends to show smaller displacements than the expected ones. On the contrary, the **u***p***S′** formulation is able to obtain proper solutions without presenting these instabilities. Furthermore, in the incompressible limit ($\nu = 0.5$), the **u***p***S′** formulation gives us precise solutions whereas the **u** formulation fails over the running stage. To end up this study, Figs. 3.22b-3.22c-3.22d show the pressure field and some components of the deviatoric PK2 stress tensor run with the **u***p***S′** formulation. As it can be clearly seen, well-defined solutions are obtained regardless the incompressibility of the material

and no oscillations can be appreciated even for this coarse mesh.

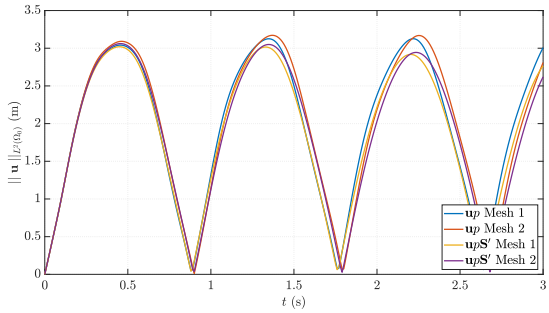

(a) $L^2(\Omega_0)$ norm displacement (m)

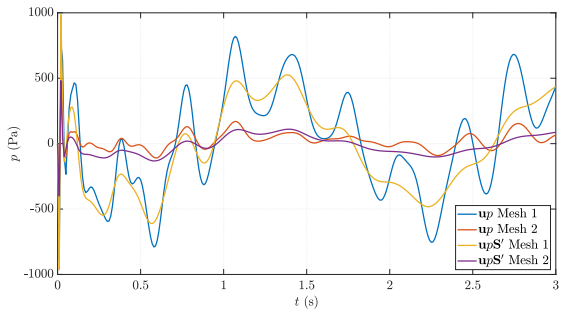

(b) Pressure (Pa)

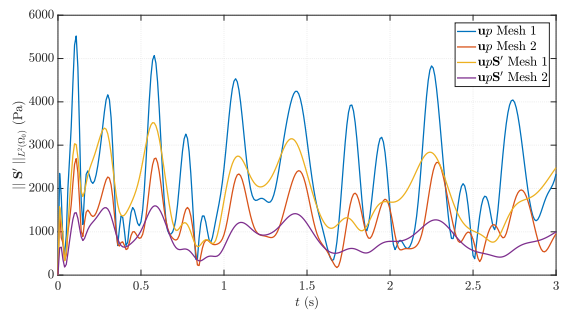

(c) $L^2(\Omega_0)$ norm deviatoric PK2 stress (Pa)

Figure 3.23: Bending beam. Evolution of point A along time for both $\mathbf{u}p$ and $\mathbf{u}p\mathbf{S}'$ formulations.

From now on, let us consider a fully incompressible material with $\nu = 0.5$. Fig. 3.23 presents the evolution of point A along time up to $T = 3$ s for both $\mathbf{u}p$ and $\mathbf{u}p\mathbf{S}'$ formulations. Figs. 3.23a-3.23b show the $L^2(\Omega_0)$ norm for the displacement field and the pressure field, respectively. As previously commented, both unknowns are considered as main variables of the problem. Very similar results can be observed for the displacement field when comparing both formulations for a

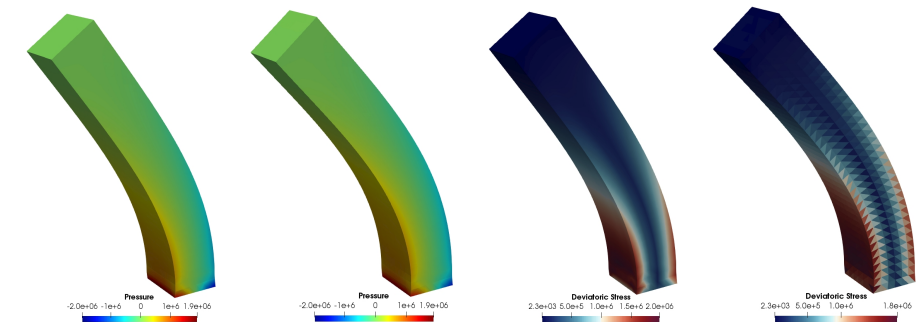

(a) $\mathbf{u}p\mathbf{S}'$ (b) $\mathbf{u}p$ (c) $\mathbf{u}p\mathbf{S}'$ (d) $\mathbf{u}p$

Figure 3.24: Bending beam. Comparison between $\mathbf{u}p\mathbf{S}'$ and $\mathbf{u}p$ at $t = 2.25$ s. Pressure field (Pa) and $L^2(\Omega_0)$ norm of the deviatoric PK2 stress (Pa)

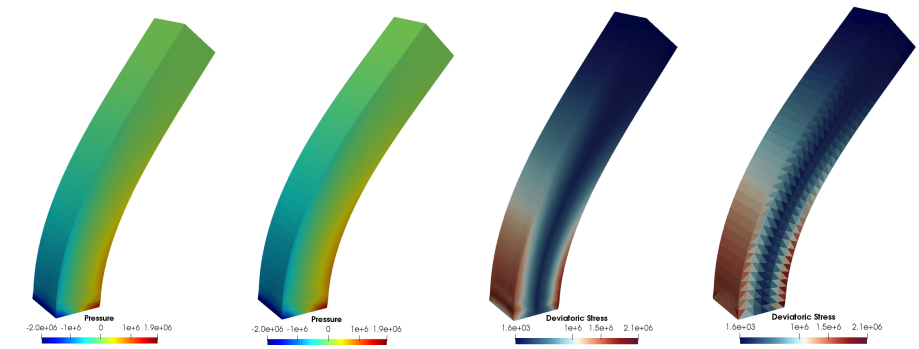

(a) $\mathbf{u}p\mathbf{S}'$ (b) $\mathbf{u}p$ (c) $\mathbf{u}p\mathbf{S}'$ (d) $\mathbf{u}p$

Figure 3.25: Bending beam. Comparison between $\mathbf{u}p\mathbf{S}'$ and $\mathbf{u}p$ at $t = 3$ s. Pressure field (Pa) and $L^2(\Omega_0)$ norm of the deviatoric PK2 stress (Pa)

fixed mesh. Despite the fact that the pressure field is a master field for both formulations, it turns out that more accurate results are obtained for the $\mathbf{u}p\mathbf{S}'$ formulation for a fixed mesh due to the capability of the method to capture stress concentrations better than the $\mathbf{u}p$ formulation. It is interesting to remark, that the observed behavior seems to be more dissipative in the three-field formulation. This indicates that including the deviatoric PK2 stress tensor as unknown of the problem in the $\mathbf{u}p\mathbf{S}'$ formulation both enhances the accuracy of the solution and its energy dissipation rate. On the contrary the $\mathbf{u}p$ formulation shows a less optimal dissipative behavior for the same mesh. Furthermore, Fig. 3.23c presents the evolution for the $L^2(\Omega_0)$ norm for the deviatoric PK2 stress field. As expected, for a fixed mesh, more accurate results are obtained when introducing the deviatoric PK2 stresses $\mathbf{S}'$ as an extra unknown of the problem in the three-field formula-

tion.

For the sake of thoroughness, we show in Figs. 3.24-3.25 the deformed beam at $t = 2.25$ s and at $t = 3$ s, respectively run with Mesh 1. First of all, we can observe that very similar deformations and pressure fields are appreciated for both formulations. Finally, regarding the deviatoric PK2 stress tensor, one can see the gain of accuracy in this field for the $\mathbf{u}p\mathbf{S}'$ formulation by including this field as primary unknown of the problem instead of computing it from the displacement derivatives.

Twisting column

As a final example, we compute again the already presented twisting column test. The initial geometry of the column is the same as the one shown in Fig. 3.21a. We consider stress free conditions and zero displacement initial conditions are applied on the corresponding boundaries. In order to make the column twist, we apply an initial sinusoidal velocity field:

$$\mathbf{v}^0(X,Y,Z) = \omega \sin\left(\frac{\pi Z}{12}\right)(Y,-X,0)^T \quad \text{m/s} \tag{3.122}$$

where $\omega = 100$ rad/s. The material is considered to be Neo-Hookean with initial density $\rho_0 = 1.1\times10^3$ kg/m^3, shear modulus $\mu = 5.7\times10^6$ Pa and Poisson ratio $\nu = 0.5$, to model a fully incompressible material. To define the deviatoric part of the material, we consider a Simo-Taylor law. Several levels of refinement have been considered to perform the computations. To construct the meshes, we select structured hexahedral elements. So we consider 3 different meshes. Mesh 1, with $6 \times 6 \times 36$ trilinear FEs, Mesh 2 with $16 \times 16 \times 96$ FEs and we end up with Mesh 3 with $32 \times 32 \times 192$ FEs. We select a time step $\Delta t = 0.002$ s.

First of all, let us perform some analysis for the different time integration schemes presented in Section 3.4. We run the same problem with different schemes and Mesh 2 and the main results can be seen in Fig. 3.26. On the one hand, left figures display the main unknowns up to $T = 0.5$ s. As it can be seen, both BDF schemes are capable of reproducing the whole event. However, BDF1 is only first-order accurate in time and it is highly dissipative, excessively mitigating physical oscillations. With regards to the BDF2 scheme, it is able to dissipate the nonphysical modes, which helps preventing

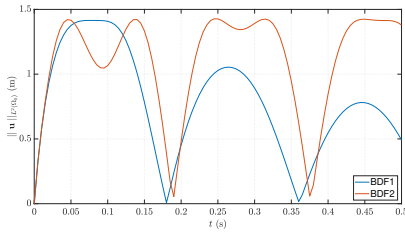

(a) Displacement BDF1 and BDF2

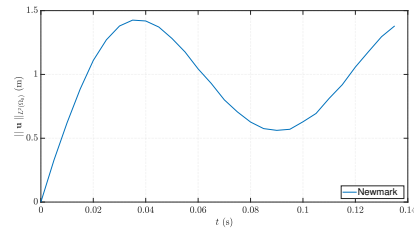

(b) Displacement Newmark

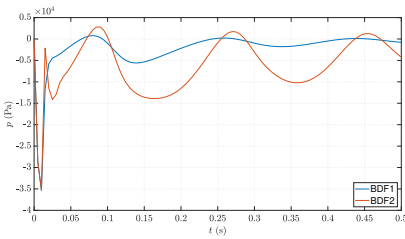

(c) Pressure BDF1 and BDF2

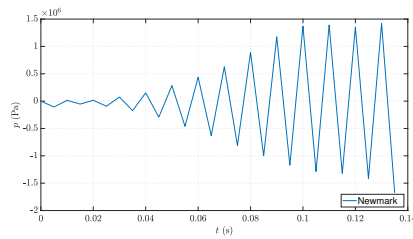

(d) Pressure Newmark

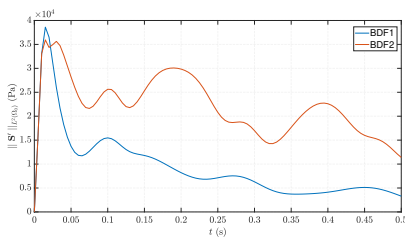

(e) Deviatoric PK2 stress BDF1 and BDF2

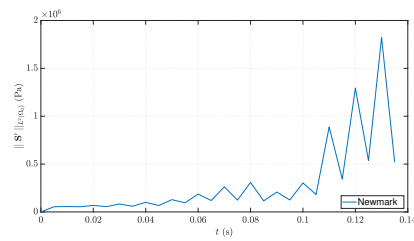

(f) Deviatoric PK2 stress Newmark

Figure 3.26: Twisting column. Time integrators comparison.

high frequency oscillations while keeping the second-order accuracy of the method. On the other hand, right figures illustrate the evolution obtained with a Newmark scheme for $\beta = \frac{1}{4}$ and $\gamma = \frac{1}{2}$, which results in a second-order scheme in time. This method does not introduce any numerical dissipation, and therefore, it does not eliminate high frequency nonphysical oscillations.

Next, let us fix BDF2 as time integration scheme and perform some comparisons between the $\mathbf{u}p$ and the $\mathbf{u}p\mathbf{S}'$ formulations. Fig. 3.27 shows the evolution of point A up to $T = 0.5$ s. In Fig. 3.27a we can observe a comparison for the displacement field. As expected, both formulations show very similar results, which become closer upon mesh refinement. Moving to the pressure field in Fig. 3.27b, one can see that for a fixed mesh, similar evolutions are obtained but the $\mathbf{u}p\mathbf{S}'$ formulation gives more accurate results taking into

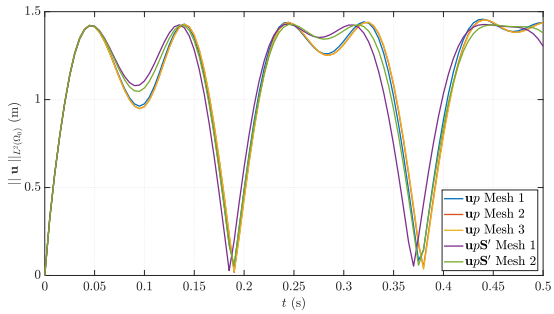

(a) $L^2\,(\Omega_0)$ norm displacement (m)

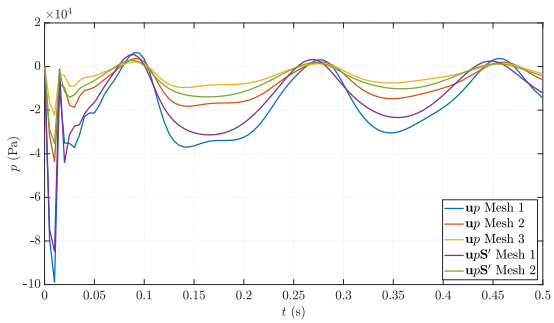

(b) Pressure

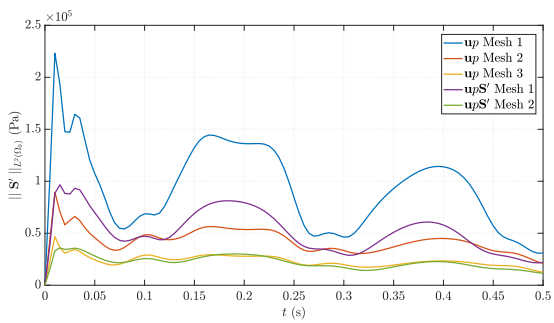

(c) $L^2\,(\Omega_0)$ norm deviatoric PK2 stress (Pa)

Figure 3.27: Twisting column. Evolution at point A.

account the evolution when refining the mesh. More interesting remarks can be made for the deviatoric PK2 stress tensor in Fig 3.27c. As it can be clearly appreciated, for a fixed mesh the three-field formulation attains more accurate results than the two-field version of the problem. In fact, we can observe that we need always an extra level of refinement for the $\mathbf{u}p$ formulation to be able to achieve the same accuracy as the one given by the $\mathbf{u}p\mathbf{S}'$ formulation.

To complete this example, Figs. 3.28-3.29 display the evolu-

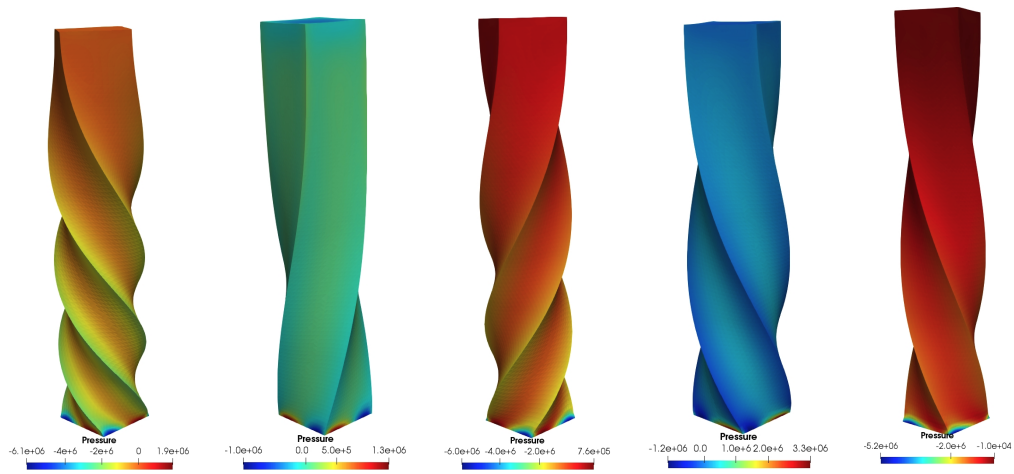

(a) 0.1 s **(b)** 0.2 s **(c)** 0.3 s **(d)** 0.4 s **(e)** 0.5 s

Figure 3.28: Twisting column. Deformation and Pressure field (Pa) along time.

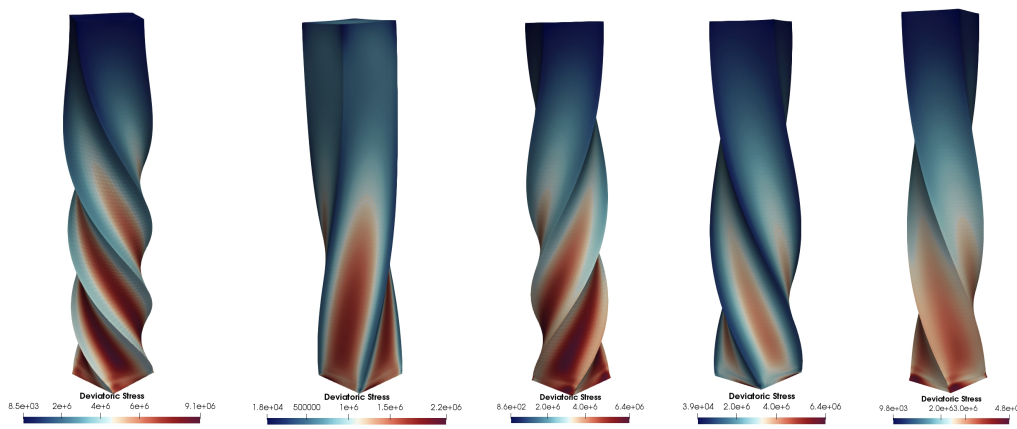

(a) 0.1 s **(b)** 0.2 s **(c)** 0.3 s **(d)** 0.4 s **(e)** 0.5 s

Figure 3.29: Twisting column. Deformation and $L^2(\Omega_0)$ norm deviatoric PK2 stress (Pa) along time.

tion of the deformation for the twisting column at different stages of the problem with Mesh 2. As it can be observed, the problem is well-captured, and no numerical oscillations can be seen neither for the pressure field nor for the deviatoric PK2 stress tensor. Let us remark, once more, the capability of the formulation to capture stress concentrations, in this case, placed at the clamped face of the twisting column.

3.7 Conclusions

In this chapter we have presented two different stabilized FE mixed formulations in finite strain solid dynamics when considering nearly and fully incompressible materials.

On the one hand, in Section 3.5 we have described a new simple stabilized two-field FEM for the study of solid dynamics when considering nearly and fully incompressible materials. The point of departure is the splitting of the Cauchy stress tensor into deviatoric and spherical components, which then translates into a splitting of the PK2 stress tensor.

Regarding the constitutive law, we have presented a formulation which works properly for any hyperelastic material model in which the strain energy function can be decomposed in deviatoric and volumetric parts, the latter in terms of the bulk modulus, κ. We have taken advantage of this decomposition to obtain a constitutive law for the pressure from the volumetric part. This law is formulated properly to obtain a simple way to impose the incompressiblity of the material automatically. The resulting equation has been added to the momentum equation to obtain a monolithic system of equations for the displacement/pressure pair.

With regards to the time integration scheme, we have shown that although any time integrator can be applied, implicit high-frequency dissipation time integration schemes are more suitable. To avoid pressure fluctuations of our solution along time, high-frequency dissipation schemes are recommended.

Concerning the computational cost of the method, we have observed that the methods proposed display quadratic nonlinear convergence, as it is expected from the implementation of a Newton-Raphson iterative procedure. The number of unknowns is only increased by one per each node with respect to the classical irreducible displacement-based formulation, which is the minimum to be able to enforce incompressibility.

On the other hand, in Section 3.6 we have described a new stabilized FEM for stress accurate analysis in finite strain solid dynamics when considering nearly and fully incompressible materials.

To design a FE technology with a high degree of accuracy of the stress field, the constitutive law for deviatoric stresses is

added to the system to obtain a monolithic system of equations for the displacement/pressure/deviatoric stress formulation. The presented three-field approach is able to deal with any hyperelastic material, including fully incompressible cases.

We have proposed several stabilization techniques based on the decomposition of the unknowns into FE scales and SGSs. Unlike the standard VMS stabilization technique, we have proposed to use the OSGS formulation. All stabilization techniques are able to circumvent the compatibility restrictions on the interpolation functions among the primary unknowns of the problem. In this approach the SGS space is supposed to be perpendicular to the FE one. As shown in the numerical examples, this stabilization exhibits better accuracy than the classical ASGS method for a fixed mesh. Furthermore, the proposed schemes shows the desired rate of convergence upon mesh refinement regardless the stabilization technique. We have shown also that the approximation of considering the SGSs to be modeled as bubble functions does not pollute the solution. It is interesting to remark that the S-OSGS stabilization technique allows us to obtain well-defined solutions and to neglect terms that do not contribute to stability. This methods turns out to be more robust for solving problems when large stress gradients are present. Likewise, for the examples we have considered, we have been able to assume quasi-static SGSs, although dynamic SGSs might need to be considered if very small time step sizes are used.

Concerning the computational cost of the method, we have observed that the proposed methods display quadratic nonlinear convergence regardless the stabilization technique, as it is expected from the implementation of a Newton–Raphson iterative procedure. The proposed three-field formulation is convergent upon mesh refinement, virtually free of any volumetric or shear locking. The technology is suitable for engineering applications in which a higher accuracy of stresses is needed. A comparison with the two-field formulation (displacement/pressure) is also carried out. Results clearly show that both the $\mathbf{u}p\mathbf{S}'$ and the $\mathbf{u}p$ formulations deal appropriately with the incompressibility constraint but the three-field formulation exhibits a higher accuracy in the stress field, even for very coarse meshes.

Topology optimization of incompressible structures

4

4.1 Introduction

Structural topology optimization (TO) aims to find the optimal layout of material within a design domain for a given set of boundary conditions such that the resulting material distribution meets a set of performance targets [79]. Several types of TO methodologies exist, such as density-based methods which include the popular SIMP technique [80, 81], hard-kill methods [82] and boundary variation methods [83], among others [84, 85]. A relatively new approach for this kind of problem is based on the topological derivative (TD) concept [2]. This derivative measures the sensitivity of a given shape functional with respect to an infinitesimal singular domain perturbation and it has become a very powerful tool due to the fact that it can be used as a steepest-descent direction in an optimization process [86–89].

An incompressible material is understood as one which keeps its volume constant throughout a motion. In many cases, this is a common idealization and accepted assumption, often invoked in continuum and computational mechanics. Numerous polymeric materials can sustain finite strains without noticeable volume changes. Furthermore, many biological materials and several types of soils can be modeled as nearly or fully incompressible [90].

In small strain solid mechanics problems, standard irreducible low order FEs are typically preferred [20]. *Standard irreducible* means that only the displacement field is considered as the primary unknown of the problem and all other fields, such as stress and strain fields, are obtained a posteriori. Unfortunately, this approach performs poorly in nearly and fully incompressible scenarios: volumetric and shear locking, pressure fluctuations and poor performance in bending dominated situations are some of the effects that can be observed [41].

To overcome these problems an approach which originated in fluid mechanics can be adapted. When considering a static, incompressible, infinitesimal strain case of the solid mechanics problem, we obtain an elliptic problem which is identical to the formulation of the Stokes problem in fluid mechanics [24, 44]. It is therefore reasonable to convey the mixed

[79]: M.P.Bendsøe et al. (2013), *Topological Optimization: Theory*

[80]: M.P.Bendsøe et al. (1988), "Generating optimal topologies in structural design using a homogenization method"

[81]: Ortigosa et al. (2020), "A stabilisation approach for topology optimisation of hyperelastic structures with the SIMP method"

[82]: X.Huang et al. (2010), "A further review of ESO type methods for topology optimization"

[83]: Dijk et al. (2013), "Level-set methods for structural topology optimization: a review"

[84]: J.D.Deaton et al. (2014), "A survey of structural and multidisciplinary continuum topology optimization: post 2000"

[85]: Ortigosa et al. (2019), "A new stabilisation approach for level-set based topology optimisation of hyperelastic materials"

[2]: A.A.Novotny et al. (2013), *Topological Derivatives in Shape Optimization*

[86]: Amstutz et al. (2006), "A new algorithm for topology optimization using a level-set method"

[87]: J.Baiges et al. (2019), "Large-scale stochastic topology optimization using adaptive mesh refinement and coarsening through a two-level parallelization scheme"

[88]: A.A.Novotny et al. (2019), "Topological Derivatives of Shape Functionals. Part I: Theory in Singularly Perturbed Geometrical Domains"

[89]: J.Oliver et al. (2019), "Variational approach to relaxed topological optimization: Closed form solutions for structural problems in a sequential pseudo-time framework"

[90]: L.R.G.Treloar (1975), *The Physics of Rubber Elasticity*

[20]: X.Oliver et al. (2017), *Continuum Mechanics for Engineers. Theory and Problems, 2nd edition*

velocity/pressure approach, used in fluid mechanics to the solid mechanics problem – becoming the two-field mixed displacement/pressure approach [45]. This approach led to the extension of different implementations in the field of fluid mechanics to the solid mechanics area. See for instance [10, 11, 48, 91], a set of works where the incompressible nonlinear material problem is stabilized using the variational multiscale method. Note that in the cited papers the orthogonal subscales method [13, 25] is used, which is a variant of the original stabilization method proposed in [6]. These works, in which both strain/displacement as well as stress/displacement pairs are used as primary variables, demonstrate the good performance of mixed FEs in solid mechanics. By using more than one primary unknown, the number of unknowns per node is considerably increased – especially when considering stresses or strains – but they also increase the accuracy notably. Furthermore, in [27] the idea of using displacement/pressure/stress or displacement/pressure/strain formulations, proposed in [26], was tested and seen to be very effective when solving incompressible cases in which also accurate results for the stress and strain field are required.

To the best of our knowledge, only few studies exist which face the TO problem of incompressible materials. In [92, 93], mixed formulations with very specific interpolation schemes for the elements are applied with a class of SIMP interpolations [94] for both the bulk and shear modulus. The subsequent optimization problem is solved using the method of moving asymptotes [95]. Further, [96] proposes the scaled boundary finite element method (SBFEM) formulation to avoid the inf-sup condition for the mixed displacement/pressure problem and applies the moving iso-surface threshold method (MIST) to solve the TO problem. Finally, in [97] a density-based TO problem is proposed for several material interpolations and by also using the mixed displacement/pressure formulation for nearly incompressible materials.

In the present work, we favor using the TD concept in combination with a level-set method to address the TO problem. However, in the context of structural topology design, the TD has been only used as a descent direction utilizing the classical displacement-based formulation [98]. This approach is therefore limited to compressible materials. Considering nearly and fully incompressible material behavior, both the formulation and the TD expression become singular. We overcome this problem by introducing the deviatoric/volu-

[41]: T.J.R.Hughes (1987), *The Finite Element Method: Linear Static and Dynamic Finite Element Analysis*

[24]: Codina (2001), "A stabilized finite element method for generalized stationary incompressible flows"

[44]: Hughes et al. (1986), "A new finite element formulation for computational fluid dynamics: V. Circumventing the babuška-brezzi condition: a stable Petrov-Galerkin formulation of the stokes problem accommodating equal-order interpolations"

[45]: Franca et al. (1988), "A new family of stable elements for nearly incompressible elasticity based on a mixed Petrov-Galerkin finite element formulation"

[10]: Cervera et al. (2010), "Mixed Stabilized Finite Element Methods in Nonlinear Solid Mechanics. Part I: Formulation"

[11]: Cervera et al. (2010), "Mixed Stabilized Finite Element Methods in Nonlinear Solid Mechanics. Part II: Strain Localization"

[48]: Chiumenti et al. (2002), "A stabilized formulation for incompressible elasticity using linear displacement and pressure interpolations"

[91]: Castañar et al. (2020), "A stabilized mixed finite element approximation for incompressible finite strain solid dynamics using a total Lagrangian formulation"

[13]: Codina (2002), "Stabilized finite element approximation of transient incompressible flows using orthogonal subscales"

[25]: Codina (2000), "Stabilization of incompressibility and convection through orthogonal subscales in finite element methods"

[6]: Hughes et al. (1998), "The variational multiscale method - A paradigm for computational mechanics"

[27]: Chiumenti et al. (2015), "A mixed three-field FE formulation for stress accurate analysis including the incompressible limit"

metric split, as presented in [27], thus obtaining a mixed formulation. Following this approach, the present work proposes a new expression for the split TD which allows us to compute the correct TD for incompressible materials. Together with a level-set method, this approach is used to obtain optimal designs.

This chapter is organized as follows. In Section 4.2 a new TD expression is defined through the volumetric-deviatoric decomposition of the Polarization tensor and several numerical examples are presented and discussed to assess the present algorithm and to validate its performance for nearly and fully incompressible linear elastic materials. Next, in Section 4.3, an approximation for the TD for finite strain hyperelastic materials is applied to incompressible materials and several numerical examples are studied for such materials. In Section 4.4 some conclusions of the proposed TO formulations are drawn.

4.2 Topological-derivative based topology optimization in linear theory of elasticity

4.2.1 Setting of the problem

In the following, the TO problem is stated under the assumption of of linear elasticity. To do so, let us consider the system of equations for either the mixed $\mathbf{u}p$ formulation (2.29-2.30) or the $\mathbf{u}p\mathbf{e}$ formulation (2.48-2.50) presented in Chapter 2. Generally speaking, the aim is to obtain an optimal topology such that it minimizes a desired functional and satisfies particular constraints.

The description of the topology is determined by the characteristic function χ, defined as

$$\chi(\mathbf{x}) = \begin{cases} 1 & \mathbf{x} \in \Omega_s \\ 0 & \mathbf{x} \in \Omega_w \end{cases}, \tag{4.1}$$

where the domain Ω has been split into two parts, $\overline{\Omega} = \overline{\Omega_s \cup \Omega_w}$, $\Omega_s \cap \Omega_w = \emptyset$. The sub-domains Ω_s and Ω_w are made of different materials. The characteristic function is in charge of determining in the whole domain Ω what part corresponds to

[26]: R.Codina (2009), "Finite element approximation of the three field formulation of the Stokes problem using arbitrary interpolations"

[92]: O.Sigmund et al. (2007), "Topology optimization using a mixed formulation: An alternative way to solve pressure load problems"

[93]: M.Bruggi et al. (2007), "Topology optimization of incompressible media using mixed finite elements"

[94]: M.Stolpe et al. (2001), "An alternative interpolation scheme for minimum compliance optimization"

[95]: K.Svanberg (1987), "The method of moving asymptotes-a new method for minimum compliance optimization"

[96]: C.Li et al. (2016), "Topology optimization of incompressible materials based on the mixed SBFEM"

[97]: G.Zhang et al. (2018), "Topology optimization with incompressible materials under small and finite deformations using mixed u/p elements"

[98]: A.A.Novotny et al. (2019), "Topological Derivatives of Shape Functionals. Part II: First-Order Method and Applications"

[27]: Chiumenti et al. (2015), "A mixed three-field FE formulation for stress accurate analysis including the incompressible limit"

either material. Such kind of problems are typically termed bi-material TO problems. The material corresponding to the domain Ω_w exhibits a very small stiffness approximating the absence of material. The material parameters of the strong domain Ω_s are denoted by E_s and ν_s and the parameters of the weak domain Ω_w are considered as $E_w = \gamma E_s$ and ν_w, where γ stands for the jump of stiffness. Note that $\gamma > 0$ is a parameter, small enough for modeling void regions and large enough to entail invertibility properties to the stiffness matrix. The characteristic function allows us to rewrite the deviatoric constitutive tensor defined in the whole domain as

$$\mathbb{C}^{\text{dev}}(\chi) = \chi \mathbb{C}_s^{\text{dev}} + (1-\chi)\mathbb{C}_w^{\text{dev}}, \tag{4.2}$$

where $\mathbb{C}_s^{\text{dev}}$ and $\mathbb{C}_w^{\text{dev}}$ are the fourth order deviatoric constitutive tensors of the stiff and the soft materials, respectively.

To obtain structures with minimum flexibility, a functional $\mathcal{J}(\chi)$ is minimized. In TO problems this functional is usually referred to as the *total potential energy functional* and is defined as

$$\begin{aligned}\mathcal{J}(\chi) = &\frac{1}{2}\int_\Omega \boldsymbol{\sigma}(\chi,\mathbf{x}) : \boldsymbol{\varepsilon}(\chi,\mathbf{x})\ d\Omega \\ &- \int_\Omega \rho\mathbf{b}\cdot\mathbf{u}(\chi,\mathbf{x})\ d\Omega - \int_{\Gamma_N} \mathbf{t}_N\cdot\mathbf{u}(\chi,\mathbf{x})\ d\Gamma.\end{aligned} \tag{4.3}$$

The whole TO problem is then formulated as the minimization of the total potential energy functional subjected to the maximum material allowed, which is written as follows

$$\begin{aligned}\min_{\chi\in\mathbb{X}_L} \mathcal{J}(\chi) = &\frac{1}{2}\int_\Omega \boldsymbol{\sigma}(\chi,\mathbf{x}) : \boldsymbol{\varepsilon}(\chi,\mathbf{x})\ d\Omega \\ &- \int_\Omega \rho\mathbf{b}\cdot\mathbf{u}(\chi,\mathbf{x})\ d\Omega - \int_{\Gamma_N} \mathbf{t}_N\cdot\mathbf{u}(\chi,\mathbf{x})\ d\Gamma \\ \text{s.t.}: \mathcal{A}(\mathbf{U},\mathbf{V}) &= \mathcal{F}(\mathbf{V}) \quad \forall\mathbf{V}\in\mathbb{W}_0, \\ \mathbb{X}_L &= \left\{\chi\in L^\infty(\Omega,\{0,1\}), \int_\Omega \chi(\mathbf{x})\ d\Omega = L|\Omega|\right\},\end{aligned} \tag{4.4}$$

where $\mathbb{X}_L$ is the feasible domain restricted to a volume constraint denoted as a fraction $0 < L < 1$ of the domain Ω and $\mathcal{A}$ and $\mathcal{F}$ are the forms which have been obtained in Chapter 2 depending upon the formulation defined as (2.34-2.35) for the $\mathbf{u}p$ formulation and as (2.54-2.55) for the $\mathbf{u}p\mathbf{e}$ formulation.

4.2.2 Material interpolation

In the traditional bi-material TD-based TO approach, the Poisson ratio remains constant, $\nu = \nu_s = \nu_w$, while only the Young modulus is modified depending on the value of the characteristic function χ. For compressible materials, this approach ensures that the soft material is not notably contributing to the stiffness of the structure. However, when dealing with incompressible materials, this leads to spurious solutions, because bubbles of weak material are still infinitely stiff with respect to volumetric deformations. To avoid this, we consider the soft material as compressible, which means $\nu_w < 0.5$. In this work, we consider that both Young modulus and Poisson ratio are modified depending on the value of the characteristic function.

Remark 4.2.1 Over the last years, a physical interpretation is given to elements cut by the discontinuity in χ in several works [99]. They are directly related with composite materials composed with strong and weak material volume fraction. Furthermore, some physical restrictions such as the Hashin-Shtrikman bounds [100] must be fulfilled.

[99]: A.Ferrer (2019), "SIMP-ALL: A generalized SIMP method based on the topological derivative concept"
[100]: M.P.Bendsøe et al. (1999), "Material interpolation schemes in topology optimization"

4.2.3 Topology optimization using the topological derivative concept

Several approaches exist to solve the TO problem (4.4) for linear elastic materials. In this work we use the TD concept [88] together with a level-set approach in order to advance to the optimal topology.

[88]: A.A.Novotny et al. (2019), "Topological Derivatives of Shape Functionals. Part I: Theory in Singularly Perturbed Geometrical Domains"

The TD is a measurement of the sensitivity of a given functional with respect to the apparition of an infinitesimal inclusion in a given point of the domain of interest. In the problem studied, the objective is to obtain the sensitivity of the functional $\mathcal{J}$ already defined in Eq. (4.3). The TD $\mathcal{D}_T$ of this functional at a point $\mathbf{x}$ can be formally computed as

$$\mathcal{D}_T \mathcal{J}(\chi, \mathbf{x}) = \boldsymbol{\varepsilon}(\chi, \mathbf{x}) : \mathbb{P} : \boldsymbol{\sigma}(\chi, \mathbf{x}) + (1-\gamma)\rho \mathbf{b} \cdot \mathbf{u}(\chi, \mathbf{x}), \quad (4.5)$$

using the *topological-shape sensitivity analysis* proposed in [98]. In the given equation, $\mathbb{P}$ stands for the fourth order *Pólya-Szegő* polarization tensor. In this work, the classical Polarization tensor expression, in which the same Poisson

[98]: A.A.Novotny et al. (2019), "Topological Derivatives of Shape Functionals. Part II: First-Order Method and Applications"

coefficient is assumed for both materials, is not suitable (see Section 4.2.2). According to [101], the Polarization tensor is defined as

$$\mathbb{P} = \frac{1}{2}\Delta\mathbb{C} : \left\{\mathbb{C}_e^{-1} + \mathbb{C}_i^{-1} : \mathbb{T}\right\}, \tag{4.6}$$

where $\mathbb{C}_i$ accounts for the constitutive tensor of the inclusion and $\mathbb{C}_e$ for the matrix material. Furthermore $\Delta\mathbb{C} \coloneqq \mathbb{C}_i - \mathbb{C}_e$ and $\mathbb{T}$ is a 4^{th}-order isotropic tensor called the Eshelby tensor, originating from Eshelby's Theorem [102, 103]. The Eshelby tensor allows us to relate the stresses in the inclusion with the ones from the matrix material. To build the Eshelby tensor $\mathbb{T}$, it is necessary to solve an equilibrium equation in linear elasticity. Two different bodies are considered (inclusion and matrix) with different Young modulus and Poisson ratios. It must be imposed that very far from the inclusion, the stresses cancel out for the matrix. Then, we impose the Eshelby theorem for the inclusion material, which asserts that the strain field inside the inclusion is constant if the loading at infinity is constant (zero in this case). Once the boundary conditions are imposed in both solids, the transmission conditions across the interface of the inclusion and the matrix must be satisfied. Regarding the stresses, the exterior problem is defined such that the jump of the traction across the interface must be equal to the normal component of the given stress tensor. Regarding the transmission conditions on displacements, we must ensure that the jump of the strains across the boundary must be zero for the inclusion. This problem is solved via symbolic calculus. Once the Eshelby tensor is obtained, the computation of the Polarization tensor is straightforward (see Appendix A to see the whole procedure).

[101]: S.M.Giusti et al. (2016), "Topological sensitivity analysis in heterogeneous anisotropic elasticity problem. Theoretical and computational aspects"

[102]: J.D.Eshelby (1957), "The determination of the elastic field of an ellipsoidal inclusion, and related problems"
[103]: J.D.Eshelby (1959), "The elastic field outside an ellipsoidal inclusion, and related problems"

Considering a plane strain scenario, the Polarization tensor is computed as

$$\mathbb{P} = -\frac{1}{2}(1+\beta)\left\{\frac{\tau_1 - \gamma}{\beta\gamma + \tau_1}\mathbb{I} - \frac{1}{4}\left(\frac{\alpha(\gamma - \tau_1\tau_2)}{\alpha\gamma + \tau_1\tau_2} + \frac{2(\tau_1 - \gamma)}{\beta\gamma + \tau_1}\right)\mathbf{I}\otimes\mathbf{I}\right\}, \tag{4.7}$$

where

$$\alpha = \frac{1}{1-2\nu_e},\ \beta = 3 - 4\nu_e,\ \tau_1 = \frac{1+\nu_i}{1+\nu_e} \text{ and } \tau_2 = \frac{1-2\nu_i}{1-2\nu_e}. \tag{4.8}$$

Considering a plane stress scenario on the other hand,

$$\mathbb{P} = -\frac{1}{2}(1+\beta)\left\{\frac{\tau_1 - \gamma}{\beta\gamma + \tau_1}\mathbb{I}\right.$$

$$-\frac{1}{4}\left(\frac{\gamma\left(\alpha+\tau_2-1\right)-\alpha\tau_1\tau_2}{\tau_1\left(\alpha\gamma+\tau_2\right)}+\frac{2\left(\tau_1-\gamma\right)}{\beta\gamma+\tau_1}\right)\mathbf{I}\otimes\mathbf{I}\Bigg\} \tag{4.9}$$

and

$$\alpha=\frac{1+\nu_\mathrm{e}}{1-\nu_\mathrm{e}},\ \beta=\frac{3-\nu_\mathrm{e}}{1+\nu_\mathrm{e}},\ \tau_1=\frac{1+\nu_\mathrm{i}}{1+\nu_\mathrm{e}}\ \text{and}\ \tau_2=\frac{1-\nu_\mathrm{i}}{1-\nu_\mathrm{e}}. \tag{4.10}$$

Independently from the strain/stress assumption, the jump of stiffness is defined as $\gamma = E_\mathrm{w}/E_\mathrm{s}$, while ν_e and ν_i are the Poisson ratios of the matrix and inclusion material.

Remark 4.2.2 If the same Poisson ratio is used for both materials $\nu_\mathrm{s} = \nu_\mathrm{w}$, and therefore, $\nu_\mathrm{i} = \nu_\mathrm{e}$, the Polarization tensors (4.7) and (4.9) reduce to

$$\mathbb{P}=-\frac{1}{2}\frac{1-\gamma}{1+\beta\gamma}\left\{(1+\beta)\,\mathbb{I}+\frac{1}{2}\left(\alpha-\beta\right)\frac{1-\gamma}{1+\alpha\gamma}\mathbf{I}\otimes\mathbf{I}\right\}, \tag{4.11}$$

which is the formulation widely used in structural topological design [104].

[104]: C.G.Lopes et al. (2015), "Topological Derivative-based Topology Optimization of Structures Subject to Multiple Load-cases"

In this work, the isotropic 2D plane strain polarization tensor has been used as an approximation for the 3D polarization tensor. By using this approximation, infinitesimal cylindrical inclusions are considered instead of spherical ones in the derivation of the TD. Although spherical inclusions would be more appropriate, experience shows that infinitesimal cylindrical inclusions behave properly in 3D examples [87].

[87]: J.Baiges et al. (2019), "Large-scale stochastic topology optimization using adaptive mesh refinement and coarsening through a two-level parallelization scheme"

Considering a domain with weak and strong material, we can expect the following two situations:

1. An inclusion of the weak material in the strong material ($\mathbf{x} \in \Omega_\mathrm{s}$),
2. An inclusion of the strong material in the weak material ($\mathbf{x} \in \Omega_\mathrm{w}$).

Consequently, rewriting the polarization tensor as $\mathbb{P}\left(\alpha,\beta,\gamma,\tau_1,\tau_2\right)$, both cases share the following properties

$$\mathbb{P}=\begin{cases}\mathbb{P}_\mathrm{s}:=\mathbb{P}\left(\alpha_\mathrm{s},\beta_\mathrm{s},\gamma,\tau_1,\tau_2\right) & \mathbf{x}\in\Omega_\mathrm{s}\\ \mathbb{P}_\mathrm{w}:=\mathbb{P}\left(\alpha_\mathrm{w},\beta_\mathrm{w},\frac{1}{\gamma},\frac{1}{\tau_1},\frac{1}{\tau_2}\right) & \mathbf{x}\in\Omega_\mathrm{w}\end{cases}. \tag{4.12}$$

where α_s and β_s are the Polarization parameters evaluated for ν_s and α_w and β_w evaluated for ν_w.

The properties of the polarization tensor ensure that

$$\mathscr{D}_T\mathscr{J}(\chi,\mathbf{x}) = \begin{cases} \boldsymbol{\varepsilon}(\chi,\mathbf{x}) : \mathbb{P}_s : \boldsymbol{\sigma}(\chi,\mathbf{x}) \\ +(1-\gamma)\rho\mathbf{b}\cdot\mathbf{u}(\chi,\mathbf{x}) \leq 0 \quad \forall \mathbf{x}\in\Omega_s \\ \boldsymbol{\varepsilon}(\chi,\mathbf{x}) : \mathbb{P}_w : \boldsymbol{\sigma}(\chi,\mathbf{x}) \\ +(1-\gamma)\rho\mathbf{b}\cdot\mathbf{u}(\chi,\mathbf{x}) \geq 0 \quad \forall \mathbf{x}\in\Omega_w \end{cases}. \tag{4.13}$$

We can now define a signed TD such that

$$\overline{\mathscr{D}_T\mathscr{J}}(\chi,\mathbf{x}) = \begin{cases} -\mathscr{D}_T\mathscr{J}(\chi,\mathbf{x}) & \mathbf{x}\in\Omega_s \\ \mathscr{D}_T\mathscr{J}(\chi,\mathbf{x}) & \mathbf{x}\in\Omega_w \end{cases}. \tag{4.14}$$

Let us now introduce the signed TD interpretation, which will be used in the subsequent sections of this work. For a given topology, computing the TD allows one to know, for each given spatial point, how the cost functional would change if the material switches. Once the optimal value for the characteristic function $\chi(\mathbf{x})$ has been reached, the following condition holds

$$\overline{\mathscr{D}_T\mathscr{J}}(\chi,\mathbf{x}) \geq \overline{\mathscr{D}_T\mathscr{J}}(\chi,\mathbf{Y}), \forall \mathbf{x}\in\Omega_s, \forall \mathbf{Y}\in\Omega_w. \tag{4.15}$$

Note that at the interface $\overline{\Omega_s}\cap\overline{\Omega_w}$, the TD has a jump, but the signed TD is continuous. Eq. (4.15) allows one to construct a level set function $\psi(\chi,\mathbf{x})$, which will implicitly characterize Ω_s and Ω_w. This level set function is defined as

$$\psi(\chi,\mathbf{x}) = \overline{\mathscr{D}_T\mathscr{J}}(\chi,\mathbf{x}) + \lambda, \tag{4.16}$$

where $\lambda\in\mathbb{R}$ is a scalar, responsible for ensuring that the volume restriction in Eq. (4.4) is fulfilled. The level-set function also allows us to characterize the descrption of the topology

$$\psi(\chi,\mathbf{x}) \begin{cases} > 0 & \mathbf{x}\in\Omega_s \\ < 0 & \mathbf{x}\in\Omega_w \end{cases}. \tag{4.17}$$

Furthermore, the level-set function allows us to keep a sharp interface when $\psi(\chi,\mathbf{x}) = 0$. The scalar λ can be computed by enforcing

$$\int_\Omega H(\psi(\chi,\mathbf{x}))\, d\Omega = L|\Omega|, \tag{4.18}$$

where H is the Heaviside step function

$$H(\psi) = \begin{cases} 1 & \text{if } \psi \geq 0 \\ 0 & \text{if } \psi < 0 \end{cases}. \tag{4.19}$$

From Eq. (4.17) and Eq. (4.19), it can be observed that for the solution of Eq. (4.4) there holds

$$\chi = H(\psi). \tag{4.20}$$

Remark 4.2.3 When considering the FE approximation of the problem, an inconsistency appears in the update of the level-set function in equation (4.16). According to expressions (4.7) and (4.9), the TD depends directly on the stresses and strains. Clearly, this kind of functions are not continuous which is, in fact, the requirement for updating the level-set function $\psi(\chi, \mathbf{x})$. As a remedy, an element-to-nodal regularization must be considered. The regularization is carried out by a projection onto the FE space (smoothing operation) but this results in a loss of a certain degree of accuracy. Nevertheless, the level-set updating (4.16) is now possible. In [105] a smoothing of the interface for projecting the TD onto the FE space is proposed, which allows one to still interpret the TD as an exact discrete gradient.

[105]: Amstutz et al. (2018), "A consistent relaxation of optimal design problems for coupling shape and topological derivatives"

4.2.4 Topological derivative for incompressible materials

Referring to expression (4.7), which is valid for both plane strain and 3D scenarios, we observe that the Polarization tensor becomes ill-defined due to the fact that when $\nu_e \to 0.5$, $\alpha = \frac{1}{1-2\nu_e} \to \infty$. It can be clearly seen that the Polarization tensor cannot be used to compute the TD for incompressible materials in both cases. In order to deal with nearly and fully incompressible materials we propose to apply the deviatoric-volumetric split introduced in Subsection 2.1.1 to the Polarization tensor as well. The volumetric and deviatoric counterparts of the Polarization tensor are

$$\mathbb{P}^{\text{vol}} = \mathbb{V} : \mathbb{P} = \frac{\alpha(1+\beta)}{8} \frac{\gamma - \tau_1\tau_2}{\alpha\gamma + \tau_1\tau_2} \mathbf{I} \otimes \mathbf{I}, \tag{4.21}$$

$$\mathbb{P}^{\text{dev}} = \mathbb{D} : \mathbb{P} = -\frac{1}{2} \frac{(1+\beta)(\tau_1 - \gamma)}{\tau_1 + \beta\gamma} \left\{ \mathbb{I} - \frac{1}{3} \mathbf{I} \otimes \mathbf{I} \right\}, \tag{4.22}$$

$$\mathbb{P} = \mathbb{P}^{\text{vol}} + \mathbb{P}^{\text{dev}}. \tag{4.23}$$

Next, we can use the Polarization tensor decomposition to compute the TD as

$$\begin{aligned}
\mathscr{D}_T\mathscr{J}(\chi,\mathbf{x}) = {} & \boldsymbol{\varepsilon}(\chi,\mathbf{x}) : \mathbb{P} : \boldsymbol{\sigma}(\chi,\mathbf{x}) + (1-\gamma)\rho\mathbf{b}\cdot\mathbf{u}(\chi,\mathbf{x}) \\
\overset{(4.23)}{=} {} & \boldsymbol{\varepsilon}(\chi,\mathbf{x}) : \left\{\mathbb{P}^{\mathrm{vol}} + \mathbb{P}^{\mathrm{dev}}\right\} : \boldsymbol{\sigma}(\chi,\mathbf{x}) \\
& + (1-\gamma)\rho\mathbf{b}\cdot\mathbf{u}(\chi,\mathbf{x}) \\
\overset{(2.13)}{=} {} & \boldsymbol{\varepsilon}(\chi,\mathbf{x}) : \left\{\mathbb{P}^{\mathrm{vol}} + \mathbb{P}^{\mathrm{dev}}\right\} : \{\mathbf{s}(\chi,\mathbf{x}) - p(\chi,\mathbf{x})\mathbf{I}\} \\
& + (1-\gamma)\rho\mathbf{b}\cdot\mathbf{u}(\chi,\mathbf{x}) \\
= {} & \boldsymbol{\varepsilon}(\chi,\mathbf{x}) : \mathbb{P}^{\mathrm{dev}} : \mathbf{s}(\chi,\mathbf{x}) \\
& - \boldsymbol{\varepsilon}(\chi,\mathbf{x}) : \mathbb{P}^{\mathrm{vol}} : p(\chi,\mathbf{x})\mathbf{I} + (1-\gamma)\rho\mathbf{b}\cdot\mathbf{u}(\chi,\mathbf{x}).
\end{aligned} \tag{4.24}$$

The last equation holds by imposing that the contraction between volumetric and deviatoric tensors is identically null. This fact allows to reduce the formulation further. It is worth to study the first two components of the decomposed TD (4.24) in detail. The first summand accounts for the TD due to deviatoric effects. By introducing the strain field decomposition (2.15) we can reduce it to

$$\begin{aligned}
\mathscr{D}_T^{\mathrm{dev}}\mathscr{J}(\chi,\mathbf{x}) &:= \boldsymbol{\varepsilon}(\chi,\mathbf{x}) : \mathbb{P}^{\mathrm{dev}} : \mathbf{s}(\chi,\mathbf{x}) \\
&= \left\{\frac{1}{3}e^{\mathrm{vol}}(\chi,\mathbf{x})\mathbf{I} + \mathbf{e}(\chi,\mathbf{x})\right\} : \mathbb{P}^{\mathrm{dev}} : \mathbf{s}(\chi,\mathbf{x}) \\
&= \mathbf{e}(\chi,\mathbf{x}) : \mathbb{P}^{\mathrm{dev}} : \mathbf{s}(\chi,\mathbf{x}).
\end{aligned} \tag{4.25}$$

The second summand in Eq. (4.24) accounts for the TD changes due to volumetric deformations. To solve the singularity which $\mathbb{P}^{\mathrm{vol}}$ still presents when dealing with nearly and fully incompressible materials, we need to introduce the pressure field as,

$$\begin{aligned}
\mathscr{D}_T^{\mathrm{vol}}\mathscr{J}(\chi,\mathbf{x}) &:= -\boldsymbol{\varepsilon}(\chi,\mathbf{x}) : \mathbb{P}^{\mathrm{vol}} : p(\chi,\mathbf{x})\mathbf{I} \\
&= -\frac{1}{3}e^{\mathrm{vol}}(\chi,\mathbf{x})\cdot p(\chi,\mathbf{x})\mathbf{I} : \mathbb{P}^{\mathrm{vol}} : \mathbf{I} \\
&\overset{(2.16)}{=} -\frac{1}{3}\nabla\cdot\mathbf{u}(\chi,\mathbf{x})\cdot p(\chi,\mathbf{x})\mathbf{I} : \mathbb{P}^{\mathrm{vol}} : \mathbf{I} \\
&\overset{(2.23)}{=} \frac{p(\chi,\mathbf{x})}{3\kappa_{\mathrm{e}}}\cdot p(\chi,\mathbf{x})\mathbf{I} : \mathbb{P}^{\mathrm{vol}} : \mathbf{I} \\
&= \left\{\frac{1}{3\kappa_{\mathrm{e}}}\mathbf{I} : \mathbb{P}^{\mathrm{vol}} : \mathbf{I}\right\} p^2(\chi,\mathbf{x}) \\
&:= \mathrm{P}^{\mathrm{vol}} p^2(\chi,\mathbf{x}),
\end{aligned} \tag{4.26}$$

where κ_e is the bulk modulus of the matrix material and $\mathrm{P}^{\mathrm{vol}}$ is defined as the volumetric Polarization parameter and it is expressed as

$$\mathrm{P}^{\mathrm{vol}} = \frac{1}{\kappa_e}\mathbf{I} : \mathbb{P}^{\mathrm{vol}} : \mathbf{I} = \frac{1+\beta}{3E_e}\frac{\gamma-\tau_1\tau_2}{\alpha\gamma+\tau_1\tau_2}. \tag{4.27}$$

By introducing the compressibility modulus κ_e in the volumetric part of the polarization tensor, we have solved the singularity that $\mathbb{P}^{\mathrm{vol}}$ is presenting.

Remark 4.2.4 In the incompressible limit, no volumetric changes should appear when both materials are incompressible. Therefore, the contribution to the TD made by $\mathrm{P}^{\mathrm{vol}}$ must be zero when $\nu = \nu_e = \nu_i = 0.5$. Indeed, we have that

$$\begin{aligned}\mathrm{P}^{\mathrm{vol}}\Big|_{\nu=0.5} &= \frac{1+\beta}{3E_e}\frac{\gamma-1}{\alpha\gamma+1} = \frac{4-4\nu}{3E_e}\frac{\gamma-1}{\frac{1}{1-2\nu}\gamma+1} \\ &= \frac{2}{3E_e}\frac{\gamma-1}{\frac{1}{0}\gamma+1} = 0\end{aligned} \tag{4.28}$$

Note that in this case, volumetric effects vanish and the TO problem is only driven by deviatoric changes.

Finally, the formula for the split TD, which is valid for nearly and fully incompressible materials and applicable in plane strain and 3D scenarios, is given as

Linear elasticity. Split topological derivative

$$\begin{aligned}\mathscr{D}_T\mathscr{J}(\chi,\mathbf{x}) = \mathbf{e}(\chi,\mathbf{x}) : \mathbb{P}^{\mathrm{dev}} : \mathbf{s}(\chi,\mathbf{x}) + \mathrm{P}^{\mathrm{vol}}p^2(\chi,\mathbf{x}) \\ + (1-\gamma)\rho\mathbf{b}\cdot\mathbf{u}(\chi,\mathbf{x}).\end{aligned} \tag{4.29}$$

Remark 4.2.5 It is worth pointing out the main differences between the two mixed formulations with regards to the split TD, shown in Eq. (4.29). When considering the $\mathbf{u}p$ formulation, both deviatoric stresses and strains are computed from the symmetric gradient of the displacements $\nabla^{\mathrm{s}}\mathbf{u}$, whereas when using the $\mathbf{u}p\mathbf{e}$ formulation, deviatoric stresses are now computed from deviatoric strains $\mathbf{e}$ which are an unknown of the problem. Therefore, the computation of the TD is expected to be more accurate.

4.2.5 Treatment of the interface elements

Let us discuss an issue related to the FE approximation of the problem. Interface elements belong partially to the strong and partially to the weak domain. These elements are therefore characterized by the material properties of both domains and special attention needs to be payed to the behavior of the TD in those elements. In order to obtain the correct combination of material properties, a homogenization technique is used.

Let us construct a conforming FE mesh $\mathscr{M}$, composed of N elements and let us also split the domain into three different sub-groups:

1. Elements which fully lie in the domain associated with the strong material $\mathscr{T}_\mathrm{s}$,
2. Elements which fully lie in the domain associated with the weak material $\mathscr{T}_\mathrm{w}$, and
3. Elements intersecting the interface, thus sharing both materials $\mathscr{T}^\Gamma$.

The description of the interface is based on the treatment of the characteristic function $\chi(\mathbf{x})$, which, in turn, is based on the treatment of the level-set function $\psi(\chi, \mathbf{x})$. For the description, two different approaches are commonly used in TO when using the TD: The *In-or-Out* approach and the P1-projection approach [86, 106]. In our work a third option, the continuous regularized characteristic function approach, is used.

[86]: Amstutz et al. (2006), "A new algorithm for topology optimization using a level-set method"
[106]: S.Amstutz et al. (2010), "Topological derivative for multi-scale linear elasticity models applied to the synthesis of microstructures"

Let us denote by K^Γ the volume of an interface element in $\mathscr{T}^\Gamma$. K_s^Γ and K_w^Γ are the subdivisions with strong and weak material obtained for that specific element when it is cut by the level-set function. Then we can define the volume fraction of stiff and soft materials as

$$\mathscr{V}_\mathrm{s} = \frac{K_\mathrm{s}^\Gamma}{K^\Gamma} \in (0,1) \quad \text{and} \quad \mathscr{V}_\mathrm{w} = \frac{K_\mathrm{w}^\Gamma}{K^\Gamma} = 1 - \mathscr{V}_\mathrm{s} \in (0,1)\,. \tag{4.30}$$

Furthermore we can redefine the regularized characteristic function as the volume fraction of the strong material, i.e.

$$\tilde{\chi}(\mathbf{x}) = \frac{K_\mathrm{s}^\Gamma}{K^\Gamma}, \quad \mathbf{x} \in K^\Gamma. \tag{4.31}$$

Note, that when the element fully lies in the domain, associated with the strong material $K_\mathrm{s}^\Gamma / K^\Gamma = 1$. In the opposite

case the ratio becomes $K_s^\Gamma/K^\Gamma = 0$. Whenever an element is cut by the level-set function, we obtain a value between 0 and 1. This definition matches the characteristic function we have defined in Eq. (4.1). We can now compute the constitutive tensor of the element according to Eq. (4.2).

Remark 4.2.6 In comparison with other approaches, the regularized characteristic function approach evolves continuously when moving the level-set function. Then, the deviatoric constitutive tensor varies between $\mathbb{C}_w^{dev}$ and $\mathbb{C}_s^{dev}$ at the interface between materials.

Remark 4.2.7 With regards to the material interpolation in the elements intersecting the interface, in this work we favor to modify the Young modulus depending upon the regularized characteristic function and to use as Poisson coefficient the one of the strong material.

Next, we can compute stresses and strains according this new, regularized characteristic function, thus allowing us to obtain continuous values of the properties for the interface elements. The deviatoric Polarization tensor and the volumetric Polarization parameter for elements K^Γ are defined as

$$\mathbb{P}^{dev} = \frac{K_s^\Gamma}{K^\Gamma}\mathbb{P}_s^{dev} + \left(1 - \frac{K_s^\Gamma}{K^\Gamma}\right)\mathbb{P}_w^{dev}, \tag{4.32}$$

$$\mathrm{P}^{vol} = \frac{K_s^\Gamma}{K^\Gamma}\mathrm{P}_s^{vol} + \left(1 - \frac{K_s^\Gamma}{K^\Gamma}\right)\mathrm{P}_w^{vol}. \tag{4.33}$$

Finally, the split TD is also computed according to Eq. (4.29).

4.2.6 The topology optimization algorithm

The last required ingredient is an algorithm to arrive to the solution of problem (4.4). In this work, we apply the iterative TO algorithm as it is defined in [87]. The sequence of the individual steps is shown in the flowchart displayed in Fig. 4.1 and explained in more detail afterwards.

[87]: J.Baiges et al. (2019), "Large-scale stochastic topology optimization using adaptive mesh refinement and coarsening through a two-level parallelization scheme"

Initially, a level set function ψ is defined with unit initial value, which means that we consider the structure to be com-

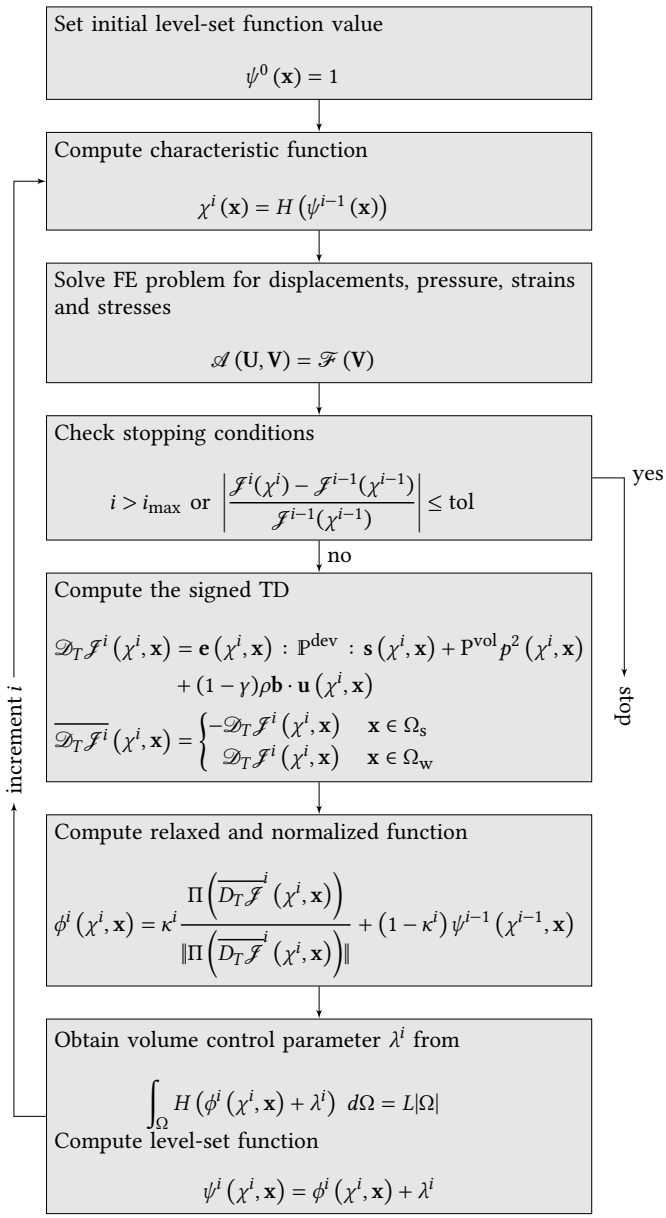

Figure 4.1: Topology optimization algorithm for linear elasticity flowchart

posed of strong material everywhere. Obviously, this first approach does not fulfill the volume constraint. We thus take

$$\psi^0(\mathbf{x}) = 1 \quad \text{in } \Omega. \tag{4.34}$$

Let ψ^{i-1} a known level set, where the superscript indicates the iteration counter. From this level set value, a characteris-

tic function can be built:

$$\chi^i(\mathbf{x}) = H\left(\psi^{i-1}(\mathbf{x})\right) \quad \text{in } \Omega, \tag{4.35}$$

which allows one to solve the solid mechanics problem and compute the signed TD $\overline{D_T\mathcal{J}^i}\left(\chi^i, \mathbf{x}\right)$. This is independent from the use of any formulation. For convergence aspects, the algorithm also requires an intermediate function $\phi^i\left(\chi^i, \mathbf{x}\right)$. This function is initially defined as the projection onto the FE space of the normalized TD in order to bound the level-set function with a relaxation scheme introduced as the iterative process advances, i.e.

$$\phi^i\left(\chi^i, \mathbf{x}\right) = \kappa^i \frac{\Pi\left(\overline{D_T\mathcal{J}}^i\left(\chi^i, \mathbf{x}\right)\right)}{\|\Pi\left(\overline{D_T\mathcal{J}}^i\left(\chi^i, \mathbf{x}\right)\right)\|} + \left(1-\kappa^i\right)\psi^{i-1}\left(\chi^{i-1}, \mathbf{x}\right). \tag{4.36}$$

The relaxation parameter κ^i is computed according to [87], and Π indicates a projection onto the FE space. In the numerical examples, Π is computed by using a lumped mass matrix approach for computational efficiency. This approach plays the role of standard filtering in TO. Finally, the level set function at the current iteration is defined as

[87]: J.Baiges et al. (2019), "Large-scale stochastic topology optimization using adaptive mesh refinement and coarsening through a two-level parallelization scheme"

$$\psi^i\left(\chi^i, \mathbf{x}\right) = \phi^i\left(\chi^i, \mathbf{x}\right) + \lambda^i, \tag{4.37}$$

where λ^i is computed by using the secant method to solve the volume constraint equation

$$\int_\Omega H\left(\psi^i\left(\chi^i, \mathbf{x}\right)\right)\, d\Omega = L|\Omega|. \tag{4.38}$$

As a stopping criteria we consider the evolution of the objective functional. The algorithm concludes if the functional has not decreased by a large enough amount. Also, a maximum number of iterations to be performed is set.

To determine κ^i, a spatial oscillation indicator is computed

$$\xi^i\left(\chi^i, \mathbf{x}\right) = \text{sign}\left\{\frac{\frac{\Pi\left(\overline{D_T\mathcal{J}}^i(\chi^i,\mathbf{x})\right)}{\|\Pi\left(\overline{D_T\mathcal{J}}^i(\chi^i,\mathbf{x})\right)\|} - \psi^{i-1}\left(\chi^{i-1}, \mathbf{x}\right)}{\psi^{i-1}\left(\chi^{i-1}, \mathbf{x}\right) - \psi^{i-2}\left(\chi^{i-2}, \mathbf{x}\right)}\right\}. \tag{4.39}$$

Note that $\xi^i\left(\chi^i, \mathbf{x}\right) = 1$, if the iterative algorithm for com-

puting the TD is advancing monotonically in the preceding iterations and $\xi^i\left(\chi^i,\mathbf{x}\right)=-1$ otherwise. This indicator allows one to detect if there are oscillations in the iterative process. If there are oscillations, the value for κ^i needs to be decreased, otherwise it can be increased up to a maximum of 1. An intermediate function $\mu^i\left(\chi^i,\mathbf{x}\right)$ is introduced as

$$\mu^i\left(\chi^i,\mathbf{x}\right)=\begin{cases}k_1\kappa^{i-1} & \text{if } \xi^i\left(\chi^i,\mathbf{x}\right)=1\\ k_2\kappa^{i-1} & \text{if } \xi^i\left(\chi^i,\mathbf{x}\right)=-1\end{cases} \tag{4.40}$$

Since $\xi^i\left(\chi^i,\mathbf{x}\right)$ is a spatial function, the information on the oscillations needs to be averaged so that a scalar value for κ^i can be obtained, which is done as follows

$$\kappa^i=\min\left\{\left(\frac{\int_\Omega\left(\mu^i\left(\chi^i,\mathbf{x}\right)\right)^{k_3}\,d\Omega}{\int_\Omega\psi^i\left(\chi^i,\mathbf{x}\right)\,d\Omega}\right)^{-k_3},1\right\}, \tag{4.41}$$

where $k_1\geq 1$, $k_2\leq 1$ and $k_3\leq 1$ are algorithmic parameters. In the numerical examples $k_1=1.1$, $k_2=0.5$ and $k_3=0.1$ are used.

Remark 4.2.8 The volume restriction is exactly fulfilled at every iteration of the algorithm unlike in alternative options. In our experience, this provides a higher global algorithmic robustness.

Remark 4.2.9 The relaxation parameter κ^i is evaluated node-to-node to observe the evolution of the TO algorithm. The spatial oscillation indicator allows us to identify those nodes which are changing their material phase between iterations. Then, we are able to slow down the relaxation scheme by introducing the weighted average equation (4.41).

Remark 4.2.10 The line search algorithm we propose is not ensuring a monotonic decrease of the cost function: the TD marks a direction in which the cost is going to decrease, but if we advance too much in that direction (and then we are far away from the point where the TD is computed) there is no guarantee that the cost is going to decrease in that iteration. This could be achieved by not allowing the algorithm to progress until the κ^i param-

eter is sufficiently small and the cost function decreases. However, in our experience the algorithm that we propose, even if not monotonic, performs well and reaches a locally optimum solution [107].

[107]: Kishida et al. (2021), "Application of a weighted sensitivity approach for topology optimization analysis of time dependent problems based on the density method"

4.2.7 Numerical examples

In this section, four numerical examples are presented to assess the performance of the proposed formulation for linear elasticity theory. The first case we consider is a simple test with different Poisson's ratio for the strong material ν_s in order to analyze the evolution of the different formulations while increasing the incompressibility of the strong material. Next, so as to analyze the effect of considering either an incompressible weak material $\nu_w = 0.5$ or a compressible weak one $\nu_w = 0.4$, we study the optimized structure of a bearing device which is obtained for both scenarios. Thereafter, a L-shaped beam is explored in order to highlight the main differences between the $\mathbf{u}p$ and the $\mathbf{u}p\mathbf{e}$ formulations. To end up, a 3D cantilever beam is studied to show the behavior of our TO algorithm in a 3D case.

With regards to the stabilization methods, both of them can be applied interchangeably. No specification is given due to the fact that no significant differences appear in the final results, as it is expected. For all subsequent numerical examples, the algorithmic parameters are set to $c_1 = 4$, $c_2 = 2$ and $c_3 = 0.1$. Unless otherwise specified, the weak material is considered to be compressible, with $\nu_w = 0.4$. The jump of stiffness γ is fixed to 10^{-3}. In all the examples presented, continuous linear interpolation is used for all the unknowns (P_1 elements), both in the $\mathbf{u}p$ and in the $\mathbf{u}p\mathbf{e}$ formulations. As a stopping criterion, we impose a relative tolerance for the objective functional tol $= 10^{-3}$, unless otherwise specified. In all presented figures, only the positive part of the level set is plotted, therefore only the strong material part is shown. The rest is filled of weak material elements, which is interpreted as the void region.

It is worth to comment about the computational efficiency of the $\mathbf{u}p$ and the $\mathbf{u}p\mathbf{e}$ formulations. For the different cases we have run, more or less between the double and triple of time is needed to solve the algebraic system for the $\mathbf{u}p\mathbf{e}$ problem with respect to the $\mathbf{u}p$ one, depending upon spacial dimensions and number of nodes. Despite this, it has been shown

previously in the literature that in many cases it pays off to use the **u***p***e** formulation, although this is not the objective of this chapter and we do not perform this kind of analysis. In [10, 11, 26, 28] the main advantages and drawbacks of several mixed formulations are presented and some situations in which the extra accuracy in the computation of the stresses is crucial are shown. For the 2D numerical examples we used direct solvers [108, 109]. In the 3D final case, the number of degrees of freedom is quite big to use a direct solver. Then we moved to iterative solvers from the PETSc package with preconditioners in the **u***p***e** case [17].

[10]: Cervera et al. (2010), "Mixed Stabilized Finite Element Methods in Nonlinear Solid Mechanics. Part I: Formulation"
[11]: Cervera et al. (2010), "Mixed Stabilized Finite Element Methods in Nonlinear Solid Mechanics. Part II: Strain Localization"
[26]: R.Codina (2009), "Finite element approximation of the three field formulation of the Stokes problem using arbitrary interpolations"
[28]: Chiumenti et al. (2021), "Stress, strain and dissipation accurate 3-field formulation for inelastic isochoric deformation"
[108]: P.R.Amestoy et al. (2001), "A Fully Asynchronous Multifrontal Solver Using Distributed Dynamic Scheduling"
[109]: P.R.Amestoy et al. (2019), "Performance and Scalability of the Block Low-Rank Multifrontal Factorization on Multicore Architectures"
[17]: Balay et al. (2015), *PETSc Web page*

Single-point load beam

As a first example, we study the TO process for a clamped-clamped beam with a single-point load (Fig. 4.2). The problem consists of a rectangular panel, clamped in both the left and the right sides and subjected to a single-point vertical load $F = 3$ N at the middle of the free bottom edge. Stress free boundary conditions are applied on the remaining boundaries. We consider a linear elastic material with a Young Modulus $E_s = 30$ Pa.

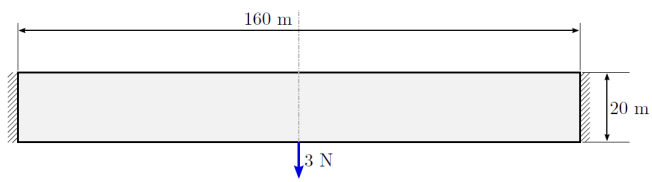

Figure 4.2: Single-point load beam. Geometry

Exploiting the symmetry of the structure, only the left half of the original domain has been discretized using about 51,200 linear triangular elements. The required final volume is set to be 40% of the initial one. Let us mention that all figures only show the left half of the clamped beam.

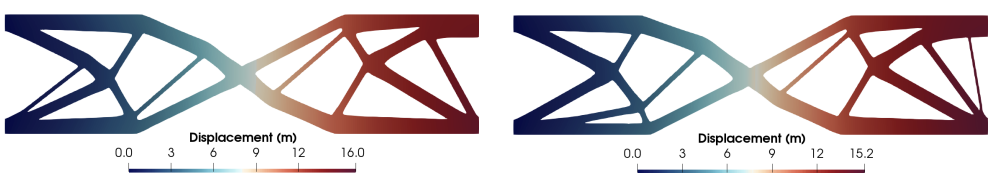

(a) $v_s = 0.4$ **(b)** $v_s = 0.5$

Figure 4.3: Single-point load beam. Final optimized structure in plane stress scenario.

First of all, let us consider the displacement-based formulation in a plane stress scenario. As explained in Subsection 4.2.4, considering plane stress, the TO problem presents no singularities when the incompressible limit is reached. Therefore, even when using the *standard irreducible* formulation, no numerical issues appear in this case. Fig. 4.3 shows the final optimized structure for both a compressible strong material $\nu_s = 0.4$ and a fully incompressible one, $\nu_s = 0.5$. As it can be observed, a well-defined solution is reached regardless of the incompressibility of the stiff material.

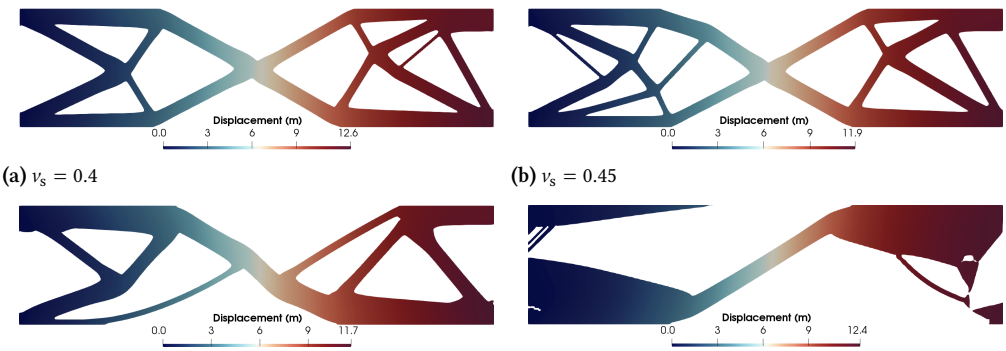

(a) $\nu_s = 0.4$ **(b)** $\nu_s = 0.45$

(c) $\nu_s = 0.49$ **(d)** $\nu_s = 0.4999$

Figure 4.4: Single-point load beam. Final optimized structure in plane strain scenario while increasing the incompressibility of the stiff material.

Let us now move to solutions obtained in a plane strain scenario. Fig. 4.4 displays the evolution of the final optimized structure when increasing the incompressibility of the strong material. As expected, the obtained result is feasible when dealing with compressible materials as it can be observed in Figs. 4.4a-4.4b. However, when the incompressibility of the stiff material is increased to a level high enough to consider the material almost incompressible, the algorithm fails to produce a physically plausible structure (Figs. 4.4c-4.4d). This phenomenon is caused by the singularities that appear in the incompressibility limit for both the displacement-based formulation (2.7) and the Polarization tensor expression (4.7).

Let us now apply stabilized mixed formulations with the split TD expression (4.29) already defined. Figs. 4.5-4.6 show both displacement and pressure fields of the final optimized structure, obtained with the $\mathbf{u}p$ and $\mathbf{u}p\mathbf{e}$ formulations, respectively, when considering compressible materials. Both figures show almost the same solution, compared to the one obtained with a displacement-based formulation, shown in Figs. 4.4a-4.4b.

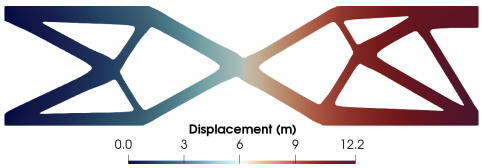

(a) $\nu_s = 0.4$. Displacement field (m)

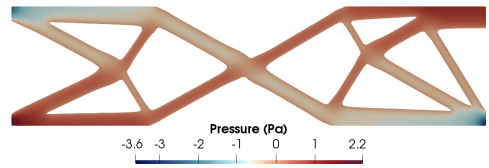

(b) $\nu_s = 0.4$. Pressure field (Pa)

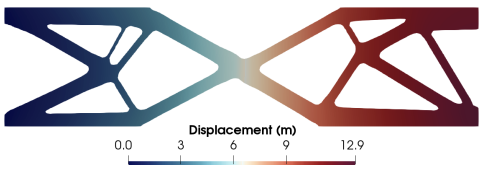

(c) $\nu_s = 0.45$. Displacement field (m)

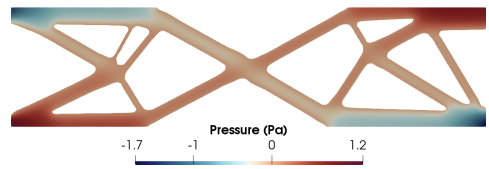

(d) $\nu_s = 0.45$. Pressure field (Pa)

Figure 4.5: Single-point load beam. Final optimized structure in plane strain scenario for compressible materials with $\mathbf{u}p$ formulation.

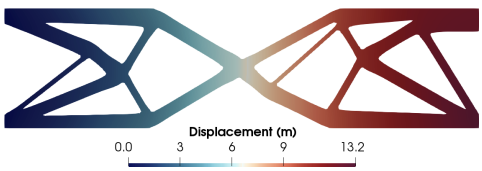

(a) $\nu_s = 0.4$. Displacement field (m)

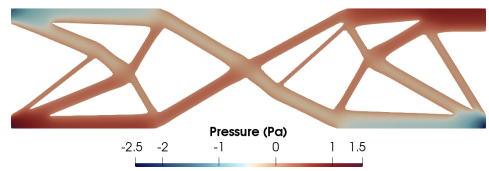

(b) $\nu_s = 0.4$. Pressure field (Pa)

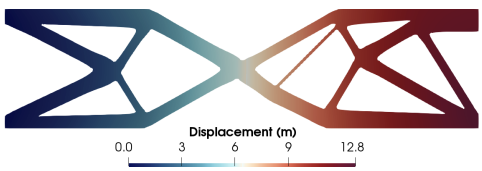

(c) $\nu_s = 0.45$. Displacement field (m)

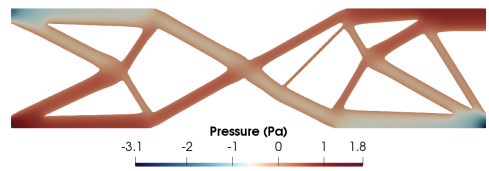

(d) $\nu_s = 0.45$. Pressure field (Pa)

Figure 4.6: Single-point load beam. Final optimized structure in plane strain scenario for compressible materials with $\mathbf{u}p\mathbf{e}$ formulation.

Fig. 4.7 presents the results obtained for both mixed formulations when dealing with a fully incompressible strong material. The obtained design for incompressible material is quite different to the one presented in compressible scenarios. This structure appears to be made of less, yet thicker, structural elements.

The minor differences that can be noticed between formulations are caused by the different ways of computing the strains. In the $\mathbf{u}p$ formulation the strains are computed from the displacement field, whereas, in the $\mathbf{u}p\mathbf{e}$ formulation, they are directly obtained as a nodal unknown.

Moving on to convergence issues, Fig. 4.8 shows a diagram

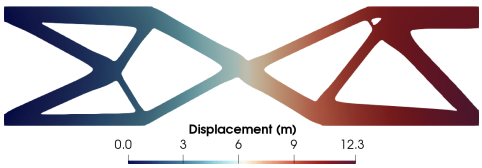

(a) **u***p* formulation. Displacement field (m)

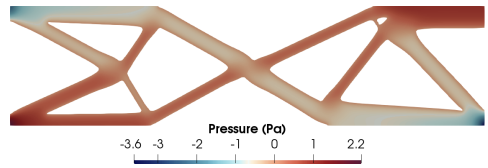

(b) **u***p* formulation. Pressure field (Pa)

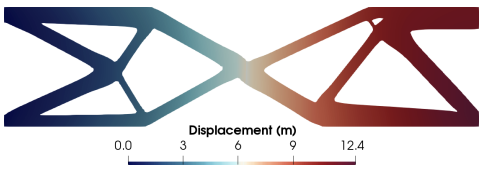

(c) **u***p***e** formulation. Displacement field (m)

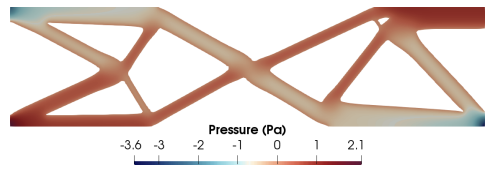

(d) **u***p***e** formulation. Pressure field (Pa)

Figure 4.7: Single-point load beam. Final optimized structure in plane strain scenario for $\nu_s = 0.5$ for both **u***p* and **u***p***e** formulations.

referring to the compliance evolution recorded during the iterative TO procedure, that leads to the designs shown in Fig. 4.7. A maximum of 100 iterations is imposed as stopping criteria to show the evolution of the objective functional. Both formulations need less than 100 iterations to minimize the compliance and achieve convergence.

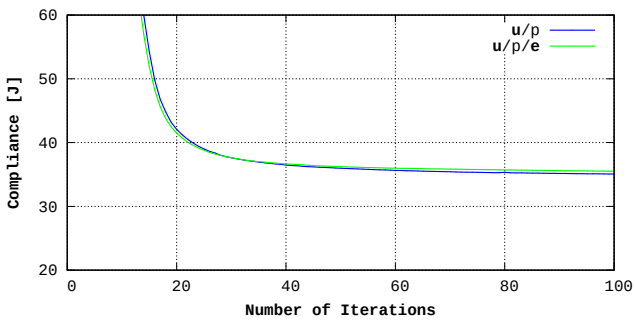

Figure 4.8: Single-point load beam. Convergence diagrams in plane strain scenario for $\nu_s = 0.5$ for both **u***p* and **u***p***e** formulations.

Bearing device

As a second example, the TO of a bearing device is explored. Since such devices are usually made of rubber we only consider the incompressible case. The geometry consists of a rectangular panel, clamped in the bottom side and subjected to a load distribution on the upper edge, $\mathbf{t} = 1,80$ N/m. Stress free boundary conditions are applied on the remaining boundaries. We consider a linear elastic material with a Young Mod-

ulus $E_s = 100$ Pa. The geometry of this problem is shown in Fig. 4.9.

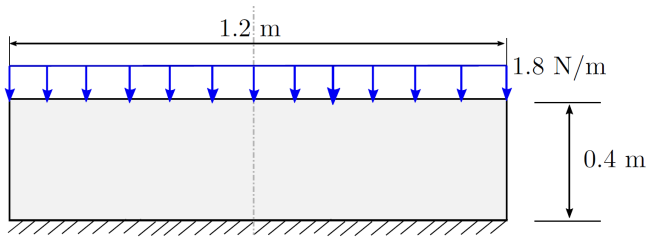

Figure 4.9: Bearing device. Geometry

Exploiting the symmetry of the structure, only the left half of the original domain has been discretized, using about 19,200 linear triangular elements. The required final volume is set to be 35% of the domain. The study is conducted using the $\mathbf{u}p$ formulation.

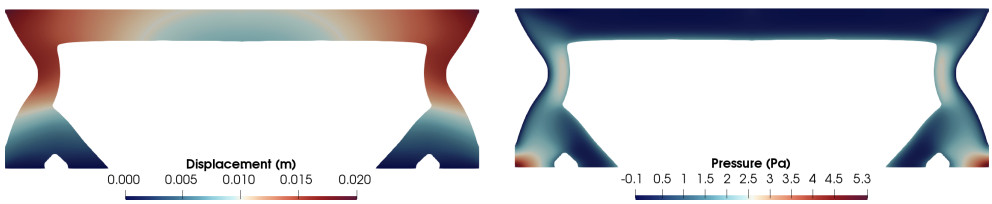

(a) Displacement field (m) **(b)** Pressure field (Pa)

Figure 4.10: Bearing device. Final optimized structure in plane strain scenario for $\nu_s = 0.5$ and $\nu_w = 0.5$ for $\mathbf{u}p$ formulation.

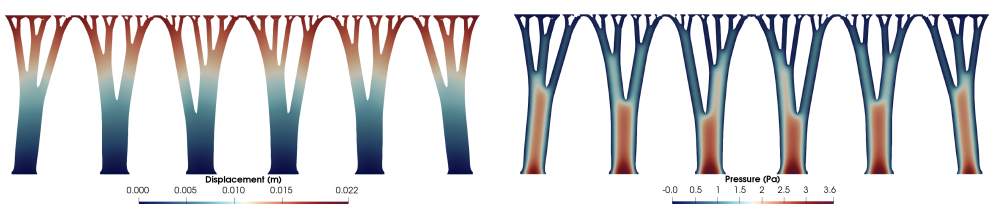

(a) Displacement field (m) **(b)** Pressure field (Pa)

Figure 4.11: Bearing device. Final optimized structure in plane strain scenario for $\nu_s = 0.5$ and $\nu_w = 0.4$ for $\mathbf{u}p$ formulation.

Fig. 4.10 shows the optimal structure obtained by using strong and weak materials, which are both incompressible. Because of the incompressibility of the weak material we obtain an extended zone of weak material elements, enclosed by a structure made of strong material, as outlined in a similar example in [93]. To avoid this kind of designs, the weak material must be considered compressible, for example with $\nu_w = 0.4$. Fig. 4.11 illustrates the optimal topology which is obtained

[93]: M.Bruggi et al. (2007), "Topology optimization of incompressible media using mixed finite elements"

when this is taken into account. By considering a compressible weak material, widespread areas of elements made of weak material are not able to transfer the external pressure to the supports.

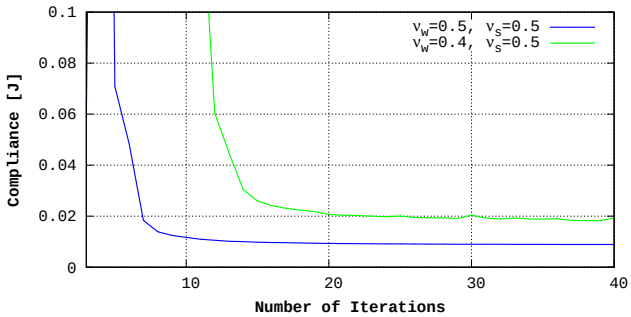

Figure 4.12: Bearing device. Convergence diagrams in plane strain scenario for $\mathbf{u}p$ formulation considering both $\nu_w = 0.4$ and $\nu_w = 0.5$.

For the sake of completeness, Fig. 4.12 shows the evolution of the compliance along iterations for the previous two considerations of the weak material. A maximum of 40 iterations is imposed as stopping criteria. In the fully incompressible case, the widespread area of weak material is able to transfer the external pressure to the constraints, which results in a very low compliance. This is the reason why the algorithm tends to this kind of 'optimal' design, where the compliance is even lower than the one obtained with a compressible weak material consideration.

It becomes evident, that weak material – if considered incompressible – can heavily contribute to the stiffness of the final structure, a behavior which goes against our assumption that the weak material is simulating void regions.

L-shaped beam

The third example is an L-shaped beam, a commonly exhibited problem in TO. The specific feature of this problem is the geometrical singularity. The structure is clamped at the top and a single point force is applied at the middle of the right edge. Stress free boundary conditions are applied on the remaining boundaries. A linear elastic material is set with a Young Modulus $E_s = 1$ MPa. The geometry of this beam is shown in Fig. 4.13.

The domain has been discretized using roughly 22,800 linear triangular elements. The objective of this problem is to highlight the main differences between the mixed formulations

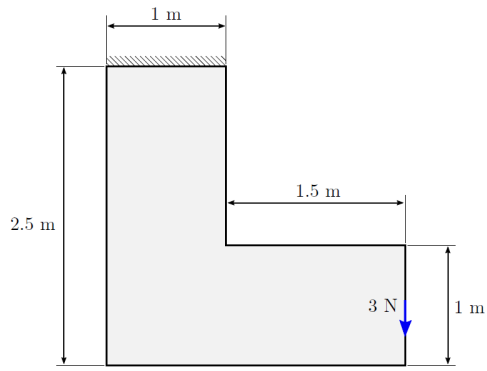

Figure 4.13: L-shaped beam. Geometry.

proposed in this work. The required final volume is set to be 50% of the initial domain.

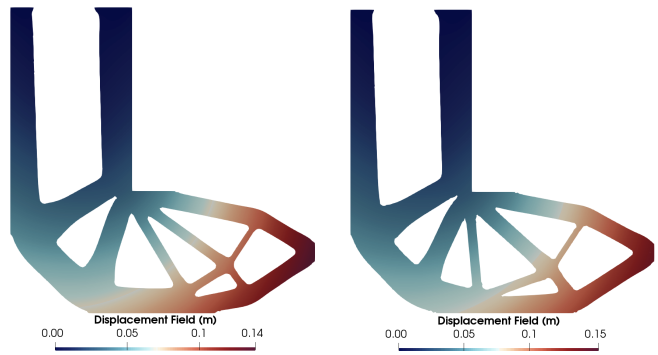

(a) **u***p* formulation **(b)** **u***pe* formulation

Figure 4.14: L-shaped beam. Displacement field for the optimized structure for $v_s = 0.5$

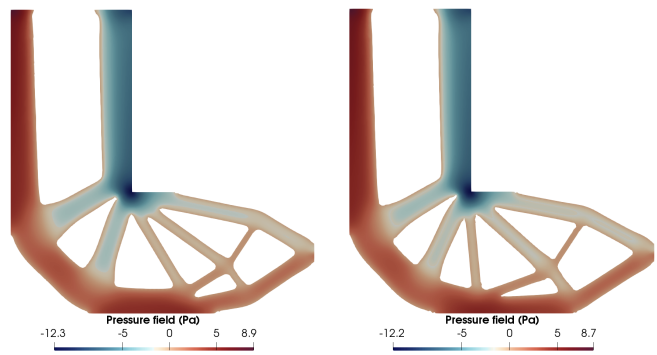

(a) **u***p* formulation **(b)** **u***pe* formulation

Figure 4.15: L-shaped beam. Pressure field for the optimized structure for $v_s = 0.5$

By using the deviatoric strains as an additional primary unknown in the **u***pe* formulation, the whole solution converges faster (upon *h*-refinement). Therefore, also the pressure and displacement fields are more accurate. This effect, however, is more dominant on coarser meshes. Due to the relatively

fine discretization of our problem, we can only observe slight differences between the displacement and pressure fields of Figs. 4.14-4.15 in the final design of the optimized topology.

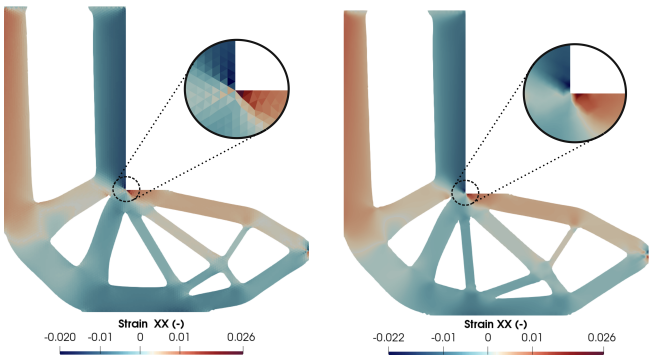

(a) $\mathbf{u}p$ formation (b) $\mathbf{u}p\mathbf{e}$ formation

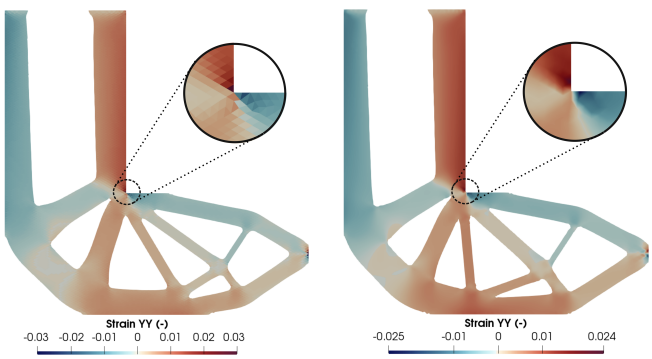

(c) $\mathbf{u}p$ formation (d) $\mathbf{u}p\mathbf{e}$ formation

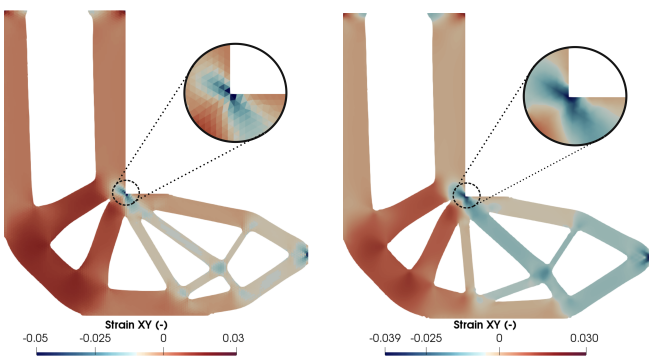

(e) $\mathbf{u}p$ formation (f) $\mathbf{u}p\mathbf{e}$ formation

Figure 4.16: L-shaped beam. Deviatoric strain field for the optimized structure for $\nu_s = 0.5$

On the contrary, Fig. 4.16 shows the deviatoric strain field, obtained from both formulations. Utilizing the $\mathbf{u}p$ formulation, the strains are computed from the displacement gradient and therefore defined element-wise. Because, linear

triangular elements were used, the strains are element-wise constant, hence particularly imprecise. Using the **u***p***e** formulation however, the deviatoric strains are also a primary unknown of the problem, and therefore defined at the nodes. The result is a continuous field, which is more precise in the first place and, secondly, does not require nodal smoothing for postprocessing. As a consequence the accuracy of the stresses is also increased.

Remark 4.2.11 This extra level of accuracy in stresses and strains can be very interesting for several problems, such as Fluid-Structure Interaction or stress-constraint problems, among others. Note, however, that the rate of convergence of stresses and strains is expected to be the same for both the **u***p* and the **u***p***e** formulations.

3D Cantilever beam

The final example is a 3D Cantilever beam. The structure is clamped at the left face and a uniform traction is applied at the lower edge of the right face. Stress free boundary conditions are applied on the remaining boundaries. A linear elastic material is applied with a Young Modulus $E_s = 1$ MPa. The geometry of this beam is shown in Fig. 4.17.

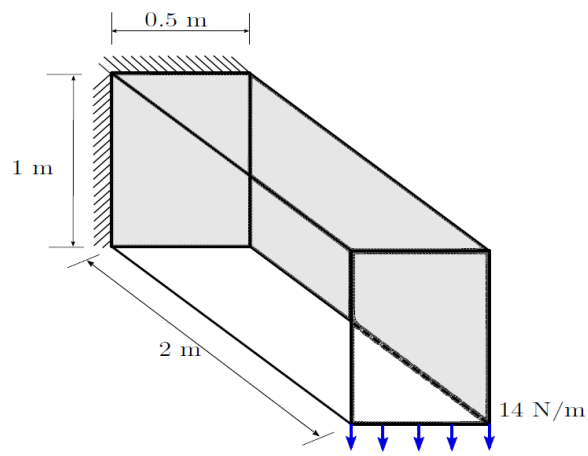

Figure 4.17: 3D Cantilever beam. Geometry.

Taking into account the symmetry of the problem, the left half of the design domain is discretized into 380,000 linear tetrahedral FEs. The required final volume is set to be 10% of the initial one. In Figs. 4.18-4.19 show the displacement and pressure fields for both formulations.

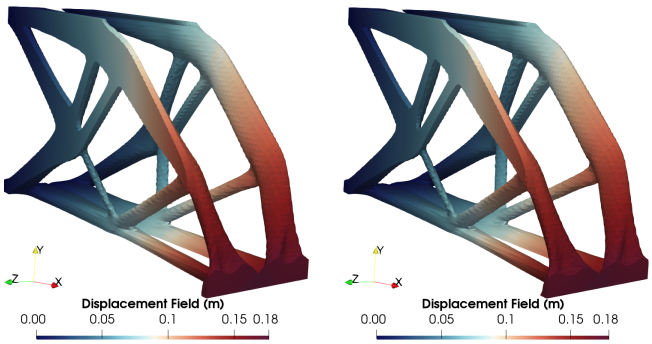

(a) up formulation (b) upe formulation

Figure 4.18: 3D Cantilever beam. Displacement field for the optimized structure in a 3D scenario for $\nu_s = 0.5$.

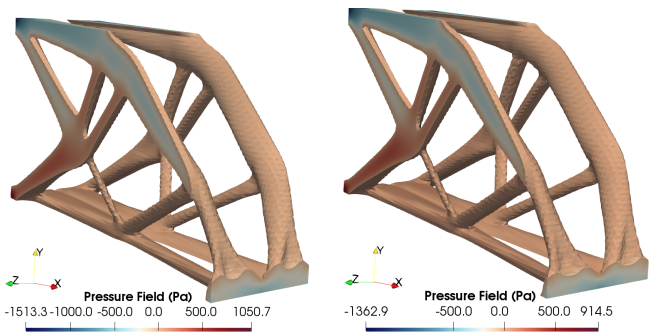

(a) up formulation (b) upe formulation

Figure 4.19: 3D Cantilever beam. Pressure field for the optimized structure in a 3D scenario for $\nu_s = 0.5$.

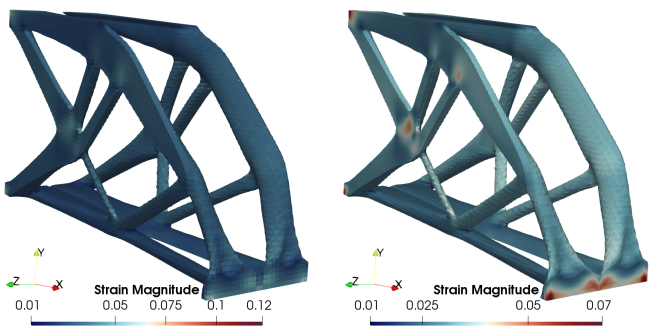

(a) up formulation (b) upe formulation

Figure 4.20: 3D Cantilever beam. Deviatoric strain field magnitude for the optimized structure in a 3D scenario for $\nu_s = 0.5$.

Fig. 4.20 presents the $L^2(\Omega)$-norm of the deviatoric strain field (Strain Magnitude) for each formulation. Again, a higher level of accuracy is obtained for the strains computed from the mixed upe formulation. The optimized structures are identical. The results of this problem indicate that it is reasonable to approximate the proper 3D polarization tensor with its isotropic 2D plane strain counterpart.

4.3 Topological-derivative based topology optimization in finite strain hyperelasticity

4.3.1 Setting of the problem

In the following, the TO problem is stated under the assumption of finite strain hyperelastic isotropic materials. To do so, let us consider the system of equations for the mixed $\mathbf{u}p$ and $\mathbf{u}p\mathbf{S}'$ formulations in finite strain hyperelasticity presented in Chapter 3.

As explained before., the description of the topology is determined by the characteristic function χ, which now is defined as a function of the material coordinates $\mathbf{X}$ as

$$\chi(\mathbf{X}) = \begin{cases} 1 & \mathbf{X} \in \Omega_{0,\mathrm{s}} \\ 0 & \mathbf{X} \in \Omega_{0,\mathrm{w}} \end{cases}, \tag{4.42}$$

where the domain Ω_0 has been split into two parts, $\overline{\Omega_0} = \overline{\Omega_{0,\mathrm{s}} \cup \Omega_{0,\mathrm{w}}}$, $\Omega_{0,\mathrm{s}} \cap \Omega_{0,\mathrm{w}} = \emptyset$. The sub-domains $\Omega_{0,\mathrm{s}}$ and $\Omega_{0,\mathrm{w}}$ are made of different materials. The material corresponding to the domain $\Omega_{0,\mathrm{w}}$ exhibits a very small stiffness approximating the absence of material. In fact, in this work, it is considered as linear elastic material to ease the highly nonlinear behavior of the problem. The material parameters of both regions are identically related with the jump of stiffness γ as explained in the linear elastic case. The characteristic function allows us to rewrite the deviatoric constitutive tensor defined in the whole domain as

$$\mathbb{C}'(\chi, \mathbf{X}) = \chi \mathbb{C}'_{\mathrm{s}}(\mathbf{X}) + (1 - \chi)\mathbb{C}'_{\mathrm{w}}, \tag{4.43}$$

where $\mathbb{C}'_{\mathrm{s}}(\mathbf{X})$ is the tangent and $\mathbb{C}'_{\mathrm{w}}$ are the total fourth order deviatoric constitutive tensors of the stiff and the soft materials, respectively.

To obtain structures with minimum flexibility, a functional $\mathcal{J}$ is minimized. In topological optimization problems this functional is usually referred to as the *total potential energy functional* and is defined as

$$\mathcal{J}(\chi) = \int_{\Omega_0} \Psi(\mathbf{C}(\chi, \mathbf{X}))\ d\Omega_0 - \int_{\Omega_0} \rho_0 \mathbf{b} \cdot \mathbf{u}(\chi, \mathbf{X})\ d\Omega_0$$

$$- \int_{\Gamma_{0,N}} \mathbf{t}_N \cdot \mathbf{u}(\chi, \mathbf{X}) \; d\Gamma_0, \tag{4.44}$$

where Ψ has been introduced in Eq. (3.9) as the strain energy function. The whole TO problem is then formulated as the minimization of the total potential energy functional subjected to the maximum material allowed, which is written as follows

$$\begin{aligned} \min_{\chi \in \mathbb{X}_L} \mathcal{J}(\chi) &= \int_{\Omega_0} \Psi(\mathbf{C}(\chi, \mathbf{X})) \; d\Omega_0 - \int_{\Omega_0} \rho_0 \mathbf{b} \cdot \mathbf{u}(\chi, \mathbf{X}) \; d\Omega_0 \\ &\quad - \int_{\Gamma_{0,N}} \mathbf{t}_N \cdot \mathbf{u}(\chi, \mathbf{X}) \; d\Gamma_0 \\ \text{s.t.} : \mathcal{A}(\mathbf{U}, \mathbf{V}) &= \mathcal{F}(\mathbf{V}) \quad \forall \mathbf{V} \in \mathbb{W}_0, \\ \mathbb{X}_L &= \left\{ \chi \in L^\infty(\Omega_0, \{0,1\}), \int_\Omega \chi(\mathbf{x}) \; d\Omega = L|\Omega_0| \right\}, \end{aligned} \tag{4.45}$$

where now $\mathbb{X}_L$ is the feasible domain restricted to a volume constraint denoted as a fraction $0 < L < 1$ of the reference domain Ω_0. Finally, $\mathcal{A}$ and $\mathcal{F}$ are the forms which have been obtained in Chapter 2 for the displacement-based formulation as (2.84-2.85) and in Chapter 3 depending upon the formulation, defined as (3.40-3.41) for the $\mathbf{u}p$ formulation and as (3.82-3.83) for the $\mathbf{u}p\mathbf{S}'$ formulation.

4.3.2 Material interpolation

Following the same procedure as the one discussed in Subsection 4.2.2, we consider the soft material to be compressible. Therefore, both Young modulus and Poisson ratio are modified depending on the value of the characteristic function. Next, we can compute Lame's parameters to define in a proper way the hyperelastic material under study.

4.3.3 An attempt to obtain the topological derivative expression for the linearized problem

Let us suppose that Ω_0 is subject to a singular circular perturbation confined in a small region $B_\varepsilon(\mathbf{X}) = \mathbf{X} + \varepsilon\omega$ with radius ε, where ω is a fixed domain. Then we assume that the total potential energy functional $\mathcal{J}_\varepsilon(\chi)$ associated with

the topologically perturbed domain $\Omega_{\varepsilon,0} \coloneqq \Omega_0 \setminus \overline{B_\varepsilon}$, admits the following topological asymptotic expansion

$$\mathscr{J}_\varepsilon(\chi) = \mathscr{J}(\chi) + f(\varepsilon)\mathscr{D}_T(\chi, \mathbf{X}) + \mathscr{O}(f(\epsilon)), \tag{4.46}$$

where $\mathscr{J}(\chi)$ is the functional associated to the unperturbed domain and $f(\varepsilon)$ is a positive function such that, $f(\varepsilon) \to 0$ when $\varepsilon \to 0$. The function $\mathscr{D}_T(\chi, \mathbf{X})$ is called the topological derivative of $\mathscr{J}(\chi)$ and it can be seen as a first order correction to approximate $\mathscr{J}_\varepsilon(\chi)$. We end up with the classical definition for the topological derivative as

$$\mathscr{D}_T(\chi, \mathbf{X}) = \lim_{\varepsilon \to 0} \frac{\mathscr{J}_\varepsilon(\chi) - \mathscr{J}(\chi)}{f(\varepsilon)}. \tag{4.47}$$

[104]: C.G.Lopes et al. (2015), "Topological Derivative-based Topology Optimization of Structures Subject to Multiple Load-cases"

In linear elasticity, the total potential energy is a linear function and an analytical expression for the topological derivative can be derived (see for example [104] for further details on the procedure). However, for finite strain hyperelasticity, the total potential energy becomes nonlinear and it is dependent upon the specific material law that is desired to study. In this work, we pretend to linearize the problem and obtain an incremental topological derivative according to a load parameter which controls the evolution of the problem. To do so, we solve the nonlinear equilibrium equations in an incremental manner $n = 0, \ldots N-1$ being N the maximum number of load increments. The external forces are controlled by an incremental load factor λ_{n+1} at a given load increment $n+1$, such that $\lambda_{n+1} = (n+1)/N$. At load increment $n+1$, the incremental weak form of the problem reads: find $\mathbf{U}$ such that the Dirichlet condition is satisfied and

$$\mathscr{A}(\mathbf{U}, \mathbf{V}) = \lambda_{n+1}\mathscr{F}(\mathbf{V}) \quad \forall \mathbf{V} \in \mathbb{W}_0. \tag{4.48}$$

The next step is consider that for each load increment $n+1$, we can compute an increment for the total potential energy functional for both the perturbed and the unperturbed domains such that

$$\mathscr{J}^{n+1}(\chi) \approx \mathscr{J}^n(\chi) + \Delta\mathscr{J}^{n+1}(\chi), \tag{4.49}$$

$$\mathscr{J}_\varepsilon^{n+1}(\chi) \approx \mathscr{J}^n(\chi) + \Delta\mathscr{J}_\varepsilon^{n+1}(\chi). \tag{4.50}$$

The main idea in this approximations is to consider that the hole is created during the load increment $n+1$, and therefore, both expansions start from the same unperturbed functional $\mathscr{J}^n(\chi)$. Taking this is mind, we can define the total potential

energy functionals as

$$\mathscr{J}(\chi) \approx \mathscr{J}^0(\chi) + \sum_{i=0}^{N-1} \Delta\mathscr{J}^{i+1}(\chi), \tag{4.51}$$

$$\mathscr{J}_\varepsilon(\chi) \approx \mathscr{J}^0(\chi) + \sum_{i=0}^{N-1} \Delta\mathscr{J}_\varepsilon^{i+1}(\chi). \tag{4.52}$$

And introducing this approximations in Eq. 4.47 we obtain

$$\begin{aligned}\mathscr{D}_T(\chi, \mathbf{X}) &\approx \lim_{\varepsilon\to 0} \frac{\sum_{i=0}^{N-1} \Delta\mathscr{J}_\varepsilon^{i+1}(\chi) - \sum_{i=0}^{N-1} \Delta\mathscr{J}^{i+1}(\chi)}{f(\varepsilon)} \\ &= \sum_{i=0}^{N-1} \lim_{\varepsilon\to 0} \frac{\Delta\mathscr{J}_\varepsilon^{i+1}(\chi) - \Delta\mathscr{J}^{i+1}(\chi)}{f(\varepsilon)} \\ &:= \sum_{i=0}^{N-1} \Delta\mathscr{D}_T^{i+1}(\chi, \mathbf{X}).\end{aligned} \tag{4.53}$$

In this manner, we can approximate the topological derivative as the sum over increments computed for each load increment $n+1$. We can approximate the strain energy function $\Psi^{n+1}(\mathbf{C})$ by means of the following Taylor series expansion

$$\begin{aligned}\Psi^{n+1}(\mathbf{C}) &\approx \Psi^n(\mathbf{C}) + \frac{1}{2}\frac{\partial\Psi(\mathbf{C})}{\partial\mathbf{C}}^n : \Delta\mathbf{C}^{n+1} \\ &\quad + \frac{1}{4}\Delta\mathbf{C}^{n+1} : \frac{\partial^2\Psi(\mathbf{C})}{\partial\mathbf{C}\partial\mathbf{C}}^n : \Delta\mathbf{C}^{n+1} \\ &= \Psi^n(\mathbf{C}) + \frac{1}{2}\mathbf{S}^n : \Delta\mathbf{C}^{n+1} + \frac{1}{4}\Delta\mathbf{C}^{n+1} : \mathbb{C}^n : \Delta\mathbf{C}^{n+1}.\end{aligned} \tag{4.54}$$

Therefore, we can compute the increment of each functional as

$$\begin{aligned}\Delta\mathscr{J}_\varepsilon^{i+1} &= \int_{\Omega_{\varepsilon,0}} \left\{\frac{1}{2}\mathbf{S}^n : \Delta\mathbf{C}_\varepsilon^{n+1} + \frac{1}{4}\Delta\mathbf{C}_\varepsilon^{n+1} : \mathbb{C}_\varepsilon^n : \Delta\mathbf{C}_\varepsilon^{n+1}\right\} d\Omega, \\ \Delta\mathscr{J}^{i+1} &= \int_{\Omega_0} \left\{\frac{1}{2}\mathbf{S}^n : \Delta\mathbf{C}^{n+1} + \frac{1}{4}\Delta\mathbf{C}^{n+1} : \mathbb{C}^n : \Delta\mathbf{C}^{n+1}\right\} d\Omega.\end{aligned} \tag{4.55}$$

From this point on, computing the increment of topological derivative consists in obtain the subtraction of the functional, which must result in an integral over the inclusion. Several unsuccessfully attempts have been performed during this thesis to obtain an analytical expression for this lin-

earized topological derivative. Therefore, this work line is postpone for future works.

4.3.4 Topology optimization using a minimization direction

When moving to solve the TO problem (4.45) for finite strain hyperelastic materials a few methodologies exist in the literature. In this thesis, we favor using an approximation to the TD concept together with a level-set approach.

Unfortunately, there is no way to obtain an analytical expression for the TD as the one obtained in linear elasticity in Eq. (4.5). However, an approximation can be found in [110, 111]. In this set of works, the topological sensitivity analysis is applied to finite strain deformation based on the total Lagrangian formulation. This analysis is represented by the TD, that gives for each point of the domain the sensitivity of the total potential energy function when an infinitesimal hole B_ϵ^0 of radius ϵ is created. In these works, the topological derivative in absence of body forces is given by the following expression

[110]: C.E.L.Pereira et al. (2008), "Topological sensitivity analysis in large deformation problems"
[111]: C.E.L.Pereira et al. (2010), "Topological sensitivity analysis for a two-parameter Mooney-Rivlin hyperelastic constitutive model"

$$\begin{aligned}\mathscr{D}_T\mathscr{J}(\chi,\mathbf{X}) &= -\lim_{\epsilon\to 0}\frac{1}{f'(\epsilon)}\int_{\partial B_\epsilon^0}\Psi(\mathbf{C}(\chi,\mathbf{X}))\,d\partial B_\epsilon^0 \\ &:= \lim_{\epsilon\to 0} d_T\mathscr{J}(\chi,\mathbf{X})\end{aligned} \tag{4.56}$$

where $f(\epsilon)$ is a regularizing function typically chosen as $f(\epsilon) = -\pi\epsilon^2$. In order to obtain the topological derivative, it is necessary that the limit for $\epsilon \to 0$ be calculated. For the present nonlinear problem, an analytic asymptotic analysis becomes impracticable. An alternative procedure based on numerical experiments for the calculation of this limit is adopted. The numerical study of the asymptotic behavior of the function $d_T\mathscr{J}(\chi,\mathbf{X})$ with relation to the radius ϵ is developed.

The TD $\mathscr{D}_T\mathscr{J}$ of this functional at a point $\mathbf{X}$ can be approximated by the minimization direction (MD) $\mathscr{M}_D\mathscr{J}$

$$\mathscr{D}_T\mathscr{J}(\chi,\mathbf{X}) \approx \mathscr{M}_D\mathscr{J}(\chi,\mathbf{X}) := \Psi(\mathbf{C}(\chi,\mathbf{X}))+(1-\gamma)\rho_0\mathbf{b}\cdot\mathbf{u}(\chi,\mathbf{X}), \tag{4.57}$$

We can now define the signed MD such that

$$\overline{\mathscr{M}_D\mathscr{J}}(\chi,\mathbf{X}) = |\mathscr{M}_D\mathscr{J}(\chi,\mathbf{X})|. \tag{4.58}$$

Once the optimal value for the characteristic function $\chi(\mathbf{X})$ has been reached, the following condition holds

$$\overline{\mathscr{M}_D\mathscr{J}}(\chi,\mathbf{X}) \geq \overline{\mathscr{M}_D\mathscr{J}}(\chi,\mathbf{Y}), \forall \mathbf{X} \in \Omega_{0,\mathrm{s}}, \forall \mathbf{Y} \in \Omega_{0,\mathrm{w}}. \quad (4.59)$$

Note that at the interface $\overline{\Omega_{0,\mathrm{s}}} \cap \overline{\Omega_{0,\mathrm{w}}}$, the MD has a jump, but the signed MD is continuous. Eq. (4.59) allows one to construct a level set function $\psi(\chi,\mathbf{X})$, which will implicitly characterize $\Omega_{0,\mathrm{s}}$ and $\Omega_{0,\mathrm{w}}$ as it was done previously in the linear elastic case in Subsection 4.2.3. From this point on, the same procedure is performed.

Remark 4.3.1 Let us discuss some important aspects about the TD approximation we are using when the infinitessimal strain assumption is considered. In such case, the TD approximation is written as

$$\mathscr{D}_T\mathscr{J}(\chi,\mathbf{x}) \approx \frac{1}{2}\boldsymbol{\varepsilon}(\chi,\mathbf{x}) : \boldsymbol{\sigma}(\chi,\mathbf{x}) + (1-\gamma)\rho\mathbf{b}\cdot\mathbf{u}(\chi,\mathbf{x}). \quad (4.60)$$

By comparing this approximation with the analytical TD obtained for linear elastic materials given in Eq. (4.5) it is quite simple to observe that these two equations match, if and only if, the Polarization tensor, $\mathbb{P}$ reduces to the 4^{th}-order identity tensor, $\mathbb{I}$ (up to constant values which does not affect the direction of the TD). In Eq. (4.11) the Polarization tensor definition is given. It is noted that, to remove the contribution given by tensor $\mathbf{I}\otimes\mathbf{I}$ it must be satisfied that $\alpha = \beta$. This only happens when $\nu = 0.25$. Therefore, the TD approximation only matches the analytical one when $\nu = 0.25$ and it must be taken as an approximation otherwise.

4.3.5 Numerical topological derivative for incompressible materials

In this subsection, we are interested in performing the TO process for incompressible materials in finite strain hyperelasticity theory. Therefore, as mentioned in Section 3.3 it is convenient to adopt the decoupled representation of the strain energy function presented in Eq. (3.10). The MD in Eq. (4.57) is rewritten as

$$\mathscr{M}_D\mathscr{J}(\chi,\mathbf{X}) = W\left(\bar{\mathbf{C}}(\chi,\mathbf{X})\right) + U(J(\chi,\mathbf{X})) + (1-\gamma)\rho_0\mathbf{b}\cdot\mathbf{u}(\chi,\mathbf{X}). \quad (4.61)$$

It is important to remark that the volumetric energy function $U(J) = \kappa G(J)$ presents a singularity for fully incompressible materials. In the incompressible limit, when $\nu_s \to 0.5$, $\kappa \to \infty$ and $G(J) \to 0$. Therefore, an indeterminate form appears and it would cause the breakdown of the MD. This problem can be easily solved by introducing the pressure p according to Eq. (3.25). This expression allows us to find, for every volumetric strain energy function, a specific function $g(J)$ such that

$$\lim_{J\to 1} g(J) = 0, \tag{4.62}$$

and we can redefine $G(J) = \frac{-p}{\kappa} g(J)$. Finally we can introduce this expression to obtain $U(J) = \kappa \frac{-p}{\kappa} g(J) = -pg(J)$. This expression allows us to avoid the singularity while giving us null volumetric strain energy in the incompressible limit, as it is expected.

Finally, the formula for the split MD, which is valid for nearly and fully incompressible hyperelastic materials is given as

Finite strain hyperelasticity. Split minimization direction

$$\begin{aligned}\mathscr{M}_D\mathscr{I}(\chi,\mathbf{X}) = W\left(\bar{\mathbf{C}}(\chi,\mathbf{X})\right) - p(\chi,\mathbf{X})\, g(J(\chi,\mathbf{X})) \\ + (1-\gamma)\rho_0 \mathbf{b}\cdot\mathbf{u}(\chi,\mathbf{X}).\end{aligned} \tag{4.63}$$

With regards to the treatment of the interface elements, the same methodology as the one applied for linear elasticity is considered.

4.3.6 The topology optimization algorithm

The last required ingredient is an algorithm to arrive to the solution of problem (4.45). In this work, we apply an iterative TO algorithm very similar to the one defined in Subsection 4.2.6. The sequence of the individual steps is shown in the flowchart displayed in Fig. 4.21. Due to the nonlinearities that can be presented in the problem, it is highly recommended to introduce the scalar n_{prg} to reduce progressively the required volume fraction until the final goal during the first TO iterations as it can be seen in the flowchart displayed in Fig. 4.21

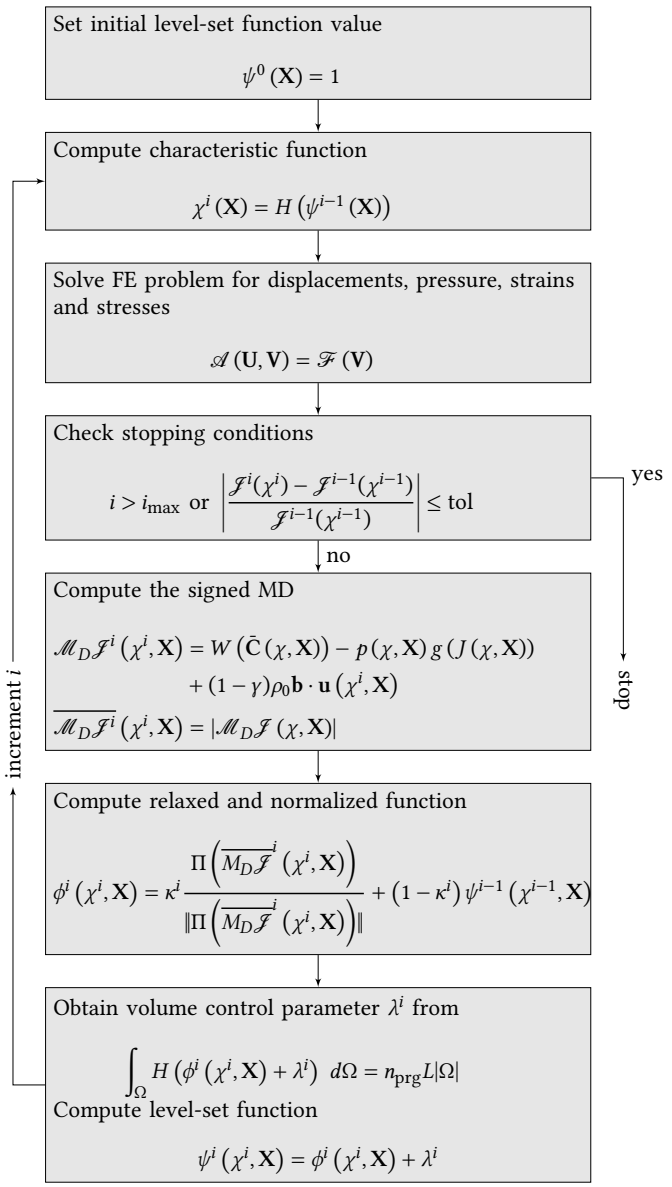

Figure 4.21: Topology optimization algorithm for finite strain hyperelasticity flowchart

4.3.7 Numerical examples

In this section, two numerical examples are presented to assess the performance of the proposed formulation for finite strain hyperelasticity theory. The first case we consider is a simple test with different Poisson's ratio for the strong material ν_s in order to analyze the evolution of the different formulations while increasing the incompressibility of the strong material. To end up, a 3D cantilever beam is studied to show

the behavior of our TO algorithm in a 3D case.

For all subsequent numerical examples, the algorithmic parameters are set to $c_1 = 1$, $c_2 = 1$ and $c_3 = 0.5$. Unless otherwise specified, the weak material is considered to be linear elastic and compressible, with $\nu_w = 0.4$. The jump of stiffness γ is fixed to 10^{-2}. In all the examples presented, continuous linear interpolation is used for all the unknowns (P_1 elements), both in the $\mathbf{u}p$ and in the $\mathbf{u}p\mathbf{S}'$ formulations. As a stopping criterion, we impose a relative tolerance for the objective functional tol $= 10^{-3}$, unless otherwise specified. The volume fraction is reduced progressively during the first 15 TO iterations for both examples. The first 5 TO iterations is fixed to 0.9 and then is reduced linearly to the final desired fraction. In all presented figures, only the positive part of the level set is plotted, therefore only the strong material part is shown. The rest is filled of weak material elements which is interpreted as the void region.

Single-point load beam

As a first example, we study the TO process for a clamped-clamped beam with a single-point load (exactly the same geometry as the one used for the linear elastic case in Fig. 4.2). The problem consists of a rectangular panel, clamped in both the left and the right sides and subjected to a single-point vertical load $F = 3$ N at the middle of the free bottom edge. Stress free boundary conditions are applied on the remaining boundaries. We consider a Neo-Hookean material with a Simo-Taylor law for the deviatoric part of the stresses, with a Young Modulus $E_s = 30$ Pa.

Exploiting the symmetry of the structure, only the left half of the original domain has been discretized using about 51,200 linear triangular elements. The required final volume is set to be 40% of the initial one. Let us mention that all figures only show the left half of the clamped beam.

Fig. 4.22 displays the evolution of the final optimized structure when increasing the incompressibility of the strong material when considering a displacement-based formulation presented in Subsection 2.1.2. As expected, the obtained result is feasible when dealing with compressible materials as it can be observed in Figs. 4.22a-4.22b-4.22c. However, when the incompressibility of the stiff material is increased to a

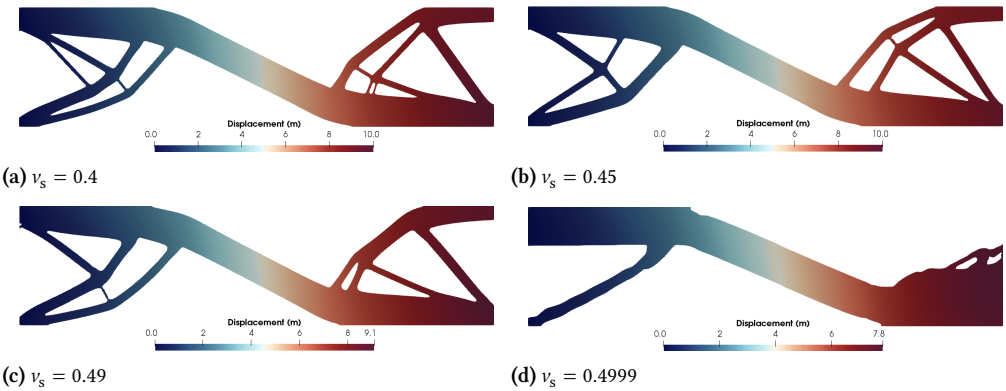

(a) $\nu_s = 0.4$ **(b)** $\nu_s = 0.45$

(c) $\nu_s = 0.49$ **(d)** $\nu_s = 0.4999$

Figure 4.22: Single-point load beam. Final optimized structure while increasing the incompressibility of the stiff material.

level high enough to consider the material almost incompressible, the algorithm fails to produce a physically plausible structure (Fig. 4.22d). This phenomenon is caused by the singularity that appears in the incompressibility limit for the u formulation (2.7). Obviously the problem crashes in the running stage when the strong material is considered fully incompressible, $\nu_s = 0.5$.

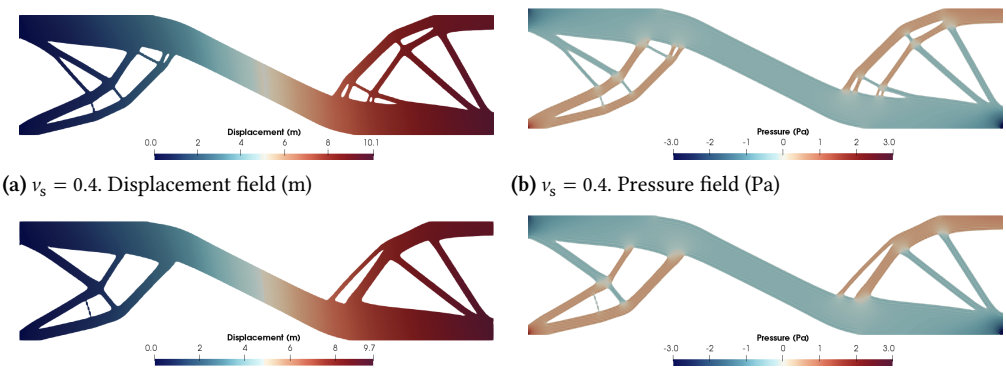

(a) $\nu_s = 0.4$. Displacement field (m) **(b)** $\nu_s = 0.4$. Pressure field (Pa)

(c) $\nu_s = 0.45$. Displacement field (m) **(d)** $\nu_s = 0.45$. Pressure field (Pa)

Figure 4.23: Single-point load beam. Final optimized structure for compressible materials with $\mathbf{u}p$ formulation.

Let us now apply the stabilized mixed formulations developed in Section 3 with the split MD expression (4.63). Fig. 4.23 shows both displacement and pressure fields of the final optimized structure, obtained with the $\mathbf{u}p$ formulation, when considering compressible materials. Both figures show almost the same solution, compared to the one obtained with a displacement-based formulation, shown in Figs. 4.22a-4.22b.

Fig. 4.24 presents the results obtained for both mixed formulations when dealing with a fully incompressible strong material. As it can be observed, plausible physical solutions are obtained and therefore, the TO problem for incompressible structures at finite strains can now be performed.

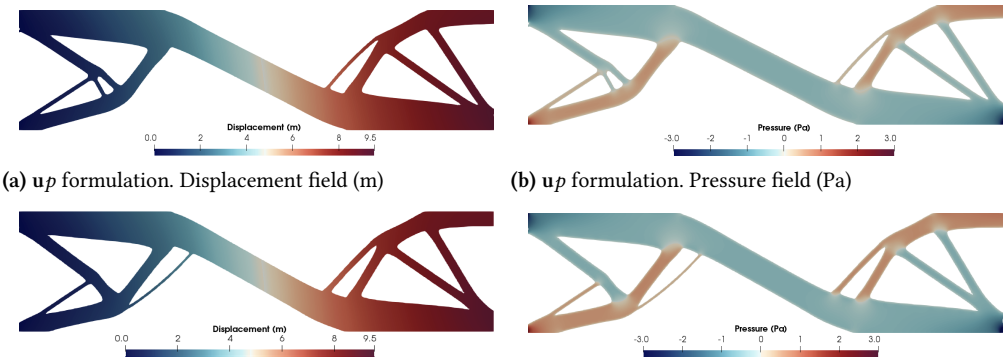

(a) $\mathbf{u}p$ formulation. Displacement field (m)

(b) $\mathbf{u}p$ formulation. Pressure field (Pa)

(c) $\mathbf{u}p\mathbf{S}'$ formulation. Displacement field (m)

(d) $\mathbf{u}p\mathbf{S}'$ formulation. Pressure field (Pa)

Figure 4.24: Single-point load beam. Final optimized structure in plane strain scenario for $\nu_s = 0.5$ for both $\mathbf{u}p$ and $\mathbf{u}p\mathbf{S}'$ formulations.

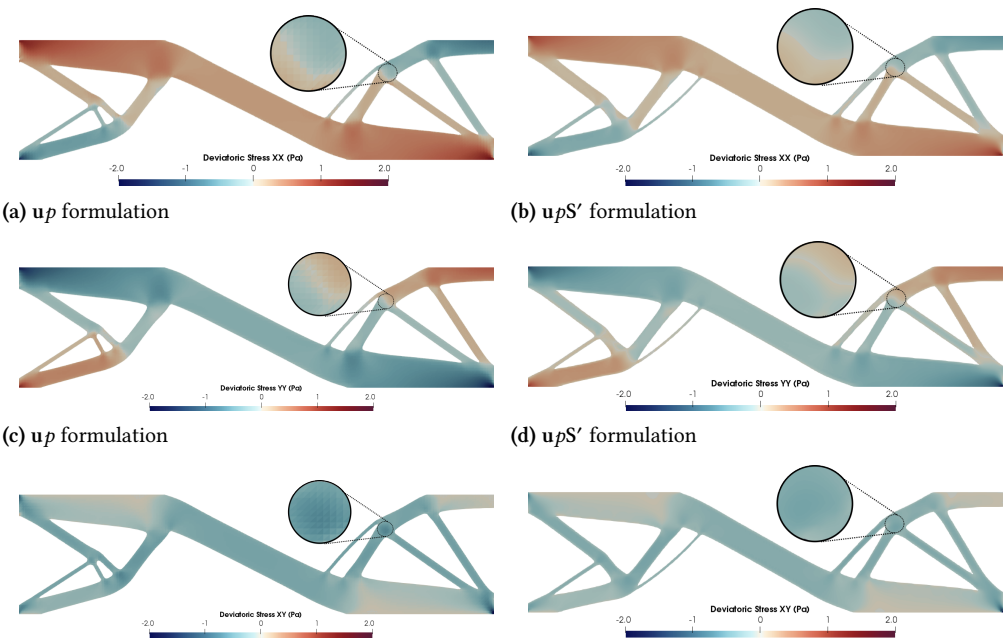

(a) $\mathbf{u}p$ formulation

(b) $\mathbf{u}p\mathbf{S}'$ formulation

(c) $\mathbf{u}p$ formulation

(d) $\mathbf{u}p\mathbf{S}'$ formulation

(e) $\mathbf{u}p$ formulation

(f) $\mathbf{u}p\mathbf{S}'$ formulation

Figure 4.25: Single-point load beam. Deviatoric stress field for the optimized structure for $\nu_s = 0.5$

The minor differences that can be noticed between formulations are caused by the different ways of computing the

stresses. In the $\mathbf{u}p$ formulation the deviatoric stresses are computed from the displacement gradient, whereas, in the $\mathbf{u}p\mathbf{S}'$ formulation, they are directly obtained as a nodal unknown.

For the sake of completeness, Fig. 4.25 shows the deviatoric stress field, obtained from both formulations. Using the $\mathbf{u}p$ formulation, the deviatoric stresses are computed from the displacement gradient and therefore defined element-wise. Because linear triangular elements were used, the stresses are element-wise constant, hence particularly imprecise. Using the $\mathbf{u}p\mathbf{S}'$ formulation however, the deviatoric stresses are also a primary unknown of the problem, and therefore defined at the nodes. The result is a continuous field, which is more precise in the first place and, secondly, does not require nodal smoothing for postprocessing.

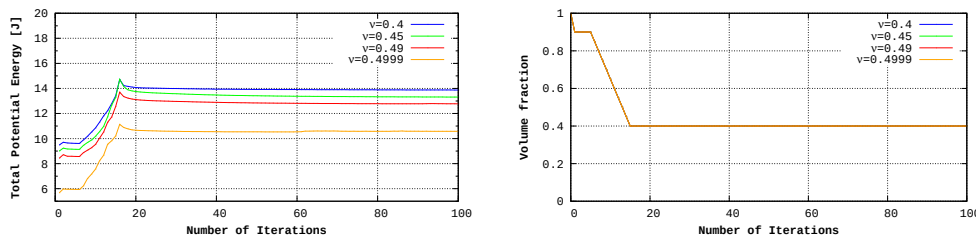

(a) Total potential energy (J) **(b)** Volume fraction

Figure 4.26: Single-point load beam. Convergence diagrams for the displacement-based formulation.

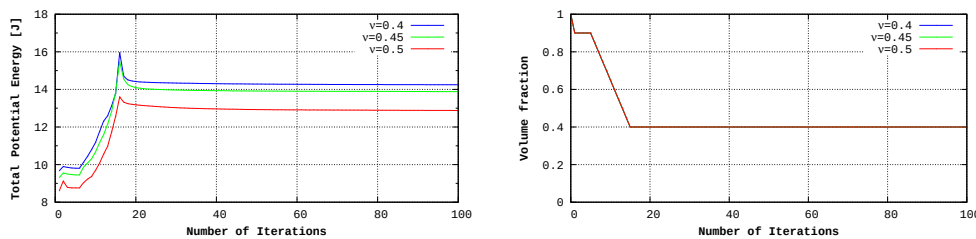

(a) Total potential energy (J) **(b)** Volume fraction

Figure 4.27: Single-point load beam. Convergence diagrams for up formulation.

Moving on to convergence issues, Figs. 4.26a-4.27a show a diagram referring to the total potential energy evolution recorded during the iterative TO procedure for both the u and $\mathbf{u}p$ formulations, respectively. A maximum of 100 iterations is imposed as stopping criteria to show the evolution of the objective functional. Both formulations need less than 100 iterations to minimize the compliance and achieve con-

vergence. To end up this numerical examples, Figs. 4.26b-4.27b present the evoluton of the volume fraction during the TO iterations. As previously commented, it is necessary to decrease the volume fraction professively due to the nonlinearities of the problem, in this case, until the required final volume fraction of 0.4.

3D Cantilever beam

The second example is the 3D Cantilever beam whose geometry is already shown in Fig 4.17. The structure is clamped at the left face and a uniform traction $t = 14$ N/m is applied at the lower edge of the right face. Stress free boundary conditions are applied on the remaining boundaries. We consider a Neo-Hookean material with a Quadratic law for the deviatoric part of the stresses, with a Young Modulus $E_s = 0.1$ MPa. Taking into account the symmetry of the problem, the left half of the design domain is discretized into 380,000 linear tetrahedral FEs. The required final volume is set to be 20% of the initial one

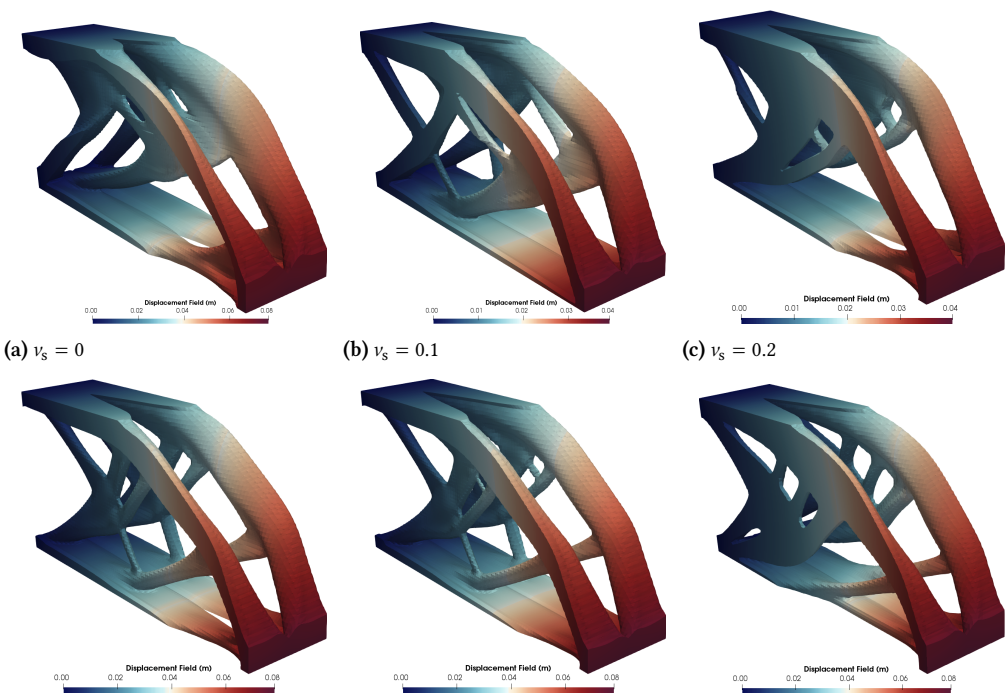

(a) $\nu_s = 0$ **(b)** $\nu_s = 0.1$ **(c)** $\nu_s = 0.2$

(d) $\nu_s = 0.3$ **(e)** $\nu_s = 0.4$ **(f)** $\nu_s = 0.45$

Figure 4.28: 3D Cantilever beam. Displacement field (m) for the optimized structure for compressible materials with irreducible formulation.

First of all, in Fig. 4.28 the final optimized structures for several Poisson ratios are displayed with the displacement-based formulation. As previously commented, the algorithm is capable of dealing with the TO problem for compressible materials.

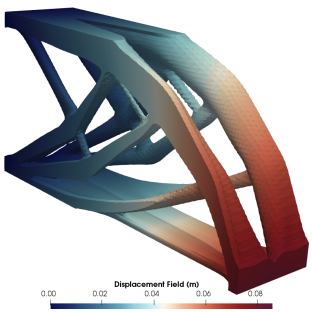

(a) up formulation

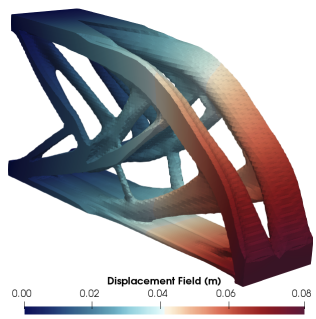

(b) upS′ formulation

Figure 4.29: 3D Cantilever beam. Displacement field for the optimized structure in a 3D scenario for $\nu_s = 0.5$.

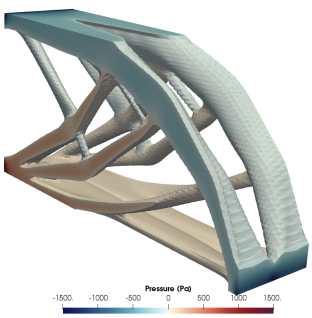

(a) up formulation

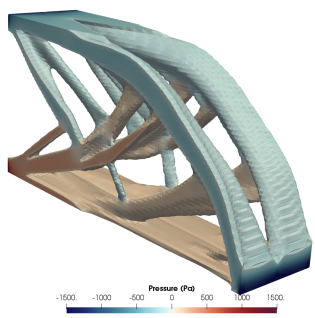

(b) upS′ formulation

Figure 4.30: 3D Cantilever beam. Pressure field for the optimized structure in a 3D scenario for $\nu_s = 0.5$.

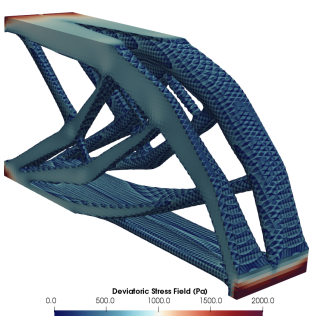

(a) up formulation

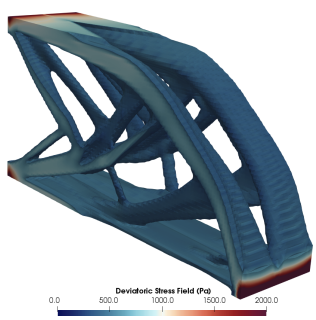

(b) upS′ formulation

Figure 4.31: 3D Cantilever beam. Deviatoric stress field for the optimized structure in a 3D scenario for $\nu_s = 0.5$.

Figs. 4.29-4.30 show the displacement and pressure fields for both formulations for a fully incompressible material. Fig. 4.31 presents the $L^2(\Omega)$-norm of the deviatoric PK2 stress field (Deviatoric Stress Field) for each formulation. Again,

a higher level of accuracy is obtained for the stresses computed from the mixed $\mathbf{u}p\mathbf{S}'$ formulation.

4.4 Conclusions

In this chapter we have proposed a new method for handling TO problems based on the TD concept for nearly and fully incompressible materials. First of all, for linear elastic materials and by departing from the splitting of the Polarization tensor into its deviatoric and spherical components, a new and simple expression for the TD has been found. With this formulation, the study of linear elasticity TO problems – while dealing with incompressible materials – is now possible.

The key to solving problems involving incompressibility was the introduction of two mixed stabilized FE formulations in Section 2.1. On one hand, the well-known $\mathbf{u}p$ formulation, in which the pressure is added as an unknown – the fundamental one, when dealing with incompressible materials. On the other hand, a relatively new three-field formulation $\mathbf{u}p\mathbf{e}$ which also adds the deviatoric strains as an unknown. In this setting, extra accuracy – particularly for strains and stresses – is obtained. This is due to the strains being no longer computed through the symmetric gradient of the displacement but directly as nodal unknowns. The computation of the TD benefits directly from this extra accuracy, since it depends directly on strains and stresses.

Thanks to the volumetric/deviatoric splitting, we have obtained two components for the Polarization tensor, one for computing the changes of the compliance shape functional caused by deviatoric effects and one for changes caused by volumetric effects. When the incompressible limit is reached, the former one presents no singularities, since it is being computed through both the deviatoric strains $\mathbf{e}$ and deviatoric stresses $\mathbf{s}$. The latter one depends on the pressure p and is formulated in terms of the bulk modulus κ to avoid singularities.

Regarding the topology optimization algorithm presented in Section 4.2.6, we have developed an iterative computation scheme for the TD. This was coupled with a level set strategy for the definition of the stiff and soft materials, which allows to keep a sharp track of the interface.

In Subsection 4.2.7 several numerical examples have been shown to asses the performance of the new split TD expression for linear elastic materials. Our formulation can automatically deal with the TO of structures regardless the incompressibility of the given material. We have shown the effects of considering an incompressible weak material and explained why this leads to undesired designs. Next, we have presented the main differences between the $\mathbf{u}p$ and the $\mathbf{u}p\mathbf{e}$ formulations with respect to the accuracy obtained for the main unknowns of the mechanical problem. Finally, a 3D example was shown to demonstrate the good performance of our implementation in a 3D case.

Next, we have proposed a methodology for handling TO problems using a MD for nearly and fully incompressible finite strain hyperelastic materials. Departing from an approximation for the TD, a simple expression for the MD has been found for incompressible materials.

Again, the main ingredient to solve problems involving incompressibility is the introduction of the two mixed stabilized FE formulations developed in Section 3.

In Subsection 4.3.7 several numerical examples have been shown to asses the performance of the new split MD expression for finite strain hyperelastic materials. Our formulation can automatically deal with the TO of structures regardless the incompressibility of the given material. Finally, a 3D example was shown to demonstrate the good performance of our implementation in a 3D case.

Numerical simulation of FSI problems with viscoelastic fluid flows

5

5.1 Introduction

Fluid-Structure Interaction (FSI) problems are nonlinear multi-physics phenomena found in many fields of engineering and applied sciences, such as aircraft and ship building [112], safe bridge design or biomedical applications [113]. They model the two-way coupling corresponding to a structure and the fluid that surrounds it. FSI problems considering Newtonian fluids have been widely studied and modeled in the past decades [114–116]. However, in some cases, fluids have a complex rheological behavior and classical Newtonian fluid models are not suitable.

A very interesting family of non-Newtonian fluids are viscoelastic fluids, which exhibit both viscous and elastic properties. Their complex internal structure and high-molecular-weight explain this particular combination of properties [117]. Moreover, viscoelastic fluids have the ability to store and recover shear-energy [118]. This justifies the necessity of considering an irreducible tensorial constitutive equation that allows one to describe their elastic nature. Numerically, this yields a coupled three-field problem where the unknowns are the elastic deviatoric stress, the velocity and the pressure [119]. In our case, both this problem and the coupled solid mechanics problem will be approximated using the FEM.

Viscoelastic Fluid-Structure Interaction (VFSI) problems are mainly encountered in biomedical research, such as blood flow in arteries or veins [120–123]. In addition, viscoelastic behavior of fluids is prevalent in a wide range of applications, including food processing, pharmaceuticals or the chemical industry [124]. One of the most important applications is in microfluidic devices, for instance memory and control devices [125] and microfluidic rectifiers [126]. However, VFSI problems in which the elasticity is dominant have not been addressed significantly. This could be explained due to the fact that computing viscoelastic fluid flows leads to several instabilities in such scenarios [127]. The dimensionless number known as the *Weissenberg number*, which is a ratio between elastic and viscous forces, is high. This number is defined as $\mathrm{We} = \lambda u/L$, where λ is the characteristic relaxation

[112]: Kamakoti et al. (2004), "Fluid-structure interaction for aeroelastic applications"

[113]: Bodnár et al. (2014), *Fluid-Structure Interactions and Biomedical Applications*

[114]: Küttler et al. (2008), "Fixed-point fluid–structure interaction solvers with dynamic relaxation"

[115]: Richter et al. (2010), "Finite Elements for Fluid-Structure Interaction in ALE and Fully Eulerian coordinates"

[116]: Richter (2017), *Fluid-Structure Interactions*

[117]: Ueda et al. (2002), "Viscoelastic properties of paint films and formability in deep drawing of pre-painted steel sheets"

[118]: Chhabra et al. (2011), *Non-Newtonian flow and applied rheology: engineering applications*

[119]: Castillo et al. (2021), "Stabilised Variational Multi-scale Finite Element Formulations for Viscoelastic Fluids"

[120]: Bathe et al. (1999), "A fluid-structure interaction finite element analysis of pulsatile blood flow through a compliant stenotic artery"

[121]: Ma et al. (1992), "Numerical simulation for the propagation of nonlinear pulsatile waves in arteries"

[122]: Perktold et al. (1995), "Computer simulation of local blood flow and vessel mechanics in a compliant carotid artery bifurcation model"

[123]: Tang et al. (1999), "A nonlinear axisymmetric model with fluid–wall interactions for steady viscous flow in stenotic elastic tubes"

[124]: Squires et al. (2005), "Microfluidics: Fluid physics at the nanoliter scale"

[125]: Groisman et al. (2003), "Microfluidic memory and control devices"

[126]: Amani et al. (2018), "A method for fluid-structure interaction problems with non-Newtonian fluid"

time of the material, u is the characteristic velocity of the flow, and L is the characteristic length of the domain. The numerical instability is brought about by the failure to compute the proper balance between the deformation rate and convection term. It is a fundamental instability, present in all constitutive models and standard numerical methods. Nevertheless, it is demonstrated that constitutive methods can predict other instabilities of mathematical character [128, 129], referred to as *constitutive instabilities*.

[127]: Fattal et al. (2005), "Time-dependent simulation of viscoelastic flows at high Weissenberg number using the log-conformation representation"

[128]: Leonov (1992), "Analysis of simple constitutive equations for viscoelastic liquids"

[129]: Kwon (2002), "Recent results on the analysis of viscoelastic constitutive equations"

[130]: Owens et al. (2002), *Computational rheology*

The difficulties when simulating high Weissenberg number flows are commonly known as the High Weissenberg Number Problem (HWNP) [130]. This is a well-known numerical phenomenon that causes the iterative non-linearity computations to breakdown for relatively low Weissenberg numbers. Usually, this manifests as a lack of convergence in the iterative method due to the hyperbolic nature of the differential constitutive equations. The source of the HWNP was recently identified: firstly, the loss of positive-definiteness of the conformation tensor, an internal variable which should be symmetric positive-definite to be physically admissible [131, 132]; secondly, regions with particularly high deformation rate, or near stagnation points, favor the breakdown of the numerical method, as it is explained by Fattal and Kupferman in [127, 131]. They describe the cause of this phenomenon as the use of inappropriate approximations to represent the stress tensor, remarking the importance of preserving its positivity.

[131]: Fattal et al. (2004), "Constitutive laws for the matrix-logarithm of the conformation tensor"

[132]: Hulsen et al. (1997), "Simulation of viscoelastic flows using Brownian configuration fields"

By following these ideas, a new formulation was proposed in [131], the so-called log-conformation reformulation (LCR), a representation of the standard equations of viscoelastic fluids, which alleviates the instability and linearizes the exponential stress profiles near the stress singularities. The aim is to treat the exponential growth of the elastic stresses, and therefore allowing to extend the range of Weissenberg numbers for computing the fluid flow. This technique will be applied in the present paper for simulating VFSI problems with high elasticity, following the modifications introduced in [15]. Although there are a variety of proposals to deal with the lack of positive-definiteness of the conformation tensor, the LCR representation is the only one capable of linearizing a exponential stress profile.

[15]: Moreno et al. (2019), "Logarithmic conformation reformulation in viscoelastic flow problems approximated by a VMS-type stabilized finite element formulation"

Due to the difficulties enumerated previously, few works can be found in which the VFSI problem is solved. For example,

in [133] some simulations for a fluid flow in a two-dimensional channel with a deformating wall are performed. Also, [134] studies the effect of the initial configuration of the governing equations on flows in a collapsible channel with an upper elastic wall. More recently, in [135], the interaction between an Oldroyd-B fluid and an elastic structure is explored by applying an implicit partitioned coupling algorithm.

In this chapter, we stabilize the approximation of the flow equations using the Variational Multi-Scale (VMS) method, introduced in [6] for the scalar convection-diffusion-reaction problem and later extended to the Navier-Stokes problem in [13, 25, 136]. In this last reference, the space of the subgrid scales of the formulation was taken as orthogonal to the FE space. This idea was adapted to the viscoelastic flow problem in [14]. Finally, for the LCR in viscoelastic fluid flow problems several methods were developed in [15].

The objective of this chapter is to study the interaction between Oldroyd-B viscoelastic fluids and hyperelastic solids using numerical schemes in a FEM framework. Moreover, the reformulation of the viscoelastic classical equations will be considered so as to be able to compute converged solutions for fluids with high elasticity. Therefore, the novelty of the work is the development of a method able to compute problems with high elastic regimes for FSI problems through the use of a stabilized LCR representation.

This chapter is organized as follows. In Section 5.2 the solid dynamics equations are summarized for hyperelastic material models. In Section 5.3 the Navier-Stokes problem in the three-field formulation for Newtonian and viscoelastic fluids with an Arbitrary Lagrangian-Eulerian (ALE) description of the fluid equations is presented. Next, in Section 5.4, the VFSI problem is presented to solve the coupled problem in a staggered approach. In Section 5.5 several VFSI numerical examples are presented and discussed to study the interaction between a viscoelastic fluid and an elastic solid. Finally, in Section 5.6 some conclusions are drawn.

[133]: Chakraborty et al. (2007), "Viscoelastic fluid flow in a 2D channel bounded above by a deformable finite thickness elastic wall"

[134]: Luo et al. (2007), "On the initial configurations of collapsible channel flow"

[135]: Chen (2014), "Numerical Modeling of Fluid-Structure Interaction with Rheologically Complex Fluids"

[6]: Hughes et al. (1998), "The variational multiscale method - A paradigm for computational mechanics"

[13]: Codina (2002), "Stabilized finite element approximation of transient incompressible flows using orthogonal subscales"

[25]: Codina (2000), "Stabilization of incompressibility and convection through orthogonal subscales in finite element methods"

[136]: Codina (2008), "Analysis of a stabilized finite element approximation of the Oseen equations using orthogonal subscales"

[14]: Castillo et al. (2014), "Variational multi-scale stabilized formulations for the stationary three-field incompressible viscoelastic flow problem"

5.2 Solid dynamics problem

5.2.1 Conservation equations

Let us start from the conservation equations already presented in Section 3.2. The conservation of linear momentum problem in finite strain theory for an ULF framework reads

$$\rho_s \frac{\partial^2 \mathbf{u}_s}{\partial t^2} - \nabla \cdot \boldsymbol{\sigma}_s = \rho_s \mathbf{b} \quad \text{in } \Omega_s(t) \times]0, T[\,, \tag{5.1}$$

where ρ_s is the density at the current configuration, $\mathbf{u}_s$ is the displacement field, $\boldsymbol{\sigma}_s$ is the Cauchy stress tensor and $\mathbf{b}$ the field of body accelerations. Mass conservation implies that

$$\rho_s J_s = \rho_{s,0} \quad \text{in } \Omega_s(t) \times]0, T[\,, \tag{5.2}$$

where $J_s = \det \mathbf{F}_s$ is the Jacobian, $\mathbf{F}_s = \frac{\partial \mathbf{x}}{\partial \mathbf{X}}$ is the deformation gradient and $\rho_{s,0}$ is the density at the initial configuration. With regards to the balance of angular momentum, it implies that the Cauchy stress tensor must be symmetric.

In this chapter, we restrict ourselves to isotropic hyperelastic models written in their coupled form as introduced in Subsection 2.1.2.

5.2.2 Governing equations

We introduce now the solid dynamics problem in detail. Let $\mathfrak{D}_s = \{(\mathbf{x}, t) | \mathbf{x} \in \Omega_s(t),\ 0 < t < T\}$ be the space-time domain where the problem is defined. The problem consists of finding a displacement $\mathbf{u}_s : \mathfrak{D}_s \longrightarrow \mathbb{R}^d$ such that

Finite strain hyperelasticity. u formulation. Governing equations in ULF

$$\rho_s \frac{\partial^2 \mathbf{u}_s}{\partial t^2} - \nabla \cdot \boldsymbol{\sigma}_s = \rho_s \mathbf{b} \quad \text{in } \Omega_s(t) \times]0, T[\,, \tag{5.3}$$

$$\mathbf{u}_s = \mathbf{u}_{s,D} \quad \text{on } \Gamma_{s,D}(t) \times]0, T[\,, \tag{5.4}$$

$$\mathbf{n}_s \cdot \boldsymbol{\sigma}_s = \mathbf{t}_{s,N} \quad \text{on } \Gamma_{s,N}(t) \times]0, T[\,, \tag{5.5}$$

$$\mathbf{u}_s = \mathbf{u}_s^0 \quad \text{in } \Omega_s(0),\ t = 0, \tag{5.6}$$

$$\frac{\partial \mathbf{u}_s}{\partial t} =: \mathbf{v}_s = \mathbf{v}_s^0 \quad \text{in } \Omega_s(0),\ t = 0. \tag{5.7}$$

A set of boundary conditions is considered which can be split into Dirichlet boundary conditions (5.4), where the displacement is prescribed, and Neumann boundary conditions (5.5), where the value of tractions $\mathbf{t}_{s,N}$ is prescribed. Vector $\mathbf{n}_s$ is the geometric unit outward normal vector on the boundary of the current configuration $\Gamma_s(t)$. The governing equations must be supplied with initial conditions for both the displacement field (5.6) and the velocity field (5.7) in $\Omega_s(0)$, with $\mathbf{u}_s^0$ and $\mathbf{v}_s^0$ given.

5.2.3 Variational form

Let Ω be the domain where a problem needs to be solved. In the case of the solid dynamics problem we are now considering, $\Omega = \Omega_s(t)$. Let $\mathbb{U} := \{\mathbf{u} \in H^1(\Omega_s(t))^d \mid \mathbf{u} = \mathbf{u}_{s,D} \text{ on } \Gamma_{s,D}(t)\}$ be the functional space where the displacement solution is well-defined for each fixed time $t \in]0,T[$. We denote by $\mathbb{U}_0$ functions in $H^1(\Omega_s(t))^d$ which vanish on the Dirichlet boundary $\Gamma_{s,D}(t)$. Note that these spaces vary in time.

The variational statement of the problem is derived by testing Eq. (5.3) against arbitrary test function, $\delta\mathbf{u} \in \mathbb{U}_0$. The weak form of the problem reads: find $\mathbf{u}_s :]0,T[\to \mathbb{U}$ such that initial conditions are satisfied and

Finite strain hyperelasticity. u formulation. Variational form in ULF

$$\left\langle \delta\mathbf{u}, \rho_s \frac{\partial^2 \mathbf{u}_s}{\partial t^2} \right\rangle + \langle \nabla^s \delta\mathbf{u}, \boldsymbol{\sigma}_s \rangle = \langle \delta\mathbf{u}, \rho_s \mathbf{b} \rangle + \left\langle \delta\mathbf{u}, \mathbf{t}_{s,N} \right\rangle_{\Gamma_{s,N}} \quad \forall \delta\mathbf{u} \in \mathbb{U}_0, \tag{5.8}$$

where $\nabla^s \delta\mathbf{u}$ is the symmetrical part of $\nabla \delta\mathbf{u}$. As usual, integration by parts has been used in order to decrease the continuity requirements of the unknown $\mathbf{u}_s$.

5.2.4 Galerkin spatial discretization

We denote by $\mathscr{P}_h$ a FE partition of the domain Ω of the problem. The diameter of an element domain $K \in \mathscr{P}_h$ is denoted by h_K and the diameter on the FE partition by $h = \max\{h_K | K \in \mathscr{P}_h\}$. Now we consider the case in which $\Omega = \Omega_s(t)$ is the solid domain. From the FE partition we can construct conforming

FE spaces $\mathbb{U}_h \subset \mathbb{U}$, as well as the corresponding subspace $\mathbb{U}_{h,0} \subset \mathbb{U}_0$ being made of functions that vanish on the Dirichlet boundary.

The Galerkin discrete version of problem (5.8) is: find $\mathbf{u}_{s,h} :]0,T[\to \mathbb{U}_h$ such that

Finite strain hyperelasticity. u formulation. Galerkin discrete problem in ULF

$$\left\langle \delta\mathbf{u}_{s,h}, \rho_s \frac{\partial^2 \mathbf{u}_{s,h}}{\partial t^2} \right\rangle + \left\langle \nabla^s \delta\mathbf{u}_{s,h}, \boldsymbol{\sigma}_{s,h} \right\rangle = \left\langle \delta\mathbf{u}_{s,h}, \rho_s \mathbf{b} \right\rangle + \left\langle \delta\mathbf{u}_{s,h}, \mathbf{t}_{s,N} \right\rangle_{\Gamma_{s,N}} \quad \forall \delta\mathbf{u}_h \in \mathbb{U}_{h,0}, \tag{5.9}$$

and satisfying the appropriate initial conditions. This system can be solved by using a Newton-Raphson linearization scheme (see [9] for further details on linearization methods).

[9]: Bonet et al. (1997), *Nonlinear Continuum mechanics for finite element analysis*

5.2.5 Time discretization

For the sake of conciseness, in this work only the implicit BDF2 is considered (see Section 3.4 for further details). In our problem, we have to approximate the second time derivative of the displacement $\left.\frac{\partial^2 \mathbf{u}_s}{\partial t^2}\right|_{t^{n+1}} := \mathbf{a}_s^{n+1}$. Therefore

$$\left.\frac{\delta_2^2 \mathbf{u}_s}{\delta t^2}\right|_{t^{n+1}} := \frac{1}{\Delta t^2}\left[2\mathbf{u}_s^{n+1} - 5\mathbf{u}_s^n + 4\mathbf{u}_s^{n-1} - \mathbf{u}_s^{n-2}\right] = \mathbf{a}_s^{n+1} + \mathcal{O}\left(\Delta t^2\right). \tag{5.10}$$

Appropriate initializations are required for $n = 1, 2$. Note that the resulting time integration scheme will not be energy-conserving (geometric or symplectic), but has the well-known dissipation of the BDF2 scheme.

5.3 Viscoelastic fluid flow problem

In this section the governing equations that model the viscoelastic fluid flow in both standard and LCR representations are presented. The approach followed can be understood as the traditional one in a broad sense, where an ULF is used to

deal with the solid dynamics problem while the fluid problem is solved by means of an ALE formulation to cope with the time dependency of the fluid domain.

5.3.1 ALE formulation of the fluid flow equations

Let now $\Omega_{\mathrm{f}}(t)$ be the domain where the fluid flows, with boundary $\Gamma_{\mathrm{f}}(t) := \partial\Omega_{\mathrm{f}}(t) = \Gamma_{\mathrm{f},N}(t) \cup \Gamma_{\mathrm{f},D}(t)$, where Dirichlet boundary conditions are prescribed on $\Gamma_{\mathrm{f},D}(t)$ and Neumann conditions on $\Gamma_{\mathrm{f},N}(t)$. These boundaries may be moving.

Let $\boldsymbol{\chi}_t$ be a family of invertible mappings, which for all $t \in [0,T]$ map a point $\mathbf{X} \in \Omega_{\mathrm{f}}(0)$ to a point $\mathbf{x} = \boldsymbol{\chi}_t(\mathbf{X}) \in \Omega_{\mathrm{f}}(t)$, with $\boldsymbol{\chi}_0 = \mathbf{I}$, the identity. If $\boldsymbol{\chi}_t$ is given by the motion of the particles, the resulting formulation would be Lagrangian, whereas if $\boldsymbol{\chi}_t = \mathbf{I}$ for all t, $\Omega_{\mathrm{f}}(t) = \Omega_{\mathrm{f}}(0)$ and the formulation would be Eulerian. Let now $t' \in [0,T]$, with $t' \leq t$, and consider the mapping

$$\begin{aligned} \boldsymbol{\chi}_{t,t'} \; : \; & \Omega_{\mathrm{f}}(t') \longrightarrow \Omega_{\mathrm{f}}(t) \\ & \mathbf{x}' \mapsto \mathbf{x} = \boldsymbol{\chi}_t \circ \boldsymbol{\chi}_{t'}^{-1}(\mathbf{x}'). \end{aligned} \tag{5.11}$$

Let $\mathfrak{D}_{\mathrm{f}} = \{(\mathbf{x},t) | \mathbf{x} \in \Omega_{\mathrm{f}}(t),\ 0 < t < T\}$ be the space-time domain where the flow problem is defined. Given a function $f : \mathfrak{D}_{\mathrm{f}} \longrightarrow \mathbb{R}$ we define

$$\left.\frac{\partial f}{\partial t}\right|_{\mathbf{x}'} (\mathbf{x},t) := \frac{\partial (f \circ \boldsymbol{\chi}_{t,t'})}{\partial t}(\mathbf{x}',t), \quad \mathbf{x} \in \Omega_{\mathrm{f}}(t),\ \mathbf{x}' \in \Omega_{\mathrm{f}}(t'). \tag{5.12}$$

In particular, the domain velocity taking as a reference the coordinates of $\Omega_{\mathrm{f}}(t')$ is given by

$$\mathbf{v}_{\mathrm{dom}} := \left.\frac{\partial \mathbf{x}}{\partial t}\right|_{\mathbf{x}'} (\mathbf{x},t). \tag{5.13}$$

Using the ALE reference, the only modification with respect to the purely Eulerian formulation is to replace the transport velocity $\mathbf{v}_{\mathrm{f}}$ of the advective term by $\mathbf{v}_{\mathrm{c}} := \mathbf{v}_{\mathrm{f}} - \mathbf{v}_{\mathrm{dom}}$. If $\mathbf{v}_{\mathrm{dom}} = \mathbf{0}$ we would recover a purely Eulerian formulation for the viscoelastic fluid.

When the flow equations are approximated using the FE method, $\mathbf{v}_{\mathrm{dom}}$ needs to be computed. It is assumed to be given on

the boundary $\Gamma_f(t)$, obtained from its position at two consecutive time steps, say t^n and t^{n+1}; thus, $t' = t^n$ and $t = t^{n+1}$ using the above terminology. To compute the values for the interior of the domain, a mesh equation must be solved. The mesh equation we use is proposed in [137]. The method considers the mesh as a fictitious linear elastic body subjected to prescribed displacements at the selected moving boundaries. The mechanical properties of each mesh element are appropriately selected in order to minimize the deformation and the distortion of the mesh elements. The mesh equation is explicitly shown in Algorithm 1.

[137]: Chiandussi et al. (1999), "A simple method for automatic update of finite element meshes"

5.3.2 Governing equations

We present now the equations associated to the incompressible viscoelastic fluid flow in $\Omega_f(t)$, accounting also for the motion of this domain. The problem to be solved is written as follows: find a velocity $\mathbf{v}_f : \mathfrak{D}_f \longrightarrow \mathbb{R}^d$, a pressure $p_f : \mathfrak{D}_f \longrightarrow \mathbb{R}$ and a deviatoric stress tensor $\mathbf{T}_f : \mathfrak{D}_f \longrightarrow \mathbb{R}^d \otimes \mathbb{R}^d$, such that

Viscoelastic fluid flow. v$p\boldsymbol{\sigma}$ formulation. Governing equations in ALE approach

$$\rho_f \frac{\partial \mathbf{v}_f}{\partial t} + \rho_f \mathbf{v}_c \cdot \nabla \mathbf{v}_f - \nabla \cdot \mathbf{T}_f + \nabla p_f = \mathbf{f} \qquad \text{in } \Omega_f(t) \times]0, T[, \tag{5.14}$$

$$\nabla \cdot \mathbf{v}_f = 0 \qquad \text{in } \Omega_f(t) \times]0, T[, \tag{5.15}$$

$$\frac{1}{2\mu_f^p}\boldsymbol{\sigma}_f - \nabla^s \mathbf{v}_f + \frac{\lambda}{2\mu_f^p}\Big(\frac{\partial \boldsymbol{\sigma}_f}{\partial t} + \mathbf{v}_c \cdot \nabla \boldsymbol{\sigma}_f - \boldsymbol{\sigma}_f \cdot \nabla \mathbf{v}_f - (\nabla \mathbf{v}_f)^T \cdot \boldsymbol{\sigma}_f\Big) = \mathbf{0} \qquad \text{in } \Omega_f(t) \times]0, T[, \tag{5.16}$$

$$\mathbf{v}_f = \mathbf{v}_{f,D} \qquad \text{on } \Gamma_{f,D}(t) \times]0, T[, \tag{5.17}$$

$$\mathbf{n}_f \cdot \boldsymbol{\sigma}_f = \mathbf{t}_{f,N} \qquad \text{on } \Gamma_{f,N}(t) \times]0, T[, \tag{5.18}$$

$$\mathbf{v}_f = \mathbf{v}_f^0 \qquad \text{in } \Omega_f(0), t = 0, \tag{5.19}$$

$$\boldsymbol{\sigma}_\mathrm{f} = \boldsymbol{\sigma}_\mathrm{f}^0 \qquad \text{in } \Omega_\mathrm{f}(0), t = 0, \tag{5.20}$$

where ρ_f denotes the constant density and $\mathbf{f}$ is the force field. Note that the convective term in both the momentum and constitutive equations has been written in non-conservation form. Despite having large gradients, the solution to these equations are expected to be smooth, without discontinuities; these would require the conservation form of the convective terms.

In general, $\mathbf{T}_\mathrm{f}$ is defined in terms of a viscous and a viscoelastic contribution as $\mathbf{T}_\mathrm{f}(\mathbf{v}_\mathrm{f}, \boldsymbol{\sigma}_\mathrm{f}) = 2\mu_\mathrm{f}^s \nabla^\mathrm{s}\mathbf{v}_\mathrm{f} + \boldsymbol{\sigma}_\mathrm{f}$, where $\boldsymbol{\sigma}_\mathrm{f}$ is the viscoelastic or elastic stress tensor. Note that the effective (or solvent) viscosity μ_f^s and the polymeric viscosity μ_f^p can be written as function of the total viscosity $\mu_\mathrm{f}^0 = \mu_\mathrm{f}^s + \mu_\mathrm{f}^p$. Therefore, an additional parameter $\beta \in [0, 1]$ is introduced to define $\mu_\mathrm{f}^s = \beta\mu_\mathrm{f}^0$ and $\mu_\mathrm{f}^p = (1-\beta)\mu_\mathrm{f}^0$. To complete the system which models the viscoelastic fluid, the constitutive equation for the viscoelastic stress tensor is defined. We employ the Oldroyd-B model (5.16), where λ is the relaxation time. Regarding the boundary conditions, $\mathbf{v}_{\mathrm{f},D}$ is a prescribed velocity on the boundary $\Gamma_{\mathrm{f},D}(t)$, $\mathbf{t}_{\mathrm{f},N}$ is a prescribed traction on the boundary $\Gamma_{\mathrm{f},N}(t)$ and $\mathbf{n}_\mathrm{f}$ is the normal to the boundary of the fluid domain. Finally, $\mathbf{v}_\mathrm{f}^0$ is the prescribed initial velocity, and $\boldsymbol{\sigma}_\mathrm{f}^0$ the prescribed initial elastic stress in $\Omega_\mathrm{f}(0)$.

In order to distinguish operators between standard and LCR formulations, we use the subscripts "std" and "log" from this point on. Also, we define operators $\mathscr{L}_\mathrm{std}$ and $\mathscr{D}_\mathrm{std}$, useful in the next subsections. Let us introduce $\mathbf{V} := [\mathbf{v}_\mathrm{f}, p_\mathrm{f}, \boldsymbol{\sigma}_\mathrm{f}]^T$, $\mathbf{f}_\mathrm{std} := [\mathbf{f}, 0, \mathbf{0}]^T$. Then, we define

$$\mathscr{L}_\mathrm{std}(\hat{\mathbf{v}}_\mathrm{f}; \mathbf{V}) := \begin{pmatrix} -\nabla\cdot\boldsymbol{\sigma}_\mathrm{f} - 2\mu_\mathrm{f}^s \nabla\cdot(\nabla^\mathrm{s}\mathbf{v}_\mathrm{f}) + \rho_\mathrm{f}\hat{\mathbf{v}}_\mathrm{c}\cdot\nabla\mathbf{v}_\mathrm{f} + \nabla p_\mathrm{f} \\ \nabla\cdot\mathbf{v}_\mathrm{f} \\ \dfrac{1}{2\mu_\mathrm{f}^p}\boldsymbol{\sigma}_\mathrm{f} - \nabla^\mathrm{s}\mathbf{v}_\mathrm{f} + \dfrac{\lambda}{2\mu_\mathrm{f}^p}\left(\hat{\mathbf{v}}_\mathrm{c}\cdot\nabla\boldsymbol{\sigma}_\mathrm{f} - 2\boldsymbol{\sigma}_\mathrm{f}\cdot\nabla^\mathrm{s}\hat{\mathbf{v}}_\mathrm{f}\right) \end{pmatrix}, \tag{5.21}$$

where $\hat{\mathbf{v}}_\mathrm{c} = \hat{\mathbf{v}}_\mathrm{f} - \mathbf{v}_\mathrm{dom}$. The notation $\hat{\mathbf{v}}_\mathrm{f}$ is introduced to distinguish the different arguments in which the velocity appears. Likewise

$$\mathscr{D}_\mathrm{std}(\mathbf{V}) := \begin{pmatrix} \rho_\mathrm{f}\dfrac{\partial\mathbf{v}_\mathrm{f}}{\partial t} \\ 0 \\ \dfrac{\lambda}{2\mu_\mathrm{f}^p}\dfrac{\partial\boldsymbol{\sigma}_\mathrm{f}}{\partial t} \end{pmatrix}. \tag{5.22}$$

As a consequence, Eqs. (5.14)-(5.16) can be rewritten, considering $\mathscr{D}_t = \mathscr{D}_{\text{std}}$, $\mathscr{L} = \mathscr{L}_{\text{std}}$ and $\mathbf{f} = \mathbf{f}_{\text{std}}$, as

$$\mathscr{D}_t(\mathbf{V}) + \mathscr{L}(\mathbf{v}_\text{f}; \mathbf{V}) = \mathbf{f}. \tag{5.23}$$

We will now briefly describe the viscoelastic equations when the LCR is considered. The LCR representation basically consists of a change of variables in terms of the matrix-logarithm of the conformation tensor, in other words, the conformation tensor is replaced by a new variable $\boldsymbol{\psi}_\text{f} = \log(\boldsymbol{\tau}_\text{f})$. Recall that this method is employed for addressing the incapability of the standard equations of solving problems with high elasticity. The change of variables allows one to preserve the positive-definiteness property of the conformation tensor and therefore it eliminates the instability and linearizes the exponential stress profiles near the stress singularities. The complete development employed is extensively explained in [15]. This reformulation is derived basically from that change of variables, where the stress tensor is replaced by $\boldsymbol{\sigma}_\text{f} = \mu_\text{f}^p \lambda_0^{-1}(\boldsymbol{\tau}_\text{f} - \mathbf{I})$, and in turn, the conformation tensor $\boldsymbol{\tau}_\text{f}$ is written as $\boldsymbol{\tau}_\text{f} = \exp(\boldsymbol{\psi}_\text{f})$ in Eqs. (5.14)–(5.16). λ_0 is defined as $\lambda_0 = \max\{k\lambda, \lambda_{0,\text{min}}\}$, k being a constant and $\lambda_{0,\text{min}}$ a given threshold. Therefore, the new equations of the LCR approach are expressed as follows:

Viscoelastic fluid flow. LCR formulation. Governing equations in ALE approach

$$\rho_\text{f}\frac{\partial \mathbf{v}_\text{f}}{\partial t} - \frac{\mu_\text{f}^p}{\lambda_0}\nabla\cdot\exp(\boldsymbol{\psi}_\text{f})$$
$$-2\mu_\text{f}^s\nabla\cdot(\nabla^\text{s}\mathbf{v}_\text{f}) + \rho_\text{f}\mathbf{v}_\text{c}\cdot\nabla\mathbf{v}_\text{f} + \nabla p_\text{f} = \mathbf{f} \qquad \text{in } \Omega_\text{f}(t)\times]0,T[\,, \tag{5.24}$$

$$\nabla\cdot\mathbf{v}_\text{f} = 0 \qquad \text{in } \Omega_\text{f}(t)\times]0,T[\,, \tag{5.25}$$

$$\frac{1}{2\lambda_0}(\exp(\boldsymbol{\psi}_\text{f}) - \mathbf{I}) - \nabla^\text{s}\mathbf{v}_\text{f}$$
$$+\frac{\lambda}{2\lambda_0}\left(\frac{\partial\exp(\boldsymbol{\psi}_\text{f})}{\partial t} + \mathbf{v}_\text{c}\cdot\nabla\exp(\boldsymbol{\psi}_\text{f})\right)$$
$$-\frac{\lambda}{\lambda_0}(-\exp(\boldsymbol{\psi}_\text{f})\cdot\nabla^\text{s}\mathbf{v}_\text{f} - 2\nabla^\text{s}\mathbf{v}_\text{f}) = 0 \qquad \text{in } \Omega_\text{f}(t)\times]0,T[\,, \tag{5.26}$$

$$\mathbf{v}_\mathrm{f} = \mathbf{v}_{\mathrm{f},D} \quad \text{on } \Gamma_{\mathrm{f},D}(t) \times]0,T[\,, \tag{5.27}$$

$$\mathbf{n}_\mathrm{f}(t) \cdot \frac{\mu_\mathrm{f}^p}{\lambda_0}(\exp(\boldsymbol{\psi}_\mathrm{f}) - \mathbf{I}) = \mathbf{t}_{\mathrm{f,N}} \quad \text{on } \Gamma_{\mathrm{f},N}(t) \times]0,T[\,, \tag{5.28}$$

$$\mathbf{v}_\mathrm{f} = \mathbf{v}_\mathrm{f}^0 \quad \text{in } \Omega_\mathrm{f}(0),\ t = 0, \tag{5.29}$$

$$\boldsymbol{\psi}_\mathrm{f} = \boldsymbol{\psi}_\mathrm{f}^0 \quad \text{in } \Omega_\mathrm{f}(0),\ t = 0, \tag{5.30}$$

where the unknowns are the velocity, the pressure, and tensor $\boldsymbol{\psi}_\mathrm{f}$. Note that the last variable depends directly on the stress tensor $\boldsymbol{\sigma}_\mathrm{f}$. Analogously to what was done for the standard formulation, calling $\mathbf{V} := [\mathbf{v}_\mathrm{f}, p_\mathrm{f}, \boldsymbol{\psi}_\mathrm{f}]^T$, $\mathbf{f}_\mathrm{log} := [\mathbf{f}, 0, \frac{1}{2\lambda_0}\mathbf{I}]^T$, we introduce

$$\mathscr{L}_\mathrm{log}(\hat{\mathbf{v}}_\mathrm{f}; \mathbf{V}) := \begin{pmatrix} -\frac{\mu_\mathrm{f}^p}{\lambda_0}\nabla \cdot \exp(\boldsymbol{\psi}_\mathrm{f}) - 2\mu_\mathrm{f}^s \nabla \cdot (\nabla^\mathrm{s}\mathbf{v}_\mathrm{f}) \\ \times\,]0,T[+ \rho_\mathrm{f}\hat{\mathbf{v}}_\mathrm{c} \cdot \nabla \mathbf{v}_\mathrm{f} + \nabla p_\mathrm{f} \\ \nabla \cdot \mathbf{v}_\mathrm{f} \\ \frac{1}{2\lambda_0}\exp(\boldsymbol{\psi}_\mathrm{f}) - \nabla^\mathrm{s}\mathbf{v}_\mathrm{f} + \frac{\lambda}{2\lambda_0}(\hat{\mathbf{v}}_\mathrm{c} \cdot \nabla \exp(\boldsymbol{\psi}_\mathrm{f}) \\ -\exp(\boldsymbol{\psi}_\mathrm{f}) \cdot \nabla \hat{\mathbf{v}}_\mathrm{f} - (\nabla \hat{\mathbf{v}}_\mathrm{f})^T \cdot \exp(\boldsymbol{\psi}_\mathrm{f}) + 2\nabla^\mathrm{s}\mathbf{v}_\mathrm{f}) \end{pmatrix}, \tag{5.31}$$

and

$$\mathscr{D}_\mathrm{log}(\mathbf{V}) := \begin{pmatrix} \rho_\mathrm{f}\frac{\partial \mathbf{v}_\mathrm{f}}{\partial t} \\ 0 \\ \frac{\lambda}{2\lambda_0}\frac{\partial \exp(\boldsymbol{\psi}_\mathrm{f})}{\partial t} \end{pmatrix}. \tag{5.32}$$

Eqs. (5.24)-(5.26) can be expressed as Eq. (5.23), where now $\mathscr{D}_t = \mathscr{D}_\mathrm{log}$, $\mathscr{L} = \mathscr{L}_\mathrm{log}$ and $\mathbf{f} = \mathbf{f}_\mathrm{log}$. Similar considerations as for the standard approach can be done for this formulation referring to the boundary conditions. In this case tensor $\boldsymbol{\psi}_\mathrm{f}$ is not prescribed, similarly to what is done with the elastic stresses $\boldsymbol{\sigma}_\mathrm{f}$ in the standard formulation.

5.3.3 Variational form

Let $\mathbb{V} = \{\mathbf{v} \in H^1(\Omega_\mathrm{f}(t))^d \mid \mathbf{v} = \mathbf{v}_{\mathrm{f},D}(t) \text{ on } \Gamma_{\mathrm{f},D}(t)\}$ be the space where the velocity needs to be sought for each time $t \in]0,T[$, and $\mathbb{V}_0$ the corresponding space of test functions, vanishing on the Dirichlet boundary $\Gamma_{\mathrm{f},D}(t)$. Let $\mathbb{P} = L^2(\Omega_\mathrm{f}(t))$

be the pressure space (up to constants if all boundary conditions are of Dirichlet type), and $\mathbb{Y} \subset L^2(\Omega_f(t))^{d\times d}$ the space for the stresses, with appropriate regularity. Let also $\mathbb{W} := \mathbb{V}\times\mathbb{P}\times\mathbb{Y}$ and $\mathbb{W}_0 := \mathbb{V}_0\times\mathbb{P}\times\mathbb{Y}$. The weak form of the standard viscoelastic problem consists of finding $\mathbf{V} = [\mathbf{v}_f, p_f, \boldsymbol{\sigma}_f] :]0,T[\longrightarrow \mathbb{W}$ such that the initial conditions are satisfied and

$$\left(\rho_f\frac{\partial \mathbf{v}_f}{\partial t}, \delta\mathbf{v}\right) + (\boldsymbol{\sigma}_f, \nabla^s\delta\mathbf{v}) + 2(\mu_f^s\nabla^s\mathbf{v}_f, \nabla^s\delta\mathbf{v}) + \langle\rho_f\hat{\mathbf{v}}_c\cdot\nabla\mathbf{v}_f, \delta\mathbf{v}\rangle - (p_f, \nabla\cdot\delta\mathbf{v}) = \langle\mathbf{f}, \delta\mathbf{v}\rangle + \langle\mathbf{t}_{f,N}, \delta\mathbf{v}\rangle_{\Gamma_{f,N}}, \tag{5.33}$$

$$(\delta p, \nabla\cdot\mathbf{v}_f) = 0, \tag{5.34}$$

$$\frac{1}{2\mu_f^p}(\boldsymbol{\sigma}_f, \delta\boldsymbol{\sigma}) - (\nabla^s\mathbf{v}_f, \delta\boldsymbol{\sigma}) + \frac{\lambda}{2\mu_f^p}\left(\frac{\partial\boldsymbol{\sigma}_f}{\partial t} + \mathbf{v}_c\cdot\nabla\boldsymbol{\sigma}_f - 2\boldsymbol{\sigma}_f\cdot\nabla^s\mathbf{v}_f, \delta\boldsymbol{\sigma}\right) = 0, \tag{5.35}$$

for all $\delta\mathbf{V} := [\delta\mathbf{v}, \delta p, \delta\boldsymbol{\sigma}] \in \mathbb{W}_0$, where it is assumed that $\mathbf{f}$ is such that $\langle\mathbf{f}, \delta\mathbf{v}\rangle$ is well defined and likewise for $\langle\mathbf{t}_f, \delta\mathbf{v}\rangle_{\Gamma_{f,N}}$. In compact form, the problem can be written as: find $\mathbf{V} :]0,T[\longrightarrow \mathbb{W}$ such that

Viscoelastic fluid flow. $\mathbf{v}p\boldsymbol{\sigma}$ formulation. Variational form in ALE approach

$$\mathcal{G}_{std}(\mathbf{V}, \delta\mathbf{V}) + B_{std}(\mathbf{v}_f; \mathbf{V}, \delta\mathbf{V}) = L_{std}(\delta\mathbf{V}), \tag{5.36}$$

for all $\delta\mathbf{V} \in \mathbb{W}_0$, where

$$\mathcal{G}_{std}(\mathbf{V}, \delta\mathbf{V}) = \left(\rho_f\frac{\partial\mathbf{v}_f}{\partial t}, \delta\mathbf{v}\right) + \frac{\lambda}{2\mu_f^p}\left(\frac{\partial\boldsymbol{\sigma}_f}{\partial t}, \delta\boldsymbol{\sigma}\right), \tag{5.37}$$

$$B_{std}(\hat{\mathbf{v}}_f; \mathbf{V}, \delta\mathbf{V}) = 2(\mu_f^s\nabla^s\mathbf{v}_f, \nabla^s\delta\mathbf{v}) + \langle\rho_f\hat{\mathbf{v}}_c\cdot\nabla\mathbf{v}_f, \delta\mathbf{v}\rangle + (\boldsymbol{\sigma}_f, \nabla^s\delta\mathbf{v}) - (p_f, \nabla\cdot\delta\mathbf{v}) + (\nabla\cdot\mathbf{v}_f, \delta p) + \frac{1}{2\mu_f^p}(\boldsymbol{\sigma}_f, \delta\boldsymbol{\sigma}) - (\nabla^s\mathbf{v}_f, \delta\boldsymbol{\sigma}) + \frac{\lambda}{2\mu_f^p}(\hat{\mathbf{v}}_c\cdot\nabla\boldsymbol{\sigma}_f - 2\boldsymbol{\sigma}_f\cdot\nabla^s\hat{\mathbf{v}}_f, \delta\boldsymbol{\sigma}), \tag{5.38}$$

$$L_{std}(\delta\mathbf{V}) = \langle\mathbf{f}, \delta\mathbf{v}\rangle + \langle\mathbf{t}_{f,N}, \delta\mathbf{v}\rangle_{\Gamma_{f,N}}. \tag{5.39}$$

Let us consider now the LCR. The spaces for the velocity and

pressure for the continuous problems are the ones defined above for the standard formulation. The space for tensor $\boldsymbol{\psi}_\mathrm{f}$ is now denoted by $\bar{\mathbb{Y}}$ for each fixed time t; it is a subspace of $L^2(\Omega_\mathrm{f}(t))^{d\times d}$ of tensor fields with the appropriate regularity.

The weak form of the problem consists of finding $\mathbf{V} = [\mathbf{v}_\mathrm{f}, p_\mathrm{f}, \boldsymbol{\psi}_\mathrm{f}] :]0,T[\longrightarrow \bar{\mathbb{W}} := \mathbb{V}\times\mathbb{P}\times\bar{\mathbb{Y}}$, such that the initial conditions are satisfied and the following equations hold

$$\left(\rho\frac{\partial \mathbf{v}_\mathrm{f}}{\partial t}, \delta\mathbf{v}\right) + \frac{\mu_\mathrm{f}^p}{\lambda_0}(\exp(\boldsymbol{\psi}_\mathrm{f}), \nabla^\mathrm{s}\delta\mathbf{v}) + 2(\mu_\mathrm{f}^s\nabla^\mathrm{s}\mathbf{v}_\mathrm{f}, \nabla^\mathrm{s}\delta\mathbf{v})$$
$$+\langle\rho\hat{\mathbf{v}}_\mathrm{c}\cdot\nabla\mathbf{v}_\mathrm{f}, \delta\mathbf{v}\rangle - (p_\mathrm{f}, \nabla\cdot\delta\mathbf{v}) = \langle\mathbf{f}, \delta\mathbf{v}\rangle + \langle\mathbf{t}_{\mathrm{f},N}, \delta\mathbf{v}\rangle_{\Gamma_{\mathrm{f},N}}, \quad (5.40)$$

$$(\delta p, \nabla\cdot\mathbf{v}_\mathrm{f}) = 0, \quad (5.41)$$

$$\frac{\lambda}{2\lambda_0}\left(-\exp(\boldsymbol{\psi}_\mathrm{f})\cdot\nabla\mathbf{v}_\mathrm{f} - (\nabla\mathbf{v}_\mathrm{f})^T\cdot\exp(\boldsymbol{\psi}_\mathrm{f}) + 2\nabla^\mathrm{s}\mathbf{v}_\mathrm{f}, \delta\boldsymbol{\sigma}\right)$$
$$+\frac{\lambda}{2\lambda_0}\left(\frac{\partial\exp(\boldsymbol{\psi}_\mathrm{f})}{\partial t} + \mathbf{v}_\mathrm{c}\cdot\nabla\exp(\boldsymbol{\psi}_\mathrm{f}), \delta\boldsymbol{\sigma}\right)$$
$$+\frac{1}{2\lambda_0}(\exp(\boldsymbol{\psi}_\mathrm{f}), \delta\boldsymbol{\sigma}) - (\nabla^\mathrm{s}\mathbf{v}_\mathrm{f}, \delta\boldsymbol{\sigma}) = \frac{1}{2\lambda_0}\langle\mathbf{I}, \delta\boldsymbol{\sigma}\rangle, \quad (5.42)$$

for all $\delta\mathbf{V} = [\delta\mathbf{v}, \delta p, \delta\boldsymbol{\sigma}] \in \mathbb{W}$. Again taking into account the new definition of $\mathbf{V}$ for this formulation, the problem can be written as

Viscoelastic fluid flow. LCR formulation. Variational form in ALE approach

$$\mathcal{G}_\mathrm{log}(\mathbf{V}, \delta\mathbf{V}) + B_\mathrm{log}(\mathbf{v}_\mathrm{f}; \mathbf{V}, \delta\mathbf{V}) = L_\mathrm{log}(\delta\mathbf{V}), \quad (5.43)$$

where each term is defined as

$$\mathcal{G}_\mathrm{log}(\mathbf{V}, \delta\mathbf{V}) = \left(\rho\frac{\partial\mathbf{v}_\mathrm{f}}{\partial t}, \delta\mathbf{v}\right) + \frac{\lambda}{2\lambda_0}\left(\frac{\partial\exp(\boldsymbol{\psi}_\mathrm{f})}{\partial t}, \delta\boldsymbol{\sigma}\right), \quad (5.44)$$

$$\begin{aligned} B_\mathrm{log}(\hat{\mathbf{v}}_\mathrm{f}; \mathbf{V}, \delta\mathbf{V}) = {} & \frac{\mu_\mathrm{f}^p}{\lambda_0}(\exp(\boldsymbol{\psi}_\mathrm{f}), \nabla^\mathrm{s}\delta\mathbf{v}) + 2(\mu_\mathrm{f}^s\nabla^\mathrm{s}\mathbf{v}_\mathrm{f}, \nabla^\mathrm{s}\delta\mathbf{v}) \\ & + \langle\rho\hat{\mathbf{v}}_\mathrm{c}\cdot\nabla\mathbf{v}_\mathrm{f}, \delta\mathbf{v}\rangle - (p_\mathrm{f}, \nabla\cdot\delta\mathbf{v}) + (\nabla\cdot\mathbf{v}_\mathrm{f}, q) \\ & + \frac{1}{2\lambda_0}(\exp(\boldsymbol{\psi}_\mathrm{f}), \delta\boldsymbol{\sigma}) - (\nabla^\mathrm{s}\mathbf{v}_\mathrm{f}, \delta\boldsymbol{\sigma}) \\ & + \frac{\lambda}{2\lambda_0}(\hat{\mathbf{v}}_\mathrm{c}\cdot\nabla\exp(\boldsymbol{\psi}_\mathrm{f}) - 2\exp(\boldsymbol{\psi}_\mathrm{f})\cdot\nabla^\mathrm{s}\hat{\mathbf{v}}_\mathrm{f}, \delta\boldsymbol{\sigma}) \\ & + \frac{\lambda}{2\lambda_0}(2\nabla^\mathrm{s}\mathbf{v}_\mathrm{f}, \delta\boldsymbol{\sigma}), \end{aligned} \quad (5.45)$$

$$L_{\log}(\delta\mathbf{V}) = \langle \mathbf{f}, \delta\mathbf{v}\rangle + \langle \mathbf{t}_{\mathrm{f},N}, \delta\mathbf{v}\rangle_{\Gamma_{\mathrm{f},N}} + \frac{1}{2\lambda_0}\langle \mathbf{I}, \delta\boldsymbol{\sigma}\rangle. \quad (5.46)$$

5.3.4 Galerkin spatial discretization

In this section the Galerkin FE approximation for problems (5.36) and (5.43) is described. The same notation regarding the FE discretization as for the solid problem will be used. In the particular case of the standard formulation, from $\mathscr{P}_h$ we may construct conforming FE spaces for the velocity, the pressure and the elastic stress, $\mathbb{V}_h \subset \mathbb{V}$, $\mathbb{P}_h \subset \mathbb{P}$, $\mathbb{Y}_h \subset \mathbb{Y}$, respectively. We will consider all these FE spaces to be made of continuous functions, even though discontinuous approximations could be used for the pressure and the stress. So, calling $\mathbb{W}_h := \mathbb{V}_h \times \mathbb{P}_h \times \mathbb{Y}_h$, the Galerkin FE approximation of the standard problem consists of finding $\mathbf{v}_h :]0,T[\longrightarrow \mathbb{W}_h$, such that

Viscoelastic fluid flow. v$p\boldsymbol{\sigma}$ formulation. Galerkin discrete problem in ALE approach

$$\mathscr{G}_{\mathrm{std}}(\mathbf{V}_h, \delta\mathbf{V}_h) + B_{\mathrm{std}}(\hat{\mathbf{v}}_{\mathrm{f},h}; \mathbf{V}_h, \delta\mathbf{V}_h) = L_{\mathrm{std}}(\delta\mathbf{V}_h), \quad (5.47)$$

for all $\delta\mathbf{V}_h = [\delta\mathbf{v}_h, \delta p_h, \delta\boldsymbol{\sigma}_h] \in \mathbb{W}_h$, and satisfying the appropriate initial conditions.

For the LCR, from $\mathscr{P}_h$ we construct the FE space for the new variable $\boldsymbol{\psi}_{\mathrm{f}}$, $\bar{\mathbb{Y}}_h \subset \bar{\mathbb{Y}}$. Thus, if $\bar{\mathbb{W}}_h := \mathbb{V}_h \times \mathbb{P}_h \times \bar{\mathbb{Y}}_h$ the Galerkin approximation consists of finding $\mathbf{V}_h :]0,T[\longrightarrow \bar{\mathbb{W}}_h$, such that

Viscoelastic fluid flow. v$p\boldsymbol{\sigma}$ formulation. Galerkin discrete problem in ALE approach

$$\mathscr{G}_{\log}(\mathbf{V}_h, \delta\mathbf{V}_h) + B_{\log}(\hat{\mathbf{v}}_{\mathrm{f},h}; \mathbf{V}_h, \delta\mathbf{V}_h) = L_{\log}(\delta\mathbf{V}_h), \quad (5.48)$$

for all $\delta\mathbf{V}_h = [\delta\mathbf{v}_h, \delta p_h, \delta\boldsymbol{\sigma}_h] \in \bar{\mathbb{W}}_h$.

It is well known that the Galerkin approximation is unstable unless convective terms are not relevant and appropriate compatibility conditions between $\mathbb{P}_h$ and $\mathbb{V}_h$ and between $\mathbb{V}_h$ and $\mathbb{Y}_h$ are met (see for example [14, 15]). To tackle with

[14]: Castillo et al. (2014), "Variational multi-scale stabilized formulations for the stationary three-field incompressible viscoelastic flow problem"
[15]: Moreno et al. (2019), "Logarithmic conformation reformulation in viscoelastic flow problems approximated by a VMS-type stabilized finite element formulation"

these instabilities we employ a VMS-based stabilized formulation described later.

5.3.5 Time discretization

Regarding the time discretization, the BDF2 is also used to approximate the first order time derivative, based on the approximation described in Subsection 2.2.2

$$\left.\frac{\delta_2 \mathbf{v}}{\delta t}\right|_{t^{n+1}} := \frac{1}{2\Delta t}\left[3\mathbf{v}^{n+1} - 4\mathbf{v}^{n} + \mathbf{v}^{n-1}\right] = \frac{\partial \mathbf{v}^{n+1}}{\partial t} + \mathcal{O}\left(\Delta t^2\right). \tag{5.49}$$

By using the approximations of the exponential described in [15], for the LCR we obtain the next expression using the BDF2 scheme:

$$\begin{aligned}\left.\frac{\delta_2(\exp(\boldsymbol{\psi}_\mathrm{f}))}{\delta t}\right|_{t^{n+1}} &:= \frac{1}{2\Delta t}\Big[3\exp\left(\hat{\boldsymbol{\psi}}_\mathrm{f}^{n+1}\right)\cdot\boldsymbol{\psi}_\mathrm{f}^{n+1} + 3\exp\left(\hat{\boldsymbol{\psi}}_\mathrm{f}^{n+1}\right) \\ &\quad - 3\exp\left(\hat{\boldsymbol{\psi}}_\mathrm{f}^{n+1}\right)\cdot\hat{\boldsymbol{\psi}}_\mathrm{f}^{n+1} - 4\exp\left(\boldsymbol{\psi}_\mathrm{f}^{n}\right) + \exp\left(\boldsymbol{\psi}_\mathrm{f}^{n-1}\right)\Big] \\ &= \left.\frac{\partial(\exp(\boldsymbol{\psi}_\mathrm{f}))}{\partial t}\right|_{t^{n+1}} + \mathcal{O}\left(\Delta t^2\right) + \mathcal{O}\left(\left(\Delta\boldsymbol{\psi}_\mathrm{f}^{n+1}\right)^2\right),\end{aligned} \tag{5.50}$$

[15]: Moreno et al. (2019), "Logarithmic conformation reformulation in viscoelastic flow problems approximated by a VMS-type stabilized finite element formulation"

where $\hat{\boldsymbol{\psi}}_\mathrm{f}^{n+1}$ stands for a previous guess of $\boldsymbol{\psi}_\mathrm{f}^{n+1}$ that depends on the linearization scheme and $\Delta\boldsymbol{\psi}_\mathrm{f}^{n+1} = \boldsymbol{\psi}_\mathrm{f}^{n+1} - \hat{\boldsymbol{\psi}}_\mathrm{f}^{n+1}$.

In any case, the stabilized FEM which will be exposed is independent of the time scheme used.

5.3.6 Stabilization

As it was stated above, the viscoelastic fluid flow problem is stabilized following the VMS framework. VMS methods consist in the splitting of the unknown $\mathbf{v}$ in a component $\mathbf{v}_h$, which can be captured by the FE space, and the remainder $\tilde{\mathbf{v}}$, that will be called sub-grid scale (SGS). The framework is based on the work by Hughes et al. [6]. In the context of a three field formulation for flow problems, see [46] and [14]. The SGS needs to be approximated in a simple manner, with the goal of capturing its effect and yielding a stable formulation. The final number of degrees of freedom is the same as for the Galerkin method. Different approaches can be followed to approximate the SGSs and to choose the

[6]: Hughes et al. (1998), "The variational multiscale method - A paradigm for computational mechanics"

[46]: Codina (2009), "Finite element approximation of the three field formulation of the Stokes problem using arbitrary interpolations"

[14]: Castillo et al. (2014), "Variational multi-scale stabilized formulations for the stationary three-field incompressible viscoelastic flow problem"

space where they are defined. In particular, we will present a stabilization in which the SGSs are time-dependent. That allows to compute problems with anisotropic space-time discretizations, in which the time step is small in relation with the mesh size [16, 138, 139]. Additionally, the stabilization employed for the fluid is not residual-based; it is a term-by-term approach which neglects terms that do not contribute to stability. It is a non-consistent method, but it presents optimal convergence regardless the order of the elements. This method turns out to be more robust than residual-based methods for solving viscoelastic fluid flow problems (for more details, see [14, 15]).

[16]: Moreno et al. (2020), "Solution of transient viscoelastic flow problems approximated by a term-by-term VMS stabilized finite element formulation using time-dependent subgrid-scales"
[138]: Badia et al. (2009), "On a multiscale approach to the transient Stokes problem. Transient subscales and anisotropic space-time discretization"
[139]: Codina et al. (2007), "Time dependent subscales in the stabilized finite element approximation of incompressible flow problems"

The problem that we pretend to approximate is Eq. (5.23) in strong form for both formulations: in variational form, the standard one is expressed in Eq. (5.36) and the logarithmic one in Eq. (5.43).

We shall start with the standard formulation. Observe that $\mathscr{L}_{\text{std}}(\hat{\mathbf{v}}_{\text{f}};\cdot)$ is a linear operator for a given $\hat{\mathbf{v}}_{\text{f}}$. Introducing the SGS decomposition and integrating by parts, the method leads to find $\mathbf{V}_h :]0,T[\longrightarrow \mathbb{W}_h$ such that

Viscoelastic fluid flow. v$p\boldsymbol{\sigma}$ formulation. Stabilized weak form in ALE approach

$$\mathscr{G}_{\text{std}}(\mathbf{V}_h,\delta\mathbf{V}_h) + B_{\text{std}}(\hat{\mathbf{v}}_{\text{f},h};\mathbf{V}_h,\delta\mathbf{V}_h) + \sum_K \langle \tilde{\mathbf{V}}, \mathscr{L}^*(\mathbf{v}_{\text{f},h};\delta\mathbf{V}_h)\rangle_K = L_{\text{std}}(\delta\mathbf{V}_h), \tag{5.51}$$

for all $\delta\mathbf{V}_h \in \mathbb{W}_h$, where $\mathscr{L}^*(\mathbf{v}_{\text{f},h};\delta\mathbf{V}_h)$ is the formal adjoint operator of $\mathscr{L}_{\text{std}}(\hat{\mathbf{v}}_{\text{f}};\cdot)$, typically without considering boundary conditions, and $\tilde{\mathbf{V}}$ is the SGS, which needs to be approximated and has components $\tilde{\mathbf{V}} := [\tilde{\mathbf{v}}, \tilde{p}, \tilde{\boldsymbol{\sigma}}]$. To justify Eq. (5.51), see e.g. [38], and recall that we are considering all approximations continuous. Also, note that the SGS contribution is neglected for the non-linear contribution of the velocity $\mathbf{v}_{\text{f},h}$. This simplification is introduced in order to improve the non-linear convergence of the problem and in our experience has little effect in the final accuracy of the solution for this kind of problems.

[38]: Codina et al. (2018), "Variational Multiscale Methods in Computational Fluid Dynamics"

Analogously, for the LCR the method leads to find $\mathbf{V}_h :]0,T[\longrightarrow$

$\bar{\mathbb{W}}_h$ such that

Viscoelastic fluid flow. LCR formulation. Stabilized weak form in ALE approach

$$\mathscr{G}_{\log}(\mathbf{V}_h, \delta\mathbf{V}_h) + B_{\log}(\hat{\mathbf{v}}_{\mathrm{f},h}; \mathbf{V}_h, \delta\mathbf{V}_h) + \sum_K \langle \tilde{\mathbf{V}}, \mathscr{L}^*(\mathbf{v}_{\mathrm{f},h}; \delta\mathbf{V}_h)\rangle_K = L_{\log}(\delta\mathbf{V}_h), \tag{5.52}$$

for all $\delta\mathbf{V}_h \in \mathbb{W}_h$. Let us remark that for both formulations (standard and logarithmic) the same operator $\mathscr{L}^*(\hat{\mathbf{v}}_{\mathrm{f}}; \cdot)$ will be employed, following the process described in [15]:

[15]: Moreno et al. (2019), "Logarithmic conformation reformulation in viscoelastic flow problems approximated by a VMS-type stabilized finite element formulation"

$$\mathscr{L}^*(\hat{\mathbf{v}}_{\mathrm{f}}; \delta\mathbf{V}) := \begin{pmatrix} \nabla\cdot\delta\boldsymbol{\sigma} - 2\mu_{\mathrm{f}}^s \nabla\cdot(\nabla^s\delta\mathbf{v}) - \rho_{\mathrm{f}}\hat{\mathbf{v}}_{\mathrm{c}}\cdot\nabla\delta\mathbf{v} - \nabla\delta p \\ -\nabla\cdot\delta\mathbf{v} \\ \frac{1}{2\mu_{\mathrm{f}}^p}\delta\boldsymbol{\sigma} + \nabla^s\delta\mathbf{v} - \frac{\lambda}{2\mu_{\mathrm{f}}^p}(\hat{\mathbf{v}}_{\mathrm{c}}\cdot\nabla\delta\boldsymbol{\sigma} + \nabla^s\hat{\mathbf{v}}_{\mathrm{f}}\cdot\delta\boldsymbol{\sigma}) \end{pmatrix}. \tag{5.53}$$

This is due to the fact that we have not changed variables in the stress test function.

Once operators $\mathscr{D}_t$ and $\mathscr{L}$ are defined for both formulations, the SGSs can be written in terms of the FE component as

$$\frac{\partial\tilde{\mathbf{V}}}{\partial t} + \boldsymbol{\alpha}^{-1}\tilde{\mathbf{V}} = \tilde{\Pi}[\mathbf{f} - \mathscr{D}_t(\mathbf{V}_h) - \mathscr{L}(\mathbf{v}_{\mathrm{f},h}; \mathbf{V}_h)], \tag{5.54}$$

where we denote as $\tilde{\Pi}$ the L^2 projection onto the space of SGSs. In this chapter $\tilde{\Pi}$ is taken as the orthogonal projection to the FE space, denoted as $\tilde{\Pi} = \Pi_h^{\perp}$, and therefore the Orthogonal SGS Stabilization (OSGS) method [24] is employed. Let us remark that $\boldsymbol{\alpha}$ is taken as a diagonal matrix of stabilization parameters, $\boldsymbol{\alpha} = \mathrm{diag}\,(\alpha_1\mathbf{I}_d, \alpha_2, \alpha_3\mathbf{I}_{d\times d})$, with $\mathbf{I}_d$ the identity on vectors of $\mathbb{R}^d$, $\mathbf{I}_{d\times d}$ the identity on second order tensors, and parameters α_i, $i = 1, 2, 3$, being defined as in [14]:

[24]: Codina (2001), "A stabilized finite element method for generalized stationary incompressible flows"

[14]: Castillo et al. (2014), "Variational multi-scale stabilized formulations for the stationary three-field incompressible viscoelastic flow problem"

$$\alpha_1 = \left[c_1\frac{\mu_{\mathrm{f}}^0}{h_1^2} + c_2\frac{\rho_{\mathrm{f}}|\mathbf{v}_{\mathrm{f},h}|}{h_2}\right]^{-1}, \tag{5.55}$$

$$\alpha_2 = \frac{h_1^2}{c_1\alpha_1}, \tag{5.56}$$

$$\alpha_3 = \left[c_3\frac{1}{2\mu_{\mathrm{f}}^p} + c_4\left(\frac{\lambda}{2\mu_{\mathrm{f}}^p}\frac{|\mathbf{v}_{\mathrm{f},h}|}{h_2} + \frac{\lambda}{\mu_{\mathrm{f}}^p}|\nabla\mathbf{v}_{\mathrm{f},h}|\right)\right]^{-1}, \tag{5.57}$$

where h_1 is the characteristic length calculated as the square root of the element area in the two-dimensional case and the cubic root of the element volume in the three-dimensional case, and h_2 is another characteristic length calculated as the element length in the streamline direction (see [140] for more details). Term $|\mathbf{v}_{\mathrm{f},h}|$ is the Euclidean norm of the velocity and $|\nabla\mathbf{v}_{\mathrm{f},h}|$ is the Frobenius norm of the velocity gradient. The constants $c_i, i = 1,..,4$ are algorithmic parameters in the formulation. The values employed in this thesis for the numerical simulations using linear elements are: $c_1 = 4.0$, $c_2 = 1.0$, $c_3 = 4.0$, $c_4 = 0.25$.

[140]: Codina et al. (1992), "The intrinsic time for the streamline upwind/Petrov-Galerkin formulation using quadratic elements"

As it was introduced previously, the stabilization approach employed in the computations is of term-by-term type, denoted from this point as "S-OSGS", developed and justified in [16]. To sum up, this stabilization has been proved to be more robust when large stress gradients are present. Essentially the method allows splitting the SGS associated to the momentum equation $\tilde{\mathbf{v}}$ as $\tilde{\mathbf{v}} = \tilde{\mathbf{v}}_1 + \tilde{\mathbf{v}}_2 + \tilde{\mathbf{v}}_3$, while the stress SGS remains as $\tilde{\boldsymbol{\sigma}}$. Therefore, the term-by-term FE formulation proposed consists of finding $\mathbf{V}_h = [\mathbf{v}_{\mathrm{f},h}, p_{\mathrm{f},h}, \boldsymbol{\sigma}_{\mathrm{f},h}] :]0,T[\longrightarrow \mathbb{W}_h$ such that

[16]: Moreno et al. (2020), "Solution of transient viscoelastic flow problems approximated by a term-by-term VMS stabilized finite element formulation using time-dependent subgrid-scales"

$$
\begin{aligned}
\mathcal{G}_{\mathrm{std}}(\mathbf{V}_h, \delta\mathbf{V}_h) + B_{\mathrm{std}}(\hat{\mathbf{v}}_{\mathrm{f},h}; \mathbf{V}_h, \delta\mathbf{V}_h) &+ \sum_K \langle \tilde{\mathbf{v}}_1, -\rho_{\mathrm{f}}\mathbf{v}_{\mathrm{f},h}\cdot\nabla\delta\mathbf{v}_h\rangle_K \\
&+ \sum_K \langle \tilde{\mathbf{v}}_2, -\nabla\delta p_h\rangle_K + \sum_K \langle \tilde{\mathbf{v}}_3, \nabla\cdot\delta\boldsymbol{\sigma}_h\rangle_K \\
&+ \sum_K \langle \tilde{p}, -\nabla\cdot\delta\mathbf{v}_h\rangle_K + \sum_K \left\langle \tilde{\boldsymbol{\sigma}}, \frac{1}{2\mu_{\mathrm{f}}^p}\delta\boldsymbol{\sigma}_h + \nabla^{\mathrm{s}}\delta\mathbf{v}_h \right\rangle_K \\
&+ \sum_K \left\langle \tilde{\boldsymbol{\sigma}}, -\frac{\lambda}{2\mu_{\mathrm{f}}^p}\left(\mathbf{v}_{\mathrm{c},h}\cdot\nabla\delta\boldsymbol{\sigma}_h + \nabla^{\mathrm{s}}\mathbf{v}_{\mathrm{f},h}\cdot\delta\boldsymbol{\sigma}_h\right) \right\rangle_K \\
&= L_{std}(\delta\mathbf{V}_h),
\end{aligned}
\tag{5.58}
$$

for all $\delta\mathbf{V}_h = [\delta\mathbf{v}_h, \delta p_h, \delta\boldsymbol{\sigma}_h] \in \mathbb{W}_h$, where B_{std} is the bilinear form defined in Eq.(5.38), and the SGSs $\tilde{\mathbf{v}}_1$, $\tilde{\mathbf{v}}_2$, $\tilde{\mathbf{v}}_3$, $\tilde{p}$ and $\tilde{\boldsymbol{\sigma}}$ are the solution of the evolution problems

$$\rho_{\mathrm{f}}\frac{\partial\tilde{\mathbf{v}}_1}{\partial t} + \alpha_1^{-1}\tilde{\mathbf{v}}_1 = -\Pi_h^{\perp}[\rho_{\mathrm{f}}\mathbf{v}_{\mathrm{c},h}\cdot\nabla\mathbf{v}_{\mathrm{f},h}], \tag{5.59}$$

$$\rho_{\mathrm{f}}\frac{\partial\tilde{\mathbf{v}}_2}{\partial t} + \alpha_1^{-1}\tilde{\mathbf{v}}_2 = -\Pi_h^{\perp}[\nabla p_{\mathrm{f},h}], \tag{5.60}$$

$$\rho_{\mathrm{f}}\frac{\partial\tilde{\mathbf{v}}_3}{\partial t} + \alpha_1^{-1}\tilde{\mathbf{v}}_3 = \Pi_h^{\perp}[\nabla\cdot\boldsymbol{\sigma}_{\mathrm{f},h}], \tag{5.61}$$

$$\alpha_2^{-1}\tilde{p} = -\Pi_h^{\perp}[\nabla\cdot\mathbf{v}_{\mathrm{f},h}], \tag{5.62}$$

$$\frac{\lambda}{2\mu_{\mathrm{f}}^{p}}\frac{\partial\tilde{\boldsymbol{\sigma}}}{\partial t}+\alpha_3^{-1}\tilde{\boldsymbol{\sigma}} = \Pi_h^{\perp}\left[-\frac{1}{2\mu_{\mathrm{f}}^{p}}\boldsymbol{\sigma}_{\mathrm{f},h}+\nabla^{\mathrm{s}}\mathbf{v}_{\mathrm{f},h}\right] + \Pi_h^{\perp}\left[-\frac{\lambda}{2\mu_{\mathrm{f}}^{p}}\left(\frac{\partial\boldsymbol{\sigma}_{\mathrm{f},h}}{\partial t}+\mathbf{v}_{\mathrm{c},h}\cdot\nabla\boldsymbol{\sigma}_{\mathrm{f},h}-2\boldsymbol{\sigma}_{\mathrm{f},h}\cdot\nabla^{\mathrm{s}}\mathbf{v}_{\mathrm{f},h}\right)\right]. \tag{5.63}$$

In this method, there are three terms that stabilize the momentum equation, the first one giving control on the convective term (5.59), the second term on the pressure gradient (5.60) and the third one on the divergence of the viscoelastic stress (5.61). This term-by-term stabilization point of view is in fact previous to the OSGS method, based on the approximation of the sub-grid scales. It is proposed in [25] and analyzed in [136].

[25]: Codina (2000), "Stabilization of incompressibility and convection through orthogonal subscales in finite element methods"

[136]: Codina (2008), "Analysis of a stabilized finite element approximation of the Oseen equations using orthogonal subscales"

Recall that $\Pi_h^{\perp}$ denotes the orthogonal projection to the FE space. Although this method is not residual-based for the momentum equation (as justified in [16]), and therefore it is not consistent in the sense used in the FE context, it has an optimal consistency error regardless the order of the elements.

[16]: Moreno et al. (2020), "Solution of transient viscoelastic flow problems approximated by a term-by-term VMS stabilized finite element formulation using time-dependent subgrid-scales"

Finally, the term-by-term stabilization proposed for the LCR approach consists of finding $\mathbf{V}_h = [\mathbf{v}_{\mathrm{f},h}, p_{\mathrm{f},h}, \boldsymbol{\psi}_{\mathrm{f},h}] :]0,T[\longrightarrow \bar{\mathbb{W}}_h$ such that

$$\begin{aligned}\mathscr{G}_{\log}(\mathbf{V}_h,\delta\mathbf{V}_h)+B_{\log}(\hat{\mathbf{v}}_{\mathrm{f},h};\mathbf{V}_h,\delta\mathbf{V}_h)&+\sum_K\langle\tilde{\mathbf{v}}_1,-\rho_{\mathrm{f}}\mathbf{v}_{\mathrm{f},h}\cdot\nabla\delta\mathbf{v}_h\rangle_K\\&+\sum_K\langle\tilde{\mathbf{v}}_2,-\nabla\delta p_h\rangle_K+\sum_K\langle\tilde{\mathbf{v}}_3,\nabla\cdot\delta\boldsymbol{\sigma}_h\rangle_K\\&+\sum_K\langle\tilde{p},-\nabla\cdot\delta\mathbf{v}_h\rangle_K+\sum_K\left\langle\tilde{\boldsymbol{\sigma}},\frac{1}{2\mu_{\mathrm{f}}^{p}}\delta\boldsymbol{\sigma}_h+\nabla^{\mathrm{s}}\delta\mathbf{v}_h\right\rangle_K\\&+\sum_K\left\langle\tilde{\boldsymbol{\sigma}},-\frac{\lambda}{2\mu_{\mathrm{f}}^{p}}\left(\mathbf{v}_{\mathrm{c},h}\cdot\nabla\delta\boldsymbol{\sigma}_h+2\nabla^{\mathrm{s}}\mathbf{v}_{\mathrm{f},h}\cdot\delta\boldsymbol{\sigma}_h\right)\right\rangle_K\\&=L_{\log}(\delta\mathbf{V}_h),\end{aligned} \tag{5.64}$$

for all $\delta\mathbf{V}_h = [\delta\mathbf{v}_h, \delta p_h, \delta\boldsymbol{\sigma}_h] \in \mathbb{W}_h$, where $B_{\log}$ is the bilinear form defined in Eq. (5.45), the SGSs $\tilde{\mathbf{v}}_3$ and $\tilde{\boldsymbol{\sigma}}$ are now defined as the solution of the equations

$$\rho\frac{\partial\tilde{\mathbf{v}}_3}{\partial t}+\alpha_1^{-1}\tilde{\mathbf{v}}_3 = \Pi_h^{\perp}\left[\frac{\mu_{\mathrm{f}}^{p}}{\lambda_0}\nabla\cdot\exp(\boldsymbol{\psi}_{\mathrm{f},h})\right]. \tag{5.65}$$

$$\frac{\lambda}{2\mu_{\mathrm{f}}^{p}}\frac{\partial\tilde{\boldsymbol{\sigma}}}{\partial t}+\alpha_3^{-1}\tilde{\boldsymbol{\sigma}}=\Pi_h^{\perp}\left[-\frac{1}{2\lambda_0}\exp\left(\psi_h\right)+\nabla^{\mathrm{s}}\mathbf{v}_{\mathrm{f},h}\right]$$
$$+\Pi_h^{\perp}\left[-\frac{\lambda}{2\lambda_0}\left(\frac{\partial\exp\left(\boldsymbol{\psi}_{\mathrm{f},h}\right)}{\partial t}+\mathbf{v}_{\mathrm{c},h}\cdot\nabla\exp\left(\boldsymbol{\psi}_{\mathrm{f},h}\right)\right)\right]$$
$$+\Pi_h^{\perp}\left[-\frac{\lambda}{2\lambda_0}\left(-2\exp\left(\boldsymbol{\psi}_{\mathrm{f},h}\right)\cdot\nabla^{\mathrm{s}}\mathbf{v}_{\mathrm{f},h}+2\nabla^{\mathrm{s}}\mathbf{v}_{\mathrm{f},h}\right)\right],\quad(5.66)$$

and the SGSs $\tilde{\mathbf{v}}_1$, $\tilde{\mathbf{v}}_2$, and $\tilde{p}$ are solutions of Eqs. (5.59), (5.60), (5.62), respectively.

5.4 Fluid-Structure Interaction

5.4.1 The FSI problem

Let $\Omega(t)$ be the whole domain of the FSI problem, formed by a fluid sub-domain $\Omega_{\mathrm{f}}(t)$ and a solid one $\Omega_{\mathrm{s}}(t)$. These two sub-domains do not overlap, so that $\bar{\Omega}(t)=\overline{\Omega_{\mathrm{f}}(t)\cup\Omega_{\mathrm{s}}(t)}$ and $\mathring{\Omega}_{\mathrm{f}}(t)\cap\mathring{\Omega}_{\mathrm{s}}(t)=\emptyset$, as shown in Fig. 5.1. The sub-domains have their own boundaries $\Gamma_{\mathrm{f}}(t)$ and $\Gamma_{\mathrm{s}}(t)$, and the interface between the two sub-domains is $\Gamma_{\mathrm{i}}(t)$. Its unit normal with respect to the spatial configuration is denoted $\mathbf{n}_{\mathrm{i}}$, pointing from the fluid side to the solid one.

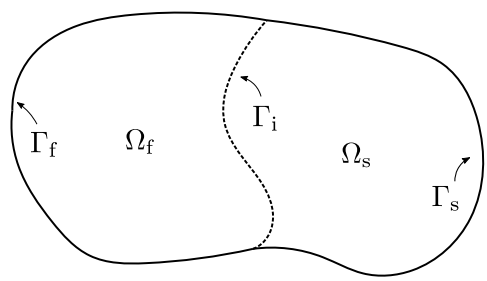

Figure 5.1: Sketch of a general FSI problem.

5.4.2 Governing equations

Borrowing the notation developed in previous sections, we can expand it to account for a moving domain and to take into account the interaction between sub-domains. The FSI problem can be stated as: find a displacement $\mathbf{u}_{\mathrm{s}}$ in the solid problem, an associated velocity $\mathbf{v}_{\mathrm{s}}=\frac{\partial\mathbf{u}_{\mathrm{s}}}{\partial t}$, and $\mathbf{V}=[\mathbf{v}_{\mathrm{f}},p_{\mathrm{f}},\boldsymbol{\sigma}_{\mathrm{f}}]$ for the standard formulation of the flow problem, or $\mathbf{V}=[\mathbf{v}_{\mathrm{f}},p_{\mathrm{f}},\boldsymbol{\psi}_{\mathrm{f}}]$ for the LCR one, such that

FSI problem. Governing equations

$$\rho_s \frac{\partial^2 \mathbf{u}_s}{\partial t^2} - \nabla \cdot \boldsymbol{\sigma}_s = \rho_s \mathbf{b} \quad \text{in } \Omega_s(t) \times]0, T[\,, \tag{5.67}$$

$$\mathbf{u}_s = \mathbf{u}_{s,D} \quad \text{on } \Gamma_{s,D}(t) \times]0, T[\,, \tag{5.68}$$

$$\mathbf{n}_s \cdot \boldsymbol{\sigma}_s = \mathbf{t}_{s,N} \quad \text{on } \Gamma_{s,N}(t) \times]0, T[\,, \tag{5.69}$$

$$\mathbf{u}_s = \mathbf{u}_s^0 \quad \text{in } \Omega_s(0),\ t = 0, \tag{5.70}$$

$$\mathbf{v}_s = \mathbf{v}_s^0 \quad \text{in } \Omega_s(0),\ t = 0, \tag{5.71}$$

$$\mathscr{D}_t(\mathbf{V}) + \mathscr{L}(\hat{\mathbf{v}}_f; \mathbf{V}) = \mathbf{f} \quad \text{in } \Omega_f(t) \times]0, T[\,, \tag{5.72}$$

$$\mathbf{v}_f = \mathbf{v}_{f,D} \quad \text{on } \Gamma_{f,D}(t) \times]0, T[\,, \tag{5.73}$$

$$\mathbf{n}_f \cdot \boldsymbol{\sigma}_f = \mathbf{t}_{f,N} \quad \text{on } \Gamma_{f,N}(t) \times]0, T[\,, \tag{5.74}$$

$$\mathbf{v}_f = \mathbf{v}_f^0 \quad \text{in } \Omega_f(0),\ t = 0, \tag{5.75}$$

$$\boldsymbol{\sigma}_f = \boldsymbol{\sigma}_f^0 \quad \text{in } \Omega_f(0),\ t = 0, \tag{5.76}$$

$$\mathbf{u}_s = \mathbf{u}_f \quad \text{on } \Gamma_i(t) \times]0, T[\,, \tag{5.77}$$

$$\mathbf{v}_s = \mathbf{v}_f \quad \text{on } \Gamma_i(t) \times]0, T[\,, \tag{5.78}$$

$$\mathbf{t}_s + \mathbf{t}_f = \mathbf{0} \quad \text{on } \Gamma_i(t) \times]0, T[\,, \tag{5.79}$$

where $\mathscr{D}_t$, $\mathscr{L}$ and $\mathbf{f}$ are identified depending upon the kind of formulation applied for the fluid, as seen in Section 5.3, and $\mathbf{t}_s = -\mathbf{n}_i \cdot \boldsymbol{\sigma}_s$. The last three equations are known as the transmission conditions between sub-domains. In order to ensure accurate and stable dynamic simulations of FSI problems, dynamic and kinematic continuity must be guaranteed on the interaction interface. They are in charge of imposing same velocities and tractions on the interface boundary $\Gamma_i(t)$. Let us recall that $\mathbf{t}_f$ is computed according with the kind of formulation selected for the fluid as

$$\mathbf{t}_f = \mathbf{n}_i \cdot \boldsymbol{\sigma}_f \tag{5.80}$$

for the standard formulation and

$$\mathbf{t}_f = \mathbf{n}_i \cdot \frac{\mu_f^p}{\lambda_0}(\exp(\boldsymbol{\psi}_f) - \mathbf{I}) \tag{5.81}$$

for the LCR.

The problem described has been written in the monolithic version, in which all unknowns are solved at once, in a fully coupled way. Coupling conditions are treated implicitly.

5.4.3 Block iterative scheme

Rather than solving the monolithic version of the problem, in this work a block-iterative coupling is considered, in which the solid and the fluid mechanics problems are solved sequentially. Strong coupling is considered; this is achieved by block-iterations that converge to the solution of the monolithic problem. This is essential to guarantee correct interface coupling as mesh displacements and velocities should be, up to a certain tolerance, equal, and continuity of tractions is also required. This coupling is of Dirichlet-Neumann type: the solid is solved with the loads computed from the fluid in a given iteration and then the fluid is computed with the velocities on the interface obtained from the solid (see below).

Dynamic sub-relaxation is an efficient way to minimize the amount of sub-iterations necessary to achieve convergence. We have implemented an Aitken relaxation scheme, in particular Aitken Δ^2, detailed in [114]. Within each time step, let us denote by a superscript k the k-th block-iteration of any variable. For clarity, let us omit the superscript with the time step counter. Suppose that from values at the k-th iteration, the solid is solved, obtaining the boundary velocities $\mathbf{v}_{\Gamma_i,s}^{k+1}$. Then, the fluid is solved from the boundary velocities $\mathbf{v}_{\Gamma_i}^{k+1}$ computed as

[114]: Küttler et al. (2008), "Fixed-point fluid–structure interaction solvers with dynamic relaxation"

$$\mathbf{v}_{\Gamma_i}^{k+1} = \mathbf{v}_{\Gamma_i}^{k} + \omega^{k+1}\mathbf{r}_{\Gamma_i}^{k+1}, \tag{5.82}$$

where

$$\mathbf{r}_{\Gamma_i}^{k+1} := \mathbf{v}_{\Gamma_i,s}^{k+1} - \mathbf{v}_{\Gamma_i}^{k}, \quad \omega^{k+1} = -\omega^{k}\frac{(\mathbf{r}_{\Gamma_i}^{k})^T(\mathbf{r}_{\Gamma_i}^{k+1} - \mathbf{r}_{\Gamma_i}^{k})}{|\mathbf{r}_{\Gamma_i}^{k+1} - \mathbf{r}_{\Gamma_i}^{k}|^2}. \tag{5.83}$$

The algorithm is initialized taking a constant relaxation parameter (usually 0.1) in the two first coupling iterations.

Remark 5.4.1 We have just considered a classical Aitken-accelerated partitioned approach to deal with the VFSI problem. Several new techniques have been developed over the last years to improve transmission conditions, such as quasi-Newton methods [141–143], domain decomposition techniques [144] or weak boundary transmission conditions [145], which could also be applied to the current problem.

[141]: Bogaers et al. (2014), "Quasi-Newton methods for implicit black-box FSI coupling"
[142]: Haelterman et al. (2016), "Improving the performance of the partitioned QN-ILS procedure for fluid–structure interaction problems: Filtering"
[143]: Zorrilla et al. (2023), "A memory-efficient MultiVector Quasi-Newton method for black-box Fluid-Structure Interaction coupling"
[144]: Abas et al. (2016), "Adaptive FEM with Domain Decomposition Method for Partitioned-Based Fluid–

Remark 5.4.2 In some works, it is recommended to apply relaxation of the displacement field instead of the velocity one. From our experience, the latter option is more convenient. If only the velocity field is relaxed, the interface between sub-domains from which the fluid solver computes tractions matches perfectly with the interface displacements.

Using the Dirichlet-Neumann iteration-by-subdomain coupling approach described earlier, the coupling algorithm to solve the problem is given in Algorithm 1. This algorithm will not be energy conserving for several reasons. First, the time integration schemes employed are second order, but dissipative, both for the solid and for the fluid. Second, the flow equations have been written in non-conservation form and, furthermore, the stabilizing terms add dissipation to the system. However, conservation will be approximated up to the accuracy order in space and time, always introducing some dissipation and therefore stability to the time evolution of the coupling.

Algorithm 1: VFSI

$n = 0$; loop over the number of time steps.

$n \leftarrow n + 1$.

$k = 0$; iterate until convergence.

$k \leftarrow k + 1$ (block iteration counter omitted in the following).

- **Solve the equations for the solid**, taking into account the tractions coming from the fluid problem $\mathbf{t}_\mathrm{f}$. At time t^n, omitting the superscript for the unknowns, these equations are:

$$\begin{aligned} \rho_\mathrm{s} \frac{\delta_2^2 \mathbf{u}_\mathrm{s}}{\delta t^2} - \nabla \cdot \boldsymbol{\sigma}_\mathrm{s} &= \rho_\mathrm{s} \mathbf{b} && \text{in } \Omega_\mathrm{s}(t^n), \\ \mathbf{u}_\mathrm{s} &= \mathbf{u}_{\mathrm{s},D} && \text{on } \Gamma_{\mathrm{s},D}(t^n), \\ \mathbf{n}_\mathrm{s} \cdot \boldsymbol{\sigma}_\mathrm{s} &= \mathbf{t}_{\mathrm{s},N} && \text{on } \Gamma_{\mathrm{s},N}(t^n), \\ \mathbf{n}_\mathrm{i} \cdot \boldsymbol{\sigma}_\mathrm{s} &= \mathbf{t}_\mathrm{f} && \text{on } \Gamma_\mathrm{i}(t^n). \end{aligned}$$

- **Compute relaxed velocities** on the interface boundary $\mathbf{v}_{\Gamma_\mathrm{i}}$ with an Aitken relaxation scheme from the solid velocities $\mathbf{v}_{\Gamma_\mathrm{i},\mathrm{s}} = \frac{\delta_2 \mathbf{u}_\mathrm{s}}{\delta t}|_{\Gamma_\mathrm{i}}$.
- **Compute the domain velocity in the fluid** by solving the problem (see [137]):

$$\begin{aligned} -\nabla \cdot \{\mathbb{C} : \nabla^\mathrm{s} \mathbf{v}_\mathrm{dom}\} &= \mathbf{0} && \text{in } \Omega_\mathrm{f}(t^n), \\ \mathbf{v}_\mathrm{dom} &= \mathbf{v}_{\Gamma_\mathrm{i}} && \text{on } \Gamma_\mathrm{i}(t^n), \\ \mathbf{v}_\mathrm{dom} &= \mathbf{0} && \text{on } \Gamma_\mathrm{f}(t^n) \setminus \Gamma_\mathrm{i}(t^n), \end{aligned}$$

  where $\mathbb{C}\left(E_\mathrm{dom}(\mathbf{x}), \nu_\mathrm{dom}\right)$ is the Constitutive 4th order tensor in linear elasticity, $E_\mathrm{dom}(\mathbf{x})$ is the Young Modulus of the mesh computed at each node according to [137] and $\nu_\mathrm{dom} = 0.065$ is the Poisson coefficient of the mesh.
- **Solve the ALE equations for the fluid**, taking into account the mesh velocity $\mathbf{v}_\mathrm{dom}$ and using the interface velocity $\mathbf{v}_{\Gamma_\mathrm{i}}$. If $\hat{\mathscr{D}}_t$ is a BDF2 approximation to $\mathscr{D}_t$, the equations to be solved at t^n are:

$$\begin{aligned} \hat{\mathscr{D}}_t(\mathbf{V}) + \mathscr{L}(\hat{\mathbf{v}}_\mathrm{f}; \mathbf{V}) &= \mathbf{f} && \text{in } \Omega_\mathrm{f}(t^n), \\ \mathbf{v}_\mathrm{f} &= \mathbf{v}_{\mathrm{f},D} && \text{on } \Gamma_{\mathrm{f},D}(t^n), \\ \mathbf{n}_\mathrm{f} \cdot \boldsymbol{\sigma}_\mathrm{f} &= \mathbf{t}_{\mathrm{f},N} && \text{on } \Gamma_{\mathrm{f},N}(t^n), \\ \mathbf{v}_\mathrm{f} &= \mathbf{v}_{\Gamma_\mathrm{i}}, && \text{on } \Gamma_\mathrm{i}(t^n). \end{aligned}$$

- **Check convergence and update unknowns**. Coupling convergence is checked based on the norm of the relative error between coupling iterations of displacements at the interface, i.e., $\|\mathbf{u}_{\Gamma_\mathrm{i},\mathrm{s}} - \mathbf{u}_{\Gamma_\mathrm{i},\mathrm{f}}\|_{L^2(\Gamma_\mathrm{i})}$ and tractions, i.e., $\|\mathbf{t}_{\Gamma_\mathrm{i},\mathrm{s}} - \mathbf{t}_{\Gamma_\mathrm{i},\mathrm{f}}\|_{L^2(\Gamma_\mathrm{i})}$, properly normalized. Convergence is achieved when this norm is below a given tolerance.

End block-iterative loop.

End loop over the number of time steps.

5.5 Numerical Examples

In this section, three numerical examples are presented to assess the performance of the proposed FSI solution strategy. In the first one, a flow through a channel with a flexible wall is considered to study the stationary solution. The main idea is to analyze the differences between the standard formulation and the logarithmic one when increasing the Weissenberg number of the problem. Next, so as to examine the effect of the viscosity, the well-known Turek's test [146] is presented. In this case, the behavior of a laminar channel flow around an elastic object is studied when elasticity becomes dominant in the fluid. To end up, the influence of arterial mechanical properties in the blood flow in an aneurysm is analyzed. In particular the blood is modeled as a viscoelastic fluid.

[146]: Turek et al. (2007), "Proposal for numerical benchmarking of fluid-structure interaction between an elastic object and laminar incompressible flow"

Concerning the iterative scheme, for all examples a maximum of 15 iterations are set for both the fluid and the solid sub-problems, whose numerical relative tolerance in the L^2 norm is 10^{-5}. Also, for the transmission conditions on the interface boundary (using again the L^2 norm), the relative tolerance is 10^{-3}. In order to solve the monolithic system of linear equations for each sub-problem, we use the Biconjugate Gradients solver, `BiCGstab` [71], which is implemented in the `PETSc` parallel solver library [17].

[71]: Vorst (1992), "Bi-CGSTAB: A fast and smoothly converging variant of Bi-CG for the solution of nonsymmetric linear systems"

[17]: Balay et al. (2015), *PETSc Web page*

It is important to mention that mesh convergence results and their corresponding error estimation for the fluid alone and the structure alone are already performed in previous works. In the case of the standard three-field formulation for the viscoelastic fluid, it can be found in [14]. With respect to the LCR it is performed in detail in [15]. On the structural side, the classical displacement-based formulation for finite strain theory is considered. This formulation is widely used and its error analysis results are presented, for example, in [9].

[14]: Castillo et al. (2014), "Variational multi-scale stabilized formulations for the stationary three-field incompressible viscoelastic flow problem"

[15]: Moreno et al. (2019), "Logarithmic conformation reformulation in viscoelastic flow problems approximated by a VMS-type stabilized finite element formulation"

[9]: Bonet et al. (1997), *Nonlinear Continuum mechanics for finite element analysis*

5.5.1 Flow through a channel with a flexible wall

This first problem is a simplified test case of a flow in an elastic tube. This test is the standard one used by many authors as a reference benchmark for both Newtonian (for example [147, 148]) and shear-dependent non-Newtonian fluids (see [149, 150]). Moreover, more recently, the works of

[147]: Luo et al. (1995), "A numerical simulation of steady flow in a 2-D collapsible channel"

[148]: Luo et al. (1996), "A numerical simulation of unsteady flow in a two-dimensional collapsible channel"

[149]: Lukáčová-Medviďová et al. (2008), "Numerical modelling of shear-thinning non-Newtonian flows in compliant vessels"

[150]: Lukáčová-Medviďová et al. (2013), "Kinematic splitting algorithm for fluid–structure interaction in hemodynamics"

[151]: Chakraborty et al. (2012), "Fluid-structure interaction in deformable microchannels"

Chakraborty et al. [151] and Chen et al. [135] also consider viscoelastic fluids to explore new possible effects. Essentially, the model consists of a steady flow in a channel where a part of the upper wall is replaced by an elastic plate. To sum up, firstly a study considering a Newtonian fluid will be performed, and later the effect of the viscoelasticity will be investigated, comparing the results with those that can be found in the literature. The benefits of the LCR approach proposed here will be highlighted.

Set up

[135]: Chen (2014), "Numerical Modeling of Fluid-Structure Interaction with Rheologically Complex Fluids"
[152]: Cai et al. (2003), "A fluid–beam model for flow in a collapsible channel"

The problem is defined according to the parameters proposed in [135, 152]. The scheme of the domain can be observed in Fig. 5.2. Regarding the channel measures, the rigid channel has height $D = 0.01$ m. The flexible wall has a length of $5D$, located at $5D$ from the channel entrance. The length of the channel downstream of the flexible wall is $30D$. For the computations, the flexible plate thickness d varies between $0.01D$ and $0.1D$.

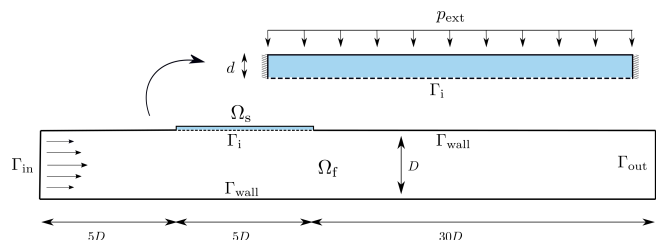

Figure 5.2: Flow through a channel with a flexible wall. Geometry.

Regarding the properties of the fluid, the density is $\rho_f = 1\,000$ kg/m^3 and the viscosity is $\mu_f^0 = 0.001$ Pa · s. For the elastic plate the properties are as follows: an initial density $\rho_{s,0} = 1\,200$ kg/m^3, a Young's modulus $E_s = 35.9$ kPa and a Poisson's ratio $\nu_s = 0.45$. A Saint Venant-Kirchhoff material law is employed (see Subsection 2.1.2 for a detailed description) and the plane strain assumption is considered.

Concerning the boundary conditions, in the inlet boundary of the fluid domain Γ_{in}, a steady Poiseuille flow with average velocity $\bar{v}_{in} = 0.03$ m/s is assumed; on the walls Γ_{wall} no-slip boundary conditions are imposed, and in the outlet Γ_{out} the pressure is set to $p_{out} = 0$ Pa. A rectangular plate is considered as the solid domain, where an external pressure $p_{ext} = 1.755$ Pa is distributed on the upper edge and it is clamped in both the left and the right sides. Therefore, the

considered Reynolds number is $\mathrm{Re} = \rho_f \bar{v}_{in} D/\mu_f^0 = 300$, where $\bar{v}_{in}$ is the average inlet velocity in the channel direction.

The domains are discretized by using bilinear structured elements (Q_1). Two meshes have been used for this example, whose numbers of elements are summarized in Table 5.1. The meshes M1f and M1s are employed for the Newtonian fluid flow study, and finer meshes M2f and M2s are used for studying all the viscoelastic cases.

Fluid mesh	Elements	Solid mesh	Elements
M1f	3 000	M1s	600
M2f	10 500	M2s	1 500

Table 5.1: Flow through a channel with a flexible wall. Main characteristics of the computational meshes.

FSI problem using a Newtonian fluid

Firstly, the validation considering a Newtonian regime is performed. For that, six different thickness have been considered to see the effect on the plate deformation. The distribution of velocities, pressures and stresses in the channel can be seen in Fig. 5.3. Note that the solution fields are similar for all six cases and, for this reason only one case is shown here. In these pictures, only the part of the domain where the plate is located has been plotted. The maximum velocity is reached in the narrowing of the channel produced by the deformed wall. Also, a peak of pressure and stress is observed in this area as a consequence of the local reduction of the channel width.

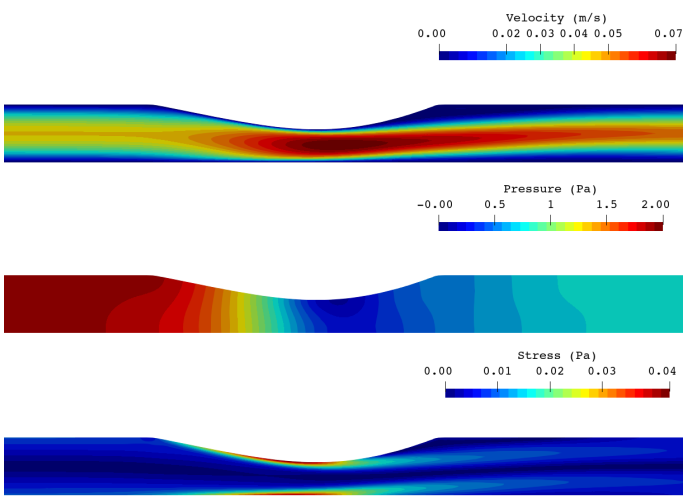

Figure 5.3: Flow through a channel with a flexible wall. Distribution of the velocity field (top), pressure (middle) and the stresses (bottom) in the fluid domain around the plate location for the plate thickness $d = 0.01D$. Velocities and stresses are plotted using their Euclidean norm.

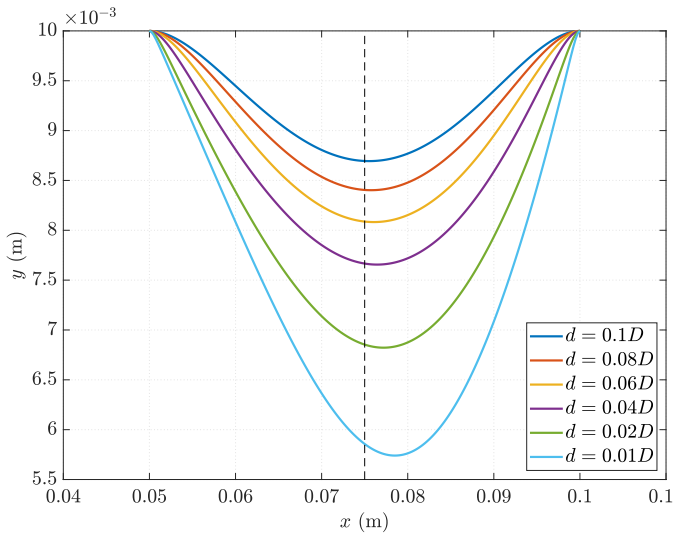

Figure 5.4: Flow through a channel with a flexible wall. Comparison of the vertical displacement of the plate for different thicknesses d using a Newtonian fluid.

The vertical displacement of the flexible plate for different thicknesses, from $d = 0.1D$ to $d = 0.01D$, can be observed in Fig. 5.4. As expected, the thickest plate is the less deformed one. The effect reported is that the slenderer the plate is, the higher the deformation of the plate becomes. Moreover, as the thickness increases, the lowest point of the wall moves upwards gradually due to the increment of forces exerted by the fluid. These results are in agreement with those reported in [134] and [135].

[134]: Luo et al. (2007), "On the initial configurations of collapsible channel flow"

[135]: Chen (2014), "Numerical Modeling of Fluid-Structure Interaction with Rheologically Complex Fluids"

FSI problem using a viscoelastic fluid

Once the Newtonian fluids have been tested, the study of the deformation for the thinnest plate (of thickness $d = 0.01D$) is carried out, but now varying the elasticity of the fluid. In other words, the problem using a viscoelastic fluid for several Weissenberg numbers is computed, so as to study the evolution of the flow when elasticity becomes dominant. The physical parameters have been set as in the previous section, with the exception of the relaxation time of the fluid and the β parameter, that now is set to 0.5.

Firstly, the deformation changes in the plate will be explored when the Weissenberg number increases, by using both fluid formulations (standard and LCR). This study is plotted in Fig. 5.5, where the deformation of the plate in each case is drawn from $\mathrm{We} = 0$ to $\mathrm{We} = 1.2$, which corresponds to relaxation times from $\lambda = 0$ s to $\lambda = 0.4$ s, respectively. Note that

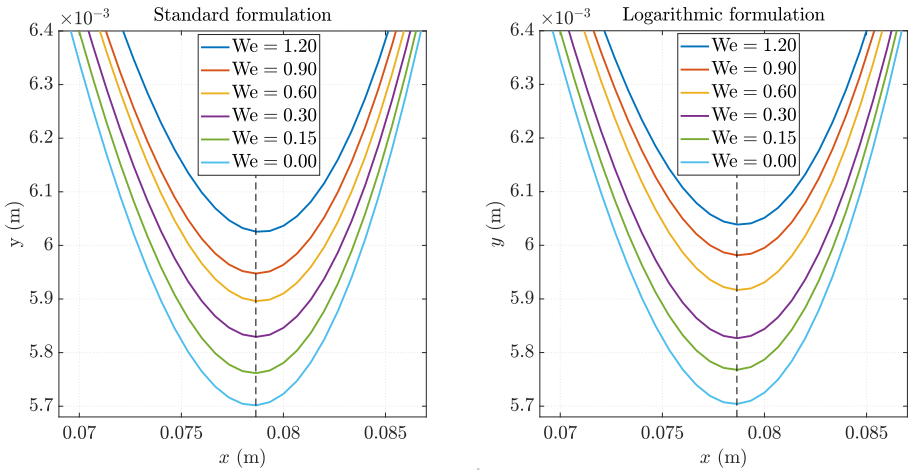

(a) Standard formulation

(b) LCR formulation

Figure 5.5: Flow through a channel with a flexible wall. Comparison of the deformation of the plate with thickness $d = 0.01D$ for several We numbers.

the results with We $= 0$ correspond exactly with the Newtonian fluid behavior. The classical Navier-Stokes equations written in a three-field formulation setting are automatically recovered (see Subsection 2.2.4).

It is interesting to highlight the phenomena produced when the elasticity becomes dominant. An attenuation of the deformation in the plate is produced. This effect is also reported in [135], and it is explained by the presence of a higher elasticity in the fluid: when elasticity increases, stresses do so significantly.

[135]: Chen (2014), "Numerical Modeling of Fluid-Structure Interaction with Rheologically Complex Fluids"

So as to clarify this physical effect, Table 5.2 shows a summary of the fluid forces on the solid and the momentum with respect to the center of gravity of the flexible wall. The external pressure p_{ext} acting over the plate causes a vertical force equal to $0.8775 \cdot 10^{-1}$ N. As it can be observed in Table 5.2, the resulting vertical fluid force increases as We number increases. That force is acting in the opposite direction to the one coming from the external pressure, reducing the deflection of the plate. It is important to mention that a small movement upwards is also appreciated in the lowest point of the wall in Fig. 5.5. Clearly it is caused by the reduction of momentum at the center of gravity of the membrane.

Both formulations (standard and LCR) show similar results for the plate displacement, although slight differences can

Table 5.2: Flow through a channel with a flexible wall. Horizontal and vertical forces and momentum with respect to the solid center of gravity.

We	F_x $[10^{-2}$ **N**$]$	F_y $[10^{-1}$ **N**$]$	M_{xy} $[10^{-2}$ **N·m**$]$
0.0	0.6225	0.4018	−0.3704
0.15	0.6056	0.4130	−0.3545
0.3	0.6098	0.4399	−0.3389
0.6	0.5734	0.4554	−0.3344
0.9	0.5416	0.4754	−0.3155
1.2	0.5534	0.5186	−0.3085

be reported for We numbers up to 0.3. These are explained by the different treatment of the stresses. However, when the element size is small enough, the solution converges exactly to the same solution, independently of the employed formulation.

Furthermore, we also study the distribution of pressure and first component of stress in the flexible wall for each computed case, plotted in Fig. 5.6. We have displayed the component σ_{xx} instead of the others because it is the most characteristic component of the stress tensor in this location. As expected, both solutions become higher when the elasticity of the fluid increases.

First of all, let us remark that for the highest elastic case computed (We = 1.2), results do not show a smooth solution for stresses when the standard formulation is employed, probably due to a lack of mesh resolution in this location; this can be clearly seen in Fig. 5.6a. This non-smoothness is also reported in [135], in which the smooth solution is reached using finer meshes. Note that this area presents large stress gradients, regions with particularly high deformation rate, and therefore this location is highly sensitive to the instability caused by the HWNP. However, through the application of the LCR approach, able to deal with the instability, a regular solution can be obtained, as it can be observed in Fig. 5.6b.

[135]: Chen (2014), "Numerical Modeling of Fluid-Structure Interaction with Rheologically Complex Fluids"

For We numbers up to 0.3, the LCR is able to capture higher values for the peaks of stresses than the standard formulation; concerning the pressure field, a bad solution is obtained for We = 1.2 for the standard formulation, as it can be observed in Fig. 5.6c. Despite the fact of obtaining a smooth solution, it should be higher than the one obtained for We = 0.9. A correct solution is obtained if the LCR for the viscoelastic fluid is used, as it is shown in Fig. 5.6d.

All the cases reported until We = 1.2 have a converged solution using both formulations. It is important to remark that the employed formulation does not affect significantly the

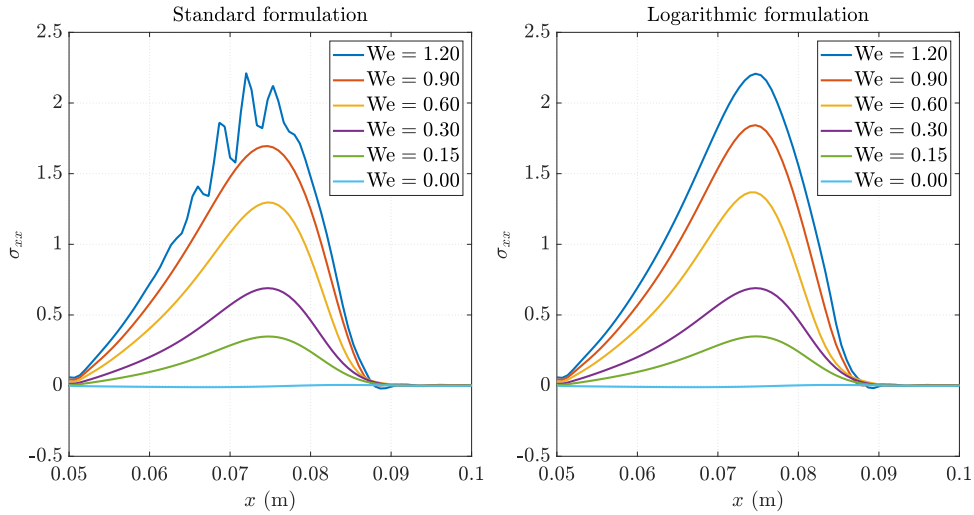

(a) Deviatoric stress σ_{xx} **(b)** Deviatoric stress σ_{xx}

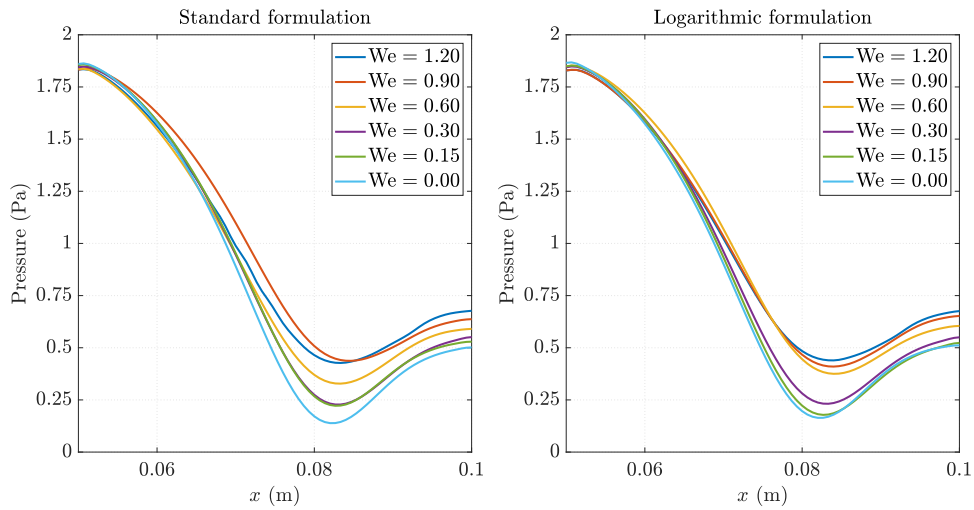

(c) Pressure p **(d)** Pressure p

Figure 5.6: Flow through a channel with a flexible wall. Comparison of the first component of stress and pressure in the plate with thickness $d = 0.01D$ using the standard and the LCR representation.

final displacement of the plate, even for the fluid flow with high Weissenberg number, as it can be seen in Fig. 5.5. However, the iterative scheme suffers a breakdown for the standard formulation when We > 1.2. This breakdown seems to be caused by the incapability of the formulation of capturing suitably both the stress and the pressure fields for the chosen mesh with We $= 1.2$ (see Fig. 5.6).

5.5.2 Turek's test

In this case, we study the FSI between an hyperelastic structure and a laminar flow. This benchmark is used by many authors as a reference test to check their implementations of the FSI problem [146]. The configuration consists of a laminar channel flow around an elastic object which results in self-induced oscillations of the structure. Firstly, a study considering a Newtonian fluid will be performed and compared with the literature, and then the effect of the viscoelasticity will be investigated.

[146]: Turek et al. (2007), "Proposal for numerical benchmarking of fluid-structure interaction between an elastic object and laminar incompressible flow"

Setup

The geometry of the problem is displayed in Fig. 5.7. The rigid channel has height $H = 0.41$ m and length $L = 2.5$ m. The circle center is positioned at point $C = (0.2, 0.2)$ m (measured from the left bottom corner of the channel) and its radius is $r = 0.05$ m. The structure bar has length $l = 0.35$ m and height $h = 0.02$ m. The right bottom corner is positioned at $(0.6, 0.19)$ m, and the left end is fully attached to the fixed cylinder.

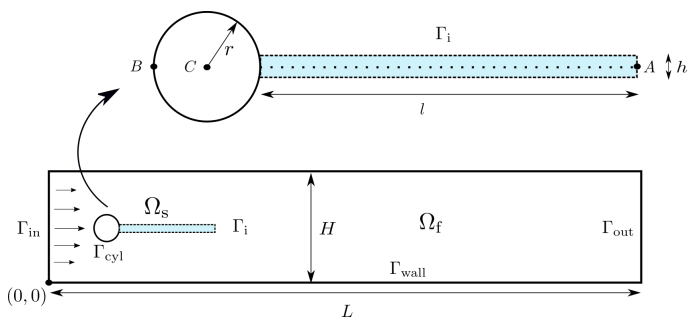

Figure 5.7: Turek's test. Geometry.

With regards to boundary conditions, a parabolic profile is prescribed at the left channel inflow, given by

$$\bar{v}_{\mathrm{f}}(0, y) = 1.5\, \bar{v}_{in} \frac{y(H - y)}{\left(\frac{H}{2}\right)^2}, \tag{5.84}$$

such that the mean inflow velocity is $\bar{v}_{in}$ and the maximum of the inflow velocity profile is $1.5\bar{v}_{in}$. A smooth increase of

the velocity profile in time is prescribed, given by

$$v_{\mathrm{f}}(0, y, t) = \begin{cases} \bar{v}_{\mathrm{f}}(0, y)\frac{1-\cos\frac{\pi}{2}t}{2} & t < 2.0 \text{ s} \\ \bar{v}_{\mathrm{f}}(0, y) & \text{otherwise} \end{cases}. \tag{5.85}$$

The outflow condition is considered stress free. Finally, a no-slip condition is prescribed for the fluid on the other boundary parts. Concerning the boundary conditions of the structure, fixed null displacement is considered in the left edge.

Two FSI tests are performed: on the one hand, FSI1, which results in a stationary solution; on the other hand, FSI2, which has a periodic solution. Table 5.3 shows the parameter settings for each FSI case. Note that here the viscosity of the fluid $\nu_{\mathrm{f}} = \mu_{\mathrm{f}}^0/\rho_{\mathrm{f}}$ is the kinematic one.

Parameter	FSI1	FSI2
$\rho_{\mathrm{s},0}$ $[10^3 \frac{\mathrm{kg}}{\mathrm{m}^3}]$	1	10
ν_{s} [-]	0.4	0.4
E_{s} $[10^6 \frac{\mathrm{kg}}{\mathrm{ms}^2}]$	1.4	1.4
ρ_{f} $[10^3 \frac{\mathrm{kg}}{\mathrm{m}^3}]$	1	1
ν_{f} $[10^{-3} \frac{\mathrm{m}^2}{\mathrm{s}}]$	1	1
$\bar{v}_{in}$ $[\frac{\mathrm{m}}{\mathrm{s}}]$	0.2	1
Re [-]	20	100

Table 5.3: Turek's test. Parameter settings for the FSI1 and FSI2 cases.

The domains are discretized using P_1 (linear) elements for the fluid domain and Q_1 (bilinear) elements for the solid one. Regarding the distribution of the elements, the mesh is finer around the cylinder and the bar, while downstream the mesh is coarser, as it can be observed in Fig. 5.8. In total, the fluid mesh is formed by 25 000 unstructured elements, and the solid mesh by 10 000 (20 × 500) structured elements.

FSI problem using a Newtonian fluid

The aim of this section is to compare our results with the ones coming from the benchmark in [146] by using a Newtonian fluid and a Saint Venant-Kirchhoff solid material. First of all, the stationary case FSI1 is validated with reference [146] in Table 5.4, which includes displacements, drag and lift forces. The results completely agree with the reference ones, as it

[146]: Turek et al. (2007), "Proposal for numerical benchmarking of fluid-structure interaction between an elastic object and laminar incompressible flow"

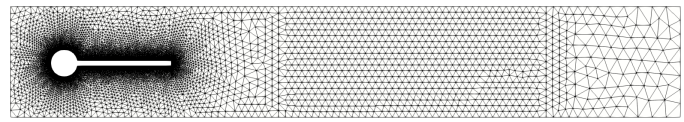

(a) Mesh of the fluid domain

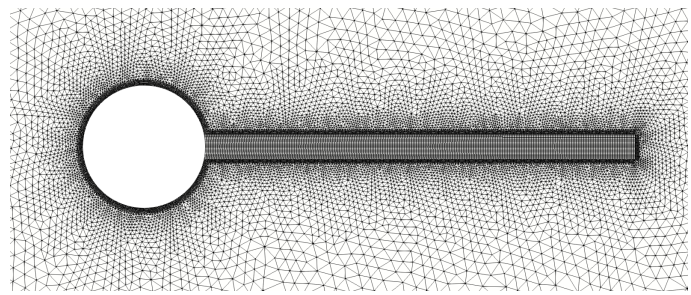

(b) Zoom around the cylinder and bar and mesh of the solid domain

Figure 5.8: Turek's test. Mesh domain.

can be observed. For these computations the LCR representation has been employed, but note that the solution would be exactly the same for the standard one due to for We $= 0$ (and therefore $\lambda = 0$) we recover exactly the Navier Stokes equations written in three-field form.

Table 5.4: Turek's test. Displacement at point A and forces exerted by the fluid on the whole submerged body (cylinder and beam) for FSI1 benchmark.

	u_x $[10^{-4}$ m]	$u_y[10^{-3}$ m]	**drag** [N]	**lift** [N]
Current	0.2241	0.8202	14.263	0.7657
[146]	0.2270	0.8209	14.295	0.7638

Moreover, the dynamic case is also tested, namely FSI2. Fig. 5.9 shows the solution for three different times. The bar displacements observed and the lift and drag obtained are also in agreement with the reference paper. We can conclude that the FSI algorithm has been suitably checked.

Finally, the three-field based formulation (with fluid unknowns velocity, pressure and stresses as stated in Subsection 2.2.4) and a two-field based one (where the unknowns are velocity and pressure as presented in Subsection 2.2.3) are compared. It is done to stand out the principal differences and to explain why the three-field one is better in terms of accuracy. The differences between stresses are highlighted in both cases in Fig. 5.10: while in the two-field algorithm the stresses are computed from the velocity gradient, and therefore constant over elements for linear FEs, in the three-field formulations the stresses are linear. The accuracy of the fluid traction computed and transmitted to the solid on its surface

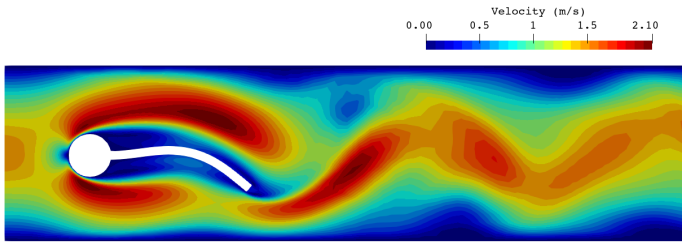

(a) $t = 34.0$ s

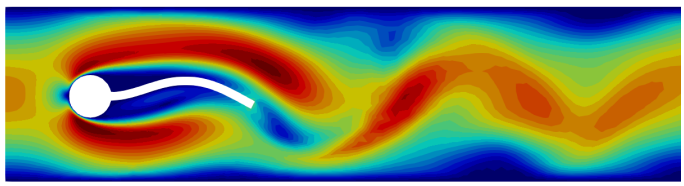

(b) $t = 34.1$ s

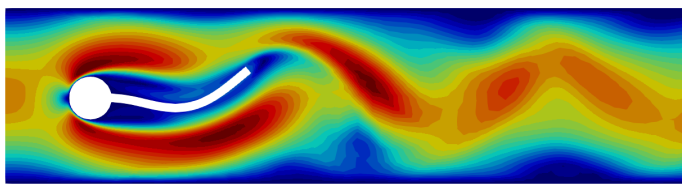

(c) $t = 34.3$ s

Figure 5.9: Turek's test. Plot of the velocity norm for test FSI2 at different times.

is enhanced by using the three-field formulation due to the increase of accuracy of the stresses. See [39] for further details between the comparison of both formulations with regards to enhanced accuracy of stresses.

[39]: Castillo et al. (2014), "Stabilized stress-velocity-pressure finite element formulations of the Navier-Stokes problem for fluids with non-linear viscosity"

FSI problem using a viscoelastic fluid flow

In this subsection, the same problem is developed using a viscoelastic fluid and a Neo-Hookean model for the solid. First of all, numerical results are presented for the FSI1 case. Table 5.5 shows the displacement of the end of the beam structure at point A and the resulting forces exerted by the fluid on the whole submerged body. In this case the effect of viscoelasticity can be clearly analyzed. When the elasticity of the fluid increases, the vertical force exerted by the fluid (lift) also becomes higher. This phenomenon is in accordance with the study done in [15] in the classic flow over a cylinder case. One can conclude that higher vertical forces on the FSI boundary will cause the beam to show higher values of deformation.

[15]: Moreno et al. (2019), "Logarithmic conformation reformulation in viscoelastic flow problems approximated by a VMS-type stabilized finite element formulation"

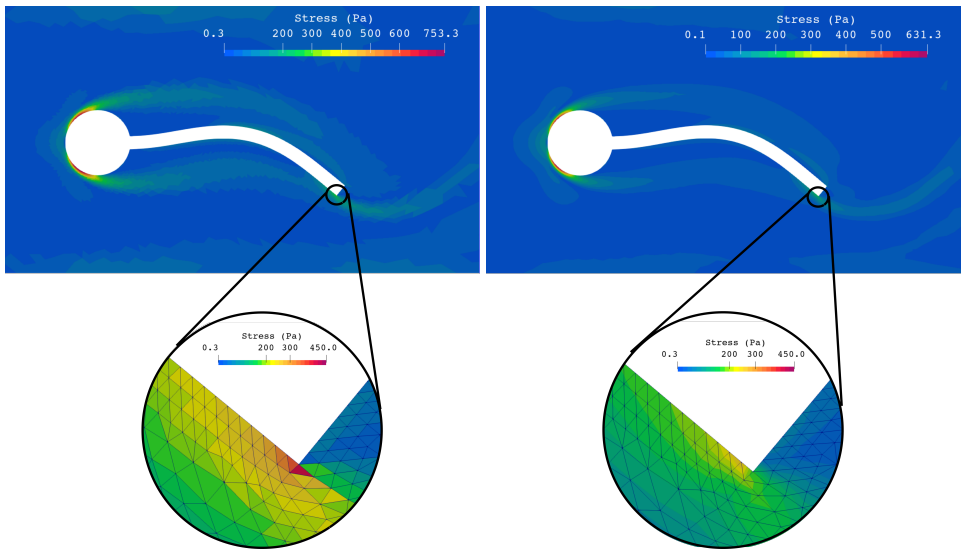

(a) vp formulation **(b)** v$p\boldsymbol{\sigma}$ formulation

Figure 5.10: Turek's test. Comparison of distribution of the stress field between the two-field formulation and the three-field one for the FSI2 test.

Table 5.5: Turek's test. Displacement at point A and forces exerted by the fluid on the beam for case FSI1.

We	u_x [10^{-4} m]	u_y [10^{-3} m]	**drag** [N]	**lift** [N]
0.0	0.2241	0.8202	14.263	0.7657
0.2	0.2107	0.9384	14.703	0.7748
0.4	0.1959	1.0650	15.250	0.7800
0.6	0.1765	1.2020	16.089	0.7873
0.8	0.1572	1.3100	17.038	0.7774
1.0	0.1435	1.3440	18.003	0.7396
1.2	0.1386	1.2520	19.054	0.6669

For the FSI2 problem, the evolution in time for displacements, lift and drag is computed for several We numbers. The maximum We number regime that the algorithm is able to simulate using this mesh is We $= 0.4$. Let us remark that the "characteristic" We number can vary depending on the problem configuration or the Reynolds number of the problem. In this case, the Reynolds number is higher than for the FSI1 problem, and therefore the maximum We number for which the algorithm is able to reproduce well-defined solutions is smaller than for case FSI1. In Fig. 5.11 the tracking of the solution of point A along a second is performed to compare the different fluid flows. Note that the phases between plot cases have been conveniently adjusted in order to ease the comparisons. In the y-displacements, minimum and maximum peaks have slight variations. While for low Weissenberg numbers, higher

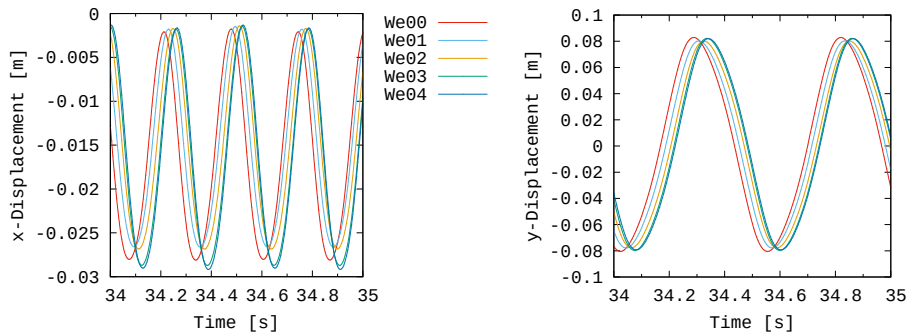

(a) Displacement u_x

(b) Displacement u_y

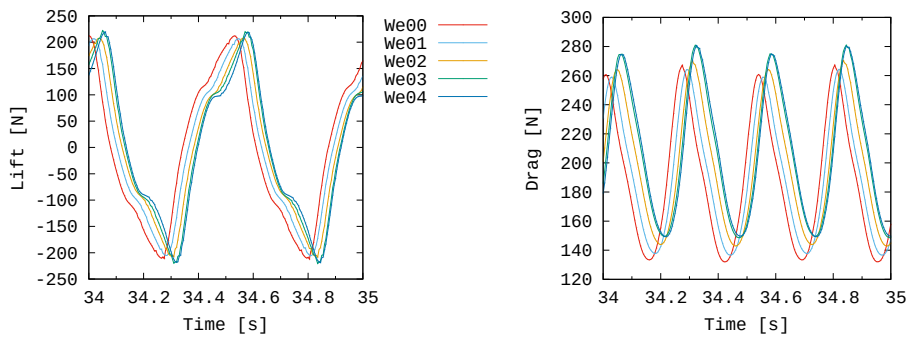

(c) Lift

(d) Drag

Figure 5.11: Turek's test. Results for FSI2.

than zero, a reduction of y-displacement is reported, when it grows up to $We = 0.3$ or $We = 0.4$ the displacements increase. This effect is connected with lift and drag force changes, which show a similar effect (see Fig. 5.11).

5.5.3 Abdominal aortic aneurysms

As a final example, an abdominal aortic aneurysm is analyzed. The study of blood flow is important to understand the mechanisms behind the onset and progression of atherosclerosis [153, 154]. Many studies related to abdominal aortic aneurysms consider the blood as a purely viscous fluid with constant viscosity, that is, a Newtonian fluid. In [155, 156] it is explained that blood can be modeled as an homogeneous shear-thinning and viscoelastic fluid characterized by the Oldroyd-B model. This is justified due to blood exhibiting non-Newtonian characteristics, mainly due to shear thinning viscosity and viscoelasticity related to stress relaxation and

[153]: Gharabi et al. (2016), "Computational fluid dynamic simulation of human carotid artery bifurcation based on anatomy and volumetric blood flow rate measured with magnetic resonance imaging"

[154]: Siasos et al. (2018), "Local low shear stress and endothelial dysfunction in patiens with nonobstructive coronary atherosclerosis"

[155]: Zaman et al. (2012), "Blood flow of an Oldroyd-B fluid in a blood vessel incorporating a Brownian stress"

[156]: Anand et al. (2013), "A new generalized Oldroyd-B model for blood flow in complex geometries"

normal stress effects. Moreover, in the case of small arteries, the microstructure and rheological behavior of blood should not be neglected since the dimension of the blood particles is of the same order as that of the vessels. The parameters we used for modeling the blood flow are taken from [157].

[157]: Elhanafy et al. (2019), "Numerical simulation of Oldroyd-B fluid with application to hemodynamics"

In [157] a two-dimensional numerical study is performed in which the blood is modeled as a viscoelastic fluid, in which the Oldroyd-B constitutive model is used to represent the viscoelastic properties of the blood. Results show that at higher volumetric flow rates, which correspond to low shear rate situations, vortices are observed. The relative error with respect to the Newtonian flow model in these cases is of order 40 % and cannot be neglected. Furthermore, in [158] the influence of arterial mechanical properties on carotid blood flow is shown by comparing models with rigid and elastic walls. The conclusion that can be quickly drawn from the study is that the reciprocal influence of both fluid and solid (blood and artery) must be taken into account, so as not to overestimate the effect of rigid walls in the blood flow. In this example, we carry on a VFSI study to approximate the behavior of blood flow as a viscoelastic flow and to consider the artery as an hyperelastic Neo-Hookean material.

[158]: Lopes et al. (2019), "Influence of arterial mechanical properties on carotid blood flow: Comparison of CFD and FSI studies"

Setup

The geometry of the problem is displayed in Fig. 5.12. In this picture, one can observe the geometry of a channel with one single aneurysm. Particularly, in Fig. 5.12a the fluid arterial domain is plotted and in Fig. 5.12b the solid domain, where a membrane thickness of $d = 0.001$ m is considered, following the one described for the carotid case in [158]. Finally, the fully coupled model is drawn in Fig. 5.12c, where a transversal cut is done to indicate the lengths adopted for the 3D domain generation. In our case, $D = 0.008$ m is the diameter of the artery at the inlet and outlet sections, $R = D/2$ is the aneurysm ratio, $L_T = 7.5D$ is the domain total length, and the other dimensions are set as $L_1 = 2.5D$ and $L_2 = 5D$. Also $D_1 = 2D$ is the maximum diameter adopted in the domain for the artery. Moreover, the geometry has been constructed using the curve

$$y = \left(\frac{D_1 - D}{2}\right)\left[1 + \sin\left(\frac{2\pi(x - L_1)}{L_2} - \frac{\pi}{2}\right)\right] + \frac{D}{2} \quad L_1 \leq x \leq L_2, \tag{5.86}$$

which has been revolutionized over the longitudinal axis (x).

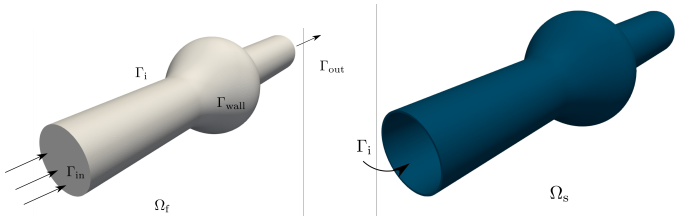

(a) Fluid domain **(b)** Solid domain

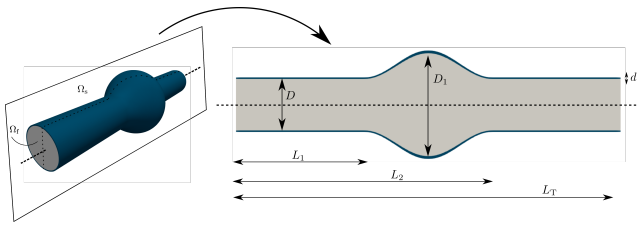

(c) Full domain

Figure 5.12: Abdominal aortic aneurysms. Geometry.

Once the geometry has been defined, the fluid and solid properties will be described. First of all, the blood in the artery is considered as a Newtonian fluid, and later as a viscoelastic one. For the Newtonian cases performed, the blood density is $\rho_{\text{f}} = 1\,060\ \text{kg/m}^3$ and the dynamic viscosity $\mu_{\text{f}} = 3.5 \cdot 10^{-3}$ Pa·s; for the viscoelastic fluid model, the properties are $\mu_{\text{f}}^{s} = 3.19 \cdot 10^{-3}$ Pa · s for the solvent viscosity and $\mu_{\text{f}}^{p} = 4 \cdot 10^{-4}$ Pa · s for the polymeric viscosity. In other words, the total viscosity is set to $\mu_{\text{f}}^{0} = 3.49$ Pa · s and $\beta = 0.88$. Concerning the relaxation time, it is set to $\lambda = 0.06$ s. Secondly, for the solid domain, which models the vessel wall deformation, an hyperelastic Neo-Hookean law is considered. Regarding the mechanical properties, the density is $\rho_{\text{s},0} = 1\,120\ \text{kg/m}^3$, the Poisson ratio is $\nu_{\text{s}} = 0.45$ and elastic modulus is $E_{\text{s}} = 1.106 \cdot 10^6$ Pa.

For the fluid domain, a no-slip boundary condition is imposed over the walls and a fully developed flow is assumed at the artery inlet, following the expression

$$v_x(0, y, z, t) = v_{\text{max}} \left(1 - \frac{(z^2 + y^2)}{R^2}\right), \tag{5.87}$$

$$v_y(0, y, z, t) = v_z(0, y, z, t) = 0. \tag{5.88}$$

Note that v_x is the main direction of the flow in the artery; the average velocity at the inlet is $\bar{v} = 0.05968$ m/s taking $v_{\text{max}} = 0.11936$ m/s as the maximum velocity reached at the inlet. The flow rate is $Q = 3 \cdot 10^{-6}\ \text{m}^3/\text{s}$. This is the maxi-

[157]: Elhanafy et al. (2019), "Numerical simulation of Oldroyd-B fluid with application to hemodynamics"

mum flow rate adopted by the reference paper [157]. While in the Newtonian regime stresses are considered free in the inlet, for the viscoelastic fluid flow case those have been fixed associated to the parabolic velocity profile. The artery exit is considered stress free, but to avoid fluid recirculations in the exit only the first component of the velocity is set to be free. Lastly, note that the Reynolds number associated to this regime is 139.7 and, for the viscoelastic fluid flow, the We number is 0.447.

Relative to the solid model, the boundaries adjacent to the inlet and outlet are fixed. On the remaining boundaries of the solid, a stress free condition is considered, which basically allows the solid to deform in any direction.

Concerning the generated mesh, it is unstructured and the domain is discretized using 582 804 tetrahedral FEs for the fluid domain, while the solid one has 286 597 hexahedral elements. The minimum element size, found on the walls of the fluid domain and in the solid domain, is about $h_{\min} = 0.00025$ m. The time step size is set to $\delta t = 0.0025$ s.

Results

[158]: Lopes et al. (2019), "Influence of arterial mechanical properties on carotid blood flow: Comparison of CFD and FSI studies"

As mentioned earlier, a similar study is performed in [157] for a 2D case to highlight the importance of choosing a viscoelastic fluid for modeling the human blood; however, we also incorporate the interaction with a solid membrane, as suggested in [158]. Its effect is quantified in the following.

Fig. 5.13 shows the fluid flow streamlines. Specifically, Fig. 5.13a plots the streamlines in the full 3D model. Here, the vortices of the flow, which are located close to the aneurysm walls, can be clearly observed. For a better comprehension of these vortices, both Fig. 5.13b (Newtonian case) and Fig. 5.13c (viscoelastic case) are displayed in a transversal cut in the $z = 0$ plane. Note that this plane is in the middle of the domain. In contrast with the Newtonian fluid, it is remarkable how the center of vortices is moved on downstream for the viscoelastic case. Note that for this Reynolds number the solution has axial symmetry.

In Fig. 5.14 the distribution of the dominant component of the stresses is shown on the plane $z = 0$. The Newtonian case

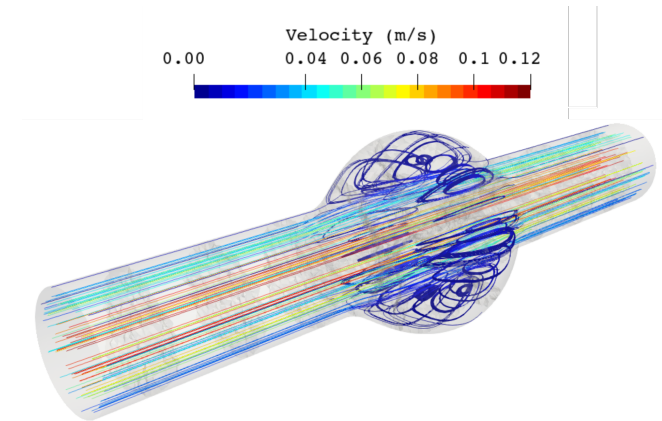

(a) Streamlines in the full 3D model

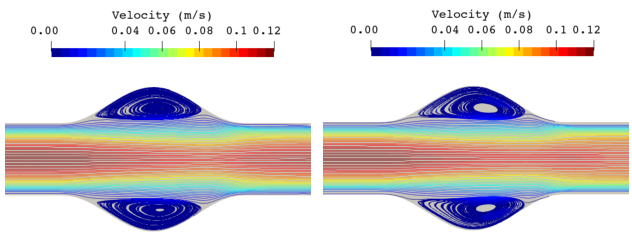

(b) Streamlines of the Newtonian fluid in a cut in the $z = 0$ plane.

(c) Streamlines of the viscoelastic fluid in a cut in the $z = 0$ plane.

Figure 5.13: Abdominal aortic aneurysms. Streamlines in the full domain and in a transversal cut, coloured with the norm of the velocity.

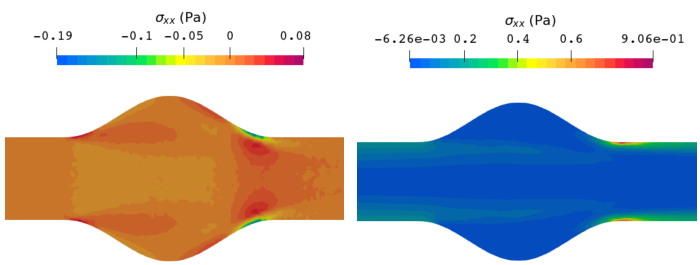

(a) Newtonian fluid

(b) Viscoelastic fluid

Figure 5.14: Abdominal aortic aneurysms. First component of the stresses. Comparison between Newtonian and viscoelastic regimes in a fluid domain transversal cut.

shows smaller values than the viscoelastic case and the maximum peaks are reached at the center of the channel. However, the viscoelastic case accumulates stresses on the walls immediately downstream of the aneurysm. This is graphically evaluated in Fig. 5.15, where the norm of stresses over the top line in the $z = 0$ plane is plotted. The difference of magnitude in this location is notable, as reported in [157]. The vertical lines indicate the region of the aneurysm. This effect is important when dealing with aneurysms, and should not be neglected. Finer elements around the walls would be

needed to obtain smoother solutions.

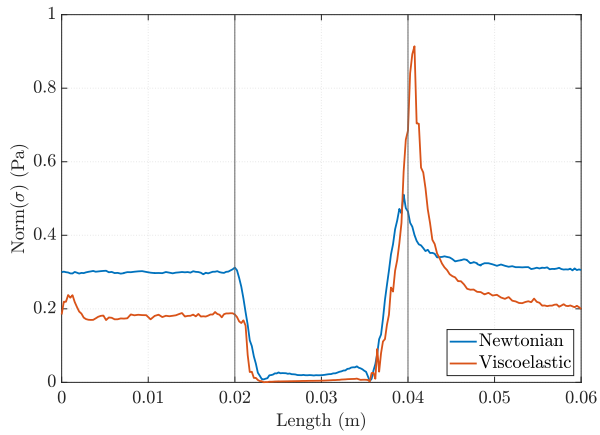

Figure 5.15: Abdominal aortic aneurysms. Comparison for the stress norm along the top wall in the plane $z = 0$ of the fluid domain.

5.6 Conclusions

In this chapter, a numerical approximation for VFSI problems with viscoelastic fluids in which elasticity can be dominant has been presented. The main idea is to reproduce scenarios with a viscoelastic fluid model and particularly using the so-called log-conformation reformulation. This technique allows to treat the exponential growth of the elastic stresses and, therefore, extend the range of Weissenberg numbers in which the VFSI problem can be solved.

Several numerical examples have been run to assess the performance of the proposed VFSI problem and its applicability to viscoelastic flows with high elasticity. First of all, some examples with Newtonian fluids have been performed to validate our FSI model and to show that both the standard and the logarithmic formulation presented in Section 5.3 match with the classical Navier-Stokes equations written in a three-field setting when $\mathrm{We} = 0$.

Regarding the elasticity of the fluid, we have shown the effect of increasing it. When elasticity increases, stresses do so significantly. This effect causes elastic forces to grow up and, therefore, fluid tractions on the solid become higher.

With regards to the three-field formulations presented in this work, several conclusions can be drawn. Firstly, we have

shown the effect of considering the stress as a primary unknown. It becomes crucial when dealing with viscoelastic flows due to the need to solve an additional differential equation for the stresses. Furthermore, more accurate results are obtained for stresses with respect to the classical two-field formulation in which these stresses are computed as a post-process. This is clearly a benefit when computing fluid tractions to be imposed in the solid problem. When facing high elasticity cases for the same mesh, the standard formulation fails to obtain smooth solutions, whereas the logarithmic formulation is able to handle these situations and regular solutions are obtained.

To end up, we have demonstrated the good performance of our implementation in a 3D problem. Furthermore, the effect of considering the blood flow as a viscoelastic fluid and to mimic the arteries as hyperelastic materials has been studied. The results prove that differences between Newtonian and viscoelastic models should not be underestimated and that viscoelastic constitutive modeling is necessary, specially when the flow rate in the artery increases.

Topology optimization of incompressible structures subject to FSI

6

6.1 Introduction

Fluid-Structure Interaction (FSI) problems involve the interaction between a fluid and a deformable solid structure. These problems arise in various engineering and scientific applications, including aerospace [112], civil engineering [159], biomechanics [113, 160], and offshore structures [161]. Numerical methods play a significant role in solving FSI problems by providing efficient and accurate solutions. These methods combine fluid dynamics and structural mechanics algorithms to simulate the coupled behavior of fluids and structures. The interaction between the fluid and the structure is typically modeled by exchanging information at the fluid-structure interface [115]. Understanding and accurately simulating FSI phenomena is crucial for designing and optimizing systems where fluid and structure interact [116, 162].

One common approach for simulating FSI problems is the partitioned approach, where separate solvers are used for the fluid and structural domains. In this approach, the fluid solver calculates the fluid flow field while treating the structure as a rigid body or prescribing its motion based on the interaction forces. The structural solver computes the deformation and stress response of the solid structure based on the fluid-induced loads. The coupling between the two solvers is achieved by iteratively exchanging information at the fluid-structure interface until convergence is reached [114, 163].

Fluid-structure interaction (FSI) problems involving incompressible structures are a subset of FSI phenomena where the solid undergoes negligible volume changes when subjected to external forces or deformations. In such problems, the fluid interacts with a solid object that remains essentially incompressible, maintaining its volume throughout the interaction [90]. The study of FSI involving incompressible solids is crucial in numerous fields, including biomechanics, bioengineering, soft robotics, and material science [164, 165]. Examples of incompressible structures include soft tissues, elastomers, gels, and certain biological materials [166–168]. Understanding the complex interactions between the fluid and

[112]: Kamakoti et al. (2004), "Fluid-structure interaction for aeroelastic applications"

[159]: Rhyzhakov et al. (2017), "A finite element model for fluid–structure interaction problems involving closed membranes, internal and external fluids"

[113]: Bodnár et al. (2014), *Fluid-Structure Interactions and Biomedical Applications*

[160]: Rhyzhakov et al. (2019), "Computational modeling of the fluid flow and the flexible intimal flap in type B aortic dissection via a monolithic arbitrary Lagrangian/Eulerian fluid-structure interaction model"

[161]: Yan et al. (2016), "Computational free-surface fluid–structure interaction with application to floating offshore wind turbines"

[115]: Richter et al. (2010), "Finite Elements for Fluid-Structure Interaction in ALE and Fully Eulerian coordinates"

[116]: Richter (2017), *Fluid-Structure Interactions*

[162]: Rhyzhakov et al. (2010), "A monolithic Lagrangian approach for fluid–structure interaction problems"

[114]: Küttler et al. (2008), "Fixed-point fluid–structure interaction solvers with dynamic relaxation"

[163]: Moreno et al. (2023), "Numerical simulation of Fluid–Structure Interaction problems with viscoelastic fluids using a log-conformation reformulation"

[90]: L.R.G.Treloar (1975), *The Physics of Rubber Elasticity*

[164]: Comellas et al. (2016), "A generalized finite-strain damage model for quasi-incompressible hyperelasticity using hybrid formulation"

[165]: Martínez-Frutos et al. (2021), "In-silico design of electrode meso-architecture for shape morphing dielectric elastomers"

the incompressible solid is essential for designing and optimizing systems in these domains.

Mixed formulations are commonly used in the context of incompressible structures to handle the incompressibility constraint. These formulations introduce additional unknowns, such as the pressure field, to enforce volume conservation. The most widely used mixed formulations are the displacement-pressure mixed formulations [23, 91] or the three-field formulations which add some extra unknown to increase its accuracy [27, 28, 169]. These formulations provide stable and accurate solutions for incompressible problems by coupling the displacement and pressure fields, and in this work, they are employed to model FSI simulations involving incompressible structures.

Topology Optimization (TO) is a powerful computational design approach that aims to optimize the material distribution within a given design domain to achieve desired performance objectives. The goal is to find the optimal arrangement or layout of material that meets specified criteria while considering design constraints [79]. The primary objective of TO of incompressible structures is to improve structural stiffness while ensuring volume conservation. In these problems, the incompressibility constraint needs to be satisfied throughout the optimization process, meaning that the total volume or the fraction of occupied material within the design domain remains constant [2, 88].

TO is an efficient method to improve mechanical systems design in engineering. In the last decade, several methods have been developed to find optimal structures inside predefined design domains by minimizing objective functions and constraints [79, 80, 82–84].

Although the field of structural optimization has become mature, many applications, such as aeronautics or biomechanics, require multiphysics design [92, 170–173]. As a consequence, methodologies for structural TO in FSI problems have become popular as they provide a framework to include FSI models in the TO design procedure.

These methodologies were classified in [174] according to the treatment applied on the interface between the fluid flow and the structure. Therefore, those cases in which only the internal part of the structure is optimized are named ”dry” or

[166]: Wex et al. (2015), “Isotropic incompressible hyperelastic models for modelling the mechanical behaviour of biological tissues: a review”

[167]: Comellas et al. (2016), “A homeostatic-driven turnover remodelling constitutive model for healing in soft tissues”

[168]: Comellas et al. (2020), “Modeling the porous and viscous responses of human brain tissue behavior”

[23]: Baiges et al. (2017), “Variational Multiscale error estimators for solid mechanics adaptive simulations: an Orthogonal Subgrid Scale approach”

[91]: Castañar et al. (2020), “A stabilized mixed finite element approximation for incompressible finite strain solid dynamics using a total Lagrangian formulation”

[27]: Chiumenti et al. (2015), “A mixed three-field FE formulation for stress accurate analysis including the incompressible limit”

[28]: Chiumenti et al. (2021), “Stress, strain and dissipation accurate 3-field formulation for inelastic isochoric deformation”

[169]: Castañar et al. (2023), “A stabilized mixed three-field formulation for stress accurate analysis including the incompressible limit in finite strain solid dynamics”

[79]: M.P.Bendsøe et al. (2013), *Topological Optimization: Theory*

[2]: A.A.Novotny et al. (2013), *Topological Derivatives in Shape Optimization*

[88]: A.A.Novotny et al. (2019), “Topological Derivatives of Shape Functionals. Part I: Theory in Singularly Perturbed Geometrical Domains”

design-independent optimization whereas the "wet" or design-dependent optimization are referred to those cases in which the geometry of the FSI boundary can be changed during the TO process.

Regarding the latter, several methodologies have been proposed during the last years. In [175] the idea of using a monolithic approach to interpolate both structural and fluid equations based on the density method was proposed for steady-state FSI problems. These ideas were lately extended to stress-based TO [176]. Another option was proposed in [177] to extend the XFEM-Level-set method reported in [174] to "wet" optimization. The bi-directional evolutionary structural optimization is also applied in [178] to disjoint the problem into two subdomains and be able to tackle them in a separate way. A body-fitted mesh evolution technique integrated into a level-set method can be found in [179]. Finally, the reaction-diffusion equation-based level-set methods are applied to solve the FSI optimization problem presented in [180]. All these works concern the interaction between a linear elastic compressible structure and viscous fluid flows governed by the incompressible Navier-Stokes equations.

In this chapter, we are interested in "dry" TO for FSI problems. In particular, FSI problems which are two-way coupled. The flow depends on the structural displacements and the structural behavior depends upon the fluid forces. As the FSI boundary remains constant over the TO procedure, we can use a staggered approach to solve individually the fluid and the structure sub-problems and satisfy the interface conditions in a strongly-coupled manner.

In this study, we propose a new "dry" TO framework for strongly-coupled FSI systems with incompressible structures. To the best of our knowledge, this is the first attempt to use TO of incompressible structures in FSI problems. Furthermore, the structural model can be either linear elastic or hyperelastic, allowing for finite strain deformations. In addition, the study of transient FSI problems is also performed.

This chapter is organized as follows. In Section 6.2 the setting of the whole TO problem of incompressible structures subject to FSI is presented. Next, the algorithm developed to reproduce such problems is presented in Section 6.3. Some numerical examples are shown in Section 6.4 to assess and validate the proposed methodology. The chapter is closed with some conclusions in Section 6.5.

[79]: M.P.Bendsøe et al. (2013), *Topological Optimization: Theory*
[80]: M.P.Bendsøe et al. (1988), "Generating optimal topologies in structural design using a homogenization method"
[82]: X.Huang et al. (2010), "A further review of ESO type methods for topology optimization"
[83]: Dijk et al. (2013), "Level-set methods for structural topology optimization: a review"
[84]: J.D.Deaton et al. (2014), "A survey of structural and multidisciplinary continuum topology optimization: post 2000"
[92]: O.Sigmund et al. (2007), "Topology optimization using a mixed formulation: An alternative way to solve pressure load problems"
[170]: Deng et al. (2013), "Topology optimization of steady and unsteady incompressible Navier-Stokes flows driven by body forces"
[171]: Shu et al. (2014), "Level set based topology optimization of vibrating structures for coupled acoustic-structural dynamics"
[172]: Wang et al. (2016), "Topological design and additive manufacturing of porous metals for bone scaffols and orthopaedic implants: a review"
[173]: Andreasen et al. (2013), "Topology optimization of fluid-structure-interaction problems in poroelasticity"
[174]: Jenkins et al. (2015), "Level set topology optimization of stationary fluid-structure interaction problems"
[175]: Yoon (2010), "Topology optimization for stationary fluid-structure interaction problems using a new monolithic formulation"
[176]: Yoon (2014), "Stress-based topology optimization method for steady-state fluid-structure interaction problems"

[177]: Jenkins et al. (2016), "An immersed boundary approach for shape and topology optimization of stationary fluid-structure interaction problems"

[174]: Jenkins et al. (2015), "Level set topology optimization of stationary fluid-structure interaction problems"

[178]: Picelli et al. (2017), "Evolutionary topology optimization for structural compliance minimization considering design-dependent FSI loads"

[179]: Feppon et al. (2020), "Topology optimization of thermal fluid-structure systems using body-fitted meshes and parallel computing"

[180]: Li et al. (2022), "Three-dimensional topology optimization of a fluid-structure system using body-fitted mesh adaption based on the level-set method"

6.2 Setting of the problem

6.2.1 Solid dynamics problem

This section focuses on the analysis and behavior of solid structures that can reach the incompressible limit under dynamic loading conditions. It explores the response of materials and structures. This section aims to provide an introductory overview of the fundamental concepts and principles related to solid dynamics for incompressible structures. Let us start by summarizing the conservation equations for both linear elasticity and finite strain hyperelasticity in solid dynamics.

Linear elasticity. Governing equations

According to Chapter 2, the equations of motion of linear elasticity can be presented as follows. Let Ω_s be the solid domain. Any point of the body is labeled with the vector $\mathbf{x}$. The boundary of the domain is denoted as $\Gamma_s := \partial\Omega_s$ and is split into a Dirichlet boundary $\Gamma_{s,D}$, where the prescribed displacements are specified and a Neumann boundary $\Gamma_{s,N}$, where prescribed tractions are applied. The interface boundary with the fluid is Γ_i. We denote as $]0,T[$ the time interval of analysis.

The continuum problem for solid dynamics, suitable for the incompressible limit, is defined by the following system of equations

Linear elasticity. Solid dynamics problem accounting for fluid tractions on Γ_i

$$\rho_s \frac{\partial^2 \mathbf{u}_s}{\partial t^2} - \nabla\cdot\mathbf{s}_s + \nabla p_s = \rho_s \mathbf{b} \qquad \text{in } \Omega_s\times]0,T[\,, \tag{6.1}$$

$$\mathbf{s}_s - \mathbb{C}^{\text{dev}} : \mathbf{e}_s = \mathbf{0} \qquad \text{in } \Omega_s\times]0,T[\,, \tag{6.2}$$

$$\nabla\cdot\mathbf{u}_s + \frac{p_s}{\kappa_s} = 0 \qquad \text{in } \Omega_s\times]0,T[\,, \tag{6.3}$$

$$\mathbf{e}_s - \mathbb{D} : \nabla^s\mathbf{u}_s = \mathbf{0} \qquad \text{in } \Omega_s\times]0,T[\,, \tag{6.4}$$

$$\mathbf{u}_s = \mathbf{u}_{s,D} \qquad \text{on } \Gamma_{s,D}\times]0,T[\,, \tag{6.5}$$

$$\mathbf{n}_s\cdot\mathbf{s}_s - p_s\mathbf{n}_s = \mathbf{t}_{s,N} \qquad \text{on } \Gamma_{s,N}\times]0,T[\,, \tag{6.6}$$

$$\mathbf{n}_\mathrm{i} \cdot \mathbf{s}_\mathrm{s} - p_\mathrm{s}\mathbf{n}_\mathrm{i} + \mathbf{t}_\mathrm{f} = \mathbf{0} \qquad \text{on } \Gamma_\mathrm{i}(t) \times]0, T[\,, \tag{6.7}$$

where ρ_s is the density, $\mathbf{u}_\mathrm{s}$ the displacement field, $\mathbf{s}_\mathrm{s}$ the deviatoric stresses, $\rho_\mathrm{s}\mathbf{b}$ the body forces, $\mathbb{C}^{\mathrm{dev}}$ the 4th-order deviatoric constitutive tensor, $\mathbf{e}_\mathrm{s}$ the deviatoric strains, p_s the pressure field, κ_s the bulk modulus and $\mathbb{D}$ the deviatoric 4th order tensor.

With regards to the boundary conditions, $\mathbf{u}_{\mathrm{s},D}$ is a prescribed value for the displacements on the Dirichlet boundary, $\mathbf{t}_{\mathrm{s},N}$ a prescribed value for the tractions on the Neumann boundary and $\mathbf{t}_\mathrm{f}$ are the tractions coming from the fluid on the interface boundary.

Two different formulations are considered to manage this problem. On the one hand, the mixed two-field $\mathbf{u}p$ formulation, on the other hand, the mixed three-field $\mathbf{u}p\mathbf{e}$ formulation, both of them presented in Subsection 2.1.1.

Finite strain hyperelasticity. Governing equations

According to Chapter 3 the equations of motion of finite strain hyperelasticity can be presented as follows. Let $\Omega_{\mathrm{s},0} \coloneqq \Omega_\mathrm{s}(0)$ be the reference configuration of the solid body, whereas the current configuration of the body at time t is denoted by $\Omega_\mathrm{s}(t)$. The motion is described by a function $\boldsymbol{\psi}$ which links a material particle $\mathbf{X} \in \Omega_{\mathrm{s},0}$ to the spatial configuration $\mathbf{x} \in \Omega_\mathrm{s}(t)$ according to

$$\boldsymbol{\psi} : \Omega_{\mathrm{s},0} \longrightarrow \Omega_\mathrm{s}(t)\,, \quad \mathbf{x} = \boldsymbol{\psi}(\mathbf{X}, t), \quad \forall \mathbf{X} \in \Omega_{\mathrm{s},0}, \quad t \geq 0. \tag{6.8}$$

The boundary of the reference configuration is denoted as $\Gamma_{\mathrm{s},0} \coloneqq \partial\Omega_{\mathrm{s},0}$ and $\Gamma_\mathrm{s}(t) \coloneqq \partial\Omega_\mathrm{s}(t)$ represents the boundary of the current configuration at time t. We always assume that the mapping between both boundaries is defined through the motion, i.e., $\boldsymbol{\psi}(\Gamma_{\mathrm{s},0}, t) = \Gamma_\mathrm{s}(t)$. The interface boundary with the fluid at the reference configuration is $\Gamma_{\mathrm{i},0}$. We denote as $]0, T[$ the time interval of analysis.

We want to deal with compressible materials that can reach the incompressible limit. The governing equations in finite strain hyperelasticity in a TLF framework are defined by

Finite strain hyperelasticity. Solid dynamics problem accounting for fluid tractions on $\Gamma_{i,0}$ in a TLF framework

$$\rho_{s,0}\frac{\partial^2 \mathbf{u}_s}{\partial t^2} - \nabla_0 \cdot \left\{\mathbf{S}_s' \mathbf{F}_s^T\right\} + \nabla_0 \cdot \left\{p_s J_s \mathbf{F}_s^{-1}\right\} = \rho_{s,0}\mathbf{b} \quad \text{in } \Omega_{s,0} \times]0,T[, \tag{6.9}$$

$$\frac{p_s}{\kappa_s} + \frac{dG}{dJ} = 0 \quad \text{in } \Omega_{s,0} \times]0,T[, \tag{6.10}$$

$$\mathbf{S}_s' - 2\frac{\partial W}{\partial \mathbf{C}_s} = \mathbf{0} \quad \text{in } \Omega_{s,0} \times]0,T[, \tag{6.11}$$

$$\mathbf{u}_s = \mathbf{u}_{s,D} \quad \text{on } \Gamma_{s,0,D} \times]0,T[, \tag{6.12}$$

$$\mathbf{n}_{s,0} \cdot \left\{\mathbf{S}_s' \mathbf{F}_s^T - p_s J_s \mathbf{F}_s^{-1}\right\} = \mathbf{t}_{s,0,N} \quad \text{on } \Gamma_{s,0,N} \times]0,T[, \tag{6.13}$$

$$\mathbf{n}_{i,0} \cdot \left\{\mathbf{S}_s' \mathbf{F}_s^T - p_s J_s \mathbf{F}_s^{-1}\right\} = J_s \mathbf{F}_s^{-1} \mathbf{t}_f \quad \text{on } \Gamma_{i,0} \times]0,T[, \tag{6.14}$$

where $\rho_{s,0}$ is the density at the reference configuration, $\mathbf{S}_s'$ the deviatoric PK2 stress tensor, $\mathbf{F}_s$ the deformation gradient, J_s the Jacobian, $\frac{dG}{dJ}$ a term related with the volumetric part of the strain energy function U, W the deviatoric part of the strain energy function and $\mathbf{C}_s$ the right Cauchy tensor.

With regards to the boundary conditions, $\mathbf{u}_{s,D}$ is a prescribed value for the displacements on the Dirichlet boundary, $\mathbf{t}_{s,0,N}$ a prescribed value for the tractions on the Neumann boundary and $\mathbf{t}_f$ are the tractions coming from the fluid on the interface boundary. Note that a pull-back transformation must be applied to fluid tractions $\mathbf{t}_f$ to apply them on the boundaries at the reference configuration.

Two different formulations are considered to manage this problem. On the one hand, the mixed two-field $\mathbf{u}p$ formulation presented in Section 3.5. On the other hand, the mixed three-field $\mathbf{u}p\mathbf{S}'$ formulation presented in Section 3.6.

6.2.2 Fluid flow problem

The next step is to define the governing equations that model the fluid flow problem for an incompressible Newtonian flow which is modeled with the well-known Navier-Stokes equations. The approach followed can be understood as the traditional one, where the fluid problem is solved by means of an ALE formulation to cope with the time dependency of the fluid domain.

ALE formulation of the fluid flow equations

Let now $\Omega_f(t)$ be the domain where the fluid flows, with boundary $\Gamma_f(t) := \partial\Omega_f(t)$, where Dirichlet boundary conditions are prescribed on $\Gamma_{f,D}(t)$ and Neumann conditions on $\Gamma_{f,N}(t)$. These boundaries may be moving. According to Subsection 5.3.1, a mesh equation must be solved to obtain the domain velocities which are needed to solve the fluid equations. Let us directly show here the system of equations that is solved according to [137] for a given velocities in the interface boundary with the solid $\mathbf{v}_{\Gamma_i}$ at time t^n

[137]: Chiandussi et al. (1999), "A simple method for automatic update of finite element meshes"

ALE formulation. Mesh equation accounting for solid velocities on Γ_i

$$-\nabla\cdot\{\mathbb{C} : \nabla^s\mathbf{v}_{dom}\} = \mathbf{0} \qquad \text{in } \Omega_f(t^n), \tag{6.15}$$

$$\mathbf{v}_{dom} = \mathbf{v}_{\Gamma_i} \qquad \text{on } \Gamma_i(t^n), \tag{6.16}$$

$$\mathbf{v}_{dom} = \mathbf{0} \qquad \text{on } \Gamma_f(t^n)\setminus\Gamma_i(t^n), \tag{6.17}$$

where $\mathbb{C}(E_{dom}(\mathbf{x}), \nu_{dom})$ is the Constitutive 4th order tensor in linear elasticity, $E_{dom}(\mathbf{x})$ is the Young Modulus of the mesh and ν_{dom} is the Poisson coefficient of the mesh.

Using the ALE reference, the only modification with respect to the purely Eulerian formulation is to replace the transport velocity $\mathbf{v}_f$ of the advective term by $\mathbf{v}_c := \mathbf{v}_f - \mathbf{v}_{dom}$.

Governing equations

According to Chapter 2 the equations of the Newtonian incompressible fluid flow assumption are presented. Let $\Omega_f(t)$ be the fluid domain in the time interval $]0, T[$, accounting also

for the motion of this domain. Let $\Gamma_f(t) := \partial\Omega_f(t)$ be its boundary. The continuum Navier-Stokes problem for Newtonian fluid flows is defined by the following system of equations

Newtonian fluid flows. Navier-Stokes problem in ALE approach accounting for solid displacements on Γ_i

$$\rho_f \frac{\partial \mathbf{v}_f}{\partial t} + \rho_f \mathbf{v}_c \cdot \nabla \mathbf{v}_f - \mu_f \nabla^2 \mathbf{v}_f + \nabla p_f = \mathbf{f} \qquad \text{in } \Omega_f(t) \times]0, T[\,, \tag{6.18}$$

$$\nabla \cdot \mathbf{v}_f = 0 \qquad \text{in } \Omega_f(t) \times]0, T[\,, \tag{6.19}$$

$$\mathbf{v}_f = \mathbf{v}_{f,D} \qquad \text{on } \Gamma_{f,D}(t) \times]0, T[\,, \tag{6.20}$$

$$\mathbf{n}_f \cdot \boldsymbol{\sigma}_f = \mathbf{t}_{f,N} \qquad \text{on } \Gamma_{f,N}(t) \times]0, T[\,, \tag{6.21}$$

$$\mathbf{v}_f = \mathbf{v}_{\Gamma_i} \qquad \text{on } \Gamma_i(t) \times]0, T[\,. \tag{6.22}$$

where $\mathbf{v}_f$ is the velocity field, p_f the pressure, $\mathbf{f}$ the vector of body forces, ρ_f the density, μ_f the dynamic viscosity and $\nabla^2(\cdot)$ is the Laplacian operator.

With regards to the boundary conditions, $\mathbf{v}_{f,D}$ is a prescribed value for the velocities on the Dirichlet boundary, $\mathbf{t}_{f,N}$ the prescribed value for the tractions on the Neumann boundary and $\mathbf{v}_{\Gamma_i}$ is the velocity field coming from the solid on the interface boundary.

In this chapter, the two-field $\mathbf{v}p$ formulation presented in Subsection 2.2.3 is considered.

6.3 TO of incompressible structures subject to FSI

6.3.1 Fluid-structure interaction

Let $\Omega(t)$ be the whole domain of the problem, formed by a fluid sub-domain $\Omega_f(t)$ and a solid one $\Omega_s(t)$ which will be optimized during the process. These two sub-domains do not overlap, so that $\bar{\Omega}(t) = \overline{\Omega_f(t) \cup \Omega_s(t)}$ and $\mathring{\Omega}_f(t) \cap \mathring{\Omega}_s(t) = \emptyset$. The

sub-domains have their own boundaries $\Gamma_f(t)$ and $\Gamma_s(t)$, and the interface between the them is $\Gamma_i(t)$. Its unit normal with respect to the spatial configuration is denoted $\mathbf{n}_i$, pointing from the fluid side to the solid one. We also define $\Gamma_{s,0}$ as the solid boundary in the initial configuration and its unit normal with respect to the material configuration is denoted by $\mathbf{n}_{i,0}$.

In this chapter, a block-iterative coupling is considered, in which the solid and the fluid mechanics problems are solved sequentially with a strong coupling. A Dirichlet-Neumann coupling is considered: the solid is solved with the loads computed from the fluid in a given iteration and then the fluid is computed with the velocities on the interface obtained from the solid. An Aitken relaxation scheme is implemented. Using the Dirichlet-Neumann iteration-by-subdomain coupling approach described earlier, the coupling algorithm to solve the problem is very similar to the one given in Algorithm 1 in Chapter 5. Let us remark that in this case, for hyperelastic materials, the solid problem is solved in a TLF framework, which means that we need to pull-back tractions coming from the fluid domain.

6.3.2 The TO of incompressible structures subject to FSI algorithm

The sequence of the individual steps is shown in Algorithm 2. Let us explain in detail the proposed strategy.

The main goal of the proposed methodology is to obtain optimized incompressible structures which are subjected to FSI loads. In this sense, we need to specify both a delay for the TO to start n_{del} and a time window N_w, which will take into account the number of steps to do a TO iteration. Obviously, the selection of this time window is not simple, and it depends upon the FSI problem. For real transient FSI problems, the problem is supposed to be statistically stationary, which means that there exists a period in the movement of the flow unless the fluid flow becomes turbulent [181–183]. The steps needed to cover this period is a suitable choice to be the time window. In this work, as a first approximation, a fixed value for the time window is imposed during the whole procedure.

[181]: Hughes et al. (2001), "Large eddy simulation of turbulent channel flows by the variational multiscale method."
[182]: Codina et al. (2010), "Finite element approximation of turbulent thermally coupled incompressible flows with numerical sub-grid scale modelling."
[183]: Colomes et al. (2015), "Assessment of variational multiscale models for the large eddy simulation of turbulent incompressible flows"

The following ingredient is to compute an additive TD $\mathscr{D}_T^{\text{add}}\mathscr{J}$ for all the steps along the time window. In each time step, we iterate until convergence our block-iterative FSI method. Once a converged solution is obtained, we can compute the split TD associated with the solid converged state according to the results obtained in Chapter 4

$$\begin{aligned}\mathscr{D}_T\mathscr{J}(\chi,\mathbf{x}) = \mathbf{e}(\chi,\mathbf{x}) : \mathbb{P}^{\text{dev}} : \mathbf{s}(\chi,\mathbf{x}) + \mathrm{P}^{\text{vol}}p^2(\chi,\mathbf{x}) \\ + (1-\gamma)\rho\mathbf{b}\cdot\mathbf{u}(\chi,\mathbf{x}),\end{aligned} \tag{6.23}$$

for linear elastic materials or

$$\begin{aligned}\mathscr{D}_T\mathscr{J}(\chi,\mathbf{X}) \approx W\left(\bar{\mathbf{C}}(\chi,\mathbf{X})\right) - p(\chi,\mathbf{X})\,g(J(\chi,\mathbf{X})) \\ + (1-\gamma)\rho_0\mathbf{b}\cdot\mathbf{u}(\chi,\mathbf{X}),\end{aligned} \tag{6.24}$$

for hyperelastic ones. The idea is to sum the contributions for all the time steps inside the time window. To do so, a simple additive function is defined as

$$\mathscr{D}_T^{\text{add}}\mathscr{J}^{n_{\text{w}}+1} = \mathscr{D}_T^{\text{add}}\mathscr{J}^{n_{\text{w}}} + \mathscr{D}_T\mathscr{J}^{n_{\text{w}}}, \tag{6.25}$$

where n_{w} is the time window counter. Once the time window is achieved, $n_{\text{w}} = N_{\text{w}}$, a single TO step is performed for the solid domain with the additive TD according with the flowchart presented in Fig. 4.1 for linear elastic materials or the flowchart presented in Fig. 4.21 for hyperelastic materials. The counter of steps and the additive TD are reset to zero.

An important aspect to mention is that "dry" TO is performed. This means that only the interior of the structure is optimized, whereas the interface boundary remains constant along the problem. To do so, we split the solid domain Ω_{s} into two sub-domains, Ω_{var} and Ω_{fix}. The former contains the interior of the structure and it is allowed to be optimized during the TO procedure, the latter contains the external layer of the structure in contact with the fluid and is fixed as strong material during the whole TO procedure. Let us remark that a bi-material TO problem is performed. The material corresponding to the weak domain exhibits a very small stiffness, approximating the absence of material. The material parameters of the strong domain are denoted by $\rho_{\text{s},0}$, $E_{\text{s},0}$ and $\nu_{\text{s},0}$ and the parameters of the weak domain are considered as $\rho_{\text{w},0} = \gamma\rho_{\text{s},0}$, $E_{\text{w},0} = \gamma E_{\text{s},0}$ and $\nu_{\text{w},0}$ where γ stands for the jump of stiffness. Note that $\gamma > 0$ is a parameter, small enough for

modeling void regions and large enough to entail invertibility properties to the stiffness matrix.

Algorithm 2: TO of incompressible structures subject to FSI

Fixed delay steps n_{del} to start the TO procedure and a time window N_{w} to do a TO step. $n = 0$; loop over the number of time steps. $n_{\text{w}} = 0$; time window counter to 0.

$n \leftarrow n + 1$

if $n > n_{\text{del}}$ then $n_{\text{w}} \leftarrow n_{\text{w}} + 1$

$k = 0$; iterate coupling iterations until convergence.

$k \leftarrow k + 1$ (block iteration counter omitted in the following).

- **Solve the equations for the solid**, taking into account the tractions coming from the fluid problem $\mathbf{t}_{\text{f}}$.
- **Compute relaxed velocities** on the interface boundary $\mathbf{v}_{\Gamma_{\text{i}}}$ with an Aitken relaxation scheme from the solid velocities $\mathbf{v}_{\Gamma_{\text{i}},\text{s}} = \frac{\delta_2 \mathbf{u}_{\text{s}}}{\delta t}|_{\Gamma_{\text{i}}}$.
- **Compute the domain velocity in the fluid** by solving the mesh equation.
- **Solve the ALE equations for the fluid**, taking into account the mesh velocity $\mathbf{v}_{\text{dom}}$ and using the interface velocity $\mathbf{v}_{\Gamma_{\text{i}}}$.
- **Check convergence and update the unknowns**. Coupling convergence is checked based on the norm of the relative error between coupling iterations of displacements at the interface, i.e., $\|\mathbf{u}_{\Gamma_{\text{i}},\text{s}} - \mathbf{u}_{\Gamma_{\text{i}},\text{f}}\|_{L^2(\Gamma_{\text{i}})}$ and tractions, i.e., $\|\mathbf{t}_{\Gamma_{\text{i}},\text{s}} - \mathbf{t}_{\Gamma_{\text{i}},\text{f}}\|_{L^2(\Gamma_{\text{i}})}$, properly normalized. Convergence is achieved when this norm is below a given tolerance.

End block-iterative loop.

- **Compute the additive TD** associated to the already converged solution at time t^n

$$\mathscr{D}_T^{\text{add}} \mathscr{J}^{n_{\text{w}}+1} = \mathscr{D}_T^{\text{add}} \mathscr{J}^{n_{\text{w}}} + \mathscr{D}_T \mathscr{J}^{n_{\text{w}}},$$

where $\mathscr{D}_T \mathscr{J}^{n_{\text{w}}}$ is the TD associated with time window counter n_{w}.

- Check if $n > n_{\text{del}}$ and $n_{\text{w}} = N_{\text{w}}$, then
  - **Perform a TO step** with the additive TD according with the flowchart presented in Fig. 4.1 for linear elastic materials or the flowchart presented in Fig. 4.21 for hyperelastic materials.

    $n_{\text{w}} = 0$; restart time window counter.

    $\mathscr{D}_T^{\text{add}} \mathscr{J}^{n_{\text{w}}} = 0$; restart additive TD.
- endif

End loop over the number of time steps.

6.4 Numerical examples

In this section, three numerical examples are presented to assess the performance of the proposed TO of incompressible structures subject to FSI strategy. In the first one, a flow through a channel with a flexible wall is considered to study a stationary solution. The main idea is to analyze the differences between mixed formulations when considering either linear elastic structures or hyperelastic ones. Next, so as to examine the effect of transient FSI solutions, the well-known Turek's test FSI2 is presented. In this case, the behavior of a laminar channel flow around an elastic object is studied when several volume fractions are considered for the optimized structure. To end up, a three-dimensional case with an incompressible flexible plate in a flow channel is considered.

On the one hand for the fluid sub-problem, we select the S-OSGS method with dynamics subscales. The algorithmic parameters are set to $c_1 = 4$, $c_2 = 2$. As a time integrator we select the BDF2 scheme for all cases. As previously discussed, the nonlinearities in the problem are solved via a Picard scheme. A maximum of 10 iterations is set, and the numerical tolerance for the $L^2(\Omega_f)$ norm is 10^{-5}.

On the other hand for the solid sub-problem, the stabilization technique is selected to be the S-OSGS method. The algorithmic parameters are set to $c_1 = 1, c_2 = 1$ and $c_3 = 0.5$ depending on the chosen formulation. As a time integrator we select the BDF2 scheme for all cases. As previously discussed, the nonlinearities in the problem are solved via a Newton-Raphson scheme. A maximum of 10 iterations is set, and the numerical tolerance for the $L^2(\Omega_s)$ norm is 10^{-5}.

In order to solve the monolithic system of linear equations for each sub-problem, we use the Biconjugate Gradients solver, `BiCGstab` [71], which is already implemented in the `PETSc` parallel solver library [17].

[71]: Vorst (1992), "Bi-CGSTAB: A fast and smoothly converging variant of Bi-CG for the solution of nonsymmetric linear systems"

[17]: Balay et al. (2015), *PETSc Web page*

Concerning the iterative scheme, a strong-coupling staggered approach is considered as mentioned in Algorithm 2. Therefore, for the transmission conditions on the interface boundary Γ_i (using again the L^2 norm), the relative tolerance is set to 10^{-3}.

With regards to the TO parameters, the weak material is considered to be compressible, with $\nu_w = 0.4$. The jump of stiff-

ness γ is fixed to 10^{-2}. As a stopping criterion for the TO algorithm, we impose a relative tolerance for the objective functional tol $= 10^{-3}$, unless otherwise specified. The volume fraction is reduced at once except where otherwise stated. In all presented figures, only the positive part of the level set is plotted, therefore only the strong material part is shown. The rest is filled of weak material elements which is interpreted as the void region.

6.4.1 Beam in a flow channel

In this first problem, we seek to determine the optimal topology of an structure immersed in a flow channel. This example is very similar to the one presented in [174, 180]. The problem presented here has a fixed interface boundary between the fluid flow and the structure. Therefore, we optimize the interior of the structure. The geometry of the problem is shown in Fig. 6.1

[174]: Jenkins et al. (2015), "Level set topology optimization of stationary fluid-structure interaction problems"
[180]: Li et al. (2022), "Three-dimensional topology optimization of a fluid-structure system using body-fitted mesh adaption based on the level-set method"

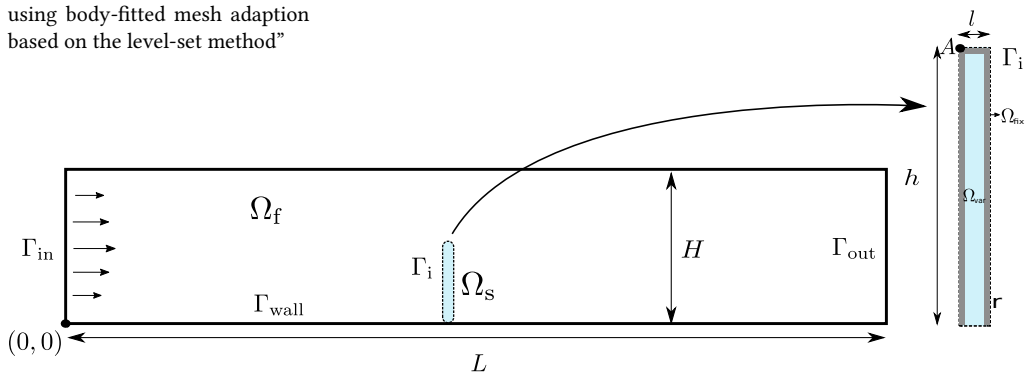

Figure 6.1: Beam in a flow channel. Geometry.

Regarding the channel measures, the rigid channel has height $H = 1$ m. The flexible wall is located at $2H$ from the channel entrance. The length of the whole channel is $L = 5$ m. The structure bar has length $l = 0.1$ m and height $h = 0.5$ m. The solid domain Ω_s is divided into two subdomains Ω_{var} and Ω_{fix}. The former contains the interior of the structure and it is allowed to be optimized during the TO procedure, the latter contains the external layer of the structure of width $r = 0.01$ m which is in contact with the fluid and is fixed as strong material during the whole TO procedure.

Regarding the properties of the fluid, the density is $\rho_f = 1$ kg/m^3 and the dynamic viscosity is $\mu_f = 1$ Pa·s. For the elastic

plate the properties are as follows: an initial density $\rho_{s,0} = 1\ \text{kg/m}^3$, a Young's modulus $E_s = 40$ kPa and a Poisson's ratio $\nu_s = 0.5$. The plane strain assumption is considered. A final volume of 50% of the initial one is stated as a volume restriction for Ω_{var}.

Concerning the boundary conditions, in the inlet boundary of the fluid domain Γ_{in}, a steady Poiseuille flow with average velocity $\bar{v}_{\text{in}}$ is assumed, given by

$$\bar{v}_f(0, y) = 1.5\, \bar{v}_{in} \frac{y(H - y)}{\left(\frac{H}{2}\right)^2}. \tag{6.26}$$

On the walls Γ_{wall} no-slip boundary conditions are imposed, and in the outlet Γ_{out} the pressure is set to $p_{\text{out}} = 0$ Pa. A rectangular plate is considered as the solid domain, and it is clamped at the bottom side.

The domains are discretized using P_1 (linear) elements for both fluid and solid domains. Regarding the distribution of the elements, both meshes are unstructured. In total, the fluid mesh is formed by 12 446 elements, and the solid mesh by 12 720 elements.

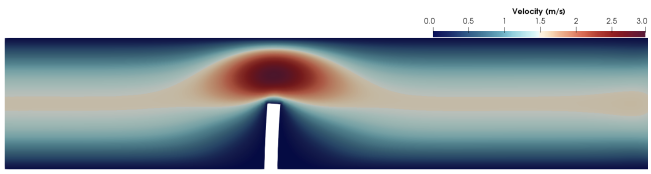

(a) Velocity field

(b) Pressure field

Figure 6.2: Beam in a flow channel. Distribution of the velocity field (top) and pressure (bottom) in the fluid domain with average velocity $\bar{v}_{\text{in}} = 1$ m/s. Velocities are plotted using their Euclidean norm.

To start the problem, a smooth increase of the velocity profile in time is prescribed, given by

$$v_f(0, y, t) = \begin{cases} \bar{v}_f(0, y) \frac{1 - \cos \frac{\pi}{2} t}{2} & t < 1.0 \text{ s} \\ v_f(0, y) & \text{otherwise} \end{cases}. \tag{6.27}$$

We select the time step $\Delta t = 0.005$ s. During the first 2.5 s, we let the FSI problem run without performing any TO iteration.

To do so, we impose a delay in the TO procedure of $500\Delta t$. At this moment, the problem has already converged to a stationary solution. From this point on, we select a time window of $50\Delta t = 0.25$ s to store the additive TD and perform a TO iteration. We continue the same procedure until a converged optimized solution is obtained for the structure.

First of all, let us consider $\bar{v}_{\text{in}} = 1$ m/s, which results in a fluid flow with Reynolds number Re = 1. For this case, the final stationary FSI solution is supposed to produce very small strains in the structure, which can be approximated with the infinitesimal strain theory. Let us start by showing the final stationary solution for the fluid domain once the optimized structure has been obtained for a linear elastic material. Both velocity and pressure fields in the flow channel are depicted in Fig. 6.2.

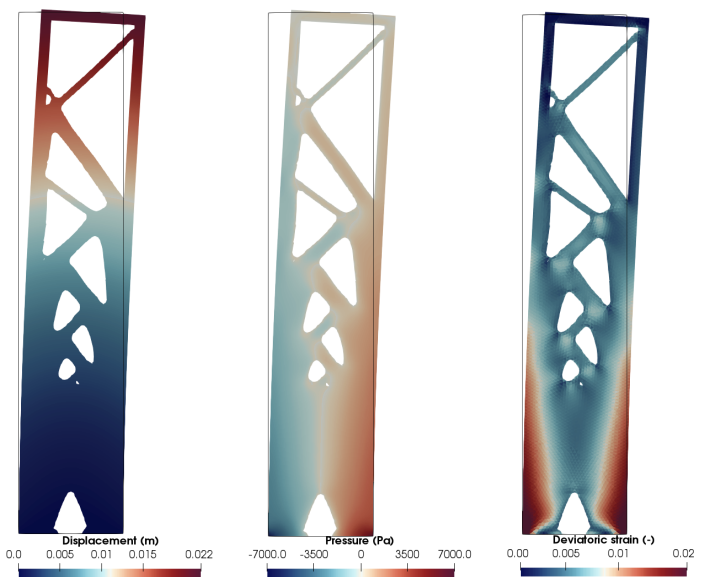

(a) Displacement field **(b)** Pressure field **(c)** Deviatoric strain field

Figure 6.3: Beam in a flow channel. Distribution of the displacement field (left), pressure (middle) and deviatoric strain field (right) in the linear elastic incompressible beam with $\mathbf{u}p$ formulation and with average velocity $\bar{v}_{\text{in}} = 1$ m/s. Displacements and deviatoric strains are plotted using their Euclidean norm.

We consider two different formulations for the structure. In Fig. 6.3 the final optimized solution with the $\mathbf{u}p$ formulation is shown whereas in Fig. 6.4 the one obtained for the three-field $\mathbf{u}p\mathbf{e}$ formulation is presented. Both solutions displays different solutions which are supposed to converge to the same one with finer meshes.

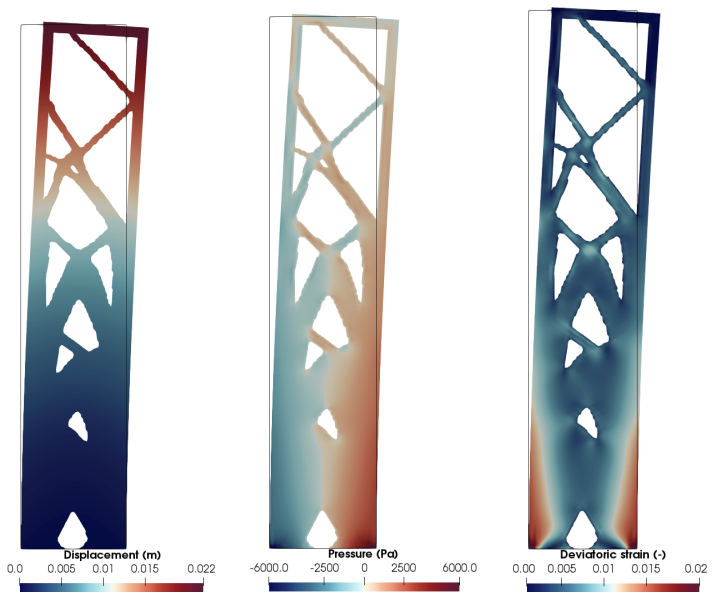

(a) Displacement field **(b)** Pressure field **(c)** Deviatoric strain field

Figure 6.4: Beam in a flow channel. Distribution of the displacement field (left), pressure (middle) and deviatoric strain field (right) in the linear elastic incompressible beam with $\mathbf{u}p\mathbf{e}$ formulation and with average velocity $\bar{v}_{\text{in}} = 1$ m/s. Displacements and deviatoric strains are plotted using their Euclidean norm.

Let us now consider a hyperelastic material by considering a Neo-Hookean law for the deviatoric law of the strain energy and a Simo-Taylor law for the volumetric one. The solution of the channel flow is very similar as the one obtained for the linear elastic case. Again, the two different solutions presented in Chapter 3 are applied. Fig. 6.5 presents the final solution obtained with the two-field $\mathbf{u}p$ formulation. Fig. 6.6 displays the solution for the $\mathbf{u}p\mathbf{S}'$ formulation. Again quite different solutions are obtained due to the nonlinearities of the problem, the iterative TO algorithm and the coarse mesh of the solid domain that we are considering.

For the sake of completeness, Table 6.1 shows the forces exerted by the fluid flow on the whole submerged beam structure and the displacement at the point A for the different cases we have studied. As it was expected, all cases display the same final properties due to the fact that infinitesimal strain theory can be considered.

Finally, in Fig. 6.7 the total potential energy is plotted against the TO iterations during the whole procedure for all the formulations considered. As expected, all formulations are decreasing the objective functional during the TO iterations

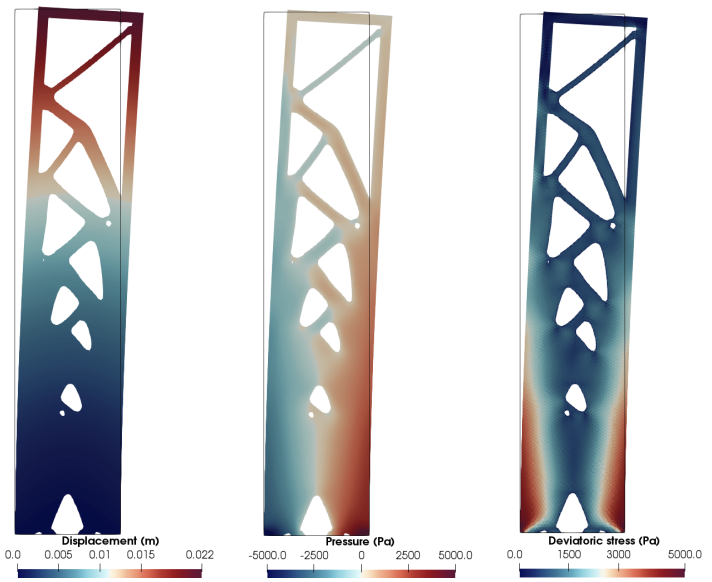

(a) Displacement field **(b)** Pressure field **(c)** Deviatoric PK2 stress field

Figure 6.5: Beam in a flow channel. Distribution of the displacement field (left), pressure (middle) and deviatoric PK2 stress field (right) in the hyperelastic incompressible beam with $\mathbf{u}p$ formulation and with average velocity $\bar{v}_{\text{in}} = 1$ m/s. Displacements and deviatoric stresses are plotted using their Euclidean norm.

until a minimum is achieved. Due to the high accuracy of strains and stresses that are obtained in the three-field formulations, we can see different values for the total potential energy. Obviously, this difference is expected to be reduced while refining the solid mesh.

Let us now consider a case which involves finite strains. To do so, we increment the average velocity to $\bar{v}_{\text{in}} = 10$ m/s, which results in a fluid flow with Reynolds number Re = 10. To perform this study let us consider only the $\mathbf{u}p$ formulations for both linear elastic and hyperelastic materials. Fig. 6.8 shows the solution for the fluid domain which seems quite similar in both cases. Figs. 6.9-6.10 show the final optimized structure for a linear elastic material and for a hyperelastic one, respectively. In this case, we can observe that strains are not infinitesimal anymore.

To show that the linear elastic theory hypothesis is not suitable in this case, Table 6.2 shows the fluid forces on the beam interface and the displacement at point A. As it can be clearly seen, quite different solutions are obtained. This example clearly shows that even in stationary FSI problems, the lin-

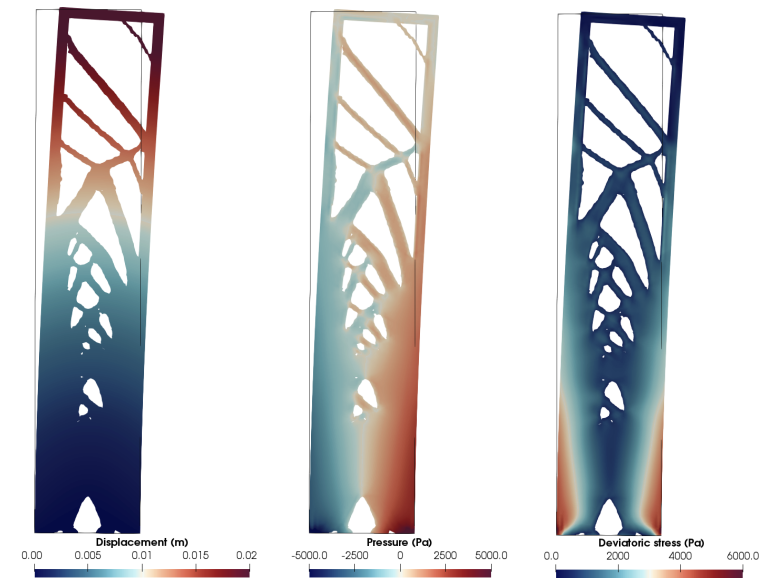

(a) Displacement field **(b)** Pressure field **(c)** Deviatoric PK2 stress field

Figure 6.6: Beam in a flow channel. Distribution of the displacement field (left), pressure (middle) and deviatoric PK2 stress field (right) in the hyperelastic incompressible beam with $\mathbf{u}p\mathbf{S}'$ formulation and with average velocity $\bar{v}_{\text{in}} = 1$ m/s. Displacements and deviatoric stresses are plotted using their Euclidean norm.

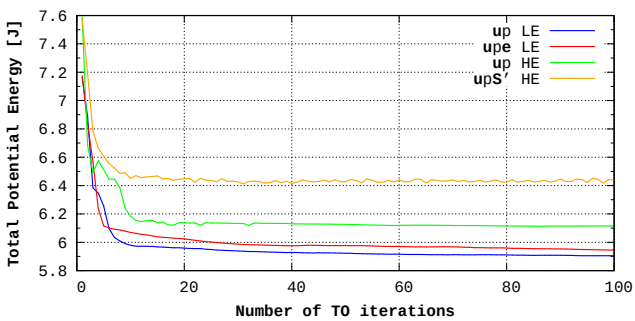

Figure 6.7: Beam in a flow channel. Convergence diagrams for both $\mathbf{u}p$ and $\mathbf{u}p\mathbf{S}'$ formulations with a hyperelastic beam with average velocity $\bar{v}_{\text{in}} = 1$ m/s. LE states for a linear elastic material and HE for a hyperelastic one.

ear theory of elasticity must be considered only when very small strains are produced in the structure. From the conceptual point of view, in this case there is no physical interaction, as the solid configuration does not change and thus the solid does not affect the fluid dynamics.

6.4.2 Turek's test

In this second case, we study the TO of an incompressible hyperelastic structure subject to FSI with a laminar flow. This

Table 6.1: Beam in a flow channel. Displacement at point A and forces exerted by the fluid on the whole submerged body with average velocity $\bar{v}_{\text{in}} = 1$ m/s. LE states for a linear elastic material and HE for a hyperelastic one.

	u_x [10^{-1} m]	u_y[10^{-2} m]	**drag** [N]	**lift** [N]
w/o TO	0.1978	0.2208	86.3563	-11.9159
$\mathbf{u}p$, LE	0.2168	0.2791	86.5657	-12.1485
$\mathbf{u}p\mathbf{e}$, LE	0.2144	0.2791	86.6162	-12.1428
$\mathbf{u}p$, HE	0.2218	0.2346	86.2957	-12.1737
$\mathbf{u}p\mathbf{S}'$, HE	0.2230	0.2304	86.2634	-12.1846

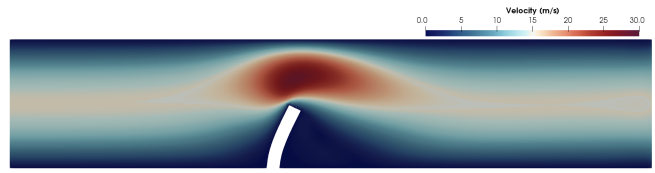

(a) Velocity field

(b) Pressure field

Figure 6.8: Beam in a flow channel. Distribution of the velocity field (top) and pressure (bottom) in the fluid domain with average velocity $\bar{v}_{\text{in}} = 10$ m/s. Velocities are plotted using their Euclidean norm.

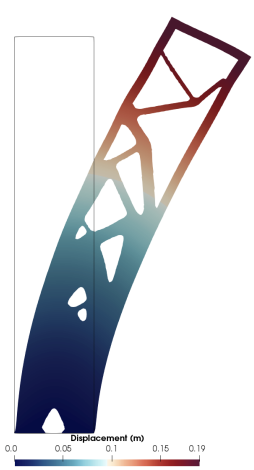

(a) Displacement field

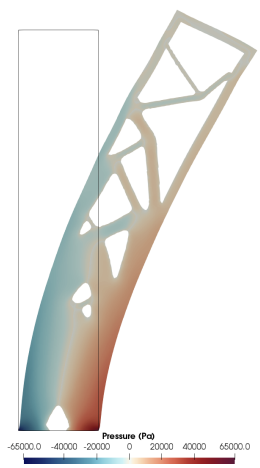

(b) Pressure field

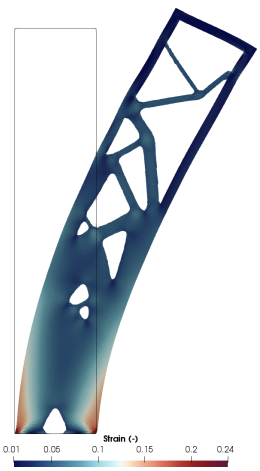

(c) Infinitesimal strain field

Figure 6.9: Beam in a flow channel. Distribution of the displacement field (left), pressure (middle) and infinitesimal strain tensor field (right) in the linear elastic incompressible beam with $\mathbf{u}p$ formulation and with average velocity $\bar{v}_{\text{in}} = 10$ m/s. Displacements and strains are plotted using their Euclidean norm.

case derives from the well-known benchmark in FSI used by many authors [146]. The configuration consists of a laminar channel flow around an elastic object which results in self-induced oscillations of the structure.

[146]: Turek et al. (2007), "Proposal for numerical benchmarking of fluid-structure interaction between an elastic object and laminar incompressible flow"

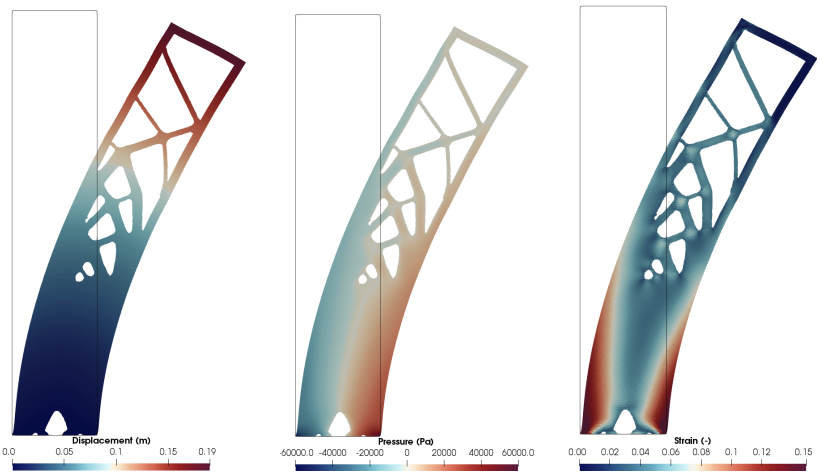

(a) Displacement field **(b)** Pressure field **(c)** Green Lagrange strain field

Figure 6.10: Beam in a flow channel. Distribution of the displacement field (left), pressure (middle) and Green Lagrange strain tensor field (right) in the hyperelastic incompressible beam with $\mathbf{u}p$ formulation and with average velocity $\bar{v}_{\text{in}} = 10$ m/s. Displacements and strains are plotted using their Euclidean norm.

	u_x [m]	$u_y[10^{-1}$ m]	**drag** [N]	**lift** [N]
w/o TO, LE	0.1797	0.2351	1071.6400	-192.8160
$\mathbf{u}p$, LE	0.1969	0.2531	1081.8600	-214.3030
w/o TO, HE	0.1758	-0.0972	887.3970	-166.3880
$\mathbf{u}p$, HE	0.1878	-0.1360	867.1500	-171.931

Table 6.2: Beam in a flow channel. Displacement at point A and forces exerted by the fluid on the whole submerged body with average velocity $\bar{v}_{\text{in}} = 10$ m/s. LE states for a linear elastic material and HE for a hyperelastic one.

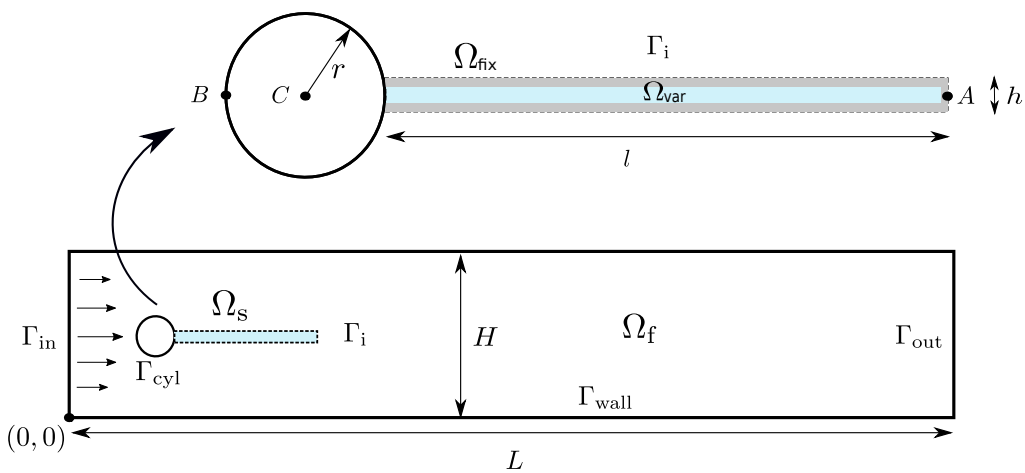

Figure 6.11: Turek's test. Geometry.

The geometry of the problem is displayed in Fig. 6.11. The rigid channel has height $H = 0.41$ m and length $L = 2.5$ m. The circle centre is positioned at point $C = (0.2, 0.2)$ m (mea-

sured from the left bottom corner of the channel) and its radius is $r = 0.05$ m. The structure bar has a length $l = 0.35$ m and a height $h = 0.02$ m. The right bottom corner is positioned at $(0.6, 0.19)$ m, and the left end is fully attached to the fixed cylinder. The solid domain Ω_s is divided into two subdomains Ω_{var} and Ω_{fix}. The former contains the interior of the structure and it is allowed to be optimized during the TO procedure, the latter contains the external layer of the structure of width $d = 0.001$ m which is in contact with the fluid and is fixed as strong material during the whole TO procedure.

With regards to boundary conditions, a parabolic profile is prescribed at the left channel inflow, given by

$$\bar{v}_f(0, y) = 1.5\, \bar{v}_{in} \frac{y(H - y)}{\left(\frac{H}{2}\right)^2}, \tag{6.28}$$

such that the mean inflow velocity is $\bar{v}_{in}$ and the maximum of the inflow velocity profile is $1.5\bar{v}_{in}$. A smooth increase of the velocity profile in time is prescribed, given by

$$v_f(0, y, t) = \begin{cases} \bar{v}_f(0, y) \frac{1 - \cos \frac{\pi}{2} t}{2} & t < 2.0 \text{ s} \\ \bar{v}_f(0, y) & \text{otherwise} \end{cases}. \tag{6.29}$$

The outflow condition is considered stress free. Finally, a no-slip condition is prescribed for the fluid on the other boundary parts. Concerning the boundary conditions of the structure, fixed null displacement is considered in the left edge.

The main goal of this example, is to perform a TO procedure of a transient solution. Therefore, the FSI2 parameter settings are taken from the benchmark. Therefore, the mean flow velocity is fixed to $\bar{v}_{in} = 1$ m/s. Regarding the properties of the fluid, the density is $\rho_f = 1\,000$ kg/m^3 and the dynamic viscosity is $\mu_f = 1$ Pa $\cdot$ s. This results in a fluid flow with Reynolds number Re $= 100$. For the incompressible elastic plate the properties are as follows: an initial density $\rho_{s,0} = 10\,000$kg/m^3, a Young's modulus $E_s = 14$ kPa and a Poisson's ratio $\nu_s = 0.5$. A Neo-Hookean law is considered for the deviatoric strain energy and a Simo-Taylor law for the volumetric one. The plane strain assumption is considered.

The domains are discretized using P_1 (linear) elements for both sub-domains. Regarding the distribution of the elements

in the fluid domain, the mesh is finer around the cylinder and the bar, while downstream the mesh is coarser, as it can be observed in Fig. 6.12. In total, the fluid mesh is formed by 13 537 unstructured elements, and the solid mesh by 15 608 unstructured elements equally distributed over the bar.

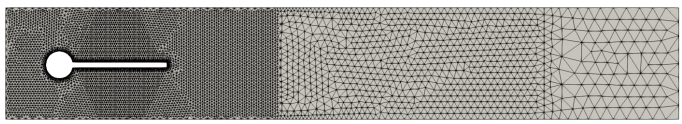

(a) Mesh of the fluid domain

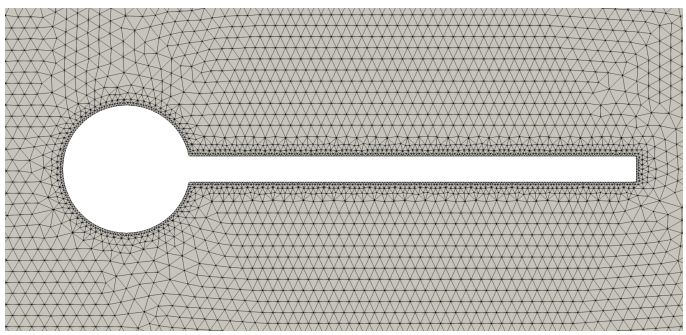

(b) Zoom around the cylinder and bar and mesh of the solid domain

Figure 6.12: Turek's test. Mesh domain.

We select the time step $\Delta t = 0.005$ s. During the first 12 s, we let the FSI problem run without performing any TO iteration. This is the time needed to arrive to a periodic solution. To do so, we impose a delay in the TO procedure of $2\,400\Delta t$. From this point on, we select a time window of $50\Delta t = 0.25$ s to store the additive TD and perform a TO iteration. This time is very close to the period in the case without TO. We continue the same procedure until a converged optimized solution is obtained for the structure. For this example, only the $\mathbf{u}p$ formulation is considered.

To show the effect of the TO procedure in a transient FSI problem, we select several volume fractions ranging from 90% to 70%. Let us first impose a final volume of 90% of the initial one. Fig. 6.13 shows both the velocity field and the pressure field at different times of the final transient solution. The final optimized structure is depicted in Fig. 6.14. As expected all the extracted material is taken from the right edge of the beam. Next, we select a final volume of 80% of the initial one. Figs. 6.15-6.16 display both the final solutions for the fluid domain and the optimized solid domain at different times, respectively. In this case, oscillations decrease compared to the ones presented in the first case. This reduction

is clearly explained due to the loss of mass in the structure. Finally, we impose a final volume of 70% of the initial one. In this case, an almost stationary solution is achieved as it can be seen in Figs. 6.17-6.18. From this study, we can draw the conclusion that TO optimization cannot only be used for reducing material volumes while minimizing an objective function, but to modify transient solutions in time by changing oscillations in some coupled problems.

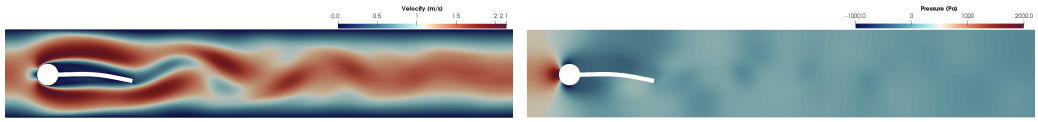

(a) $t = 25.0$ s. Velocity field **(b)** $t = 25.0$ s. Pressure field

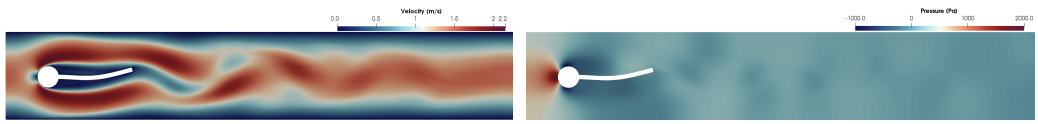

(c) $t = 25.25$ s. Velocity field **(d)** $t = 25.25$ s. Pressure field

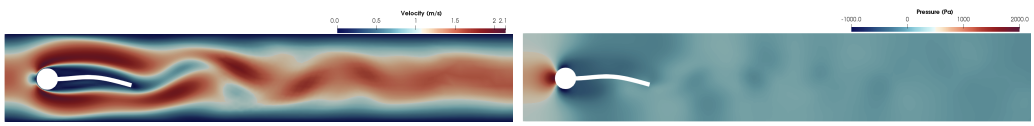

(e) $t = 25.5$ s. Velocity field **(f)** $t = 25.5$ s. Pressure field

Figure 6.13: Turek's test. Distribution of the velocity field (left) and pressure (right) in the fluid domain with 90% of final volume at several times. Velocities are plotted using their Euclidean norm.

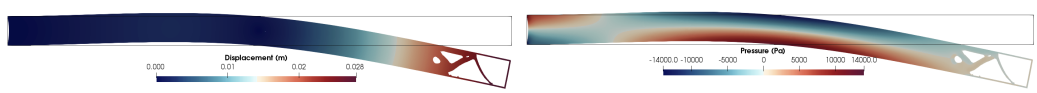

(a) $t = 25.0$ s. Displacement field **(b)** $t = 25.0$ s. Pressure field

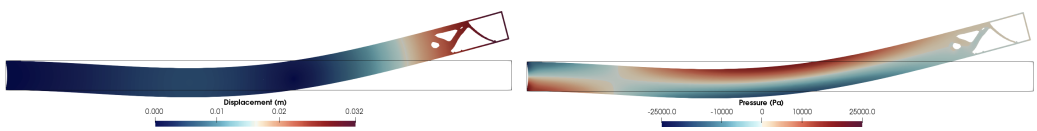

(c) $t = 25.25$ s. Displacement field **(d)** $t = 25.25$ s. Pressure field

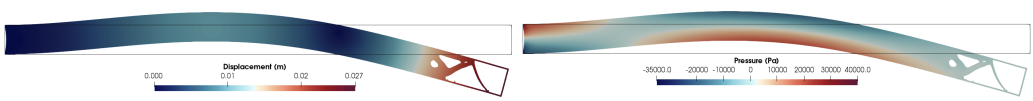

(e) $t = 25.5$ s. Displacement field **(f)** $t = 25.5$ s. Pressure field

Figure 6.14: Turek's test. Distribution of the displacement field (left) and pressure (right) in the solid domain with 90% of final volume at several times. Displacements are plotted using their Euclidean norm.

To show clearly the effects that are exposed in the previous paragraph, both forces exerted by the fluid in the whole sub-

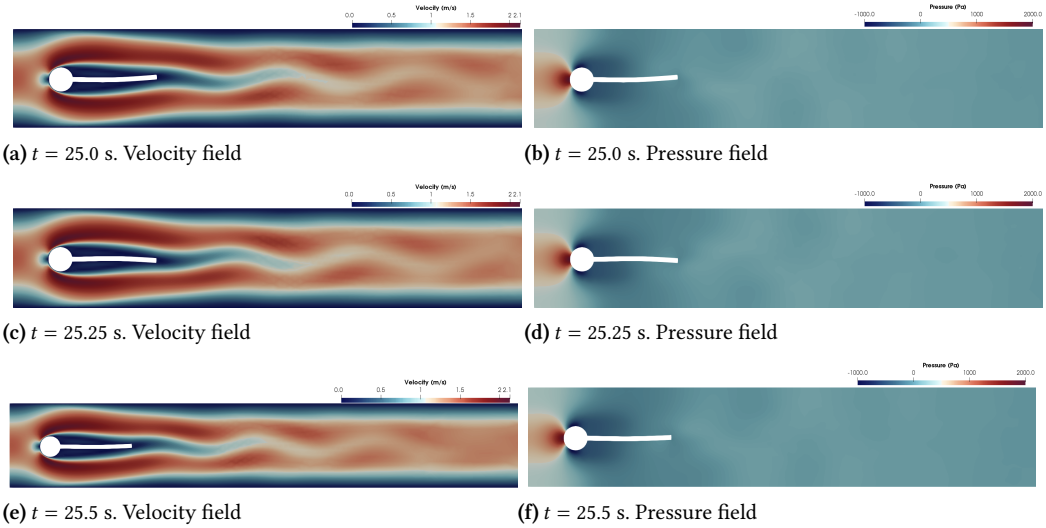

(a) $t = 25.0$ s. Velocity field

(b) $t = 25.0$ s. Pressure field

(c) $t = 25.25$ s. Velocity field

(d) $t = 25.25$ s. Pressure field

(e) $t = 25.5$ s. Velocity field

(f) $t = 25.5$ s. Pressure field

Figure 6.15: Turek's test. Distribution of the velocity field (left) and pressure (right) in the fluid domain with 80% of final volume at several times. Velocities are plotted using their Euclidean norm.

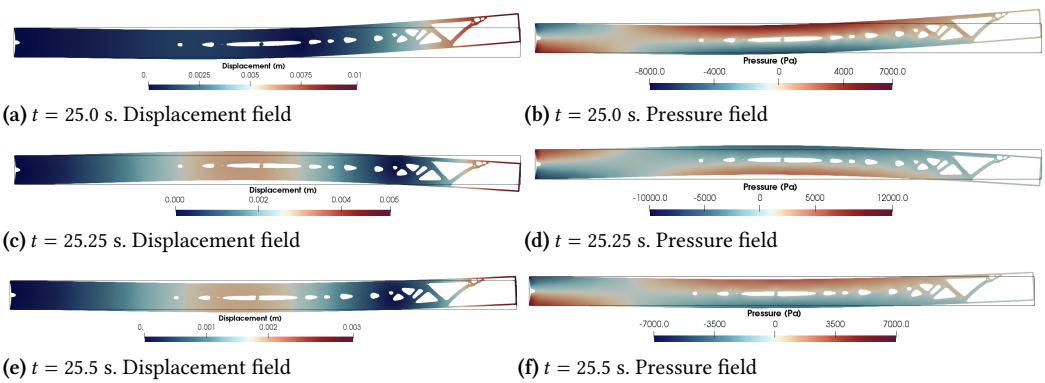

(a) $t = 25.0$ s. Displacement field

(b) $t = 25.0$ s. Pressure field

(c) $t = 25.25$ s. Displacement field

(d) $t = 25.25$ s. Pressure field

(e) $t = 25.5$ s. Displacement field

(f) $t = 25.5$ s. Pressure field

Figure 6.16: Turek's test. Distribution of the displacement field (left) and pressure (right) in the solid domain with 80% of final volume at several times. Displacements are plotted using their Euclidean norm.

merged body (cylinder plus beam) and the displacement at point A are plotted in Fig. 6.19 for all the volume fractions considered. All volume fractions arrive with the same oscillations at time $t = 12$ s. At this point each one decreases to the final volume fraction required. As it can be seen, drag and lift are decreasing while decreasing the final volume fraction and therefore, the displacement at point A is also decreasing. For the case of 70% of the final volume, we can see that all figures end with a stationary solution.

To end this example, in Fig. 6.20 the evolution of the total

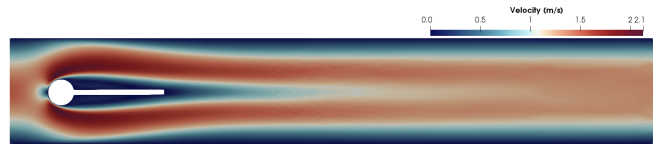

(a) Velocity field

(b) Pressure field

Figure 6.17: Turek's test. Distribution of the velocity field (top) and pressure (bottom) in the fluid domain with 70% of final volume. Velocities are plotted using their Euclidean norm.

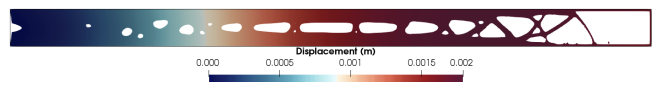

(a) Displacement field

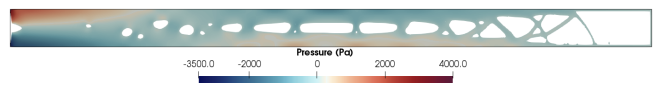

(b) Pressure field

Figure 6.18: Turek's test. Distribution of the displacement field (top) and pressure (bottom) in the solid domain with 70% of final volume. Displacements are plotted using their Euclidean norm.

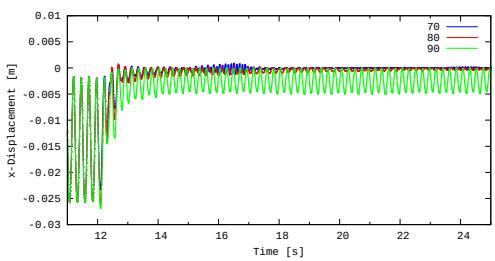

(a) Displacement u_x

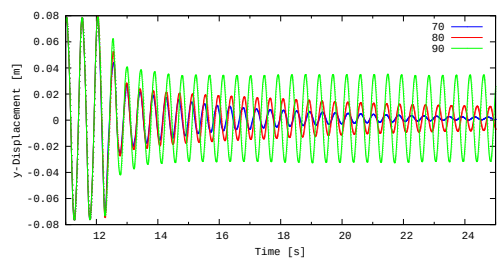

(b) Displacement u_y

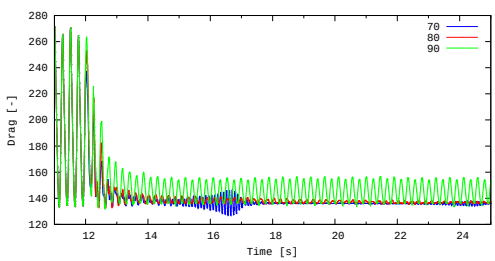

(c) Drag

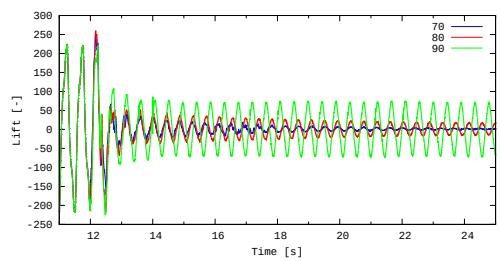

(d) Lift

Figure 6.19: Turek's test. Results for TO FSI2.

potential energy for the three cases along TO iterations is shown. As it is expected, the functional decreases for the three cases until a point in which we consider that a min-

imum is achieved. It is worth to mention, that in the 70% case, the stationary solution means that almost no forces are done by the fluid flow to the solid, this is the reason why the energy is almost 0. Let us also point that some oscillations appear in the 90% case due to the fact that the compliance in this case depends also upon time. If we want to remove this effect, a higher time window for the TO iterations should be considered to neglect this dependence.

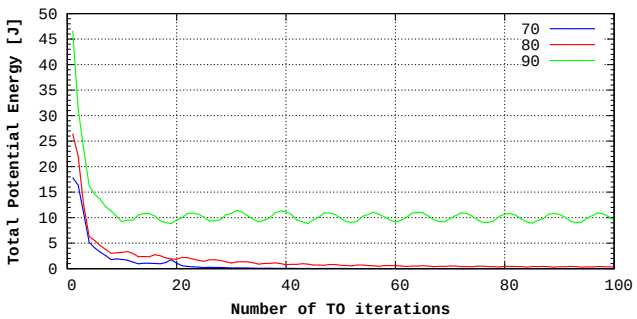

Figure 6.20: Turek's test. Convergence diagram.

6.4.3 Flexible plate in a flow channel

As a final example we study the optimization of the internal structural layout of a challenging three-dimensional test case which exhibits highly dynamic transient FSI. The problem geometry is depicted in Fig. 6.21. A plate of length $l = 0.07$ m, width $w = 0.6$ m and height $h = 0.35$ m is mounted at the bottom of a flow channel. The plate is located at $L_1 = 0.49$ m from the channel entrance. The channel is a cuboid-shaped domain of length $L = 1.5$ m, width $W = 1.2$ m and height $H = 0.6$ m. The solid domain Ω_s is divided into two subdomains Ω_{var} and Ω_{fix}. The former contains the interior of the structure and it is allowed to be optimized during the TO procedure, the latter contains the external layer of the structure of width $r = 0.007$ m which is in contact with the fluid and is fixed as strong material the whole TO procedure.

A parabolic profile for the velocity at the channel inlet face is prescribed, given by

$$\bar{v}_f(0, y, z) = \bar{v}_{max} \frac{2500}{81} z\,(z - 0.6)\,(y + 0.6)\,(y - 0.6)\,, \qquad (6.30)$$

where the maximum velocity is $\bar{v}_{max} = 1$ m/s and it is varied

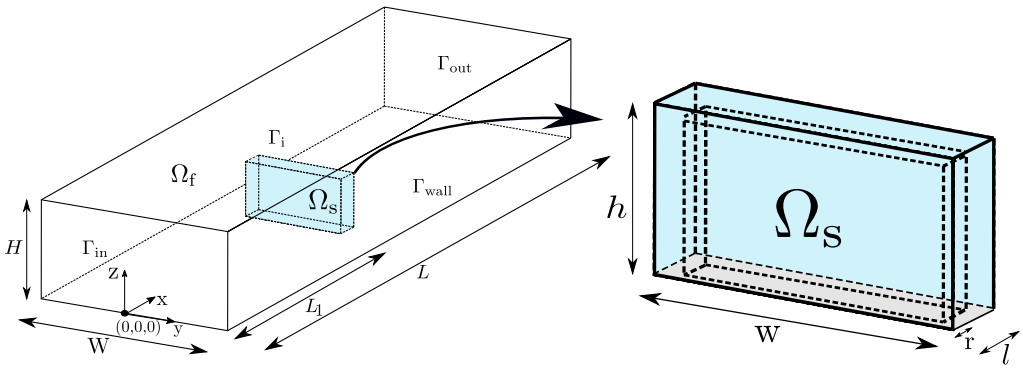

Figure 6.21: Flexible plate in a flow channel. Geometry.

by a temporal factor

$$v_f(0, y, z, t) = \begin{cases} \bar{v}_f(0, y, z)\frac{1-\cos\frac{\pi}{2}t}{2} & t < 0.1 \text{ s} \\ \bar{v}_f(0, y, z) & \text{otherwise} \end{cases}. \tag{6.31}$$

The time $t = 0.1$ s denotes the final time of the excitation phase. Therefore, the flow entering the domain excites the structural flap to initially bend and deform. No-slip wall boundary conditions at the four sides perpendicular to the inlet prevent the flow to escape. A stress-free condition is applied on the outlet boundary. The bottom face of the flexible beam is considered clamped.

The material properties are chosen as follows: the flow is assumed incompressible with kinematic viscosity $\nu_f = 0.01\ \mathrm{m}^2/s$ and a density $\rho_f = 1\ \mathrm{kg/m}^3$. Based on the maximum inflow velocity and the width of the flap, the Reynolds number Re ranges from 0–60. The structure exhibits a Neo-Hookean material law for the deviatoric part of the strain energy with a Young's modulus $E_s = 3\,000$ Pa, a Poisson's ratio $\nu_s = 0.5$ and an initial density $\rho_{s,0} = 250\ \mathrm{kg/m}^3$ for which large and dynamic deformations are expected. A final volume of 60% of the initial one is stated as a volume restriction for Ω_{var}.

The domains are discretized using tetrahedral elements for both fluid and solid domains. Regarding the distribution of the elements, both meshes are unstructured and with smaller elements concentrated on the interface boundary $\Gamma_{i,0}$. In total, the fluid mesh is formed by 140 600 elements, and the solid mesh by 660 000 elements.

We select the time step $\Delta t = 0.001$ s. During the first 0.6 s,

we let the FSI problem run without performing any TO iteration. To do so, we impose a delay in the TO procedure of $600\Delta t$. At this moment, the problem converges to a stationary solution. From this point on, we select a time window of $50\Delta t = 0.05$ s to store the additive TD and perform a TO iteration. We continue the same procedure until a converged optimized solution is obtained for the structure. For this example, only the $\mathbf{u}p$ formulation is considered.

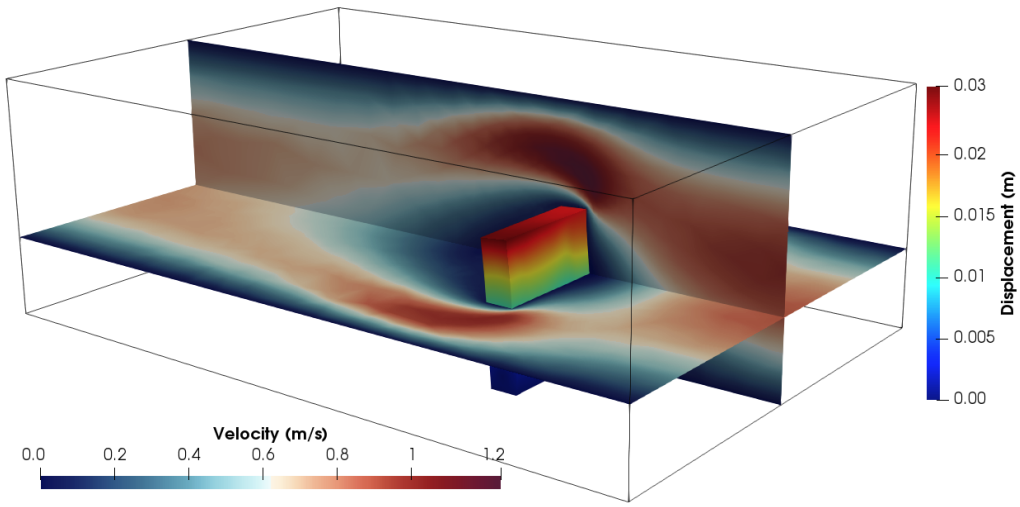

Figure 6.22: Flexible plate in a flow channel. Final stationary solution.

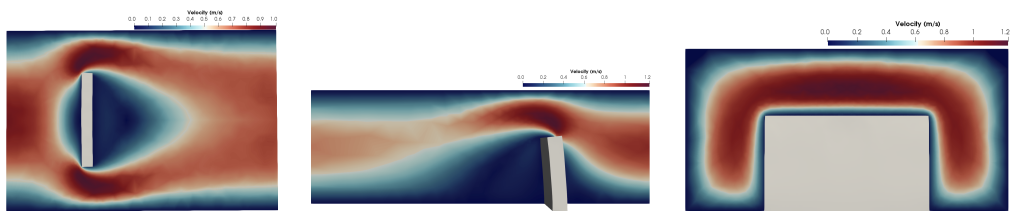

(a) Plane xy. Velocity field **(b)** Plane xz. Velocity field **(c)** Plane yz. Velocity field

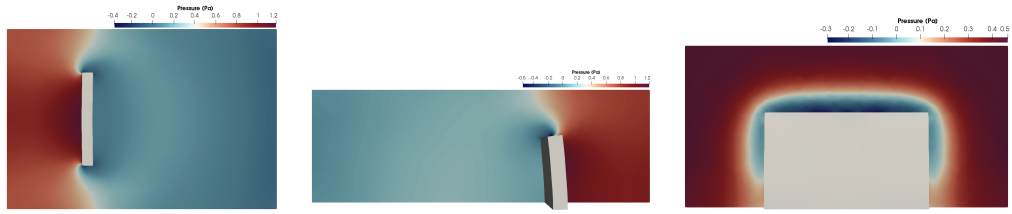

(d) Plane xy. Pressure field **(e)** Plane xz. Pressure field **(f)** Plane yz. Pressure field

Figure 6.23: Flexible plate in a flow channel. Distribution of the velocity field (top) and pressure (bottom) in the fluid domain. Velocities are plotted using their Euclidean norm.

First of all, let us show the final stationary FSI solution in

Fig. 6.22. As explained before, "dry" TO is performed and therefore the boundary of the solid which is in contact with the fluid flow remains constant. It is important to mention that strains of the order of 10^{-1} are obtained, which means that the small strain theory is not suitable in this case and finite strain theory fits better with the kind of problem that we are modeling. Both velocity and pressure fields in the flow channel from different points of view are depicted in Fig. 6.23.

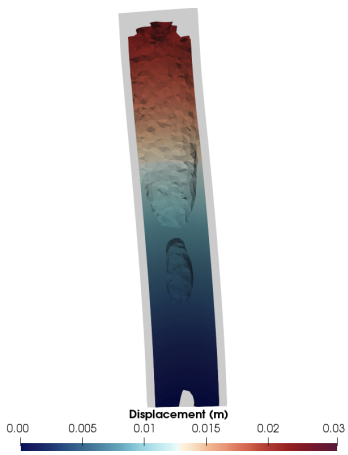

(a) Plane xz. Displacement field

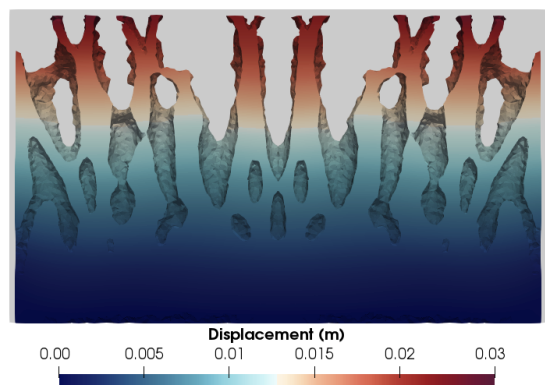

(b) Plane yz. Displacement field

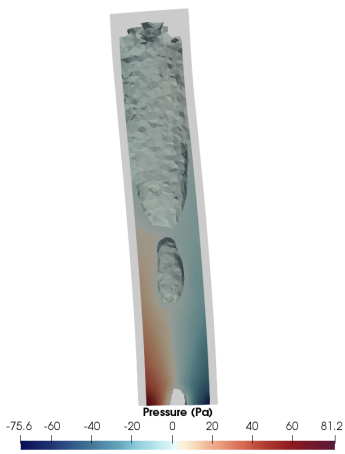

(c) Plane xz. Pressure field

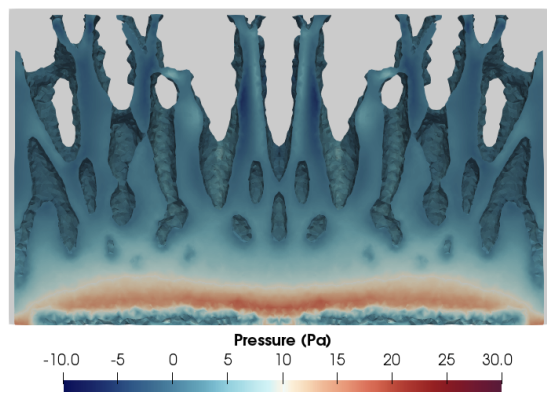

(d) Plane yz. Pressure field

Figure 6.24: Flexible plate in a flow channel. Distribution of the displacement field (top) and pressure (bottom) in the final optimized structures. Displacements are plotted using their Euclidean norm.

Let us now move to the solid domain. Fig. 6.24 displays the final optimized incompressible structure once a stationary solution is achieved and the objective function is not decreas-

ing anymore (according to a tolerance). To show the interior of the solid, which is the one which is optimized, we are showing a cut of the middle of the structure from different viewpoints and the fixed part is shown in gray. For the sake of completeness, in Fig. 6.25 the evolution of both the total potential energy and the volume fraction during the TO iterations is shown. As expected, the objective function increases while we start decreasing the volume fraction progressively, just to avoid numerical problems due to the highly nonlinear behavior of the whole problem. Once the volume fraction of 60 % is fixed, the objective function starts decreasing until a minimum is obtained and, therefore, the problem is ended.

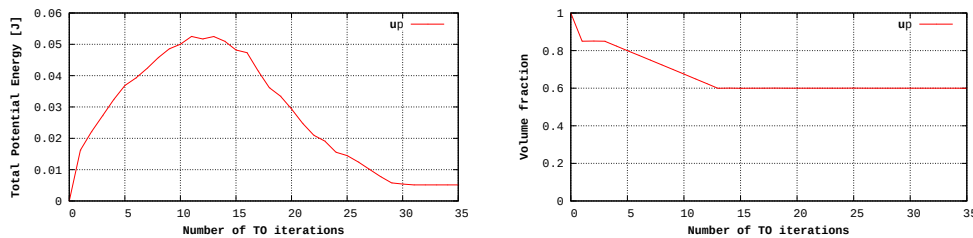

(a) Total potential energy (J)

(b) Volume fraction

Figure 6.25: Flexible plate in a flow channel. Convergence diagrams.

6.5 Conclusions

In this chapter, a TD-based TO algorithm has been presented to deal with incompressible structures subjected to FSI loads. The main goal of the chapter was to combine an additive TD with a level set method to optimize the internal structural layout of FSI problems. The structural response is modeled assuming either infinitesimal strains or finite ones. The fluid model is studied with the incompressible Navier-Stokes model and the coupling problem is treated in a staggered way with strong-coupling between sub-problems.

The key to solving problems involving incompressible structures was the introduction of the mixed stabilized FE formulations presented in Section 2.1 for linear elastic materials or in Chapter 3 for hyperelastic ones. On one hand, the well-known $\mathbf{u}p$ formulation, in which the pressure is added as an unknown – the fundamental one, when dealing with incompressible materials. On the other hand, three-field formulations which also add stresses as an unknown. Thanks to the

split TD formulae that we have obtained in Chapter 4 the TO algorithm of incompressible structures is possible for both infinitesimal and finite strain assumptions.

In Section 6.4 several numerical examples have been shown to assess the performance of the new TO algorithm for incompressible structures subjected to FSI loads. First of all, a flow through a channel with a flexible wall is considered. This case is supposed to converge to a stationary solution. Several cases have been performed, showing different optimized structures depending upon the kind of structure that is considered. The evolution of the total potential energy is also shown to decrease along TO steps. Next, the well-known Turek's FSI2 test is performed. The main idea of this problem is to show how the TO algorithm works in transient FSI problems. To do so, several volume fractions for the final structure are considered. Two final transient solutions are obtained for 90% and 80% of the final volume, but a stationary one is achieved when considering a 70% of material. Fluid forces and beam displacements are shown to see the effect of reducing the mass in the beam and how this can modify the physics of the FSI problem. To end up, a 3D case is performed to show the good performance of the methodology in three-dimensional cases.

Conclusions 7

7.1 Achievements

The main objective of this study was to set the bases for a general computational framework capable of computing the topology optimization problem of incompressible structures subject the interaction with a surrounding fluid ranging from the formulation to the implementation using the in-house finite element code FEMUSS (See Section 1.7).

- **Chapter 3** In this chapter, two different stabilized FE mixed formulations in finite strain solid dynamics are developed to be capable of considering nearly and fully incompressible materials. Both formulations exhibit optimal convergence properties. The numerical results presented in this chapter clearly demonstrate that both formulations appropriately deal with the incompressibility constraint. Finally, the three-field formulation exhibits a higher accuracy in the stress field than the two-field formulation, even for very coarse meshes.

- **Chapter 4** In this chapter, we describe the development of an algorithm for TO based on the topological derivative concept. A new decomposition of the Polarization tensor is applied for linear elasticity and the decomposition of an approximation in finite strain hyperelasticity is introduced. We use mixed formulations to obtain a general framework capable of addressing the TO problem of incompressible structures. The numerical examples presented in this chapter clearly demonstrate the capability of this framework to deal with the incompressible limit. In addition, the main differences between the two-and three-field formulations with respect to the accuracy obtained for the main unknowns are highlighted during the iterative TO process.

- **Chapter 5** In this chapter, a numerical approximation for VFSI problems with viscoelastic fluids in which elasticity can be dominant is presented. To this end, an LCR formulation is applied. Several numerical examples are used to assess the performance of the proposed

VFSI problem and its applicability to viscoelastic flows with high elasticity.

- **Chapter 6** In this chapter, an algorithm for TO problems of incompressible structures, under both small and finite strain assumptions, in which the loads come from the interaction with a surrounding fluid is developed. This methodology is applied to fluid-structure interaction problems for Newtonian fluid flows to demonstrate the good performance of this general framework.

7.2 Future work

The framework built for the TO problem of incompressible structures subjected to the interaction of a surrounding fluid is an excellent basis for future developments. The possible future directions are as follows:

- **Thermal coupling** Consideration of thermal effects in the context of finite strain solid dynamics is fundamental to obtain a realistic representation of stresses when a solid undergoes a complex and rapidly evolving deformation pattern. Focusing on thermal problems, the first law of thermodynamics can be incorporated as an extra conservation law in the mixed formulations developed in this study.

- **Two-field uE and three-field upE formulations** In [75], several methodologies for dealing with quasi-brittle cracking in fracture mechanics with small deformations are presented. The mixed formulation $\mathbf{u}\boldsymbol{\varepsilon}$ exhibits superior computational efficiency in the resolution of linear problems in solid mechanics, producing mesh objective results with a fraction of the computational cost required in the phase-field method. To extend this study to finite strain problems, it would be extremely interesting to develop a formulation in which the Green-Lagrange strain tensor $\mathbf{E}$ is introduced as main unknown of the problem to define the mixed two-field $\mathbf{uE}$ formulation. Finally, to deal with nearly and fully incompressible materials, the three-field $\mathbf{u}p\mathbf{E}$ formulation would be very powerful, in which the pressure would also be added as a primary unknown.

[75]: Cervera et al. (2022), "A Comparative Review of XFEM, Mixed FEM and Phase-Field Models for Quasi-brittle Cracking"

- **Fractional step schemes** The monolithic resolution of the system of equations obtained for the mixed formulations presented here (especially for the $\mathbf{u}p\mathbf{S}'$ formulation) can be computationally expensive, particularly for large-scale problems or 3D cases. Instead of solving this system, an alternative is to develop fractional step methods in time, in which different equations need to be solved for the different unknowns in an uncoupled manner. These fractional step formulations exhibit an important reduction in CPU time with respect to the monolithic case. See [184–187] for further details on this topic.

- **Linearized topological derivative for finite strain hyperelasticity** In Chapter 4 an approximation of the topological derivative is applied. Even though this approximation turns out to be efficient in the numerical examples we run, there is no way to show analytically that this expression converges to the minimum. Therefore, it is extremely interesting to study the topological derivative concept in the finite strain theory. Unfortunately, this problem is not linear, and there is no analytical solution for finding a closed-form expression. Our first proposal is to linearize the problem and find a closed-form expression for the topological derivative of a specific increment. If this step can be achieved, then the topological derivative would be computed as a combination of the different topological derivative increments that have been collected along the number of load factors.

- **Buckling phenomena in TO problems for finite strain hyperelasticity** In this study, buckling analysis was avoided. In this sense, it would be extremely interesting to include the study of possible buckling effects along the TO process and design techniques to remove areas where buckling can occur. Obviously, the final optimized structure must not present any buckling effect [81, 85].

- **Extend to TO problems subjected to FSI loads with viscoelastic fluid flows** In this work, we study the TO algorithm for incompressible structures subjected to FSI load when considering Newtonian fluid flows. In Chapter 5 we propose a methodology for dealing with viscoelastic fluid flows with a high We number. The

[184]: Castillo et al. (2015), "First, second and third order fractional step methods for the three-field viscoelastic flow problem"
[185]: Parada et al. (2020), "A fractional step method for computational aeroacoustics using weak imposition of Dirichlet boundary conditions"
[186]: Parada et al. (2021), "Development of an algebraic fractional step scheme for the primitive formulation of the compressible Navier-Stokes equations"
[187]: Parada et al. (2022), "A VMS–based fractional step technique for the compressible Navier–Stokes equations using conservative variables"

[81]: Ortigosa et al. (2020), "A stabilisation approach for topology optimisation of hyperelastic structures with the SIMP method"
[85]: Ortigosa et al. (2019), "A new stabilisation approach for level-set based topology optimisation of hyperelastic materials"

next step is to introduce an LCR formulation that is capable of considering such flows in the TO procedure.

- **Apply Correction terms to TO problems subjected to FSI loads** In [188], correction terms coming from ANN to increase the accuracy of the ROM models are developed. The next idea is to apply the ROM model to the fluid domain in the TO procedure of a structure when the loads come from a surrounding fluid.

[188]: Baiges et al. (2020), "A finite element reduced-order model based on adaptive mesh refinement and artificial neural networks"

- **Extend to "wet" TO problems for FSI** In Chapter 6 a new methodology for performing TO of incompressible structures subjected to FSI is developed. This methodology is only capable of optimizing the internal part of the structure, and the interface boundary between the solid and the fluid must remain constant. The next step would be expand this methodology to allow the geometry of the interface boundary to change during the TO procedure.

Appendix

Analytical solution of the isotropic linear elastic exterior problem

A

In this Appendix, we aim at solving analytically the exterior problem in order to compute the final expression of the topological derivative. It consists in solving a two dimensional problem in plane strain for an isotropic infinite domain (hereafter referred matrix) with a unitary centered circular inclusion inserted of another isotropic material. Two kind of boundary conditions are considered; firstly, at infinity the stresses are imposed to be zero; and secondly, due to the Eshelby theorem [189, 190] a constant behavior of the stresses is imposed in the inclusion. In addition, the transmission conditions (in stresses and displacements) across the interface of the inclusion and the matrix are also considered. All that conditions are necessary for solving the free constants appearing in the problem.

[189]: S.A.Nazarov (2009), "Elasticity polarization tensor, surface enthalpy, and Eshelby theorem"
[190]: V.A.Eremeyev et al. (2019), "On the correspondence between two- and three-dimensional Eshelby tensors"

A.1 Equilibrium and Beltrami-Michell equations

The general equilibrium equation neglecting both body forces and inertial terms is normally expressed as

$$\nabla \cdot \boldsymbol{\sigma} = \mathbf{0}.$$

Using a Cartesian coordinate system, the equilibrium equation is written as

$$\frac{\partial \sigma_x}{\partial x} + \frac{\partial \sigma_{xy}}{\partial y} + \frac{\partial \sigma_{xz}}{\partial z} = 0,$$

$$\frac{\partial \sigma_{xy}}{\partial x} + \frac{\partial \sigma_y}{\partial y} + \frac{\partial \sigma_{yz}}{\partial z} = 0,$$

$$\frac{\partial \sigma_{xz}}{\partial x} + \frac{\partial \sigma_{yz}}{\partial y} + \frac{\partial \sigma_z}{\partial z} = 0.$$

If we assume a 2D plane strain behavior, then we have to impose that

$$\sigma_{xz} = \sigma_{yz} = 0 \quad \text{and} \quad \sigma_z = \sigma_z(x, y) = \nu \left(\sigma_x + \sigma_y \right),$$

and the equilibrium equation reduces to

$$\frac{\partial \sigma_x}{\partial x} + \frac{\partial \sigma_{xy}}{\partial y} = 0, \qquad \frac{\partial \sigma_{xy}}{\partial x} + \frac{\partial \sigma_y}{\partial y} = 0.$$

Then, the Airy function $\phi(x, y)$ is defined by enforcing the second derivatives to fulfill

$$\sigma_x = \frac{\partial^2 \phi}{\partial y^2}, \qquad \sigma_y = \frac{\partial^2 \phi}{\partial x^2}, \qquad \sigma_{xy} = \frac{\partial^2 \phi}{\partial y \partial x}.$$

Note that with this definition the reduced equilibrium equation is automatically satisfied. The equilibrium equation is necessary but not sufficient to be a solution of an elasticity problem. In addition, the compatibility conditions must be satisfied, which in terms of stresses (commonly called Beltrami-Michell compatibility conditions) with considering no body forces takes the following form

$$\begin{aligned}\Delta\left(\sigma_x + \sigma_y + \sigma_z\right) &= \Delta\left(\sigma_x + \sigma_y + \nu\left(\sigma_x + \sigma_y\right)\right) \\ &= \Delta\left((\nu+1)\left(\sigma_x + \sigma_y\right)\right) = (\nu+1)\Delta\left(\sigma_x + \sigma_y\right) \\ &= 0 \;\Leftrightarrow\; \Delta\left(\sigma_x + \sigma_y\right) = 0.\end{aligned}$$

Thus, the Laplacian of the trace of the stress tensor must be zero. Clearly, in Cartesian coordinates, the Laplacian is denoted as

$$\Delta = \left(\frac{\partial^2}{\partial x^2} + \frac{\partial^2}{\partial y^2}\right).$$

Inserting the stresses in terms of the Airy function in the Beltrami-Michel compatibility equation, we obtain

$$\Delta\left(\sigma_x + \sigma_y\right) = \Delta\left(\frac{\partial^2 \phi}{\partial x^2} + \frac{\partial^2 \phi}{\partial y^2}\right) = \Delta\Delta\phi = 0,$$

which stands for the biharmonic equation for the Airy function. Commonly, it is also expressed as

$$\left(\frac{\partial^2}{\partial x^2} + \frac{\partial^2}{\partial y^2}\right)\left(\frac{\partial^2}{\partial x^2} + \frac{\partial^2}{\partial y^2}\right)\phi = 0.$$

However, since we deal with a circular inclusion, it is more appropriate to reformulate the problem in polar coordinates. We can now proceed analogously to the equilibrium equations which in this case are writing in the following form

$$\frac{\partial \sigma_r}{\partial r} + \frac{1}{r}\frac{\partial \sigma_{r\theta}}{\partial \theta} + \frac{\partial \sigma_{rz}}{\partial z} + \frac{1}{r}\left(\sigma_r - \sigma_\theta\right) = 0,$$

$$\frac{\partial \sigma_{r\theta}}{\partial r} + \frac{1}{r}\frac{\partial \sigma_{\theta}}{\partial \theta} + \frac{\partial \sigma_{\theta z}}{\partial z} + \frac{2}{r}\sigma_{r\theta} = 0,$$
$$\frac{\partial \sigma_{rz}}{\partial r} + \frac{1}{r}\frac{\partial \sigma_{\theta z}}{\partial \theta} + \frac{\partial \sigma_{z}}{\partial z} + \frac{1}{r}\sigma_{rz} = 0.$$

If we assume a 2D plane strain behavior, then we have to impose that

$$\sigma_{xz} = \sigma_{yz} = 0 \Rightarrow \sigma_{rz} = \sigma_{\theta z} = 0 \text{ and } \sigma_z = \sigma_z(r,\theta) = \nu\left(\sigma_r + \sigma_\theta\right),$$

and the equilibrium equation reduces to

$$\frac{\partial \sigma_r}{\partial r} + \frac{1}{r}\frac{\partial \sigma_{r\theta}}{\partial \theta} + \frac{1}{r}\left(\sigma_r - \sigma_\theta\right) = 0, \qquad \frac{\partial \sigma_{r\theta}}{\partial r} + \frac{1}{r}\frac{\partial \sigma_{\theta}}{\partial \theta} + \frac{2}{r}\sigma_{r\theta} = 0.$$

Similarly, the Airy function $\phi(r,\theta)$ is defined fulfilling

$$\sigma_r = \frac{1}{r}\frac{\partial \phi}{\partial r} + \frac{1}{r^2}\frac{\partial^2 \phi}{\partial \theta^2}, \qquad \sigma_\theta = \frac{\partial^2 \phi}{\partial r^2}, \qquad \sigma_{r\theta} = -\frac{\partial}{\partial r}\left(\frac{1}{r}\frac{\partial \phi}{\partial \theta}\right).$$

Note that, again, with these definitions, the equilibrium equation in polar coordinates is automatically satisfied. Considering the independence of the first invariant on the system of coordinates, that is $x + y = r + \theta$, we have

$$\begin{aligned}\Delta\left(\sigma_x + \sigma_y + \sigma_z\right) &= \Delta\left(\sigma_r + \sigma_\theta + \sigma_z\right) = \Delta\left(\sigma_r + \sigma_\theta + \nu\left(\sigma_r + \sigma_\theta\right)\right) \\ &= \Delta\left(\left(\nu + 1\right)\left(\sigma_r + \sigma_\theta\right)\right) = \left(\nu + 1\right)\Delta\left(\sigma_r + \sigma_\theta\right) \\ &= 0 \;\Leftrightarrow\; \Delta\left(\sigma_r + \sigma_\theta\right) = 0.\end{aligned}$$

Likewise, the Laplacian in polar coordinates takes the following form,

$$\Delta = \left(\frac{\partial^2}{\partial r^2} + \frac{1}{r}\frac{\partial}{\partial r} + \frac{1}{r^2}\frac{\partial^2}{\partial \theta^2}\right).$$

Substituting the stresses in terms of the Airy function into the Beltrami-Michel equation, we obtain the biharmonic equation for the Airy function in polar coordinates, that is,

$$\Delta\left(\sigma_r + \sigma_\theta\right) = \Delta\left(\frac{1}{r}\frac{\partial \phi}{\partial r} + \frac{1}{r^2}\frac{\partial^2 \phi}{\partial \theta^2} + \frac{\partial^2 \phi}{\partial r^2}\right) = \Delta\Delta\phi = 0.$$

For simplicity, the biharmonic equation is also commonly expressed more schematically in the following form

$$\left(\frac{\partial^2}{\partial r^2} + \frac{1}{r}\frac{\partial}{\partial r} + \frac{1}{r^2}\frac{\partial^2}{\partial \theta^2}\right)\left(\frac{\partial^2}{\partial r^2} + \frac{1}{r}\frac{\partial}{\partial r} + \frac{1}{r^2}\frac{\partial^2}{\partial \theta^2}\right)\phi = 0.$$

A.2 Boundary and transmission conditions

For the solution of the biharmonic equation, we need to define the boundary conditions that must be satisfied. It is worth mentioning that since we consider two bodies (inclusion and matrix), two Airy function appear as the unknowns of the problem, one for each body. Regarding the matrix, in the way that the exterior problem is defined, we impose that at infinity the stresses cancel, this is,

$$\lim_{r\to\infty} \sigma_r^e(r,\theta) = \lim_{r\to\infty} \sigma_\theta^e(r,\theta) = \lim_{r\to\infty} \sigma_{r\theta}^e(r,\theta) = 0.$$

Note that all the variables (Airy function $\phi(r,\theta)$, the stresses $\boldsymbol{\sigma}$ and the strains $\boldsymbol{\varepsilon}$) are hereafter denoted by a super-index e in the case of the matrix and i in the case of the inclusion Regarding the boundary conditions for the inclusion, we impose the Eshelby theorem, which asserts that the strain fields inside the inclusion are constant if the loading at infinity is constant (zero in this case). Thus, for the case of elastic materials, the constant value of the strain field brings constant value of the stress field, i.e.,

$$\sigma_r^i(r,\theta) \neq f(r), \qquad \sigma_\theta^i(r,\theta) \neq f(r), \qquad \sigma_{r\theta}^i(r,\theta) \neq f(r).$$

Note that the dependency is due to the basis (polar) on which it is expressed, but not on the values of the tensor. If it is expressed in the principal coordinates no dependency will appear. This dependency is clearly seen when we impose the jump on traction across the boundary of the inclusion. Thus, once the boundary conditions are imposed in both solids, the transmission conditions across the interface of the inclusion and the matrix must be satisfied. Regarding the stresses, the exterior problem is defined such that the jump of the traction across the interface must be equal to the normal component of the given stress tensor $\mathbf{S}$, this is

$$\left\{\boldsymbol{\sigma}^e(1,\theta) - \boldsymbol{\sigma}^i(1,\theta)\right\}\cdot\mathbf{n} = \mathbf{S}\cdot\mathbf{n} \;\Rightarrow\; \begin{bmatrix} \sigma_r^e(1,\theta) - \sigma_r^i \\ \sigma_{r\theta}^e(1,\theta) - \sigma_{r\theta}^i \end{bmatrix} = \begin{bmatrix} S_r \\ S_{r\theta} \end{bmatrix} \quad \forall\theta.$$

Thus, the stresses will be discontinuous across the interface. Although the exterior problem is solved in polar coordinates, the data $\mathbf{S}$ and the solution must be provided into Cartesian coordinates. Thus, we try to re-express the tensor $\mathbf{S}$ in polar coordinates in terms of its Cartesian counterpart. Pre

and post-multiplying by the standard rotation matrix, we obtain

$$\begin{bmatrix} S_r & S_{r\theta} \\ S_{r\theta} & S_\theta \end{bmatrix} = \begin{bmatrix} \cos\theta & \sin\theta \\ -\sin\theta & \cos\theta \end{bmatrix} \begin{bmatrix} S_x & S_{xy} \\ S_{xy} & S_y \end{bmatrix} \begin{bmatrix} \cos\theta & -\sin\theta \\ \sin\theta & \cos\theta \end{bmatrix}.$$

Accordingly, if we proceed to express the relation in vector notation as

$$\begin{bmatrix} S_r \\ S_\theta \\ S_{r\theta} \end{bmatrix} = \begin{bmatrix} \frac{S_x+S_y}{2} & \frac{S_x-S_y}{2} & S_{xy} \\ \frac{S_x+S_y}{2} & \frac{S_y-S_x}{2} & -S_{xy} \\ 0 & S_{xy} & \frac{S_y-S_x}{2} \end{bmatrix} \begin{bmatrix} 1 \\ \cos 2\theta \\ \sin 2\theta \end{bmatrix}.$$

Thus, both the first and the last equation of the above expression are going to be considered in the transmission conditions. Note that although the tensor $\mathbf{S}$ is constant, a dependency on θ appears due to its representation on the polar basis of the tensor. This is analogous to the inclusion stresses $\boldsymbol{\sigma}^i$ dependency that appear in the Eshelby conditions. The dependency on the angle θ appears due to its representation on the polar basis. Regarding the transmission conditions on displacements, we must ensure, in polar coordinates, that the jump across the boundary of the inclusion of the component of the strains must be zero, i.e.,

$$\varepsilon_\theta^e(1,\theta) - \varepsilon_\theta^i = 0 \quad \forall\theta.$$

The biharmonic equation jointly with all these conditions are the necessary ingredients for solving the exterior problem.

A.3 Resolution of the biharmonic equation

Since we have to satisfy the transmission conditions and the tensor $\mathbf{S}$ is expressed as a combination of 1, $\cos(\theta)$, $\sin(\theta)$, the Airy function is proposed at least depending on that terms. More specifically, that is

$$\begin{aligned} \phi(r,\theta) &= \begin{bmatrix} \phi_o(r) & \phi_c(r) & \phi_s(r) \end{bmatrix} \begin{bmatrix} 1 \\ \cos(2\theta) \\ \sin(2\theta) \end{bmatrix} \\ &= \phi_o(r) + \phi_c(r)\cos(2\theta) + \phi_s(r)\sin(2\theta). \end{aligned}$$

Introducing the above expression in the biharmonic equation, we obtain

$$\Delta^2\phi = \Delta^2\phi_o(r) + \Delta^2\left(\phi_c(r)\cos(2\theta)\right) + \Delta^2\left(\phi_s(r)\sin(2\theta)\right) = 0.$$

Considering the biharmonic operator, the following equations can be written

$$\frac{\partial^4\phi_o}{\partial r^4} + \frac{2}{r}\frac{\partial^3\phi_o}{\partial r^3} - \frac{1}{r^2}\frac{\partial^2\phi_o}{\partial r^2} + \frac{1}{r^3}\frac{\partial\phi_o}{\partial r} = 0,$$

$$\frac{\partial^4\phi_c}{\partial r^4} + \frac{2}{r}\frac{\partial^3\phi_c}{\partial r^3} - \frac{9}{r^2}\frac{\partial^2\phi_c}{\partial r^2} + \frac{9}{r^3}\frac{\partial\phi_c}{\partial r} = 0,$$

$$\frac{\partial^4\phi_s}{\partial r^4} + \frac{2}{r}\frac{\partial^3\phi_s}{\partial r^3} - \frac{9}{r^2}\frac{\partial^2\phi_s}{\partial r^2} + \frac{9}{r^3}\frac{\partial\phi_s}{\partial r} = 0.$$

We now proceed to study and solve (up to constant parameters) each term of the Airy function and then we sum them up. Regarding the term ϕ_o, it must satisfy

$$\frac{\partial^4\phi_o}{\partial r^4} + \frac{2}{r}\frac{\partial^3\phi_o}{\partial r^3} - \frac{1}{r^2}\frac{\partial^2\phi_o}{\partial r^2} + \frac{1}{r^3}\frac{\partial\phi_o}{\partial r} = 0,$$

and after applying the change of variable $r = e^t$, the above equation becomes the following linear one

$$\frac{\partial^4\phi_o}{\partial t^4} - 4\frac{\partial^3\phi_o}{\partial t^3} + 4\frac{\partial^2\phi_o}{\partial t^2} = 0.$$

Since it has linear behavior, we can solve it through the characteristic equation

$$t^4 - 4t^3 + 4t^2 = 0,$$

whose roots (both doubles) are $t = 0$ and $t = 2$. Thus the solution of the equation reads as

$$\phi_o(t) = A_o t + B_o t e^{2t} + C_o e^{-2t} + D_o,$$

and after undoing the change of variable, we obtain

$$\phi_o(r) = A_o \log(r) + B_o r^2 \log(r) + C_o r^2 + D_o,$$

which can be expressible in a vector form as

$$\phi_o(r) = \begin{bmatrix} A_o & B_o & C_o & D_o \end{bmatrix} \begin{bmatrix} r^2 \\ r^2 \log(r) \\ \log(r) \\ 1 \end{bmatrix} = K_o^T R_o.$$

We proceed similarly for the function $\phi_c(r)$. The compatibility equation is written as

$$\frac{\partial^4 \phi_c}{\partial r^4} + \frac{2}{r}\frac{\partial^3 \phi_c}{\partial r^3} - \frac{9}{r^2}\frac{\partial^2 \phi_c}{\partial r^2} + \frac{9}{r^3}\frac{\partial \phi_c}{\partial r} = 0.$$

After applying the same change of variable $r = e^t$ and solving the characteristic equation, we obtain that the term $\phi_c(t)$ is of the form

$$\phi_c(t) = A_c e^{2t} + B_c e^{4t} + C_c e^{-2t} + D_c.$$

Undoing again the change of variable, we end up with the expression for $\phi_c(r)$ as

$$\phi_c(r) = A_c r^2 + B_c \frac{1}{r^2} + C_c r^4 + D_c,$$

which can be written in a vector form as

$$\phi_c(r) = \begin{bmatrix} A_c & B_c & C_c & D_c \end{bmatrix} \begin{bmatrix} r^2 \\ \frac{1}{r^2} \\ r^4 \\ 1 \end{bmatrix} = K_c^T R_c.$$

Since $\phi_c(r)$ has to solve the same equation than $\phi_s(r)$, it can be written in the same terms, that is

$$\phi_s(r) = \begin{bmatrix} A_s & B_s & C_s & D_s \end{bmatrix} \begin{bmatrix} r^2 \\ \frac{1}{r^2} \\ r^4 \\ 1 \end{bmatrix} = K_s^T R_s.$$

Thus, the Airy function is compactly expressible as

$$\phi(r,\theta) = \begin{bmatrix} R_o & R_c & R_s \end{bmatrix} \begin{bmatrix} K_o^T & 0 & 0 \\ 0 & K_c^T & 0 \\ 0 & 0 & K_s^T \end{bmatrix} \begin{bmatrix} 1 \\ \cos(2\theta) \\ \sin(2\theta) \end{bmatrix}.$$

The free parameters are collected in the vectors K_o, K_c and K_s and are going to be determined after applying both boundary

and transmission conditions.

A.4 Resolution of free parameters

Once we have the expression of the Airy function, we move to compute the $\boldsymbol{\sigma}$ field. According to previous relations we obtain

$$\begin{bmatrix}\sigma_r\\ \sigma_\theta\\ \sigma_{r\theta}\end{bmatrix} = \begin{bmatrix}\frac{1}{r}\frac{\partial}{\partial r}+\frac{1}{r^2}\frac{\partial^2}{\partial\theta^2}\\ \frac{\partial^2}{\partial r^2}\\ -\frac{\partial}{\partial r}\left(\frac{1}{r}\frac{\partial}{\partial\theta}\right)\end{bmatrix}\begin{bmatrix}\phi_o(r) & \phi_c(r) & \phi_s(r)\end{bmatrix}\begin{bmatrix}1\\ \cos(2\theta)\\ \sin(2\theta)\end{bmatrix}$$
$$= \begin{bmatrix}K_o^T\left(\frac{1}{r}\frac{\partial}{\partial r}\right)R_o & K_c^T\left(\frac{1}{r}\frac{\partial}{\partial r}-\frac{4}{r^2}\right)R_c & K_s^T\left(\frac{1}{r}\frac{\partial}{\partial r}-\frac{4}{r^2}\right)R_s\\ K_o^T\left(\frac{\partial^2}{\partial r^2}\right)R_o & K_c^T\left(\frac{\partial^2}{\partial r^2}\right)R_c & K_s^T\left(\frac{\partial^2}{\partial r^2}\right)R_s\\ 0 & -2K_s^T\left(\frac{\partial}{\partial r}\left(\frac{1}{r}\right)\right)R_s & 2K_c^T\left(\frac{\partial}{\partial r}\left(\frac{1}{r}\right)\right)R_c\end{bmatrix}$$
$$\cdot\begin{bmatrix}1\\ \cos(2\theta)\\ \sin(2\theta)\end{bmatrix}.$$

Note that each term of the matrix stands for a scalar product between the K_o, K_c and K_s and some derivatives of R_o, R_c and R_s. Let us define the following relation by

$$\begin{bmatrix}\sigma_r\\ \sigma_\theta\\ \sigma_{r\theta}\end{bmatrix} = \begin{bmatrix}K_o^T dR_o^r & K_c^T dR_c^r & K_s^T dR_s^r\\ K_o^T dR_o^\theta & K_c^T dR_c^\theta & K_s^T dR_s^\theta\\ 0 & -2K_s^T dR_s^{r\theta} & 2K_c^T dR_c^{r\theta}\end{bmatrix}\begin{bmatrix}1\\ \cos(2\theta)\\ \sin(2\theta)\end{bmatrix},$$

where

$$dR_o^r = \left(\frac{1}{r}\frac{\partial}{\partial r}\right)R_o = \left(\frac{1}{r}\frac{\partial}{\partial r}\right)\begin{bmatrix}r^2\\ r^2\log(r)\\ \log(r)\\ 1\end{bmatrix} = \begin{bmatrix}2\\ 1+2\log(r)\\ \frac{1}{r^2}\\ 0\end{bmatrix}.$$

$$dR_o^\theta = \left(\frac{\partial^2}{\partial r^2}\right)R_o = \left(\frac{\partial^2}{\partial r^2}\right)\begin{bmatrix}r^2\\ r^2\log(r)\\ \log(r)\\ 1\end{bmatrix} = \begin{bmatrix}2\\ 3+2\log(r)\\ -\frac{1}{r}\\ 0\end{bmatrix}.$$

$$dR_c^r = dR_s^r = \left(\frac{1}{r}\frac{\partial}{\partial r}-\frac{4}{r^2}\right)R_c = \left(\frac{1}{r}\frac{\partial}{\partial r}-\frac{4}{r^2}\right)\begin{bmatrix}r^2\\ \frac{1}{r^2}\\ r^4\\ 1\end{bmatrix} = \begin{bmatrix}-2\\ -\frac{6}{r^4}\\ 0\\ -\frac{4}{r^2}\end{bmatrix}.$$

$$dR_c^\theta = dR_s^\theta = \left(\frac{\partial^2}{\partial r^2}\right) R_c = \left(\frac{\partial^2}{\partial r^2}\right) \begin{bmatrix} r^2 \\ \frac{1}{r^2} \\ r^4 \\ 1 \end{bmatrix} = \begin{bmatrix} 2 \\ \frac{6}{r^4} \\ 12r^2 \\ 0 \end{bmatrix}.$$

$$dR_c^{r\theta} = dR_s^{r\theta} = \left(\frac{\partial}{\partial r}\left(\frac{1}{r}\right)\right) R_c = \left(\frac{\partial}{\partial r}\left(\frac{1}{r}\right)\right) \begin{bmatrix} r^2 \\ \frac{1}{r^2} \\ r^4 \\ 1 \end{bmatrix} = \begin{bmatrix} 1 \\ -\frac{3}{r^4} \\ 3r^2 \\ -\frac{1}{r^2} \end{bmatrix}.$$

A.4.1 Boundary conditions in the matrix

To determine the free parameters, we first apply on the matrix the condition of zero stress at infinity which leads to cancel the following constants

$$A_o^e = B_o^e = A_c^e = A_s^e = C_c^e = C_s^e = 0.$$

Since the last term of dR_0^r and dR_o^θ is canceled there is no reason of keeping the constant D_o^e; hence

$$D_o^e = 0.$$

Consequently, the vectors K_o, K_c and K_s become

$$K_o = C_o^e, \qquad K_c = \begin{bmatrix} B_c^e \\ D_c^e \end{bmatrix}, \qquad K_s = \begin{bmatrix} B_s^e \\ D_s^e. \end{bmatrix}$$

and similarly the dR vectors becomes

$$dR_o^r = \frac{1}{r^2}, \qquad dR_o^\theta = -\frac{1}{r^2}, \qquad dR_c^r = dR_s^r = \begin{bmatrix} -\frac{6}{r^4} \\ -\frac{4}{r^2} \end{bmatrix},$$

$$dR_c^\theta = dR_s^\theta = \begin{bmatrix} \frac{6}{r^4} \\ 0 \end{bmatrix}, \qquad dR_c^{r\theta} = dR_s^{r\theta} = \begin{bmatrix} -\frac{3}{r^4} \\ -\frac{1}{r^2} \end{bmatrix}.$$

Substituting all these reduced expression into the stress field relation, we are ready to compute the term $\boldsymbol{\sigma}^e(1,\theta)$ that appears in the transmission condition just imposing $r = 1$ as follows

$$\boldsymbol{\sigma}^e = \begin{bmatrix} \sigma_r^e(1,\theta) \\ \sigma_\theta^e(1,\theta) \\ \sigma_{r\theta}^e(1,\theta) \end{bmatrix} = \begin{bmatrix} C_o^e & -6B_c^e - 4D_c^e & -6B_s^e - 4D_s^e \\ -C_o^e & 6B_c^e & 6B_s^e \\ 0 & 6B_c^e + 2D_c^e & -6B_s^e - 2D_s^e \end{bmatrix} \begin{bmatrix} 1 \\ \cos 2\theta \\ \sin 2\theta \end{bmatrix}.$$

A.4.2 Boundary conditions in the inclusion

Regarding the conditions on the inclusion, we have to impose a constant value of the stresses. Thus, all the constants that multiply terms that depend on variable r are canceled, that is

$$C_o^i = B_o^i = B_c^i = B_s^i = D_c^i = D_s^i = C_c^i = C_s^i = 0.$$

And similarly, since D_o^i is arbitrary and it does not appear on the stress, there is no reasons to keep it. Hence,

$$D_o^i = 0.$$

Consequently, the vector K_o, K_c and K_s become

$$K_o^i = A_o^i, \qquad K_c^i = A_c^i, \qquad K_s^i = A_s^i,$$

and the dR vector are reduced to the following expression

$$dR_o^r = 2, \qquad dR_o^\theta = 2,$$

$$dR_c^r = dR_s^r = -2, \qquad dR_c^\theta = dR_s^\theta = 2, \qquad dR_c^{r\theta} = dR_s^{r\theta} = 1.$$

In order to apply the transmission condition, substituting the above reduced expression in the stress field equation, we obtain the constant stress field in the inclusion as

$$\boldsymbol{\sigma}^i = \begin{bmatrix} \sigma_r^i(1,\theta) \\ \sigma_\theta^i(1,\theta) \\ \sigma_{r\theta}^i(1,\theta) \end{bmatrix} = \begin{bmatrix} 2A_o^i & -2A_c^i & -2A_s^i \\ 2A_o^i & 2A_c^i & 2A_s^i \\ 0 & -2A_s^i & 2A_c^i \end{bmatrix} \begin{bmatrix} 1 \\ \cos 2\theta \\ \sin 2\theta \end{bmatrix}.$$

Note that since the stresses are constant in the inclusion, the above expression stands also for the stresses on the interface. It is worth mentioning that if we write the stresses into the Cartesian components as

$$\boldsymbol{\sigma}^i = \begin{bmatrix} \sigma_r^i(1,\theta) \\ \sigma_\theta^i(1,\theta) \\ \sigma_{r\theta}^i(1,\theta) \end{bmatrix} = \begin{bmatrix} \frac{\sigma_x^i+\sigma_y^i}{2} & \frac{\sigma_x^i-\sigma_y^i}{2} & \sigma_{xy}^i \\ \frac{\sigma_x^i+\sigma_y^i}{2} & \frac{\sigma_y^i-\sigma_x^i}{2} & -\sigma_{xy}^i \\ 0 & \sigma_{xy}^i & \frac{\sigma_y^i-\sigma_x^i}{2} \end{bmatrix} \begin{bmatrix} 1 \\ \cos 2\theta \\ \sin 2\theta \end{bmatrix},$$

and we identify all the terms of both matrices, we can relate the Cartesian components of the stresses with the constants A_o^i, A_c^i and A_s^i as

$$\sigma_x^i = 2\left(A_o^i - A_c^i\right), \qquad \sigma_y^i = 2\left(A_o^i + A_c^i\right), \qquad \sigma_{xy}^i = -A_s^i,$$

which in matrix notation is written as

$$\begin{bmatrix} \sigma_x^i \\ \sigma_y^i \\ \sigma_{xy}^i \end{bmatrix} = 2 \begin{bmatrix} 1 & -1 & 0 \\ 1 & 1 & 0 \\ 0 & 0 & -1/2 \end{bmatrix} \begin{bmatrix} A_o^i \\ A_c^i \\ A_s^i \end{bmatrix} = 2\mathbf{T} \begin{bmatrix} A_o^i \\ A_c^i \\ A_s^i \end{bmatrix}.$$

That last relation will be useful to find the final expression for the topological derivative. With all these boundary conditions imposed, we end up with 8 unknowns A_o^i, A_c^i , A_s^i, B_c^e ,B_s^e ,C_o^e ,D_c^e and D_s^e that are going to be determined after imposing transmission conditions.

A.4.3 Stress transmission condition

We apply the transmission condition in stresses across the interface. The first equation imposes continuity on the radial component of the stress as

$$\sigma_r^e(1,\theta) - \sigma_r^i = S_r \quad \forall\theta.$$

Considering the matrix representation of the stress $\mathbf{S}$ and comparing it with the difference with the matrix representation of the stresses on the matrix and the inclusion, we can identify the 1, $\cos 2\theta$ and $\sin 2\theta$ terms and write the following equations

$$\begin{aligned} C_o^e - 2A_o^i &= \frac{S_x^i + S_y^i}{2} \quad (1), \\ -6B_c^e - 4D_c^e + 2A_c^i &= \frac{S_x^i - S_y^i}{2} \quad (\cos 2\theta), \\ -6B_s^e - 4D_s^e + 2A_s^i &= S_{xy} \quad (\sin 2\theta). \end{aligned}$$

Similarly, the continuity of the shear component $\sigma_{r\theta}$ is imposed as

$$\sigma_{r\theta}^e(1,\theta) - \sigma_{r\theta}^i = S_{r\theta} \quad \forall\theta.$$

Considering again the matrix representation of $\mathbf{S}$, $\sigma_{r\theta}^e$ and $\sigma_{r\theta}^i$ and identifying the 1, $\cos 2\theta$ and $\sin 2\theta$ terms, we can write the second group of equations as

$$\begin{aligned} 0 &= 0 \quad (1), \\ 6B_s^e + 2D_s^e + 2A_c^i &= S_{xy} \quad (\cos 2\theta), \\ -6B_c^e - 2D_c^e - 2A_c^i &= \frac{S_y^i - S_x^i}{2} \quad (\sin 2\theta). \end{aligned}$$

A.4.4 Strain transmission condition

The last condition to impose is the strain transmission condition. Since we assume an isotropic material behavior, the strain can be related with the stresses for both the matrix and the inclusion through the following inverse constitutive relation

$$\begin{bmatrix} \varepsilon_r \\ \varepsilon_\theta \\ \varepsilon_z \\ \varepsilon_{r\theta} \\ \varepsilon_{rz} \\ \varepsilon_{\theta z} \end{bmatrix} = \frac{1}{E} \begin{bmatrix} 1 & -\nu & -\nu & 0 & 0 & 0 \\ -\nu & 1 & -\nu & 0 & 0 & 0 \\ -\nu & -\nu & 1 & 0 & 0 & 0 \\ 0 & 0 & 0 & (1+\nu) & 0 & 0 \\ 0 & 0 & 0 & 0 & (1+\nu) & 0 \\ 0 & 0 & 0 & 0 & 0 & (1+\nu) \end{bmatrix} \begin{bmatrix} \sigma_r \\ \sigma_\theta \\ \sigma_z \\ \sigma_{r\theta} \\ \sigma_{rz} \\ \sigma_{\theta z} \end{bmatrix}.$$

As $\sigma_{rz} = \sigma_{\theta z} = 0$, then $\varepsilon_{rz} = \varepsilon_{\theta z} = 0$ and rows and columns 5 and 6 can be neglected from the system

$$\begin{bmatrix} \varepsilon_r \\ \varepsilon_\theta \\ \varepsilon_z \\ \varepsilon_{r\theta} \end{bmatrix} = \frac{1}{E} \begin{bmatrix} 1 & -\nu & -\nu & 0 & 0 & 0 \\ -\nu & 1 & -\nu & 0 & 0 & 0 \\ -\nu & -\nu & 1 & 0 & 0 & 0 \\ 0 & 0 & 0 & (1+\nu) & 0 & 0 \end{bmatrix} \begin{bmatrix} \sigma_r \\ \sigma_\theta \\ \sigma_z \\ \sigma_{r\theta} \end{bmatrix}.$$

In the plane strain assumption, we consider that $\varepsilon_z = 0$. Therefore,

$$\varepsilon_z = \frac{1}{E}\{-\nu\sigma_r - \nu\sigma_\theta + \sigma_z\} = 0 \quad \Leftrightarrow \quad \sigma_z = \nu(\sigma_r + \sigma_\theta),$$

$$\begin{aligned} \varepsilon_r &= \frac{1}{E}\{\sigma_r - \nu\sigma_\theta - \nu\sigma_z\} = \frac{1}{E}\left\{\sigma_r - \nu\sigma_\theta - \nu^2\sigma_r - \nu^2\sigma_\theta\right\} \\ &= \frac{1-\nu^2}{E}\sigma_r - \frac{\nu(1+\nu)}{E}\sigma_\theta = \frac{1+\nu}{E}\{(1-\nu)\sigma_r - \nu\sigma_\theta\}, \end{aligned}$$

$$\begin{aligned} \varepsilon_\theta &= \frac{1}{E}\{\sigma_\theta - \nu\sigma_r - \nu\sigma_z\} = \frac{1}{E}\left\{\sigma_\theta - \nu\sigma_r - \nu^2\sigma_r - \nu^2\sigma_\theta\right\} \\ &= \frac{1-\nu^2}{E}\sigma_\theta - \frac{\nu(1+\nu)}{E}\sigma_r = \frac{1+\nu}{E}\{(1-\nu)\sigma_\theta - \nu\sigma_r\}. \end{aligned}$$

Then we obtain for both the matrix and the inclusion,

$$\begin{aligned} \varepsilon_\theta^e(1,\theta) &= \frac{1+\nu^e}{E^e}\left\{(1-\nu^e)\sigma_\theta^e(1,\theta) - \nu^e\sigma_r^e(1,\theta)\right\}, \\ \varepsilon_\theta^i(1,\theta) &= \frac{1+\nu^i}{E^i}\left\{(1-\nu^i)\sigma_\theta^i - \nu^i\sigma_r^i\right\}, \end{aligned}$$

where E^e, E^i, ν^e and ν^i represents the Young modulus and Poisson ratio for the matrix and the inclusion. Regarding the transmission conditions on strains, we must ensure, in polar coordinates, that the jump across the boundary of the inclusion of the component of the strains must be zero, i.e.,

$$\varepsilon^e_\theta(1,\theta) - \varepsilon^i_\theta = 0 \quad \forall\theta.$$

Inserting the above relation in the transmission condition, we can write the last group of equations as

$$\begin{aligned}
\frac{1+\nu^e}{E^e}C^e_o + 2\frac{(1-2\nu^i)(1+\nu^i)}{E^i}A^i_o = 0 \quad (1),\\
6\frac{1+\nu^e}{E^e}B^e_c + 4\frac{\nu^e(1+\nu^e)}{E^e}D^e_c - 2\frac{1+\nu^i}{E^i}A^i_c = 0 \quad (\cos 2\theta),\\
6\frac{1+\nu^e}{E^e}B^e_s + 4\frac{\nu^e(1+\nu^e)}{E^e}D^e_s - 2\frac{1+\nu^i}{E^i}A^i_s = 0 \quad (\sin 2\theta).
\end{aligned}$$

A.4.5 System of equations for the free parameters

Adding and rearranging all the group of equations, we can split them in three groups as

$$\begin{bmatrix} 1 & -2 \\ \frac{1+\nu^e}{E^e} & 2\frac{(1-2\nu^i)(1+\nu^i)}{E^i} \end{bmatrix}\begin{bmatrix} C^e_o \\ A^i_o \end{bmatrix} = \begin{bmatrix} \frac{S^i_x+S^i_y}{2} \\ 0 \end{bmatrix},$$

$$\begin{bmatrix} -6 & -4 & 2 \\ -6 & -2 & -2 \\ 6\frac{1+\nu^e}{E^e} & 4\frac{\nu^e(1+\nu^e)}{E^e} & -2\frac{1+\nu^i}{E^i} \end{bmatrix}\begin{bmatrix} B^e_c \\ D^e_c \\ A^i_c \end{bmatrix} = \begin{bmatrix} \frac{S^i_x-S^i_y}{2} \\ \frac{S^i_y-S^i_x}{2} \\ 0 \end{bmatrix},$$

$$\begin{bmatrix} -6 & -4 & 2 \\ 6 & 2 & 2 \\ 6\frac{1+\nu^e}{E^e} & 4\frac{\nu^e(1+\nu^e)}{E^e} & -2\frac{1+\nu^i}{E^i} \end{bmatrix}\begin{bmatrix} B^e_s \\ D^e_s \\ A^i_s \end{bmatrix} = \begin{bmatrix} S_{xy} \\ S_{xy} \\ 0 \end{bmatrix}.$$

The matrices of the three system of equations are invertible, thus, all the constants can be uniquely determined. Regarding the A^i_o, A^i_c and A^i_s, we provide its values in a matrix form as

$$\begin{bmatrix} A^i_o \\ A^i_c \\ A^i_s \end{bmatrix} = \frac{1}{4}\begin{bmatrix} -d_1 & -d_1 & 0 \\ d_2 & -d_2 & 0 \\ 0 & 0 & d_2 \end{bmatrix}\begin{bmatrix} S_x \\ S_y \\ S_{xy} \end{bmatrix} = \frac{1}{4}\mathbf{D}\begin{bmatrix} S_x \\ S_y \\ S_{xy} \end{bmatrix},$$

where the matrix $\mathbf{D}$ has been introduced and the dimensionless constants d_1 and d_2 take the following values

$$d_1 = \frac{1}{1+\frac{E^e(1-2\nu^i)(1+\nu^i)}{E^i(1+\nu^e)}} = \frac{\alpha\gamma}{\alpha\gamma+\tau_1\tau_2},$$
$$d_2 = \frac{1}{1+\frac{E^e(1+\nu^i)}{E^i(1+\nu^e)(3-4\nu^e)}} = \frac{\beta\gamma}{\beta\gamma+\tau_1},$$

where $\alpha = \frac{1}{1-2\nu_e}$, $\beta = 3-4\nu_e$, $\tau_1 = \frac{1+\nu_i}{1+\nu_e}$, $\tau_2 = \frac{1-2\nu_i}{1-2\nu_e}$. Thus, we can write the stresses on the inclusion in terms of the stresses $\mathbf{S}$ as

$$\begin{bmatrix}\sigma_x^i\\ \sigma_y^i\\ \sigma_{xy}^i\end{bmatrix} = 2\mathbf{T}\begin{bmatrix}A_o^i\\ A_c^i\\ A_s^i\end{bmatrix} = 2\mathbf{T}\frac{1}{4}\mathbf{D}\begin{bmatrix}S_x\\ S_y\\ S_{xy}\end{bmatrix}$$
$$= \frac{1}{2}\begin{bmatrix}-d_1-d_2 & -d_1+d_2 & 0\\ -d_1+d_2 & -d_1-d_2 & 0\\ 0 & 0 & -d_2\end{bmatrix}\begin{bmatrix}S_x\\ S_y\\ S_{xy}\end{bmatrix} = \mathbf{A}\begin{bmatrix}S_x\\ S_y\\ S_{xy}\end{bmatrix}.$$

From here we can obtained the expression for the 4-th order tensor $\mathbb{A}$

$$\mathbb{A} = -d_2\mathbb{I} + \frac{d_2-d_1}{2}\mathbf{I}\otimes\mathbf{I}$$
$$= -\frac{\beta\gamma}{\beta\gamma+\tau_1}\mathbb{I} + \frac{1}{2}\gamma\left\{\frac{\beta\gamma}{\beta\gamma+\tau_1} - \frac{\alpha\gamma}{\alpha\gamma+\tau_1\tau_2}\right\}\mathbf{I}\otimes\mathbf{I}.$$

A.5 Polarization tensor

$\mathbb{P}$ can be recognized as the Pólya-Szegö polarization tensor, given explicitly by

$$\mathbb{P} = \frac{1}{2}\Delta\mathbb{C}\left\{\mathbb{C}_e^{-1} + \mathbb{C}_i^{-1}\mathbb{T}\right\},$$

where $\Delta\mathbb{C} = \mathbb{C}_i - \mathbb{C}_e$.

$$\mathbb{P} = \frac{1}{2}\Delta\mathbb{C} : \left\{\mathbb{C}_e^{-1} + \mathbb{C}_i^{-1} : \mathbb{T}\right\} = \frac{1}{2}\left\{\mathbb{C}_i - \mathbb{C}_e\right\} : \left\{\mathbb{C}_e^{-1} + \mathbb{C}_i^{-1} : \mathbb{T}\right\}$$
$$= \frac{1}{2}\mathbb{C}_i : \mathbb{C}_e^{-1} + \frac{1}{2}\mathbb{C}_i : \mathbb{C}_i^{-1} : \mathbb{T} - \frac{1}{2}\mathbb{C}_e : \mathbb{C}_e^{-1} - \frac{1}{2}\mathbb{C}_e : \mathbb{C}_i^{-1} : \mathbb{T}$$
$$= \frac{1}{2}\mathbb{C}_i : \mathbb{C}_e^{-1} + \frac{1}{2}\mathbb{T} - \frac{1}{2}\mathbb{I} - \frac{1}{2}\mathbb{C}_e : \mathbb{C}_i^{-1} : \mathbb{T}.$$

We define the Constitutive Tensors $\mathbb{C}_e$ and $\mathbb{C}_i$ as

$$\mathbb{C}_e = 2\mu^e\mathbb{I} + \lambda^e\mathbf{I}\otimes\mathbf{I} = \frac{E^e}{1+\nu^e}\mathbb{I} + \frac{E^e\nu^e}{(1+\nu^e)(1-2\nu^e)}\mathbf{I}\otimes\mathbf{I},$$

$$\begin{aligned}\mathbb{C}_i &= 2\mu^i\mathbb{I} + \lambda^i\mathbf{I}\otimes\mathbf{I} = \frac{E^i}{1+\nu^i}\mathbb{I} + \frac{E^i\nu^i}{(1+\nu^i)(1-2\nu^i)}\mathbf{I}\otimes\mathbf{I}\\ &= \frac{E^e}{1+\nu^e}\frac{\gamma}{\tau_1}\mathbb{I} + \frac{E^e\nu^e}{(1+\nu^e)(1-2\nu^e)}\frac{\gamma\tau_3}{\tau_1\tau_2}\mathbf{I}\otimes\mathbf{I}\\ &= \frac{\gamma}{\tau_1}\left\{\frac{E^e}{1+\nu^e}\mathbb{I} + \frac{\tau_3}{\tau_2}\frac{E^e\nu^e}{(1+\nu^e)(1-2\nu^e)}\mathbf{I}\otimes\mathbf{I}\right\},\end{aligned}$$

where $\gamma = \frac{E^i}{E^e}$ is the jump of stiffness and $\tau_1 = \frac{1+\nu^i}{1+\nu^e}$, $\tau_2 = \frac{1-2\nu^i}{1-2\nu^e}$, $\tau_3 = \frac{\nu^i}{\nu^e}$ are the contrast parameters. Note that, by considering $\nu^e = \nu^i$, the parameters $\tau_i = 1$. And we also define the inverse Constitutive Tensors $\mathbb{C}_e^{-1}$ and $\mathbb{C}_i^{-1}$ as

$$\mathbb{C}_e^{-1} = \frac{1+\nu^e}{E^e}\mathbb{I} - \frac{\nu^e(1+\nu^e)}{E^e}\mathbf{I}\otimes\mathbf{I},$$

$$\begin{aligned}\mathbb{C}_i^{-1} &= \frac{1+\nu^i}{E^i}\mathbb{I} - \frac{\nu^i(1+\nu^i)}{E^i}\mathbf{I}\otimes\mathbf{I}\\ &= \frac{\tau_1}{\gamma}\frac{1+\nu^e}{E^e}\mathbb{I} - \frac{\tau_3\tau_1}{\gamma}\frac{\nu^e(1+\nu^e)}{E^e}\mathbf{I}\otimes\mathbf{I}.\end{aligned}$$

Now we compute

$$\mathbb{C}_i\mathbb{C}_e^{-1} = \frac{\gamma}{\tau_1}\mathbb{I} + \frac{\gamma\nu^e(\tau_3-\tau_2)}{\tau_1\tau_2}\mathbf{I}\otimes\mathbf{I},$$

$$\mathbb{C}_e\mathbb{C}_i^{-1} = \frac{\tau_1}{\gamma}\mathbb{I} + \frac{\nu^e\tau_1(\tau_3-1)}{\gamma(2\nu^e-1)}\mathbf{I}\otimes\mathbf{I}.$$

And the fourth order tensor $\mathbb{S}$ reads as

$$\mathbb{S} = \mathbb{I} - \mathbb{C}_i\mathbb{C}_e^{-1} = \left\{1 - \frac{\gamma}{\tau_1}\right\}\mathbb{I} - \frac{\gamma\nu^e(\tau_3-\tau_2)}{\tau_1\tau_2}\mathbf{I}\otimes\mathbf{I}.$$

Now we can compute tensor $\mathbb{T}$ as

$$\begin{aligned}\mathbb{T} = \mathbb{A} : \mathbb{S} &= \left\{-\frac{\beta\gamma}{\beta\gamma+\tau_1}\mathbb{I} + \frac{1}{2}\gamma\left\{\frac{\beta\gamma}{\beta\gamma+\tau_1} - \frac{\alpha\gamma}{\alpha\gamma+\tau_1\tau_2}\right\}\mathbf{I}\otimes\mathbf{I}\right\}\\ &: \left\{\left\{1-\frac{\gamma}{\tau_1}\right\}\mathbb{I} - \frac{\gamma\nu^e(\tau_3-\tau_2)}{\tau_1\tau_2}\mathbf{I}\otimes\mathbf{I}\right\}.\end{aligned}$$

We end up by computing the Polarization tensor as

$$\mathbb{P} = -\frac{1}{2}(1+\beta)\left\{\frac{\tau_1-\gamma}{\beta\gamma+\tau_1}\mathbb{I} - \frac{1}{4}\left(\frac{\alpha(\gamma-\tau_1\tau_2)}{\alpha\gamma+\tau_1\tau_2} + \frac{2(\tau_1-\gamma)}{\beta\gamma+\tau_1}\right)\mathbf{I}\otimes\mathbf{I}\right\}.$$

A.6 The plane stress case

A similar procedure can be performed to obtain the expression for plane stress scenarios. The only condition to change with respect to the plane strain case is the strain transmission condition. Since we assume an isotropic material behavior, the strain can be related with the stresses for both the matrix and the inclusion through the same inverse constitutive relation

$$\begin{bmatrix}\varepsilon_r\\ \varepsilon_\theta\\ \varepsilon_z\\ \varepsilon_{r\theta}\\ \varepsilon_{rz}\\ \varepsilon_{\theta z}\end{bmatrix} = \frac{1}{E}\begin{bmatrix}1 & -\nu & -\nu & 0 & 0 & 0\\ -\nu & 1 & -\nu & 0 & 0 & 0\\ -\nu & -\nu & 1 & 0 & 0 & 0\\ 0 & 0 & 0 & (1+\nu) & 0 & 0\\ 0 & 0 & 0 & 0 & (1+\nu) & 0\\ 0 & 0 & 0 & 0 & 0 & (1+\nu)\end{bmatrix}\begin{bmatrix}\sigma_r\\ \sigma_\theta\\ \sigma_z\\ \sigma_{r\theta}\\ \sigma_{rz}\\ \sigma_{\theta z}\end{bmatrix}.$$

As $\sigma_{rz} = \sigma_{\theta z} = 0$, then $\varepsilon_{rz} = \varepsilon_{\theta z} = 0$ and rows and columns 5 and 6 can be neglected from the system

$$\begin{bmatrix}\varepsilon_r\\ \varepsilon_\theta\\ \varepsilon_z\\ \varepsilon_{r\theta}\end{bmatrix} = \frac{1}{E}\begin{bmatrix}1 & -\nu & -\nu & 0 & 0 & 0\\ -\nu & 1 & -\nu & 0 & 0 & 0\\ -\nu & -\nu & 1 & 0 & 0 & 0\\ 0 & 0 & 0 & (1+\nu) & 0 & 0\end{bmatrix}\begin{bmatrix}\sigma_r\\ \sigma_\theta\\ \sigma_z\\ \sigma_{r\theta}\end{bmatrix}.$$

In the plane stress assumption, we consider that $\sigma_z = 0$. Therefore,

$$\varepsilon_z = \frac{1}{E}\{-\nu\sigma_r - \nu\sigma_\theta + \sigma_z\} = -\frac{\nu}{E}\{\sigma_r + \sigma_\theta\},$$

$$\varepsilon_r = \frac{1}{E}\{\sigma_r - \nu\sigma_\theta - \nu\sigma_z\} = \frac{1}{E}\{\sigma_r - \nu\sigma_\theta\},$$

$$\varepsilon_\theta = \frac{1}{E}\{\sigma_\theta - \nu\sigma_r - \nu\sigma_z\} = \frac{1}{E}\{\sigma_\theta - \nu\sigma_r\}.$$

Then we obtain for both the matrix and the inclusion,

$$\varepsilon^e_\theta(1,\theta) = \frac{1}{E^e}\left\{\sigma^e_\theta(1,\theta) - \nu^e\sigma^e_r(1,\theta)\right\},$$
$$\varepsilon^i_\theta(1,\theta) = \frac{1}{E^i}\left\{\sigma^i_\theta - \nu^i\sigma^i_r\right\},$$

where E^e, E^i, ν^e and ν^i represents the Young modulus and Poisson ratio for the matrix and the inclusion. Regarding the transmission conditions on strains, we must ensure, in polar coordinates, that the jump across the boundary of the inclusion of the component of the strains must be zero, i.e.,

$$\varepsilon^e_\theta(1,\theta) - \varepsilon^i_\theta = 0 \quad \forall\theta.$$

Inserting the above relation in the transmission condition, we can write the last group of equations as

$$\begin{aligned}
-\frac{1+\nu^e}{E^e}C^e_o - 2\frac{(1-\nu^i)}{E^i}A^i_o = 0 \quad (1),\\
6\frac{1+\nu^e}{E^e}B^e_c + 4\frac{\nu^e}{E^e}D^e_c - 2\frac{1+\nu^i}{E^i}A^i_c = 0 \quad (\cos 2\theta),\\
6\frac{1+\nu^e}{E^e}B^e_s + 4\frac{\nu^e}{E^e}D^e_s - 2\frac{1+\nu^i}{E^i}A^i_s = 0 \quad (\sin 2\theta).
\end{aligned}$$

Changing these equations and following the same procedure as in the plane strain scenario case, we end up with this expression for the Polarization tensor

$$\begin{aligned}
\mathbb{P} = -\frac{1}{2}(1+\beta)\Bigg\{&\frac{\tau_1-\gamma}{\beta\gamma+\tau_1}\mathbb{I}\\
&-\frac{1}{4}\left(\frac{\gamma(\alpha+\tau_2-1)-\alpha\tau_1\tau_2}{\tau_1(\alpha\gamma+\tau_2)} + \frac{2(\tau_1-\gamma)}{\beta\gamma+\tau_1}\right)\mathbf{I}\otimes\mathbf{I}\Bigg\},
\end{aligned}$$

where the parameters are defined as

$$\alpha = \frac{1+\nu_\mathrm{e}}{1-\nu_\mathrm{e}},\ \beta = \frac{3-\nu_\mathrm{e}}{1+\nu_\mathrm{e}},\ \tau_1 = \frac{1+\nu_\mathrm{i}}{1+\nu_\mathrm{e}} \text{ and } \tau_2 = \frac{1-\nu_\mathrm{i}}{1-\nu_\mathrm{e}}.$$

Bibliography

Here are the references in citation order.

[1] G. A. Holzapfel. *Nonlinear Solid Mechanics: A Continuum Approach for Engineering*. John Wiley & Sons, 2000 (cited on pages 7, 21, 36, 51, 56, 59).

[2] A.A.Novotny and J.Sokolowski. *Topological Derivatives in Shape Optimization*. Springer, 2013 (cited on pages 9, 113, 202).

[3] A.A.Novotny et al. "Topological sensitivity analysis." In: *Computer Methods in Applied Mechanics and Engineering* 192.7 (2003), pp. 803–829 (cited on page 9).

[4] A.A.Novotny et al. "Topological sensitivity analysis for three-dimensional linear elasticity problem." In: *Computer Methods in Applied Mechanics and Engineering* 196 (2007), pp. 4354–4364 (cited on page 9).

[5] T. J. Hughes. "Multiscale phenomena : Green's functions, the Dirichlet-to-Neumann formulation, subgrid scale models, bubbles and the origins of stabilized methods." In: *Computer Methods in Applied Mechanics and Engineering* 127.1 (1995), pp. 387–401. DOI: https://doi.org/10.1016/0045-7825(95)00844-9 (cited on page 10).

[6] T. J. R. Hughes et al. "The variational multiscale method - A paradigm for computational mechanics." In: *Computer Methods in Applied Mechanics and Engineering* 166 (1998), pp. 3–24 (cited on pages 10, 28, 52, 67, 92, 114, 159, 171).

[7] T. Richter. *Fluid-structure interactions: models, analysis and finite elements*. Vol. 118. Springer, 2017 (cited on page 10).

[8] T. Belytschko, W. K. Liu, and B. Moran. *Nonlinear Finite Elements for Continua and Structures*. Wiley, 2001 (cited on pages 11, 21, 36, 37, 51, 56, 58).

[9] J. Bonet and R.D. Wood. *Nonlinear Continuum mechanics for finite element analysis*. Cambridge University Press, 1997 (cited on pages 11, 21, 36, 55, 56, 103, 162, 181).

[10] M. Cervera, M. Chiumenti, and R. Codina. "Mixed Stabilized Finite Element Methods in Nonlinear Solid Mechanics. Part I: Formulation." In: *Computer Methods in Applied Mechanics and Engineering* 199.37–40 (2010), pp. 2559–2570 (cited on pages 11, 29, 33, 52, 99, 114, 130).

[11] M. Cervera, M. Chiumenti, and R. Codina. "Mixed Stabilized Finite Element Methods in Nonlinear Solid Mechanics. Part II: Strain Localization." In: *Computer Methods in Applied Mechanics and Engineering* 199.37–40 (2010), pp. 2571–2589 (cited on pages 11, 85, 114, 130).

[12] R.Codina et al. *Variational Multiscale Methods in Computational Fluid Dynamics*. John Wiley & Sons Ltd., 2017 (cited on pages 12, 28, 30, 67, 92).

[13] R. Codina. "Stabilized finite element approximation of transient incompressible flows using orthogonal subscales." In: *Computer Methods in Applied Mechanics and Engineering* 191 (2002), pp. 4295–4321. DOI: https://doi.org/10.1016/S0045-7825(02)00337-7 (cited on pages 12, 52, 114, 159).

[14] E. Castillo and R. Codina. "Variational multi-scale stabilized formulations for the stationary three-field incompressible viscoelastic flow problem." In: *Computer Methods in Applied Mechanics and Engineering* 279 (2014), pp. 579–605 (cited on pages 12, 159, 170–173, 181).

[15] L. Moreno et al. "Logarithmic conformation reformulation in viscoelastic flow problems approximated by a VMS-type stabilized finite element formulation." In: *Computer Methods in Applied Mechanics and Engineering* 354 (2019), pp. 706–731 (cited on pages 12, 97, 158, 159, 166, 170–173, 181, 191).

[16] L. Moreno, R. Codina, and J. Baiges. "Solution of transient viscoelastic flow problems approximated by a term-by-term VMS stabilized finite element formulation using time-dependent subgrid-scales." In: *Computer Methods in Applied Mechanics and Engineering* 367 (2020), p. 113074 (cited on pages 12, 172, 174, 175).

[17] S. Balay et al. *PETSc Web page*. http://www.mcs.anl.gov/petsc. 2015 (cited on pages 20, 72, 98, 130, 181, 213).

[18] U. Ayachit. *The ParaView Guide: A Parallel Visualization Application*. Kitware, 2015 (cited on page 20).

[19] W. Schroeder, K. Martin, and B. Lorensen. *The Visualization Toolkit (4th ed.)*. Kitware, 2006 (cited on page 20).

[20] X.Oliver and C.A. de Saracibar. *Continuum Mechanics for Engineers. Theory and Problems, 2nd edition*. 2017 (cited on pages 21, 113).

[21] C.A. de Saracibar. *Nonlinear Continuum Mechanics. An Engineering Approach, 1st edition*. Springer, 2022 (cited on page 21).

[22] I. Babuška. "Error-Bounds for Finite Element Method." In: *Numerische Mathematik* 16.4 (1971), pp. 322–333 (cited on pages 27, 51, 66, 91).

[23] J. Baiges and R. Codina. "Variational Multiscale error estimators for solid mechanics adaptive simulations: an Orthogonal Subgrid Scale approach." In: *Computer Methods in Applied Mechanics and Engineering* 325 (2017), pp. 37–55 (cited on pages 29, 52, 53, 202).

[24] R. Codina. "A stabilized finite element method for generalized stationary incompressible flows." In: *Computer Methods in Applied Mechanics and Engineering* 190 (2001), pp. 2681–2706 (cited on pages 29, 52, 113, 114, 173).

[25] R. Codina. "Stabilization of incompressibility and convection through orthogonal sub-scales in finite element methods." In: *Computer Methods in Applied Mechanics and Engineering* 190 (2000), pp. 1579–1599 (cited on pages 29, 71, 114, 159, 175).

[26] R.Codina. "Finite element approximation of the three field formulation of the Stokes problem using arbitrary interpolations." In: *SIAM Journal on Numerical Analysis* 47 (2009), pp. 699–718 (cited on pages 30, 47, 114, 115, 130).

[27] M. Chiumenti, M. Cervera, and R. Codina. "A mixed three-field FE formulation for stress accurate analysis including the incompressible limit." In: *Computer Methods in Applied Mechanics and Engineering* 283 (2015), pp. 1095–1116 (cited on pages 30, 52, 53, 69, 87, 94, 114, 115, 202).

[28] M. Chiumenti et al. "Stress, strain and dissipation accurate 3-field formulation for inelastic isochoric deformation." In: *Finite Elements in Analysis and Design* 192 (2021), p. 103534 (cited on pages 30, 33, 85, 130, 202).

[29] K.B. Sautter et al. "Limitations of the St. Venant–Kirchhoff material model in large strain regimes." In: *International Journal of Non-Linear Mechanics* 147 (2022), p. 104207 (cited on page 36).

[30] T. Belytschko and D. F. Schoeberle. "On the Unconditional Stability of an Implicit Algorithm for Nonlinear Structural Dynamics." In: *Journal of Applied Mechanics* 42.4 (1975), pp. 865–869 (cited on page 38).

[31] J. C. Simo, N. Tarnow, and K. K. Wong. "Exact energy-momentum conserving algorithms and symplectic schemes for nonlinear dynamics." In: *Computer Methods in Applied Mechanics and Engineering* 100.1 (1992), pp. 63–116 (cited on page 38).

[32] O. Gonzalez. "Exact energy and momentum conserving algorithms for general models in nonlinear elasticity." In: *Computer Methods in Applied Mechanics and Engineering* 190 (2000), pp. 1763–1783 (cited on page 38).

[33] P. Betsch and A. Janz. "An energy–momentum consistent method for transient simulations with mixed finite elements developed in the framework of geometrically exact shells." In: *International Journal of Numerical Methods in Engineering* 108.5 (2016), pp. 423–455 (cited on page 38).

[34] D. Magisano, L. Leonetti, and G. Garcea. "Unconditional stability in large deformation dynamic analysis of elastic structures with arbitrary nonlinear strain measure and multi-body coupling." In: *Computer Methods in Applied Mechanics and Engineering* 393 (2022), p. 114776 (cited on page 38).

[35] L. D. Landau and E. M. Lifshitz. *Fluid Mechanics*. Second Ed. Vol. 6. Course of Theoretical Physics. Pergamon, 1987 (cited on page 41).

[36] R. Aris. *Vectors, Tensors and the Basic Equations of Fluid Mechanics*. Dover Publications Inc., 1989 (cited on page 41).

[37] G. K. Batchelor. *An Introduction to Fluid Dynamics*. Cambridge Mathematical Library. Cambridge University Press, 2000 (cited on page 41).

[38] R. Codina et al. "Variational Multiscale Methods in Computational Fluid Dynamics." In: *Encyclopedia of Computational Mechanics, Second Edition* (2018), pp. 1–28. DOI: https://doi.org/10.1002/9781119176817.ecm2117 (cited on pages 46, 172).

[39] E. Castillo and R. Codina. "Stabilized stress-velocity-pressure finite element formulations of the Navier-Stokes problem for fluids with non-linear viscosity." In: *Computer Methods in Applied Mechanics and Engineering* 279 (2014), pp. 554–578. DOI: 10.1016/j.cma.2014.07.003 (cited on pages 46, 50, 191).

[40] G. A. Holzapfel. "Biomechanics of soft tissue." In: *The Handbook of Materials Behavior* 3 (2001), pp. 1049–1063 (cited on pages 51, 85).

[41] T.J.R.Hughes. *The Finite Element Method: Linear Static and Dynamic Finite Element Analysis*. Prentice-Hall,Englewood Cliffs, New Jersey, 1987 (cited on pages 51, 113, 114).

[42] D. S. Malkus and T. J. R. Hughes. "Mixed finite element methods - Reduced and selective integration techniques: A unification of concepts." In: *Computer Methods in Applied Mechanics and Engineering* 15 (1978), pp. 63–81 (cited on page 51).

[43] T. Elguedj et al. "$\bar{B}$ and $\bar{F}$ projection methods for nearly incompressible linear and nonlinear elasticity and plasticity using higher-order NURBS elements." In: *Computer Methods in Applied Mechanics and Engineering* 197 (2008), pp. 2732–2762 (cited on page 51).

[44] T. J. R. Hughes, L. P. Franca, and M. Balestra. "A new finite element formulation for computational fluid dynamics: V. Circumventing the babuška-brezzi condition: a stable Petrov-Galerkin formulation of the stokes problem accommodating equal-order interpolations." In: *Computer Methods in Applied Mechanics and Engineering* 59 (1986), pp. 85–99 (cited on pages 52, 113, 114).

[45] L. P. Franca et al. "A new family of stable elements for nearly incompressible elasticity based on a mixed Petrov-Galerkin finite element formulation." In: *Numerische Mathematik* 53.1–2 (1988), pp. 123–141 (cited on pages 52, 114).

[46] R. Codina. "Finite element approximation of the three field formulation of the Stokes problem using arbitrary interpolations." In: *SIAM Journal on Numerical Analysis* 47 (2009), pp. 699–718 (cited on pages 52, 92, 99, 171).

[47] S. Badia and R. Codina. "Unified stabilized finite element formulations for the Stokes and the Darcy problems." In: *SIAM Journal on Numerical Analysis* 47.3 (2009), pp. 1971–2000 (cited on pages 52, 70).

[48] M. Chiumenti et al. "A stabilized formulation for incompressible elasticity using linear displacement and pressure interpolations." In: *Computer Methods in Applied Mechanics and Engineering* 191 (2002), pp. 1095–1116 (cited on pages 52, 53, 74, 114).

[49] R. Codina and O. Turk. "Modal analysis of elastic vibrations of incompressible materials using a pressure-stabilized finite element method." In: *Finite Elements in Analysis and Design* 206 (2022), p. 103760 (cited on pages 52, 53).

[50] R. Rossi, R. Zorrilla, and R. Codina. "A stabilized displacement-volumetric strain formulation for nearly incompressible and anisotropic materials." In: *Computer Methods in Applied Mechanics and Engineering* 377 (2021), p. 113701 (cited on pages 52, 53).

[51] J. Bonet and A. J. Burton. "A simple average nodal pressure tetrahedral element for incompressible and nearly incompressible dynamic explicit applications." In: *Computer Methods in Applied Mechanics and Engineering* 1.4 (1998), pp. 437–449 (cited on page 53).

[52] C. H. Lee, A. J. Gil, and J. Bonet. "Development of a cell centred upwind finite volume algorithm for a new conservation law formulation in structural dynamics." In: *Computers and Structures* 118 (2013), pp. 13–38 (cited on page 53).

[53] M. Aguirre et al. "A vertex centred finite volume Jameson-Schmidt-Turkel (JST) algorithm for a mixed conservation formulation in solid dynamics." In: *Journal of Computational Physics* 259 (2014), pp. 672–699 (cited on page 53).

[54] C. H. Lee J. Haider, A. J. Gil, and J. Bonet. "A first-order hyperbolic framework for large strain computational solid dynamics. An upwind cell centred Total Lagrangian scheme." In: *International Journal for Numerical Methods in Engineering* 109 (2017), pp. 407–456 (cited on page 53).

[55] C.H. Lee, A. J. Gil, and J. Bonet. "Development of a stabilised Petrov-Galerkin formulation for linear tetrahedral elements in compressible, nearly incompressible and truly incompressible fast dynamics." In: *Computer Methods in Applied Mechanics and Engineering* 268 (2014), pp. 40–64 (cited on pages 53, 54).

[56] C.H. Lee et al. "A stabilised Petrov-Galerkin formulation for linear tetrahedral elements in compressible, nearly incompressible and truly incompressiblefast dynamics." In: *Computer Methods in Applied Mechanics and Engineering* 276 (2014), pp. 659–690 (cited on pages 53, 54).

[57] M. Aguirre et al. "An upwind vertex centred finite volume solver for Lagrangian solid dynamics." In: *Journal of Computational Physics* 300 (2015), pp. 387–422 (cited on pages 53, 54).

[58] J. Bonet et al. "A first order hyperbolic framework for large strain computational solid dynamics. Part I : Total Lagrangian isothermal elasticity." In: *Computer Methods in Applied Mechanics and Engineering* 283 (2015), pp. 689–732 (cited on pages 53, 54, 72, 80, 97).

[59] A. J. Gil et al. "A first order hyperbolic framework for large strain computational solid dynamics. Part II : Total Lagrangian compressible, nearly incompressible and truly incompressible elasticity." In: *Computer Methods in Applied Mechanics and Engineering* 300 (2016), pp. 146–181 (cited on pages 53, 54, 72, 80, 97).

[60] O. I. Hassan et al. "An upwind vertex centred finite volume algorithm for nearly and truly incompressible explicit fast solid dynamic applications: Total and Updated Lagrangian formulations." In: *Journal of Computational Physics : X* 3 (2019), p. 100025 (cited on pages 53, 54).

[61] G. Scovazzi et al. "A simple, stable, and accurate linear tetrahedral finite element for transient, nearly, and fully incompressible solid dynamics: a dynamic variational multiscale approach." In: *International Journal For Numerical Methods in Engineering* 106 (2016), pp. 799–839 (cited on pages 53, 54, 58, 72, 74, 78, 80, 83, 97, 102).

[62] S. Rossi, N. Abboud, and G. Scovazzi. "Implicit finite incompressible elastodynamics with linear finite elements: A stabilized method in rate form." In: *Computer Methods in Applied Mechanics and Engineering* 311 (2016), pp. 208–249 (cited on pages 53, 54, 60, 72, 74, 78, 80, 97).

[63] R. Nemer et al. “Stabilized finite element method for incompressible solid dynamics using an updated Lagrangian formulation.” In: *Computer Methods in Applied Mechanics and Engineering* 384 (2021), p. 113923 (cited on pages 53, 54).

[64] W. Boscheri, R. Loubère, and P. Maire. “A 3D cell-centered ADER MOOD Finite Volume method for solving updated Lagrangian hyperelasticity on unstructured grids.” In: *Journal of Computational Physics* 449 (2022), p. 110779 (cited on pages 53, 55).

[65] C. O. Horgan and J. G. Murphy. “On the volumetric part of strain-energy functions used in the constitutive modeling of slightly compressible solid rubbers.” In: *International Journal of Solids and Structures* 46 (2009), pp. 3028–3085 (cited on page 58).

[66] J.C. Simo, R.L. Taylor, and K.S. Pister. “Variational and projection methods for the volume constraint in finite deformation elasto-plasticity.” In: *Computer Methods in Applied Mechanics and Engineering* 51.1–3 (1985), pp. 177–208 (cited on page 58).

[67] C. Miehe. “Aspects of the formulation and finite element implementation of large strain isotropic elasticity.” In: *International Journal for Numerical Methods in Engineering* 12 (1994), pp. 1981–2004 (cited on page 59).

[68] C. H. Liu, G. Hofstetter, and H. A. Mang. “3D finite element analysis of rubber-like materials at finite strains.” In: *Engineering Computations* 11.2 (1994), pp. 111–128 (cited on page 59).

[69] C. Sansour. “On the physical assumptions underlying the volumetric-isochoric split and the case of anisotropy.” In: *European Journal of Mechanics A/Solids* 27 (2008), pp. 28–39 (cited on page 61).

[70] R. Codina et al. “Finite element approximation of the modified Boussinesq equations using a stabilized formulation.” In: *International Journal For Numerical Methods in Engineering* 57 (2008), pp. 1249–1268 (cited on page 70).

[71] H. A. Van der Vorst. “Bi-CGSTAB: A fast and smoothly converging variant of Bi-CG for the solution of nonsymmetric linear systems.” In: *SIAM, Journal of Scientific and Statistical Computing* 13.2 (1992), pp. 631–644. DOI: https://doi.org/10.1137/0913035 (cited on pages 72, 98, 181, 213).

[72] J. Chung and G. M. Hulbert. “A Time Integration Algorithm for Structural Dynamics with improved numerical dissipation: The Generalized-α Method.” In: *Journal of Applied Mechanics* 60.2 (1993), pp. 371–375 (cited on page 78).

[73] C.A. Moreira et al. “Accurate thermal-induced structural failure analysis under incompressible conditions.” In: *Engineering Structures* 261 (2022), p. 114213 (cited on page 85).

[74] N. Dialami, M. Chiumenti, and M. Cervera. “Defect Formation and Material Flow in Friction Stir Welding.” In: *European Journal of Mechanics A / Solids* 80 (2020), p. 103912 (cited on page 85).

[75] M. Cervera et al. “A Comparative Review of XFEM, Mixed FEM and Phase-Field Models for Quasi-brittle Cracking.” In: *Archives of Computational Methods in Engineering* 29 (2022), pp. 1009–1083 (cited on pages 85, 234).

[76] P. E. Farrell et al. “Mixed Kirchhoff stress-displacement-pressure formulations for incompressible hyperelasticity.” In: *Computer Methods in Applied Mechanics and Engineering* 374 (2021), p. 113562 (cited on page 85).

[77] R. Ruiz-Baier et al. “Thermo-electric effects in an anisotropic active-strain electromechanical model.” In: *Communications in Computational Physics* 27.1 (2020), pp. 87–115 (cited on page 85).

[78] A. Propp et al. “An orthotropic electro-viscoelastic model for the heart with stress-assisted diffusion.” In: *Biomechanics and Modeling in Mechanobiology* 19.2 (2020), pp. 633–659 (cited on page 85).

[79] M.P.Bendsøe and O.Sigmund. *Topological Optimization: Theory.* Springer, 2013 (cited on pages 113, 202, 203).

[80] M.P.Bendsøe and N.Kikuchi. “Generating optimal topologies in structural design using a homogenization method.” In: *Computer Methods in Applied Mechanics and Engineering* 71.2 (1988), pp. 197–224 (cited on pages 113, 202, 203).

[81] R. Ortigosa et al. “A stabilisation approach for topology optimisation of hyperelastic structures with the SIMP method.” In: *Computer Methods in Applied Mechanics and Engineering* 364 (2020), p. 112924 (cited on pages 113, 235).

[82] X.Huang and Y.Xie. “A further review of ESO type methods for topology optimization.” In: *Structural and Multidisciplinary Optimization* 41 (2010), pp. 671–683 (cited on pages 113, 202, 203).

[83] N.P. van Dijk et al. “Level-set methods for structural topology optimization: a review.” In: *Structural and Multidisciplinary Optimization* 48 (2013), pp. 437–472 (cited on pages 113, 202, 203).

[84] J.D.Deaton and R.V.Grandhi. “A survey of structural and multidisciplinary continuum topology optimization: post 2000.” In: *Structural and Multidisciplinary Optimization* 49 (2014), pp. 1–38 (cited on pages 113, 202, 203).

[85] R. Ortigosa et al. “A new stabilisation approach for level-set based topology optimisation of hyperelastic materials.” In: *Structural and Multidisciplinary Optimization* 60 (2019), pp. 2343–2371 (cited on pages 113, 235).

[86] S. Amstutz and H. Andrä. “A new algorithm for topology optimization using a level-set method.” In: *Journal of computational physics* 216.2 (2006), pp. 573–588 (cited on pages 113, 124).

[87] J.Baiges et al. “Large-scale stochastic topology optimization using adaptive mesh refinement and coarsening through a two-level parallelization scheme.” In: *Computer Methods in Applied Mechanics and Engineering* 343 (2019), pp. 186–206 (cited on pages 113, 119, 125, 127).

[88] A.A.Novotny, J.Sokolowski, and A.Zochowski. “Topological Derivatives of Shape Functionals. Part I: Theory in Singularly Perturbed Geometrical Domains.” In: *Journal of Optimization Theory and Applications* 180 (2019), pp. 341–373 (cited on pages 113, 117, 202).

[89] J.Oliver et al. "Variational approach to relaxed topological optimization: Closed form solutions for structural problems in a sequential pseudo-time framework." In: *Computer Methods in Applied Mechanics and Engineering* 355 (2019), pp. 779–819 (cited on page 113).

[90] L.R.G.Treloar. *The Physics of Rubber Elasticity*. Oxford, NY: Oxford University Press, 1975 (cited on pages 113, 201).

[91] I. Castañar, J. Baiges, and R. Codina. "A stabilized mixed finite element approximation for incompressible finite strain solid dynamics using a total Lagrangian formulation." In: *Computer Methods in Applied Mechanics and Engineering* 368 (2020), p. 113164 (cited on pages 114, 202).

[92] O.Sigmund and P.M.Clausen. "Topology optimization using a mixed formulation: An alternative way to solve pressure load problems." In: *Computer Methods in Applied Mechanics and Engineering* 196 (2007), pp. 1874–1889 (cited on pages 114, 115, 202, 203).

[93] M.Bruggi and P.Venini. "Topology optimization of incompressible media using mixed finite elements." In: *Computer Methods in Applied Mechanics and Engineering* 196 (2007), pp. 3151–3164 (cited on pages 114, 115, 134).

[94] M.Stolpe and K.Svanberg. "An alternative interpolation scheme for minimum compliance optimization." In: *Structural and Multidisciplinary Optimization* 22.2 (2001), pp. 116–124 (cited on pages 114, 115).

[95] K.Svanberg. "The method of moving asymptotes-a new method for minimum compliance optimization." In: *International Journal For Numerical Methods in Engineering* 24 (1987), pp. 359–373 (cited on pages 114, 115).

[96] C.Li and L.Tong. "Topology optimization of incompressible materials based on the mixed SBFEM." In: *Computers and Structures* 165 (2016), pp. 24–33 (cited on pages 114, 115).

[97] G.Zhang, R.Alberdi, and K.Khandelwal. "Topology optimization with incompressible materials under small and finite deformations using mixed u/p elements." In: *International Journal For Numerical Methods in Engineering* 115 (2018), pp. 1015–1052 (cited on pages 114, 115).

[98] A.A.Novotny, J.Sokolowski, and A.Zochowski. "Topological Derivatives of Shape Functionals. Part II: First-Order Method and Applications." In: *Journal of Optimization Theory and Applications* 180 (2019), pp. 683–710 (cited on pages 114, 115, 117).

[99] A.Ferrer. "SIMP-ALL: A generalized SIMP method based on the topological derivative concept." In: *International Journal For Numerical Methods in Engineering* 120.3 (2019), pp. 361–381 (cited on page 117).

[100] M.P.Bendsøe and O.Sigmund. "Material interpolation schemes in topology optimization." In: *Archive of Applied Mechanics* 69 (1999), pp. 635–654 (cited on page 117).

[101] S.M.Giusti, A.Ferrer, and J. Oliver. "Topological sensitivity analysis in heterogeneous anisotropic elasticity problem. Theoretical and computational aspects." In: *Computer Methods in Applied Mechanics and Engineering* 311 (2016), pp. 134–150 (cited on page 118).

[102] J.D.Eshelby. "The determination of the elastic field of an ellipsoidal inclusion, and related problems." In: *Proceedings of the Royal Society: Section A* 241 (1957), pp. 376–396 (cited on page 118).

[103] J.D.Eshelby. "The elastic field outside an ellipsoidal inclusion, and related problems." In: *Proceedings of the Royal Society: Section A* 252 (1959), pp. 561–569 (cited on page 118).

[104] C.G.Lopes, R.Batista dos Santos, and A.A.Novotny. "Topological Derivative-based Topology Optimization of Structures Subject to Multiple Load-cases." In: *Latin American Journal of Solids and Structures* 12 (2015), pp. 834–860 (cited on pages 119, 142).

[105] S. Amstutz, C. Dapogny, and A. Ferrer. "A consistent relaxation of optimal design problems for coupling shape and topological derivatives." In: *Numerische mathematik,* 140.1 (2018), pp. 35–94 (cited on page 121).

[106] S.Amstutz et al. "Topological derivative for multi-scale linear elasticity models applied to the synthesis of microstructures." In: *International Journal for Numerical Methods in Engineering* 84.6 (2010), pp. 733–756 (cited on page 124).

[107] M. Kishida, T. Kurahashi, and J. Baiges. "Application of a weighted sensitivity approach for topology optimization analysis of time dependent problems based on the density method." In: *Japan Society for Industrial and Applied Mathematics Letters* 13 (2021), pp. 68–71 (cited on page 129).

[108] P.R.Amestoy et al. "A Fully Asynchronous Multifrontal Solver Using Distributed Dynamic Scheduling." In: *SIAM Journal on Matrix Analysis and Applications* 23.1 (2001), pp. 15–41 (cited on page 130).

[109] P.R.Amestoy et al. "Performance and Scalability of the Block Low-Rank Multifrontal Factorization on Multicore Architectures." In: *ACM Transactions on Mathematical Software* 45 (1 2019), 2:1–2:26 (cited on page 130).

[110] C.E.L.Pereira and M.L.Bittencourt. "Topological sensitivity analysis in large deformation problems." In: *Structural and Multidisciplinary Optimization* 37 (2008), pp. 149–163 (cited on page 144).

[111] C.E.L.Pereira and M.L.Bittencourt. "Topological sensitivity analysis for a two-parameter Mooney-Rivlin hyperelastic constitutive model." In: *Latin American Journal of Solids and Structures* 7 (2010), pp. 391–411 (cited on page 144).

[112] R. Kamakoti and W. Shyy. "Fluid-structure interaction for aeroelastic applications." In: *Progress in Aerospace Sciences* 40 (2004), pp. 535–558 (cited on pages 157, 201).

[113] T. Bodnár, G. P. Galdi, and S. Nečasová. *Fluid-Structure Interactions and Biomedical Applications.* ISBN 978-3-0348-0821-7. Springer, 2014 (cited on pages 157, 201).

[114] U. Küttler and W. A. Wall. "Fixed-point fluid–structure interaction solvers with dynamic relaxation." In: *Computational Mechanics* 43.1 (2008), pp. 61–72 (cited on pages 157, 178, 201).

[115] T. Richter and T. Wick. "Finite Elements for Fluid-Structure Interaction in ALE and Fully Eulerian coordinates." In: *Computer Methods in Applied Mechanics and Engineering* 199 (2010), pp. 2633–2642 (cited on pages 157, 201).

[116] T. Richter. *Fluid-Structure Interactions*. ISBN 978-3-31-963970-7. Springer, 2017 (cited on pages 157, 201).

[117] K. Ueda, H. Kanai, and Ta. Amari. "Viscoelastic properties of paint films and formability in deep drawing of pre-painted steel sheets." In: *Progress in Organic Coatings* 45.1 (2002), pp. 15–21 (cited on page 157).

[118] R. P. Chhabra and J. F. Richardson. *Non-Newtonian flow and applied rheology: engineering applications*. Butterworth-Heinemann, 2011 (cited on page 157).

[119] E. Castillo et al. "Stabilised Variational Multi-scale Finite Element Formulations for Viscoelastic Fluids." In: *Archives of Computational Methods in Engineering* 296 (2021), pp. 1987–2019. DOI: https://doi.org/10.1007/s11831-020-09526-x (cited on page 157).

[120] M. Bathe and R.D. Kamm. "A fluid-structure interaction finite element analysis of pulsatile blood flow through a compliant stenotic artery." In: *Journal of Biomechanical Engineering* 121.4 (1999), pp. 361–369 (cited on page 157).

[121] X. Ma, G.C. Lee, and S.G. Wu. "Numerical simulation for the propagation of nonlinear pulsatile waves in arteries." In: *Journal of Biomechanical Engineering* 114 (1992), pp. 490–496 (cited on page 157).

[122] K. Perktold and G. Rappitsch. "Computer simulation of local blood flow and vessel mechanics in a compliant carotid artery bifurcation model." In: *Journal of Biomechanics* 28.7 (1995), pp. 845–856 (cited on page 157).

[123] D. Tang et al. "A nonlinear axisymmetric model with fluid–wall interactions for steady viscous flow in stenotic elastic tubes." In: *Journal of Biomechanics* 121 (1999), pp. 494–501 (cited on page 157).

[124] T. M. Squires and S. R. Quake. "Microfluidics: Fluid physics at the nanoliter scale." In: *Reviews of Modern Physics* 77.3 (2005), p. 977 (cited on page 157).

[125] A. Groisman, M. Enzelberger, and S.R. Quake. "Microfluidic memory and control devices." In: *Science* 300.5621 (2003), pp. 955–958 (cited on page 157).

[126] A. Amani et al. "A method for fluid-structure interaction problems with non-Newtonian fluid." In: *Proceedings of the 6th European Conference on Computational Mechanics (Solids, Structures and Coupled Problems) and the 7th European Conference on Computational Fluid Dynamics, Glasgow, UK*. 2018, pp. 101–110 (cited on page 157).

[127] R. Fattal and R. Kupferman. "Time-dependent simulation of viscoelastic flows at high Weissenberg number using the log-conformation representation." In: *Journal of Non-Newtonian Fluid Mechanics* 126.1 (2005), pp. 23–37 (cited on pages 157, 158).

[128] A.I. Leonov. "Analysis of simple constitutive equations for viscoelastic liquids." In: *Journal of Non-Newtonian Fluid Mechanics* 42.3 (1992), pp. 323–350 (cited on page 158).

[129] Y. Kwon. "Recent results on the analysis of viscoelastic constitutive equations." In: *Korea-Australia Rheology Journal* 14.1 (2002), pp. 33–45 (cited on page 158).

[130] R. G. Owens and T. N. Phillips. *Computational rheology*. Vol. 14. World Scientific, 2002 (cited on page 158).

[131] R. Fattal and R. Kupferman. "Constitutive laws for the matrix-logarithm of the conformation tensor." In: *Journal of Non-Newtonian Fluid Mechanics* 123.2-3 (2004), pp. 281–285 (cited on page 158).

[132] M.A. Hulsen, A.P.G. Van Heel, and B.H.A.A. Van Den Brule. "Simulation of viscoelastic flows using Brownian configuration fields." In: *Journal of Non-Newtonian Fluid Mechanics* 70.1-2 (1997), pp. 79–101 (cited on page 158).

[133] D. Chakraborty and J. R. Prakash. "Viscoelastic fluid flow in a 2D channel bounded above by a deformable finite thickness elastic wall." In: *Computers and Structures* 218 (2007), pp. 83–98 (cited on page 159).

[134] X. Luo et al. "On the initial configurations of collapsible channel flow." In: *Computers and Structures* 85 (2007), pp. 977–987 (cited on pages 159, 184).

[135] X. Chen. "Numerical Modeling of Fluid-Structure Interaction with Rheologically Complex Fluids." PhD thesis. Technische Universität Darmstadt, 2014 (cited on pages 159, 182, 184–186).

[136] R. Codina. "Analysis of a stabilized finite element approximation of the Oseen equations using orthogonal subscales." In: *Applied Numerical Mathematics* 58 (2008), pp. 264–283. DOI: https://doi.org/10.1016/j.apnum.2006.11.011 (cited on pages 159, 175).

[137] G. Chiandussi, G. Bugeda, and E. Oñate. "A simple method for automatic update of finite element meshes." In: *Communications in Numerical Methods in Engineering* 16 (1999), pp. 1–19 (cited on pages 164, 180, 207).

[138] S. Badia and R. Codina. "On a multiscale approach to the transient Stokes problem. Transient subscales and anisotropic space-time discretization." In: *Applied Mathematics and Computation* 207 (2009), pp. 415–433 (cited on page 172).

[139] R. Codina et al. "Time dependent subscales in the stabilized finite element approximation of incompressible flow problems." In: *Computer Methods in Applied Mechanics and Engineering* 196 (2007), pp. 2413–2430. DOI: https://doi.org/10.1016/j.cma.2007.01.002 (cited on page 172).

[140] R. Codina, E. Oñate, and M. Cervera. "The intrinsic time for the streamline upwind/Petrov-Galerkin formulation using quadratic elements." In: *Computer Methods in Applied Mechanics and Engineering* 94.2 (1992), pp. 239–262 (cited on page 174).

[141] A.E.J. Bogaers et al. "Quasi-Newton methods for implicit black-box FSI coupling." In: *Computer Methods in Applied Mechanics and Engineering* 279 (2014), pp. 113–132 (cited on page 178).

[142] R. Haelterman et al. "Improving the performance of the partitioned QN-ILS procedure for fluid–structure interaction problems: Filtering." In: *Computers and Structures* 171 (2016), pp. 9–17 (cited on page 178).

[143] R. Zorrilla and R. Rossi. "A memory-efficient MultiVector Quasi-Newton method for black-box Fluid-Structure Interaction coupling." In: *Computers and Structures* 275 (2023), p. 106934 (cited on page 178).

[144] A. Abas and R. Abdul-Rahman. "Adaptive FEM with Domain Decomposition Method for Partitioned-Based Fluid–Structure Interaction." In: *Arabian Journal for Science and Engineering* 41 (2016), pp. 611–622 (cited on page 178).

[145] E. Burman, M. A. Fernández, and S. Frei. "A Nitsche-based formulation for fluid-structure interactions with contact." In: *ESAIM: Mathematical Modelling and Numerical Analysis* 54.2 (2020), pp. 531–564 (cited on page 178).

[146] S. Turek and J. Hron. "Proposal for numerical benchmarking of fluid-structure interaction between an elastic object and laminar incompressible flow." In: *Fluid–structure interaction. Lecture Notes on Computational Science and Engineering* (2007), pp. 371–385 (cited on pages 181, 188–190, 220).

[147] X.Y. Luo and T.J. Pedley. "A numerical simulation of steady flow in a 2-D collapsible channel." In: *Journal of Fluids and Structures* 9.2 (1995), pp. 149–174 (cited on page 181).

[148] X.Y. Luo and T.J. Pedley. "A numerical simulation of unsteady flow in a two-dimensional collapsible channel." In: *Journal of Fluid Mechanics* 314 (1996), pp. 191–225 (cited on page 181).

[149] M. Lukáčová-Medviďová and A. Zaušková. "Numerical modelling of shear-thinning non-Newtonian flows in compliant vessels." In: *International Journal for Numerical Methods in Fluids* 56.8 (2008), pp. 1409–1415 (cited on page 181).

[150] M. Lukáčová-Medviďová, G. Rusnáková, and A. Hundertmark-Zaušková. "Kinematic splitting algorithm for fluid–structure interaction in hemodynamics." In: *Computer Methods in Applied Mechanics and Engineering* 265 (2013), pp. 83–106 (cited on page 181).

[151] D. Chakraborty et al. "Fluid-structure interaction in deformable microchannels." In: *Physics of Fluids* 24.10 (2012), p. 102002 (cited on page 182).

[152] Z.X. Cai and X.Y. Luo. "A fluid–beam model for flow in a collapsible channel." In: *Journal of Fluids and Structures* 17.1 (2003), pp. 125–146 (cited on page 182).

[153] H. Gharabi et al. "Computational fluid dynamic simulation of human carotid artery bifurcation based on anatomy and volumetric blood flow rate measured with magnetic resonance imaging." In: *International Journal of Advances in Engineering Sciences and Applied Mathematics* 8.1 (2016), pp. 40–60 (cited on page 193).

[154] G. Siasos et al. "Local low shear stress and endothelial dysfunction in patiens with nonobstructive coronary atherosclerosis." In: *Journal of the American College of Cardiology* 71.19 (2018), pp. 2092–2102 (cited on page 193).

[155] G. Zaman et al. "Blood flow of an Oldroyd-B fluid in a blood vessel incorporating a Brownian stress." In: *Science China Physics, Mechanics and Astronomy* 55.1 (2012), pp. 125–131 (cited on page 193).

[156] M. Anand, J. Kwack, and A. Masud. "A new generalized Oldroyd-B model for blood flow in complex geometries." In: *International Journal of Engineering Science* 72 (2013), pp. 78–88 (cited on page 193).

[157] A. Elhanafy, A. Guaily, and A. Elsaid. "Numerical simulation of Oldroyd-B fluid with application to hemodynamics." In: *Advances in Mechanical Engineering* 11.5 (2019), p. 1687814019852844 (cited on pages 194, 196, 197).

[158] D. Lopes et al. “Influence of arterial mechanical properties on carotid blood flow: Comparison of CFD and FSI studies.” In: *International Journal of Mechanical Sciences* 160 (2019), pp. 209–218 (cited on pages 194, 196).

[159] P.B. Rhyzhakov and E. Oñate. “A finite element model for fluid–structure interaction problems involving closed membranes, internal and external fluids.” In: *Computer Methods in Applied Mechanics and Engineering* 326 (2017), pp. 422–445 (cited on page 201).

[160] P. Rhyzhakov, E. Soudah, and N. Dialami. “Computational modeling of the fluid flow and the flexible intimal flap in type B aortic dissection via a monolithic arbitrary Lagrangian/Eulerian fluid-structure interaction model.” In: *International Journal of Numerical Methods in Biomedical Engineering* 35 (11 2019), e3239 (cited on page 201).

[161] J. Yan et al. “Computational free-surface fluid–structure interaction with application to floating offshore wind turbines.” In: *Computer and Fluids* 141 (2016), pp. 155–174 (cited on page 201).

[162] P.B. Rhyzhakov et al. “A monolithic Lagrangian approach for fluid–structure interaction problems.” In: *Computational Mechanics* 46 (2010), pp. 883–899 (cited on page 201).

[163] L. Moreno et al. “Numerical simulation of Fluid–Structure Interaction problems with viscoelastic fluids using a log-conformation reformulation.” In: *Computer Methods in Applied Mechanics and Engineering* 410 (2023), p. 115986 (cited on page 201).

[164] E. Comellas, F.J. Bellomo, and S. Oller. “A generalized finite-strain damage model for quasi-incompressible hyperelasticity using hybrid formulation.” In: *International Journal for Numerical Methods in Engineering* 105 (10 2016), pp. 781–800 (cited on page 201).

[165] J. Martínez-Frutos, R. Ortigosa, and A.J. Gil. “In-silico design of electrode meso-architecture for shape morphing dielectric elastomers.” In: *Journal of the Mechanics and Physics of Solids* 157 (2021), p. 104594 (cited on page 201).

[166] C. Wex et al. “Isotropic incompressible hyperelastic models for modelling the mechanical behaviour of biological tissues: a review.” In: *Biomedical Engineering* 60 (6 2015), pp. 577–592 (cited on pages 201, 202).

[167] E. Comellas et al. “A homeostatic-driven turnover remodelling constitutive model for healing in soft tissues.” In: *Journal of the Royal Society Interface* 13 (116 2016), p. 20151081 (cited on pages 201, 202).

[168] E. Comellas et al. “Modeling the porous and viscous responses of human brain tissue behavior.” In: *Computer Methods in Applied Mechanics and Engineering* 369 (2020), p. 113128 (cited on pages 201, 202).

[169] I. Castañar, R. Codina, and J. Baiges. “A stabilized mixed three-field formulation for stress accurate analysis including the incompressible limit in finite strain solid dynamics.” In: *International Journal for Numerical Methods in Engineering* 124.10 (2023), pp. 2341–2366 (cited on page 202).

[170] Y. Deng, Z. Liu, and Y. Wu. "Topology optimization of steady and unsteady incompressible Navier-Stokes flows driven by body forces." In: *Structural and Multidisciplinary Optimization* 47.4 (2013), pp. 555–570 (cited on pages 202, 203).

[171] L. Shu, M. Y. Wang, and Z. Ma. "Level set based topology optimization of vibrating structures for coupled acoustic-structural dynamics." In: *Computers and Structures* 132 (2014), pp. 34–42 (cited on pages 202, 203).

[172] X. Wang et al. "Topological design and additive manufacturing of porous metals for bone scaffols and orthopaedic implants: a review." In: *Biomaterials* 83 (2016), pp. 127–141 (cited on pages 202, 203).

[173] C. S. Andreasen and O. Sigmund. "Topology optimization of fluid-structure-interaction problems in poroelasticity." In: *Computer Methods in Applied Mechanics and Engineering* 258 (2013), pp. 55–62 (cited on pages 202, 203).

[174] N. Jenkins and K. Maute. "Level set topology optimization of stationary fluid-structure interaction problems." In: *Structural and Multidisciplinary Optimization* 52 (2015), pp. 179–195 (cited on pages 202–204, 214).

[175] G. H. Yoon. "Topology optimization for stationary fluid-structure interaction problems using a new monolithic formulation." In: *International Journal of Numerical Methods in Engineering* 82 (2010), pp. 591–616 (cited on page 203).

[176] G. H. Yoon. "Stress-based topology optimization method for steady-state fluid-structure interaction problems." In: *Computer Methods in Applied Mechanics and Engineering* 278 (2014), pp. 499–523 (cited on page 203).

[177] N. Jenkins and K. Maute. "An immersed boundary approach for shape and topology optimization of stationary fluid-structure interaction problems." In: *Structural and Multidisciplinary Optimization* 54 (2016), pp. 1191–1208 (cited on pages 203, 204).

[178] R. Picelli, W. M. Vicente, and R. Pavanello. "Evolutionary topology optimization for structural compliance minimization considering design-dependent FSI loads." In: *Finite Elements in Analysis and Design* 135 (2017), pp. 44–55 (cited on pages 203, 204).

[179] F. Feppon et al. "Topology optimization of thermal fluid-structure systems using body-fitted meshes and parallel computing." In: *Journal of Computational Physics* 417 (2020), p. 109574 (cited on pages 203, 204).

[180] H. Li et al. "Three-dimensional topology optimization of a fluid-structure system using body-fitted mesh adaption based on the level-set method." In: *Applied Mathematical Modelling* 101 (2022), pp. 276–308 (cited on pages 203, 204, 214).

[181] T. J. R. Hughes, A. A. Oberai, and L. Mazzei. "Large eddy simulation of turbulent channel flows by the variational multiscale method." In: *Physics of Fluids* 13 (2001), pp. 1784–1799. DOI: https://doi.org/10.1063/1.1367868 (cited on page 209).

[182] R. Codina, J. Principe, and M. Avila. "Finite element approximation of turbulent thermally coupled incompressible flows with numerical sub-grid scale modelling." In: *International Journal of Numerical Methods for Heat & Fluid Flow* 20 (2010), pp. 492–516. DOI: https://doi.org/10.1108/09615531011048213 (cited on page 209).

[183] O. Colomes et al. “Assessment of variational multiscale models for the large eddy simulation of turbulent incompressible flows.” In: *Computer Methods in Applied Mechanics and Enginneering* 285 (2015), pp. 32–63. DOI: https://doi.org/10.1016/j.cma.2014.10.041 (cited on page 209).

[184] E. Castillo and R. Codina. “First, second and third order fractional step methods for the three-field viscoelastic flow problem.” In: *Journal of Computational Physics* 296 (2015), pp. 113–137. DOI: https://doi.org/10.1016/j.jcp.2015.04.027 (cited on page 235).

[185] S. Parada, J. Baiges, and R. Codina. “A fractional step method for computational aeroacoustics using weak imposition of Dirichlet boundary conditions.” In: *Computers & Fluids* 197 (2020), p. 104374. DOI: https://doi.org/10.1016/j.compfluid.2019.104374 (cited on page 235).

[186] S. Parada, R. Codina, and J. Baiges. “Development of an algebraic fractional step scheme for the primitive formulation of the compressible Navier-Stokes equations.” In: *Journal of Computational Physics* 433 (2021), p. 110017. DOI: https://doi.org/10.1016/j.jcp.2020.110017 (cited on page 235).

[187] S. Parada, R. Codina, and J. Baiges. “A VMS–based fractional step technique for the compressible Navier–Stokes equations using conservative variables.” In: *Journal of Computational Physics* 459 (2022), p. 111137. DOI: https://doi.org/10.1016/j.jcp.2022.111137 (cited on page 235).

[188] J. Baiges et al. “A finite element reduced-order model based on adaptive mesh refinement and artificial neural networks.” In: *International Journal of Numerical Methods in Engineering* 121 (2020), pp. 588–601 (cited on page 236).

[189] S.A.Nazarov. “Elasticity polarization tensor, surface enthalpy, and Eshelby theorem.” In: *Journal of Mathematical Sciences* 159 (2009), pp. 133–167 (cited on page 239).

[190] V.A.Eremeyev and V.Konopińska-Zmyslowska. “On the correspondence between two- and three-dimensional Eshelby tensors.” In: *Continuum Mechanics and Thermodynamics* 31 (2019), pp. 1615–1625 (cited on page 239).